Investigating Perfusion of the Human Placenta

Rosalind Janie Aughwane

A thesis submitted for the degree of
Doctor of Philosophy

Institute for Women's Health
University College London

2018

Declaration

I, Rosalind Aughwane, confirm that the work presented in this thesis is my own. Where information has been derived from other sources, I confirm that this has been indicated in the thesis.

Acknowledgements

I wish to thank, first and foremost, my three supervisors, Anna David, Sebastien Ourselin and Andrew Melbourne. Anna, thank you for your constant encouragement and belief in me, for your career advice, and for being such an inspirational role model. Seb, thank you for providing me with a unique opportunity to work within an engineering project; I have learnt more than I could have imagined, and will never think the same way again. And Andrew, thank you for your endless humor, patience and generosity, and for teaching a clinician to code. Developing ideas from our different perspectives and areas of expertise has been a joy. I hope it continues.

The micro-CT work would not have been possible without forming a collaboration with the team at Great Ormond Street Hospital, so I must thank Owen Arthurs and Neil Sebire for their expert input in the project. Also, Alex Virasami, for help in histological slide preparation. But mostly I need to thank Ciaran Hutchinson, micro-CT guru, for late nights in the cave, and for PhD support and moaning.

The MRI work would not have been possible without a large multidisciplinary team at UCLH. Giles Kendall set up the MRI service at UCLH, and has been incredibly supportive of this work. Roxanne Gunney, Clinical Radiologist, reported all fetal brain imaging. Magdalena Sokolska went above and beyond the call of duty, optimising the sequences, with late nights spent playing in the scanners, and Lee expertly scanned our women, whilst maintaining a remarkable tolerance for back seat scanners. Thank you also to David Atkinson and Alan Bainbridge, for encouraging me to do this work and providing expert guidance.

I need to thank the clinical teams and Research Midwives on the Fetal Medicine Unit at UCLH for supporting this work. Raj for teaching me to scan. And Bekah for being my partner in crime.

Data transfer was possible thanks to the hard work of Tom Doel and James Moggridge, who set up GIFT-Cloud and kept it working. I must also thank all the members of the GIFT-Surg team, for being so welcoming of a clinician, and in particular mention Efthymios, Michael, Guotai and Prem. Tom Vercauteren provided a lot of help and support during this work, and is an inspiration.

Thank you to Nat for the lunches/counselling sessions, and Sara for being my career mentor – I do everything you say. Also, thank you to Tash, for all your encouragement, and for making me run.

I thank all my friends and family for their endless support. And finally, thank you to my wonderful husband Paul, for supporting me completely in everything I do. And for all the tea.

Abstract

Placental insufficiency is a significant cause of morbidity and mortality, accounting for one third of antenatal stillbirths. It occurs when the maternal spiral arteries fail to remodel normally in early pregnancy, leading to inadequate maternal perfusion of the placenta. The fetus becomes hypoxic and if not delivered prematurely may ultimately die. Assessing the placenta is therefore clinically important, to diagnose placental insufficiency *in vivo,* and investigate poor pregnancy outcome *ex vivo*.

Ex vivo placental assessment relies on subjective histological analysis of a small proportion of the placenta, looking for features such as oedema, inflammation and the presence of avascular villi. Regional variation and heterogeneity are not defined. *In utero* clinical assessment is via ultrasound Doppler measurements, looking for increased resistance in the uterine arteries, suggesting poor spiral artery remodeling, and increased resistance within the umbilical artery, suggesting inadequate development of the feto-placental microcirculation. There is therefore an urgent need to develop new ways to evaluate the perfusion of the placenta both *in* and *ex vivo*.

In this thesis I investigate two imaging modalities with the potential to improve our understanding of placental perfusion. *Ex vivo* I develop a placental perfusion and micro-CT imaging technique, to directly visualise the feto-placental microcirculation, before applying the technique to investigate heterogeneity within a cohort of normal term placentae. I investigate differences in vascular density through the placenta at multiple scales.

In vivo I investigate a novel Magnetic Resonance Imaging model of placental perfusion, that combines diffusion weighted imaging with T2 relaxometry, to estimate maternal and fetal placental perfusion. I develop this technique, exploring MRI parameters relating to perfusion in normally grown and growth restricted pregnancies.

This work is important as the techniques developed improve our ability to investigate and understand placental perfusion, and provide potential new parameters of placental function *in vivo*.

Impact Statement

Placental insufficiency is the leading cause of still birth in developed countries, and contributes to lifelong morbidity in affected individuals. At present our understanding of placental function is limited, as is our ability to diagnose it. There is no treatment currently available, however there is ongoing research into developing treatments, so improving our understanding of placental function is a priority.

This work developed two novel imaging techniques, with the potential to improve our understanding of the placental microcirculation and fetal and maternal placental perfusion. Microfocus Computed Tomography (Micro-CT) directly imaged the microcirculation of *ex vivo*, contrast perfused placentas. Magnetic Resonance Imaging was used to image *in vivo* placentas, and the first multi-compartment model specific to the placenta was developed. This allowed quantification of fetal and maternal perfusion throughout the placenta, and non-invasive measurement of fetal blood oxygen saturation.

The micro-CT imaging technique developed in this thesis could now be utilised to understand changes in placental microcirculation associated with obstetric syndromes, such as fetal growth restriction, pre-eclampsia and gestational diabetes. This may improve our understanding of the underlying mechanisms that increase the chance of poor outcome in these conditions. Imaging may be useful as part of larger studies, so that changes in growth factors, immunology, or *in vivo* imaging can be correlated to structural changes within the microcirculation. This imaging method may also prove useful clinically, in diagnosing placental pathology after poor obstetric outcome.

The MRI model developed in this thesis may improve our understanding of placental function in health and disease. We can now investigate matching of maternal and fetal perfusion throughout the placenta, and how this varies in health and pathology. Imaging may help us understand the degree of heterogeneity within normally functioning placentas, and at what point placentas start to fail. We can use this technology to improve our understanding of placental insufficiency, and other obstetric conditions, such as pre-eclampsia and gestational diabetes. This imaging may also be beneficial in improving our understanding of other placental conditions, such as complications in monochorionic twins (twin-to-twin transfusion syndrome and selective growth restriction) and in morbidly adherent placentation. This imaging model may also impact on other areas of research, such as the development of novel treatments for placental insufficiency, where it could be used to monitor the response to treatment. This imaging technique may be sensitive to diagnosing placental insufficiency earlier than current clinical imaging, so may become an important clinical tool in the future.

Contribution; Published and Presented Work from the Thesis

Micro Computer Tomography

Pratt, R, Hutchinson JC, Melbourne, A, Zuluaga, MA, Virasami, A, Vercauteren, T, Ourselin, S, Sebire, NJ, Arthurs, O, David, AL. Imaging the human placental microcirculation with micro-focus computed tomography: Optimisation of tissue preparation and image acquisition, *Placenta*, 2017; 60 :36 – 9.

Pratt R, Melbourne A, Hutchinson, JC, Arthurs O, Sebire N, Vercauteren T, Ourselin S, David A. Investigating the site of umbilical cord insertion site on placental perfusion. Poster Presentation at 27th World Congress on Ultrasound in Obstetrics and Gynaecology, 16th September 2017, Vienna, Austria. Ultrasound Obstet Gynecol 50 (2017) 363-4.

Melbourne A**, Pratt R,** Hutchinson, JC, Arthurs O, Sebire N, Vercauteren T, Ourselin S, David A. Quantitative Analysis of the three dimensional fetoplacental vascular tree in normal, term placenta. Oral Presentation at International Federation of Placenta Associations, 2nd September 2017, Manchester, UK. Placenta 57 (2017) 239-40.

Pratt R, Melbourne A, Hutchinson, JC, Arthurs O, Sebire N, Vercauteren T, Ourselin S, David A. MicroCT to investigate the heterogeneity of villous vascular density in normal placentae. Poster Presentation at International Federation of Placenta Associations, 1st September 2017, Manchester, UK. Placenta 57 (2017) 333-34.

Magnetic Resonance Imaging

Melbourne A*, **Aughwane R***, Sokolska M, Owen D, Kendall G, Flouri D, Bainbridge A, Atkinson D, Deprest J, Vercauteren T, David AL, Ourselin, S.Seperating fetal and maternal placenta circulations using multiparametric MRI. *Magn Reson Med*. 2018.

Aughwane R, Sokolska M, Atkinson D, Kendall G, Bainbridge A, Vercauteren T, David AL, Ourselin, S, Melbourne A. MRI Measurement of Placental Perfusion and Fetal Blood Oxygen Saturation in Normal Pregnancy and Placental Insufficiency. *Medical Image Computing and Computer Assisted Intervention* 2018, Granada, Spain.

Pratt R, Melbourne A, Sokolska M, Owen D, Bainbridge A, Atkinson D, Kendall G, Deprest J, Vercauteren T, David AL, Ourselin, S. Novel placental evaluation using multi-modal MRI. Oral Presentation at 27th World Congress on Ultrasound in Obstetrics and Gynaecology, 17th September 2017, Vienna, Austria. Ultrasound Obstet Gynecol 50 (2017) 62.

Melbourne A, **Pratt R**, Sokolska M, Owen D, Bainbridge A, Atkinson D, Kendall G, Deprest J, Vercauteren T, David AL, Ourselin, S. Separation of the Fetal and Maternal Circulation using Multi-modal MRI. Poster Presentation at International Federation of Placenta Associations, 31st August 2017, Manchester, UK. Placenta 57 (2017) 291.

Doel T, Shakir DI, **Pratt R**, Aertsen M, Moggridge J, Bellon E, David AL, Deprest J, Vercauteren T, Ourselin, S. GIFT-Cloud: A data sharing and collaboration platform for medical imaging research. *Computer Methods and Programs in Biomedicine*, 2017; 139: 181-90

Melbourne A, **Pratt R**, Owen D, Sokolska M, Bainbridge A, Atkinson D, Kendall G, Deprest J, Vercauteren T, David AL, Ourselin, S. DECIDE: Diffusion-RElaxation Combined Imaging for Detailed Placental Evaluation. In *ISMRM* (pp. 4800) April 2016. Honolulu, Hawaii, USA.

Melbourne A, **Pratt R,** Owen D, Sokloska M, Bainbridge A, Atkinson D, Kendall G, Deprest J, Vercauteren T, David AL, Ourselin S. Placental Image Analysis using Coupled Diffusion-Weighted and Multi-Echo T2 MRI and a Multi-Compartment Model. In *Medical Image Computing and Computer Assisted Intervention: Perinatal, Preterm and Paediatric Image Analysis workshop*. 2016, Athens, Greece.

I published under my maiden name, Rosalind Pratt, until August 2018.

Award Winning Images from this Thesis

Winner of International Federation of Placenta Association (IFPA) Image Competition 2017

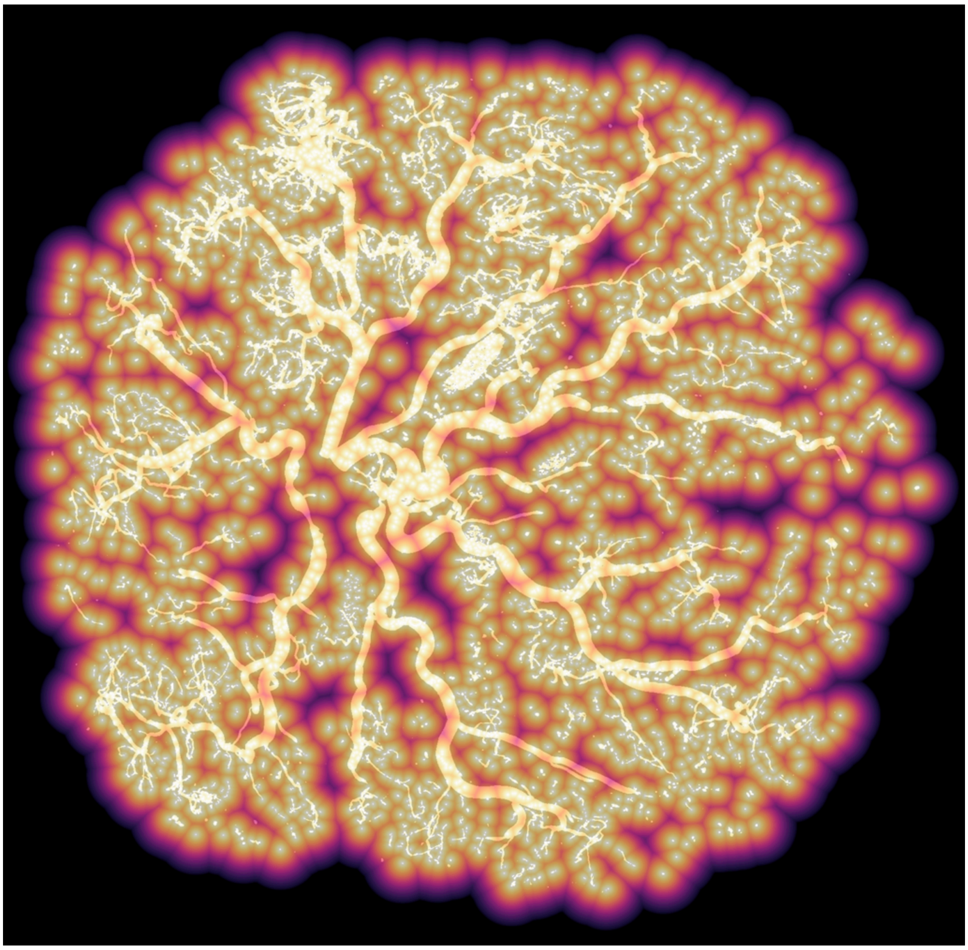

Building effective networks

Exchange of oxygen and food between mum and baby occurs in the placenta. This vibrant image, generated from 3D micro-CT and customised analysis software, shows the distance to the nearest exchanging vessel. The placenta effectively distributes the blood, ensuring a large surface area for exchange and an efficient vascular network.

Second Place in Wired and Wonderful Category of Engineering and Physical Sciences Research Council (EPSRC) Image Competition 2018

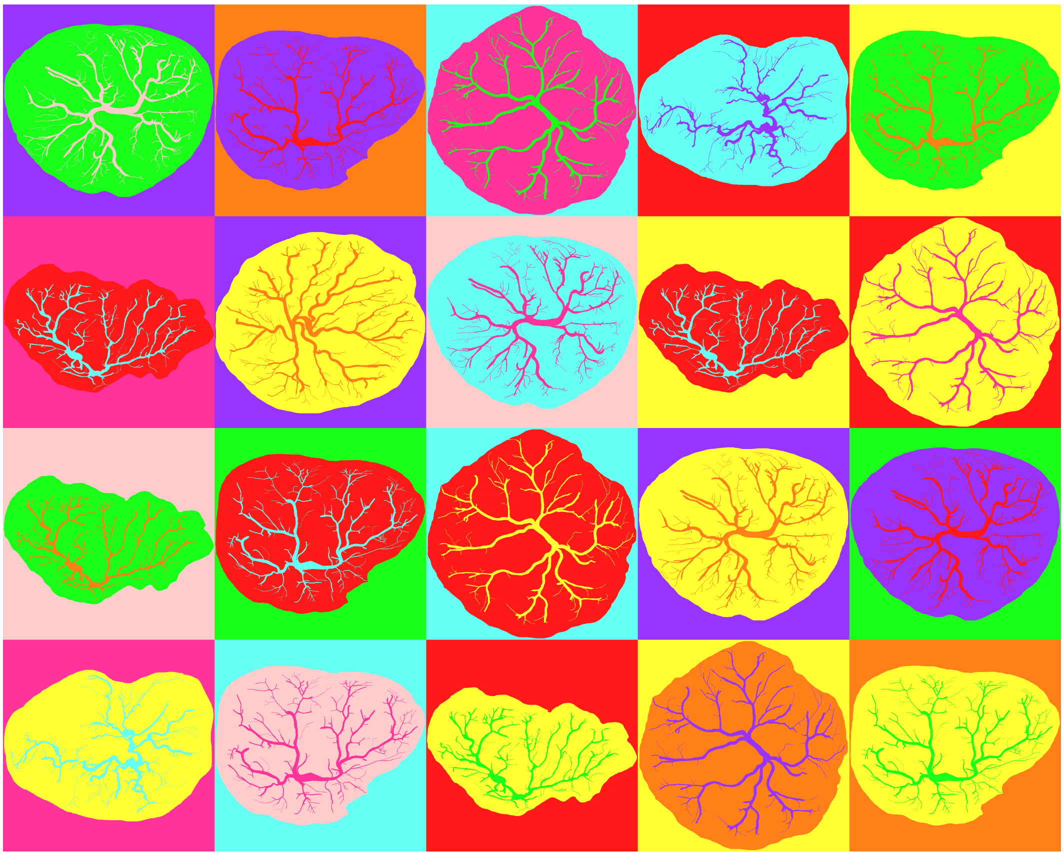

Placental Pop-Art

Placentas are fantastically diverse in shape and appearance, but each one of these examples in our montage successfully supported a new life; our simple colour palette reflects how diversity can arise whilst providing this vitally important life-creating role.

Table of Contents

Table of Figures

TABLE OF TABLES

Abbreviations

ADC	Apparent Diffusion Coefficient
ANOVA	Analysis of Variance
ASL	Arterial Spin Labelling
BOLD	Blood Oxygen Level Dependent
CCI	Cord Centrality Index
CI	Confidence Interval
CNR	Contrast to Noise Ratio
CPR	Cerebroplacental Ratio
DCC	Distance of Cord from Placental Centre
DECIDE	Diffusion-rElaxation Combined Imaging for Detailed Placental
DW-MRI	Diffusion Weighted Magnetic Resonance Imaging
FGR	Fetal Growth Restriction
GIFT-Surg	Guided Instrumentation for Fetal Therapy and Surgery
GUI	Graphic User Interface
H&E	Hematoxylin and Eosin
IVIM	Intravoxel Incoherent Motion
MCA	Middle Cerebral Artery
MHRA	Medicines and Healthcare Products Regulatory Agency
Micro-CT	Micro Computed Tomography
MIP	Maximum Intensity Projection
MRI	Magnetic Resonance Imaging
NR	Not Reported
PE	Placental Eccentricity
PPIAG	Patient Public Involvement Group
R&D	Research and Development
REC	Research Ethics Committee
ROI	Region of Interest
SAR	Specific Absorption Rate
SD	Standard Deviation
SGA	Small for Gestational Age
sIUGR	Selective Intrauterine Growth Restriction
SNR	Signal to Noise Ratio
T	Tesla
TE	Echo Time
TR	Repetition Time
TTTS	Twin to Twin Transfusion Syndrome
UCL	University College London
UCLH	University College London Hospital
VEGF	Vascular Endothelial Growth Factor

1 Introduction

1.1 Summary

In this chapter I present the current knowledge of the placental vascular structure, and understanding of fetal and maternal perfusion in normally grown and growth restricted pregnancies.

The human placenta brings fetal and maternal blood into close proximity, allowing exchange of oxygen and nutrients between the mother and growing fetus. Fetal blood travels within a complex, highly branching fetoplacental vascular network, providing a large surface area for exchange. Maternal blood arrives via the uterine spiral arteries, and perfuses the intervillous space, bathing the fetal vascular tree. When the placental-derived trophoblast cells fail to invade the uterine spiral artery circulation normally in early pregnancy, placental insufficiency occurs, which is an important pathology, accounting for one third of antenatal stillbirths[1]. Normal placenta perfusion and the changes seen in association with placental insufficiency, are poorly understood due to challenges investigating this complex organ. Human maternal placental perfusion is difficult to investigate *ex vivo*, and only limited information is available from the most commonly clinically utilised diagnostic tool, ultrasound Doppler studies of the uterine arteries. The fetal microcirculation is complex and heterogeneous throughout the placenta. Histological studies have been unable to identify a consistent diagnostic sign for placental insufficicency, with 25% of cases complicated by placental insufficiency having a histologically normal placental appearance.

In this thesis, I investigate two imaging methods, *ex vivo* micro-CT and *in vivo* MRI, both of which have the potential to improve our understanding of placental perfusion, and the changes associated with placental insufficiency.

1.2 Placental Circulation

Placental Architecture

The mature human singleton placenta is a discoid organ, approximately 20-25cm in diameter, 3cm thick, and weighing 400-600g. The placenta is supplied with fetal blood via the umbilical cord, which normally has two arteries carrying deoxygenated blood towards the placenta, and one vein returning oxygenated blood to the fetus. The umbilical cord can insert anywhere on the fetal surface of the placenta, known as the chorionic plate, from where the blood is transported across the placental surface via the chorionic arteries. From here deep branching vessels, stem arteries, radiate down into the placental tissue. A lobule is the branching structure attached to a stem artery arising from the chorionic plate[2]. Cotyledons, or lobes, the more commonly used nomenclature, are the placental units visible on the basal plate of the placenta, separated from each other by the placental septae. Each lobe may contain more than one lobule[3].

The villus tree arises via a stem villi, and branches repeatedly to provide a large surface area of 12-14m^2. The villous capillaries form a complex, multi-branching vascular bed within the villi. A minority of villi extend between the chorionic and basal plates, known as anchoring villi, whilst the majority are free floating in the intervillous space. Vessels are covered with only a single cell layer of syncytiotrophoblast, so the fetal blood is in close proximity with the surrounding maternal blood, as little as 1-2µm, allowing gas, nutrient and waste product exchange to occur between the mother and fetus[4].

Chorionic Vascular Tree

The chorionic vessels serve to distribute the blood throughout the placenta. From the point of umbilical cord insertion two main chorionic arteries radiate. These repeatedly divide, through 6 to 8 generations, to form vessels feeding the entire placental tissue. Arterial divisions are both dichotomous, with two equal sized daughter vessels and a mother-to-daughter diameter ratio of 0.6-0.8, and monopodial, with a main daughter vessel staying of similar diameter, and a much smaller daughter vessel with a ratio of 0.1-0.3[5]. The proportion of dichotomous to monopodial divisions appears to differ between placentas with a central and eccentric cord insertion, with the trees of more eccentric insertion placentas being dominated by monopodial divisions, which may be more efficient in transporting blood longer distances, whilst the trees of more central insertion placentas are dominated by dichotomous divisions[5].

Villous Vascular Tree

The villous tree is the functional unit of the placenta. At term the placental villous tree is predominately made up of stem, mature intermediate and terminal villi.

- Stem villi act as the scaffolding of the villous tree, and predominate in the subchorionic region. They have up to four generations of short thick branches, from which further dichotomous branches radiate[6]. Stem villi contain arteries, veins, arterioles and venules, and occasionally superficial capillaries.
- Mature intermediate villi branch directly from the stem villi and contain arterioles and venules mixed with capillaries.
- Terminal villi are the final ramifications, and appear as protruding outgrowths from the intermediate villi. They contain sinusoidally dilated capillary loops of approximately 10-20μm diameter[7], and are the main area of exchange.

Fetal Placenta Perfusion

Fetal blood arrives via two umbilical arteries, then chorionic arteries that run across the placentas surface
↓
Stem vessels branch deep into the placental parenchyma
↓
A complex villous vascular tree provides large surface area for transfer between fetal and maternal blood

Exchange

The intervillous space is filled with oxygenated maternal blood
↑
The spiral arteries remodel in early pregnancy, providing high volumes of blood at low pressure
↑
Maternal blood arrives via the uterine, arcuate and radial arteries

Maternal Placenta Perfusion

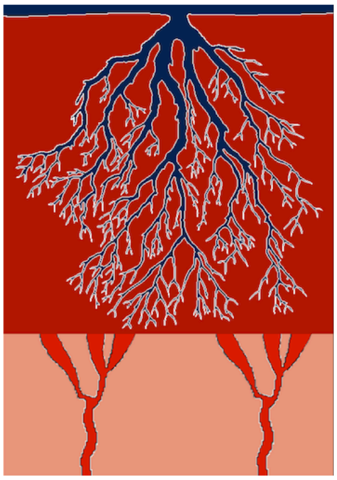

Figure 1; Schematic of placental architecture and fetal and maternal placental perfusion.

1.3 Normal Placental Perfusion

The placenta is a unique organ being perfused by (at least) two cardiovascular systems from the mothers and the fetus(es) (Figure 1). Uterine spiral arteries supply oxygenated maternal blood to the growing placenta and fetus. In early pregnancy extravillous trophoblast cells proliferate from anchoring chorionic villi and invade the decidualised endometrium. Cells invade the endometrium, inner myometrium, and the lumen of the spiral arteries, becoming incorporated in the spiral artery wall as intramural trophoblast. The endothelium, vascular smooth muscle and elastic lamina are destroyed, and replaced by fibrinoid, transforming the spiral arteries from muscular vessels to distended, thin walled vessels by the end of the first trimester[8]. The placenta thus establishes its own low pressure, high conductance vascular system early in pregnancy, ensuring adequate supply of maternal blood.

Flow rate within the intervillous space is difficult to measure, and there is therefore a paucity of data. There have however been some attempts to estimate it. The most direct measurement was by Burchell et al[9], who performed angiographic studies at different stages of pregnancy, measuring the time taken for a radioactive dye to disperse, finding a mean velocity within the intervillous space of $6x10^{-4}$ m/s. Other approaches have estimated flow based on the input volume of blood divided by the intervillous space volume within the placenta, giving a flow rate of 5×10^{-4} m/s[10], and computational modelling using 3D confocal imaging of the villous structure, giving a flow rate of 1×10^{-3} m/s[11].

The feto-placental vascular network is a result of vasculogenesis, the development of blood vessels de novo from pluripotent mesenchymal stem cells, and angiogenesis, the creation of new blood vessel networks by branching and elongating previously existing blood vessels, and trophoblast mediated arterial remodelling[12]. Numerous factors are important in placental angiogenesis and vasculogenesis, including Vascular Endothelial Growth Factor (VEGF), Fibroblast Growth Factor, Placental Growth Factor, Epidermal Growth Factor and Angiopoietins[13].

Vasculogenesis starts at day 21 post conception, with the differentiation of haemangiogenic progenitor cells, which in turn differentiate into hematopoietic cells and angioblastic cells, the precursors of the first vessels[12]. From these, angiogenesis creates the entire vascular network. Highly branched villous capillary beds develop during the first half of pregnancy, known as the branching phase. Capillaries transform to muscularised arterioles, and arterioles enlarge into arteries, which lengthen the arterial tree allowing efficient delivery of blood to distal regions of the placenta[13] .

From about 25 weeks' gestation angiogenesis switches from branching to non-branching in the peripheral villi. Long, poorly branched capillary loops form, causing a large increase in the volume of capillaries in the late second and third trimesters[14], without a change in the mean capillary diameter in the same time period[15]. The increase in capillary bed results in a reduction in fetoplacental blood flow impedance.

Blood flow within the fetal capillaries is difficult to estimate. Computer modelling work using 3D confocal volumes of villous capillaries have estimated flow to be in the region of 3×10^{-4} m/s[16], which is in keeping with the standard estimation of capillary blood flow in other organs. Another approach, calculating flow rate based on the villous volume and the blood volumetric flow rate in the umbilical artery, estimated a flow rate of 2.75×10^{-4} m/s for the intermediate vessels, and 7.35×10^{-4} m/s for the terminal capillaries[17].

There is a definite relationship between maternal spiral arteries and fetal lobules, although the nature of this relationship is not clear[6]. Two schemata have been proposed; that the spiral arteries feed into the centre of the fetal lobule, with blood flowing laterally into the interlobular area[18], or that blood is delivered into the interlobular space, and circulating around and into the lobule[19]. Whichever is true, each lobule forms an independent materno-fetal exchange unit.

Variation in vascularisation of normal placenta

There are considerable variations in villous morphology within a normal placenta[20]. Histological analysis by Fox et al showed geometric variation in the proportion of fibrotic villi and villi with excessive thickening of the basement membrane, histological signs pertaining to placental hypoxia secondary to reduced maternal perfusion, with increased frequency in the subchorionic compared to the maternal area, and peripheral compared to the central zone[20]. They found no statistically significant geometric relationship in the number of hypovascular or avascular villi, their measure of feto-placental vascularisation, although they did show an increase through the placental stroma approaching the chorionic plate (156 maternal area vs 196 intermediate area vs 232 subchorionic area) and with the distance from cord insertion (156 centrally vs 222 peripherally), suggesting there may be reduced vascular density in the placental peripheries.

Variation in feto-placental vascular density has been hypothesised to relate to variation in maternal perfusion, and there is evidence that the fetoplacental blood flow can be modulated, via stem artery vasoconstriction, to match maternal perfusion[6]. Romney and Reid suggested the arteries within stem villi may be spiral to allow control over the rate of fetal blood delivery to a particular region[21]. Sebire et al hypothesised that there may be a mechanism by which the villous tree reacts to local uteroplacental oxygenation via autoregulation of vascular constriction of the smooth muscle in the arterial wall of stem vessels[22]. These theories support maternal-fetal perfusion matching, which would facilitate efficient exchange regardless of physiological changes in maternal blood supply, that could occur daily secondary to maternal position. The mechanism by which vasoconstriction may occur is not known, with proposed mechanisms including nitric oxide released by the villous vascular tree causing vasodilation in stem arteries supplying well oxygenated areas[22], or inhibition of potassium channels causing vasoconstriction in the smooth muscle or small arterial walls in poorly oxygenated areas[23].

1.4 Pathological Placental Vascularisation; Placental Insufficiency

Pathophysiology of Placental Insufficiency

Placental insufficiency is a condition of inadequate placental perfusion[24], resulting in a decrease in the exchange of oxygen and nutrients between the mother and fetus. It is a consequence of inadequate remodelling of the maternal spiral arteries by trophoblast cells in early pregnancy, resulting in reduced utero-placental blood supply[25].

In normal pregnancy, extra villous cytotrophoblast invades beyond the decidua into the inner myometrium, the spiral arteries dilate, especially distally, funnelling the blood and creating a high flow low pressure supply of maternal blood to the placenta. In placental insufficiency superficial invasion and minimal spiral artery dilation result in low volume, high pressure delivery of turbulent blood to the intervillous space[26].

The fetoplacental microvascular tree in placental insufficiency shows a predisposition to non-branching angiogenesis, increased intervillous space, longer intermediate and terminal villi, and reduced mature intermediate and terminal villi density[2527]. There is disagreement on whether the density of stem vessels differs in placental insufficiency, with some studies reporting reduced density in association with abnormal umbilical Doppler studies[28,29], whilst others have found a normal density of stem arteries, but a reduced volume of intermediate and terminal vessels[30,31]. Abnormality of stem vessels have also been reported, with vessel wall thickening, decreased vessel lumen size[32], and an increased frequency of luminal obliterations[33] all reported in association with placental insufficiency.

The changes seen in the microvasculature were originally thought to be caused by a primary defect in terminal villi development[32,34] . However, it is now thought they are secondary to poor maternal perfusion, with two hypothesised mechanisms. High pressure turbulent maternal flow may damage the villous architecture[26], leading to hypoxia, ischaemia-reperfusion injury, and oxidative stress, all of which are proposed aetiologies for the changes seen in the vascular tree[25]. Alternatively, chronic stem vessel vasoconstriction, in response to low maternal oxygenation, may lead to irreversible changes to stem vessels[35]. This would be widespread and chronic in a situation of poor placentation, leading to permanent artery wall thickening and eventual destruction of the distal vasculature[35](Figure 2).

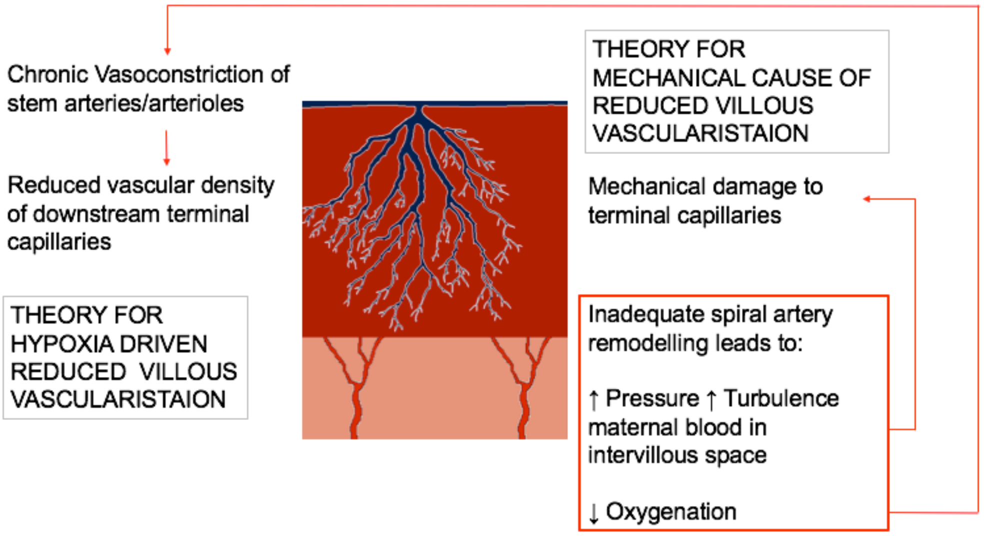

Figure 2; Diagram showing the two proposed mechanisms of reduced fetoplacental villous vascular density seen in placental insufficiency. The mechanical theory propose mechanical damage to the terminal capillaries from high pressure, turbulent maternal blood, delivered by poorly re-modelled maternal spiral arteries[25,26]. The hypoxic theory proposes chronic proximal constriction of small stem arteries ad arterioles secondary to hypoxia due to poor maternal blood supply, resulting ultimately in reduced villous vascular density down-stream[35].

Fetal and maternal consequences of placental insufficiency

Placental insufficiency is a significant cause of morbidity and mortality, accounting for 32% of antenatal stillbirths and 26% of intrapartum stillbirths in high-income countries[1].

Placental insufficiency manifests clinically in a variety of fetal and maternal conditions. The mother can develop gestational hypertension, or proteinuric hypertension, known as pre-eclampsia. Left untreated this can have severe complications such as eclampsia, liver rupture, stroke, pulmonary oedema, kidney failure and death[36]. It remains one of the main causes of maternal mortality worldwide[37].

The growing fetus is starved and hypoxic, resulting in reduced fetal growth, known as fetal growth restriction (FGR). FGR usually refers to a fetus that has not reached their growth potential, as opposed to small for gestational age (SGA) which refers to a small fetus with an estimated fetal weight below a specified cut off, usually 10%. By definition 10% of normal fetuses will be SGA. It should also be noted that an FGR fetus is not necessarily small, but failing to achieve their growth potential and may in fact appear to be appropriately grown. FGR is a clinical diagnosis which has previously been poorly defined in the literature, however a recently published Delphi consensus determined standardised definitions for FGR[38], which should help unify future studies.

FGR can be further divided into two different phenotypes, with onset either early or late in gestation. Early onset affects 1-2% of pregnancies, representing 20-30% of all FGR cases, and is associated with severe placental disease and high rates of maternal pre-eclampsia[39]. There is a high level of fetal hypoxia, with associated changes in fetal cardiovascular output, and therefore changes to ultrasound measurement of fetal Doppler parameters[40], as discussed below. Late onset FGR affects 3-5% of pregnancies and is associated with much milder placental disease. There is a much lower rate of maternal pre-ecalmpsia, and the fetus is less hypoxic. Fetal Doppler measurements often remain normal in this group, making diagnosis more challenging[41]. The mortality is lower, although it is a common cause for late still birth due to the mature fetus having a low tolerance to hypoxia[40].

To diagnose FGR, clinicians look for signs suggestive of hypoxia and starvation on ultrasound examination, including reduced growth velocity and abnormal maternal and fetal Doppler measurements[40]. Fetal growth is commonly asymmetric, with proportionally smaller femur length and abdominal circumference, compared to head circumference. In the later stages of chronic hypoxia, there is cardiac output redistribution, in an attempt to divert blood to the brain and therefore protect neurodevelopment[42]. However in severe chronic anaemia this strategy is not sufficient, and changes in brain structure associated with FGR include reduced total brain volume, altered cortical volume and structure, myelination defects, and impaired brain connectivity, with less efficient networks and evidence of neuronal migration deficits[42]. The effect hypoxia has on the developing brain depends on the severity and timing of the hypoxia, and the timing of delivery, with severity and the gestational age at onset being the best predictors of neurological outcome[43]. Phenotypic outcome is variable, but FGR infants demonstrate significantly poorer motor and cognitive ability at school age compared to normally grown age-matched controls[44], as well as having higher rates of memory and neuropsychological dysfunction[42]. FGR is also a significant risk factor for developing cerebral palsy[42].

Other key organs also become hypoxic. Renal under perfusion results in reduced glomerulofiltration rate, and therefore a reduced liquor volume in which the fetus can move to develop their musculoskeletal system, and breathe in amniotic fluid to develop their lungs. This may explain the increased rate of respiratory distress syndrome at birth in FGR neonates compared to age matched controls[45]. There is also an increased rate of neonatal necrotising enterocolitis, which may be secondary to poor perfusion of the gut in utero[45].

As well as having immediate affects, placental insufficiency is linked to metabolic remodeling of the fetus, which increases the risk of many diseases later in life, including coronary heart disease, stroke, hypertension, insulin resistance and diabetes [3,46,47].

If hypoxia becomes too prolonged and severe, fetal death will occur.

Clinical Assessment of Placental Function

Diagnosis of placental insufficiency is via ultrasound assessment. Maternal placental perfusion is estimated *in vivo* with Doppler measurement of uterine artery blood flow. Uterine arteries dilate during normal pregnancy, providing low impedance blood flow. This does not occur in placental insufficiency, making the uterine arteries a surrogate marker of downstream maternal placental perfusion. Uterine arteries are found to have a smaller diameter, and the quantified blood volume flow is significantly reduced, in pregnancies complicated by FGR compared to normal controls[48,49].

The test used in clinical practice to measure maternal perfusion is the uterine artery pulsatility index. This is a ratio which avoids the errors associated with measuring uterine artery volume blood flow which is derived from the time-average velocity and vessel diameter and is therefore prone to a high error rate and difficulties with reproducibility. There is a well-established association between increased uterine artery pulsitility index in the late second trimester, and the development of early onset pre-eclampsia and FGR[50,51,52,53]. However, the specificity of the test is poor, with most pregnancies that have raised uterine artery Doppler pulsatility index not developing placental insufficiency or FGR. It is therefore not useful in screening a low risk population. In addition, the majority of late onset FGR cases have a normal uterine artery pulsatility index[53].

The fetoplacental circulation can be examined *in vivo* with umbilical artery Doppler measurements. Umbilical blood flow increases three-fold between 22 weeks gestational age and term[54]. End-diastolic velocity increases throughout gestation, becoming around 50% of systolic velocity at term in normal pregnancies, likely signifying decrease in flow impedance secondary to the large increase in terminal capillary volume in the third trimester. There is strong evidence of an association between increased umbilical artery pulsatility index and decrease or reversed end-diastolic flow, and increased resistance in the fetoplacental vascular bed, as seen in placental insufficiency[6,55].

This relationship has been validated in animal models, where progressive embolization of fetal vessels in sheep resulted in progression from normal to absent to reversed end diastolic flow in the umbilical artery[56].

Cardiac output redistribution can also be detected antenatally, as a low middle cerebral artery (MCA) pulsatility index, caused by cerebrovascular dilation aiming to increase cerebral blood flow.

The two measures can be combined in the cerebroplacental ratio (CPR), which is calculated by dividing the MCA and umbilical artery pulsatility indexes. Abnormal CPR has been shown to be associated with lower birthweight centile, higher rates of fetal distress in labour, increased rates of fetal acidosis on cord blood pH, and increased rates of admission to the neonatal intensive care unit[57]. It may be particularly useful in late onset FGR, where umbilical artery and MCA Doppler parameters often remain individually within the normal range, but the ratio suggests relative brain vasodilation and cord vasoconstriction suggesting fetal compromise.

There is currently no clinically available method to measure the fetal or maternal perfusion of the placenta itself, and therefore no way to investigate, in human pregnancy, the heterogeneity of perfusion or matching of fetal and maternal perfusion within the placenta across the placental barrier.

Histopathological Assessment of the Placenta

There is no pathognomonic feature on placental histology that is diagnostic of placental insufficiency or FGR, and there is no single finding that can be correlated with severity of phenotype. There are several reasons for this. Firstly, studies historically have included early and late onset disease, with and without pre-eclampsia, and of different severities. Secondly, different studies have used different definitions for FGR, often using only a cut off birthweight centile, and so including placentas from normally grown small as well as FGR pregnancies. The result has been examination of placentas from a heterogeneous population. The development of Doppler measures of fetal and maternal placental perfusion, and the increased understanding of the different phenotypes and importance of separating them, has improved our ability to study more homogenous groups of pathology, which has improved this situation.

These difficulties may provide explanation to why one quarter of placentas from pregnancies thought to be growth restricted appear histologically normal[58]. The most common abnormal finding is patchy placental infarcts, which is seen in 25% of term FGR placentas, compared to 10% of the normal population[58]. Other, non-specific, findings include villous infarct and placental abruption or subchorionic haemorrhage. Lesions relating to hypoxia, and therefore suggestive of reduced maternal perfusion, include syncytiotrophoblast knots, excess cytotrophoblast cells, thickened basement membranes, villous fibrosis, and hypovascular terminal villi, with reduced villous volume, reduced intervillous space, and non-specific inflammatory lesions. The rate of these hypoxic lesions appears to be higher in FGR pregnancies associated with abnormal uterine artery Doppler parameters, compared to FGR pregnancies with normal Doppler's, or normal controls[59]. Villous fibrosis and hypovascular terminal villi may be more common findings in FGR associated with early onset pre-eclampsia compared to FGR alone[60].

From the perspective of fetal vascularisation, there are increased rates of small, fibrotic terminal villi seen in FGR compared to normal placentas, the frequency of which increases when umbilical artery Doppler's are abnormal[61].

Histological findings in late onset FGR are even less common than in early onset FGR. There is an increased rate of infarct compared to normal controls, but fewer lesions are seen than in early onset FGR, and many placentas appear normal[62].

Treatment of Placental Insufficiency

At present, there is no effective treatment for placental insufficiency, so monitoring aims to determine the most appropriate gestational age for delivery, balancing the risks of a chronically compromised fetus in utero against the risk of severe prematurity.

In the future, treatment may be possible, and there is on-going research into potential therapies[63], including sildenafil citrate[64] and maternal gene therapy with over expression of Vascular Endothelial Growth Factor (VEGF) within the uterine arteries, both of which have been shown to improve maternal blood flow to the placenta in animal models[65,66].

1.5 Investigating the feto-placental vascular tree

In order to assess a vascular tree, we need to be able to acquire detailed three-dimensional imaging of the vascular tree, with sufficient resolution to resolve the smallest vessels of interest, and a quantitative statistical method for summarising the vascular tree that is biologically and physiologically meaningful.

There have been several attempts to investigate the fetoplacental vascular tree in three dimensions, to further our understanding of the changes in vascular structure in the pathologies discussed above. Techniques include reconstructions of serial semi-thin sections, which were photographed, magnified and converted into drawings[67], corrosion casts scanned using electron microscopy[68], whole slide three dimensional digital reconstruction[69] and confocal laser microscopy[70,71]. All of these methods are limited as they rely on reconstruction of 2D slices rather than capturing three-dimensional volumes. They also lack the field of view to capture the majority of the vascular tree, or the resolution to resolve the microcirculation.

1.6 Micro Computed Tomography

Microfocus Computed Tomography (micro-CT) utilises X-rays in order to produce three-dimensional image volumes. X-rays are electromagnetic radiation, like visible light, but with a shorter wavelength of around 0.01-10 nanometres.

Micro-CT scanners produce X-rays by creating electrons within a vacuum from a hot cathode. The electrons are accelerated, using a high voltage, into a beam which is focused through a magnetic lens into a small spot on a metal target. The subsequent sudden deceleration of the charged electrons when they hit the target produces both heat (99.3%) and X-rays (0.7%). The area on the target that is struck by the electron beam is referred to as the focal spot. Micro-CT machines utilise a micro-focus source, meaning the size of the focal spot is only a few microns across, compared to millimetres in clinical machines, allowing a higher degree of magnification and preventing blurring of the images.

A micro-CT scanner produces a spectrum of X-rays, rather than a single energy band, as is achieved in a synchrotron. Characteristic X-rays are produced when an electron with sufficient energy collides with an inner shell electron belonging to an atom within the metal target. The atomic electron is displaced and the resultant promotion of an outer shell electron to a more stable (lower energy) position within the atom results in the emission of an X-ray. This type of X-Ray emission is dependent on the particular material in the metal target[72]. It can be seen as a characteristic spike of energy within the X-ray spectrum. Bremstrahlung (braking) radiation is also generated within a micro-CT X-ray source. This occurs when an electron within the generated beam passes close to the nucleus of an atom within the metal target but does not collide with an atomic electron. The resultant slowing, or braking, of the electron results in X-ray emission at a range of energies.

X-rays leave the source as a cone beam. The X-ray beam passes from the source to the detector, with the object to be imaged being placed on a turntable in between

(Figure 3). X-rays passing through the object are attenuated, forming a shadow on the detector. The detector converts the X-rays into light via a scintillator material, and a photodiode in each pixel of the detector array generates an electrical signal in proportion to the light produced, forming the digitised radiograph. Magnification is achieved by bringing the object closer to the X-ray source (Figure 3).

Micro-CT scanners create radiographs of the object through multiple degrees of rotation (usually 180 or 360 degrees' of rotation), by rotating the object on a turn-table[72]. Computer algorithms, such as Feldkamp's filtered back projection, reconstruct the 3D internal structure using the intensity values of the projected images[72].

The resulting volumes are made up of elements called voxels, each with a grey-scale value that represents the X-ray attenuation at the corresponding location in the scanned object[73]. Voxel size represents the volume elements into which a reconstructed micro-CT volume is divided. The voxel size is a function of the detector pixel size and the geometric magnification, being dependent on the source-to-object and source-to-detector distances (Figure 3)[74]. Features that are smaller than the voxel size are difficult to distinguish on the reconstructed CT image.

Spatial resolution is a measure of the imaging resolving power of a micro-CT system, the ability to separate two adjacent features[73]. It is determined by the imaging system, with focal spot size, detector pixel size and cone beam geometry being important[72]. The imaging noise and number of projections per rotation also play a role[75]. Finally the reconstruction algorithms used also influence the final volume resolution[75].

The modulation transfer function of a system is its ability to transfer contrast at a specific resolution from an object to an image volume[76]. This can be calculated by imaging a phantom with a range of fixed line widths, and has units of line pairs per distance unit[73]. This approach however is limited by not taking into account the noise in the imaging[73].

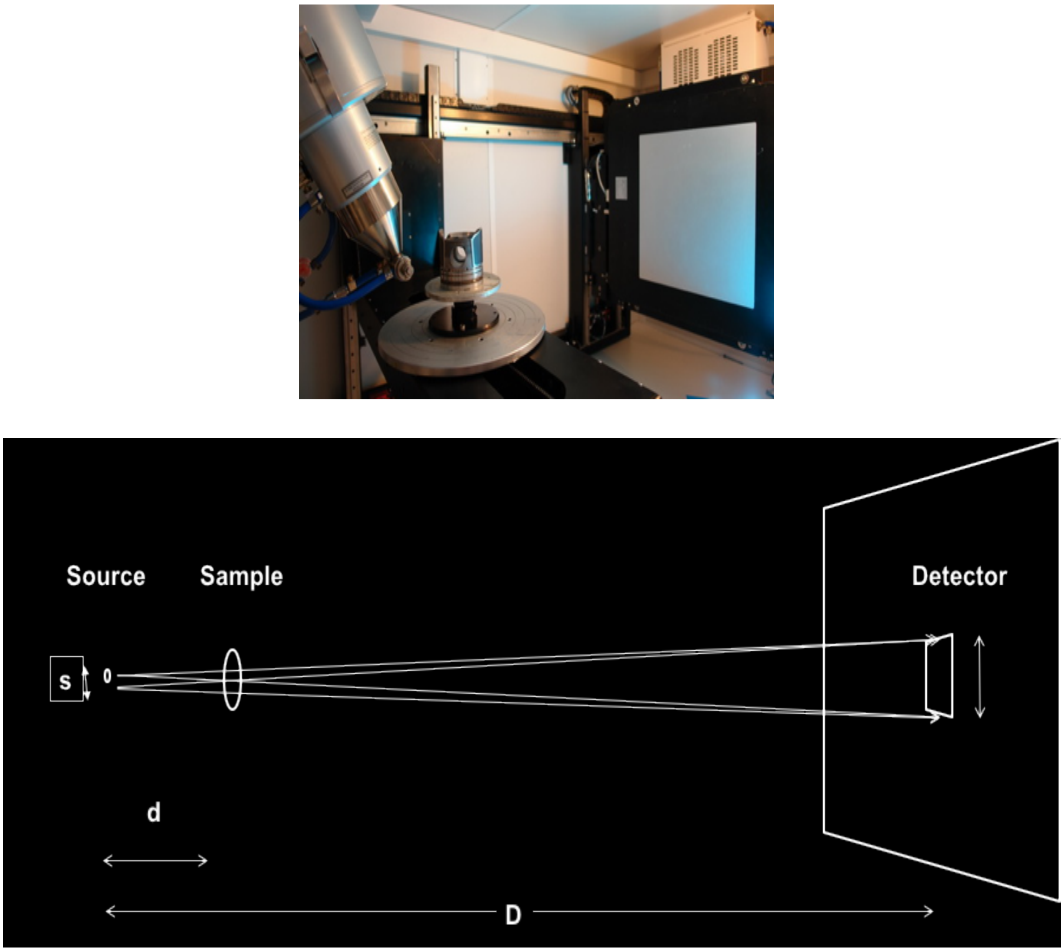

Figure 3; Micro Computed Tomography Hardware.
Upper; Photo of a micro-CT scanner, showing the X-ray source, turn table, and detector (XTH225 ST Micro-CT, Nikon Metrology, Tring, UK). Lower; Diagrammatic representation of the geometry of a micro-CT scanner. The closer the sample is to the source (d) the greater the magnification. d=source-to-object, D = source-to-detector.

Micro Computed Tomography of the Fetoplacental Vascular Tree

The ability of micro-CT to non-destructively capture three dimensional images at high resolution has made it a method of interest in biological investigation[74]. The technique naturally lends itself to image structures with high X-ray contrast, such as bone[77,78]. However the use of radio-opaque contrast agents has made examination of the vascular system possible[79,80], and has been used to investigate organs such as kidney[81], liver[82] and heart[83].

Rennie et al[84] have utilised micro-CT extensively to investigate the contrast perfused feto-placental circulation of the mouse placenta. The small size of the organ allowed complete visualisation of the placental vascular tree. They perfused the tissue with Microfil and imaged with an isotropic voxel size of 13µm. Their first work examined development of the vascular tree with increasing gestational age, finding an increasingly complex branching pattern as gestational age increased[84]. Further work investigated the effect of exposure to polycyclic aromatic hydrocarbons (found in environmental pollutants and cigarette smoke) on the feto-placental vascular tree[85]. This work was analysed with automated vascular segmentation, allowing assessment of the branching structure, and haemodynamic modelling with calculation of vascular resistance. They found polycyclic aromatic hydrocarbon exposure led to a sparse vascular tree, with increased vessel tortuosity and vascular resistance, thus reducing blood flow[85].

Langheinrich et al[86,87] were the first to investigate the potential of micro-CT as a method to investigate the human placental vascular tree. Placental vessels were perfused with either barium sulphate or the lead based, proprietary microvascular contrast agent Microfil (Flow Tech, Carver, MA), and then full depth 2mm blocks were imaged with an isotropic voxel size of 12µm, then 4µm. Images were reconstructed, and the vascular density calculated. They found a significant reduction in vascular density in FGR placentas compared to placentas from uncomplicated pregnancies (20.5 +/- 0.9% vs 7.9 +/- 0.9% uncomplicated vs FGR placentas, $p<0.001$)[87]. These vascular density findings are consistent with other published data on vascularisation using more conventional stereological techniques. However they only looked at very small samples of the placenta, and did not use the technology to investigate the vascular tree.

Junaid et al took a different approach imaging the whole human placenta, using a corrosion casting technique[88]. 12 normal placentas, and 6 from pregnancies complicated with FGR were imaged with a voxel size of 80 to 100µm. They found a significantly smaller number of chorionic artery branches in FGR placentas compared to controls, however when normalised for placental weight this difference was no longer apparent[88]. Further work comparing 12 normal and 12 FGR placentas found longer venous and shorted arterial vasculature in FGR compared to normal placentas[89]. They went on to investigate the branching structure, dividing the branches into deciles, and showed a reduction in branch numbers from the fourth centile up in FGR compared to normal placentas[89]. This work was important as it was the first work in the human placenta to attempt analysis of the complex vascular tree, and to show difference in the vascular tree in FGR placentas. This work suggests the technique could be useful in improving our understanding of placental vascularisation, and in the changes in pathology, that may improve our understanding of placental disease. However, it also demonstrated the difficulty in working with such complex data.

1.7 Investigating Fetal and Maternal Placental Perfusion in vivo

To investigate the maternal and fetal perfusion of the human placenta *in vivo*, an imaging method must be capable of detecting signal that relates to blood flow with a sensitivity that is likely to detect the changes in perfusion seen in placental insufficiency. It should ideally to be able to separate fetal and maternal perfusion, and to be able to capture the entire placenta at any gestational age, allowing investigation of whole placental function. Higher resolution imaging is likely to provide the most detailed assessment.

Most importantly, imaging must be safe for both the mother and fetus. For this reason, ionising radiation should be avoided, due to its link to childhood cancers, as should use of an exogenous contrast agent, unless known to be safe in pregnancy. Unfortunately, this excludes the majority of medical perfusion imaging techniques, that rely on contrast agents.

With the increasingly widespread availability of three-dimensional ultrasonography, there has been interest in 3D power Doppler measurement of placental perfusion. Interobserver variability has been reported to be low[90], and normal ranges have been reported[91], and an association between indices and estimated fetal weight centile[92]. When this approach has been investigated to compare normal and FGR placentas, only some FGR placentas have shown abnormal values[93], or values have been found to be significantly lower in FGR only after umbilical artery Doppler measurements have become abnormal[94].

An important limitation of this technique is the inability to image the whole placenta at later gestational ages, due to the field of view of ultrasound. A ‘placental biopsy’ approach has been adopted from the second trimester, selecting small areas of interest within the placenta, but results have been found to be dependent on the sampling site[94]. This technique therefore suffers from placental spatial variability.

1.8 Placental Magnetic Resonance Imaging

Magnetic resonance imaging (MRI) uses strong magnetic field gradients and radiofrequency pulses to generate images of the body. It utilises a property of protons called spin. In the presence of the external magnetic field, spins of many protons form a magnetisation. Magnetisation can be manipulated by radio-frequency pulses, that alter its alignment away from the direction of the main magnetic field[95]. Once the radio frequency is stopped, magnetisation returns to the original orientation, inducing current in the receiver coil. The rate at which magnetisation returns to the equilibrium depends on the properties of the proton spins, which depend on how the water molecule is interacting with its environment, and this signal provides the contrast of MR images[95].

There are two ways in which the net proton magnetisation relaxes to the original state; T1, or spin-lattice, and T2, or spin-spin, relaxation. These form the basis for much of the imaging contrast.

When a radiofrequency pulse is applied, protons change from being aligned with the main magnetic field into a transverse magnetic field, and gain additional energy. In order to return to their original energy state they must lose this energy to the surrounding tissue, or lattice, which has a much larger volume[95]. As the protons loose transverse magnetisation and recover longitudinal magnetisation they return to their original alignment in relation to the main magnetic field, so that the net magnetisation returns to its original value[95]. This is known as T1, or spin-lattice, relaxation, and is characterised by the interaction between the protons and their environment, the lattice[95].

When a radio frequency pulse is applied to a tissue, the net spin of the protons precesses at a specific frequency, known as the Larmor frequency, with the spins all in phase or alignment[95]. Once the radiofrequency pulse stops, the spins start to dephase. This occurs when two protons come close to one another, affecting each other’s magnetic field and therefore changing the precession frequency. Once they move apart they return to precessing at the Larmor frequency, but their phase angle will have changed[95]. Over time multiple interactions cause all the phase angles to change, so that the spins are no longer aligned. An exponential decay in net dephasing is detected, from the maximum straight after the excitation pulse, down to zero[95]. This signal is known as T2, or spin-spin, relaxation and is dependent on the interaction of molecules within a tissue.

There are two types of pulse sequences used to acquire images; spin-echo and spin-gradient. Both start with a radiofrequency excitation pulse. In spin-echo sequences the spins are then allowed to dephase naturally, before applying a second pulse which flips the spins 180 degrees, reversing their phase angles[95]. After the same length of time as was allowed for the protons to dephase, the spins come back into phase, producing an echo[95]. By reversing the phase, the magnitude of echo produced is dependent on T2 relaxation and diffusion, but not on magnetic field inhomogeneity or tissue susceptibility.

With gradient-echo sequences, which have the advantage of being much quicker, instead of a 180-degree refocusing pulse, a positive gradient is applied. This reverses the magnetic field gradient so that the spins all come back together, producing the echo. However, unlike the refocusing pulse in spin-echo sequences, the positive gradient does not compensate for inhomogeneity in the magnetic field[95]. The signal from gradient-echo sequences is therefore known as T2*, and is dependent not only on T2 and diffusion, but also magnetic field inhomogeneity and tissue susceptibility[95].

Structural Placental MRI

The placenta can easily be visualized on MRI, with a clear boundary against the amniotic fluid, and a less clear placental-uterine myometrial boundary. T2 weighted structural imaging shows a homogenous structure with relatively high T2 signal intensity, giving it a light grey appearance. The T2 value falls in placental insufficiency, giving the placenta a darker appearance, and the placenta becomes more heterogeneous, possibly due to areas of infarction and fibrosis[96] (Figure 4). The placenta is smaller in FGR compared to normally grown controls, and has a thickened, globular appearance[97].

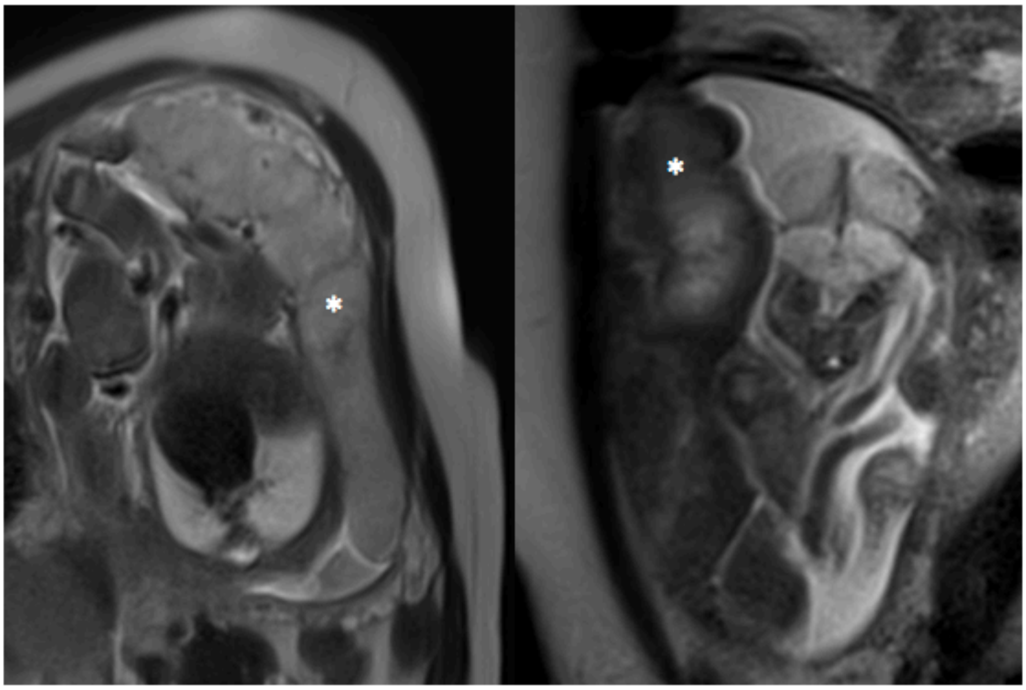

Figure 4; MRI of placenta from a normally grown (left) and FGR (right) fetus. The placentas are marked with white stars. Note the difference in appearance inT2 weighted imaging, with the normal placenta appearing lighter in colour and more homogenous than the FGR placenta.

Quantitative MRI of Tissue Properties relating to Perfusion

The gold standard of perfusion MRI is Dynamic Contrast Enhanced Imaging, but this normally uses exogenous Gadolinium contrast agents, the safety of which is not known for the developing fetus[98]. There are however less sensitive MR measures of tissue properties that relate to the perfusion of tissue.

T1 Relaxometry

T1 relaxation time correlates well with the tissue water content[95]. Changes seen in pathology are thought to relate to differences in the extra-cellular fluid volume fraction, and changes in membrane and fibrillary surface area[99].

In the placenta T1 relaxation time decreases with increasing gestational age[100,101], and is lower in fetal growth restriction than normal controls[100].

T1 is also thought to be sensitive to the partial pressure of oxygen, as R1 (1/T1) changes in proportion to the concentration of oxygen molecules dissolved in plasma. Oxygen enhanced MRI looks at the difference in signal between normoxic and hyperoxic conditions. R1 has been shown to change significantly in normal placentas when the mother is breathing oxygen compared to air, with the difference decreasing with increasing gestational age[102,103]. Both baseline R1, and the change in R1 with hyperoxygenation, have been shown to be significantly different in normal placentas compared to FGR[104].

T2 Relaxometry

T2 relaxometry is the quantitative measure of spin-spin relaxation times and is defined as the time taken for the transverse component of the magnetisation to decay to 37% of its original value. The relaxation time is different for each tissue; solid tissue has a short T2 relaxation time, whilst blood has a much longer T2 relaxation time. Tissues with greater all over surface area, whether in the form of cellular membranes or intracellular or extracellular fibrillary macromolecules, tend to have shorter T2 values[99]. T2 relaxometry can therefore be used as a biomarker. In the placenta T2 relaxation time decreases with increasing gestation[100], possibly because of the proportional increase in villous tissue compared to intervillous space, and increasing fibrin volume density[101]. T2 relaxation times are significantly reduced in pregnancies complicated by FGR compared to those with appropriate growth (88ms vs 149ms, $p<0.0001$)[105], possibly due to increases in fibrosis, necrosis and infarction within the placental parenchyma. There is an association between T2 relaxation time and uterine artery Doppler pulsatility index ($r=-0.75$, $p<0.0001$)[105]. This suggests T2 relaxometry is capable of detecting the changes in placental tissue morphology seen in FGR, although in a non-specific way.

T2 Relaxometry*

As described above, the gradient-echo contrast T2* is not only dependent on tissue T2 properties, but also on magnetic field inhomogeneity[95]. Deoxyhaemoglobin in strongly paramagnetic, whereas oxyhaemoglobin is weakly diamagnetic. The paramagnetic properties of deoxygenated haemoglobin affect the spins of neighboring protons, and so T2* is sensitive to tissue oxygenation[95]. In hypoxic tissue, deoxygenated haemoglobin reduces T2* signal[95].

T2* of the placenta has been shown to be reproducible, and like T2, T2* relaxation time decreases with increasing gestational age[106]. There has also been shown to be a significant correlation between birth weight and T2*, with histological findings suggestive of placenta vascular malformation in reduced T2*[107].

Blood Oxygen Level Dependent (BOLD)

Blood Oxygenation Level Dependent (BOLD) was first developed to investigate brain function, and measures this signal over time. When an area of brain tissue becomes active there is a large increase in the blood supplied, and the influx of oxygenated blood causes a brighter signal to be seen. By taking multiple shots of the same tissue before and after activity, and then applying post-processing, an active area of tissue can be seen. This is the technique used in functional brain imaging[95].

BOLD has also been investigated as a way of non-invasively measuring fetal oxygenation levels using oxygen enhanced MRI. It has been shown that there is an association between maternal oxygenation levels and placental BOLD signal[102], as well as heterogeneity of placental oxygenation in normoxic conditions[108]. There is evidence that BOLD detects changes in FGR placentas compared to controls[104,109] and that the brain sparing effect in hypoxia can also be detected, with brain BOLD signal being much less sensitive to hypoxia than other fetal organs, such as liver, spleen and kidney[110].

Diffusion Weighted Imaging

Diffusion-weighted Magnetic Resonance Imaging (DW-MRI) allows quantification of water diffusivity in a hindered environment, such as biological tissue. It is sensitive to the random diffusion of hydrogen protons, which is modified in tissue when movement is restricted, for example by cell membranes, or hindered, for example by macromolecules in the intracellular space.

DW-MRI can be performed at different diffusion weightings, known as b-values. The b-value is a factor that reflects the strength and timing of the gradients used to generate diffusion-weighted images. A larger b value is achieved by increasing the gradient amplitude and duration or by widening the interval between paired gradient pulses. The higher the b-value, the stronger the diffusion sensitisation.

By performing DW-MRI at two or more b-values an apparent diffusion coefficient (ADC) can be calculated. The value is calculated for each voxel within an image, and this is displayed as a parametric ADC map. Voxels with great attenuation with increasing b-value have higher ADC values, representing a greater degree of water diffusion such as within fluid, compared with signals with less signal attenuation and low ADC values, representing restricted and hindered diffusion such as within cellular tissue. Hence the higher the waters ability to diffuse, the more rapid the loss of signal.

The ADC depends on the tissue being imaged, and if pathology is present. There are published tables of normal ADC for the brain[111].

Several studies have looked at DW-MRI of the placenta. Three studies have compared DW-MRI with gestational age, one finding a correlation between gestation and ADC[112], which the other studies did not replicate [113, 114].

DWI has also been used to investigate FGR, with placental ADC values being found to be significantly lower in the placentas of FGR pregnancies compared to normal controls[115,116]. This suggests the micro-architectural or vascular disturbance in FGR placentas is measurable with MRI.

Intravoxel Incoherent Motion

When DW-MRI is performed in well perfused, vascular tissues, the measured signal attenuation at low b-values is not only due to free water diffusion (*d*) in tissue but also from microcirculation within the capillary network. Le Bihan described this effect, known as Intravoxel Incoherent Motion (IVIM) [117].

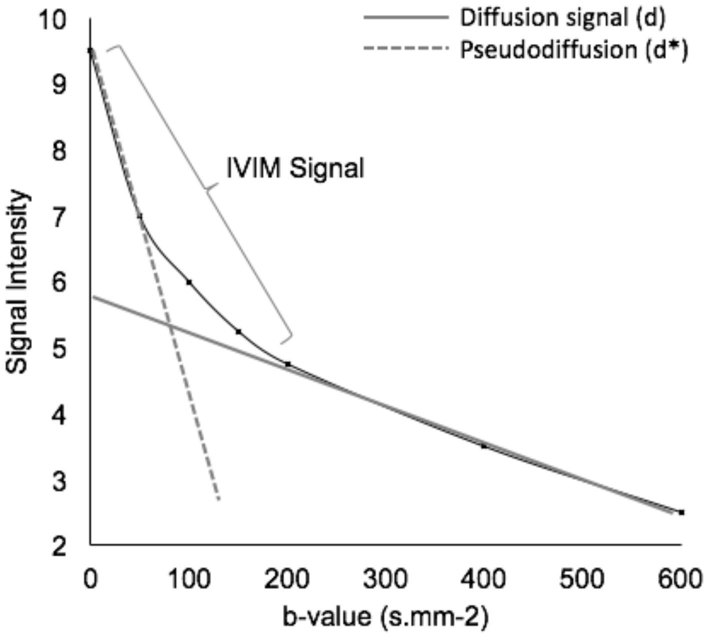

Figure 5; Typical plot of the signal intensity against b-values.
Highly vascular tissue has a steeper portion at lower b-values, and is best described using a bi-exponential IVIM fit. The steeper portion at the lower b-value represents pseudodiffusion (d*), and the less steep section at higher b-values represents Brownian diffusion (*d*).

As movement of blood within a network of capillaries would have no specific orientation and is dependent on the vascular architecture and velocity of the blood it is termed “pseudodiffusion” (d^*). At high b-values pseudodiffusion only accounts for a small proportion of the measured signal, however at low b-values, less than 200 s/mm^2, the signal is significantly attenuated due to the larger distance of water movement during the motion probing gradients. Imaging using low b-values is therefore critical to IVIM.

The perfusion fraction (*f*, %) measures the volume of blood flowing within the capillaries in each voxel compared to the total voxel volume of water, the fraction of water molecules moving at the rate *d** relative to those diffusing at d. Variation in f is thought to be related to the number and diameter of capillaries[118].

A limitation of this technique is that the perfusion component may reflect other physiological bulk flow phenomena, for examples glandular secretions or ductal flows. Values therefore need to be interpreted with caution in glandular tissues. Also, slow flow will become indistinguishable from the normal diffusion process.

Moore et al[119] were the first to investigate IVIM in the human placenta, finding the average f to be 26% +/- 6%, with a weak trend towards reduction in signal with increasing gestational age. They further investigate IVIM in normal and FGR pregnancies[120], fitting values for f, d and d^* in defined areas of interest on the fetal (inner) and maternal (outer) side of the placenta. The parameter $f_{out} – f_{in}$ was calculated, and found to be positive in 12 out of 13 normally grown cases (the last being zero), but negative in all FGR pregnancies ($p<0.002$), suggesting that growth restricted pregnancies show reduced flow of blood on the maternal side. Hayot et al[121] reported finding a significant linear correlation between f and fetal birthweight ($p=0.008$) and placental weights ($p=0.05$), and basal plate IVIM has been found to be significantly lower in pregnancies complicated by pre-eclampsia compared with normal control pregnancies (27% +/- 5% vs 36%+/-5%, $p<0.005$)[122].

IVIM at 4.7T has also been used to investigate placental perfusion in a surgically created mouse model of FGR[123], with f value significantly reduced in placentas in ligated uterine horns compared to normal horns[123], demonstrating that the surgically reduced uterine blood flow was observable with placental IVIM imaging.

Arterial Spin Labelling

Arterial spin labelling (ASL) involves magnetically labelling water hydrogen protons in the arterial blood supply. Arterial blood water is magnetically labelled upstream from the region of interest using a radiofrequency inversion pulse. This magnetised tracer flows into the slice of interest, reducing the total tissue magnetisation, and consequently reducing the MR signal and image intensity. The difference between a labelled and un-labelled control image provides a measure of perfusion[124]. The main difficulty with ASL is the very low SNR of the signal difference between the labelled and control images, which requires many signal averages to overcome, extending the imaging time[124], and increases the susceptibility to motion and perfusion variation.

Gowland et al[125] were the first to inestigate ASL imaging of placental perfusion. 15 normal, healthy pregnant women were scanned in the third trimester at 0.5T. Their technique calculated total placental perfusion and found an average perfusion rate of 176 +/- 24 ml/100mg/min, with no correlation with gestational age. In growth restriction and pre-eclampsia they found no change in perfusion between normal and compromised pregnancies[126]. However when perfusion maps were created showing the percentage of pixels that fell into four categories (<100, 100-300, 300-500 and 500-1000ml/100mg/min), there was a significant difference in placental perfusion between normal and FGR pregnancies ($p<0.0001$) with FGR pregnancies having a significantly higher proportion of low flow[127].

Derwig et al[128] compared IVIM and ASL to assess placental perfusion in the second trimester in normal and FGR pregnancies. There was a significant reduction in basal plate ASL signal between normally grown and FGR pregnancies (2359 (1196-3542) vs 923 (465-1721) arbitrary units; $p=0.003$). Basal plate, central placental and whole placental IVIM vascular density was also different between normally grown and FGR pregnancies (40.7% (37.5-48.4%) vs 37.8% (29.6-42.5%) $p=0.046$, 35.1% (25.8 – 38.1%) vs 24.3% (21.1-33.2%) $p= 0.014$, and 36.2% (30.2 – 39.8%) vs 27.9% (22.2-31.0%) $p= 0.001$ respectively).

These studies demonstrate that quantitative MRI signals can be used as non-directly measures of placental perfusion, that are sensitive to the changes associated with FGR.

Safety of Fetal MRI

There is no evidence that fetal Magnetic Resonance Imaging (MRI) produces harmful effects on the fetus. However, as with all aspect of obstetrics, long-term safety is difficult to definitively demonstrate, and therefore safety concerns continue to be discussed and investigated.

There are three main areas of concern with regard to fetal MRI. First is exposure to the static magnetic field, second is the energy deposition from the radiofrequency pulses, and last is the safety of the loud noises produced by the rapidly switched gradient coils on the developing fetal auditory system.

Static Magnetic fields

The static magnetic fields applied are agreed to be safe in pregnancy up to 4 tesla (T), above which little is known, and it is advised to avoid in pregnancy at present[129].

Radio Frequency Fields

The main concern with radio frequency energy is thermal heating. This is of concern in obstetrics as it is known that a 2 degree temperature rise for over 24 hours can result in deformity of the fetus at early gestations[130], however it is not known if short term heating affects the fetus.

The rate at which energy is absorbed by the human body (per unit mass) when exposed to radio frequency magnetic fields is called the specific absorption rate

(SAR (W/Kg)). The heating effect on the fetus has been investigated in animal models such as piglets[131] and fetal sheep[132], and no significant temperature rise in utero has been found.

Additionally mathematic models of the heating effect of fetal MRI have shown that the fetus is exposed to 40-70% of the SAR that the mother is exposed to[133,134], with a minimal rise in temperature, to a maximum of 37.7 degrees Centigrade[134], or 0.3 degree above the resting state[135]. The increase in temperature occurs only when radiofrequency pulses are applied, allowing cooling between pulses. This is optimised in adults with environmental conditions, but harder to account for in the fetus. However it has been shown that the actual time spent scanning is approximately one third of the total scan time[136], which is also likely to be protective for the fetus.

The International Commission on Non-Ionising Radiation Protection recommend a close control of SAR values[137]. The Medicines and Healthcare Products Regulatory Agency (MHRA) recommend that all pregnant patients should be scanned in normal mode (2W/Kg), as this will prevent any potential detrimental effects for the fetus[129].

Auditory Effect on the Fetus

A major concern in fetal MRI is the noise generated by the MRI system. The rapid switching of currents in the gradient coils, combined with the presence of a strong magnetic field, produces significant Lorentz forces. These forces make the coils vibrate producing a loud knocking noise. The effect that MRI noise has on the fetus is of concern to the MRI community as headphones or earplugs protect the mother, but not the fetus. Prolonged high occupational noise exposure in pregnancy has been weakly associated with fetal hearing loss, shortened gestation and lower birth weight[138]. However, it has been suggested that this is caused by the maternal stress resulting from such exposure, and that suitable maternal hearing protection alleviates this affect.

Studies looking at the hearing of children exposed in utero to MRI have found no evidence of hearing impairment[139,140,141,142,143], or differences in birth weight[143], communication skills[142], or motor skills[142], compared to the unexposed population. Investigations using hydrophones placed in the uteruses of pregnant ewes[132,144] have demonstrated attenuation of noise with a frequency greater than 200Hz by up to 20dB, however enhancement of lower frequency sounds by less than 5dB was also observed[132,144], with similar results being found in women in labour[145, 146]. The fetal outer and middle ear and Eustachian tube is fluid filled and this renders the normal route of sound transmission through the ossicular chain less efficient[147], so the main route of sound transmission in the fetus is through bone[148]. The total sound attenuation from maternal tissues and the fluid filled inner ear has been measured in ewes to be 11.1dB at 125Hz, 35dB at 500Hz, 38dB at 1000Hz and 45dB at 2000Hz[147].

Frequency spectrums of MR pulse sequences show that the noise is normally from 500 Hz to 2000 Hz[149], a level that is heavily attenuated. All available evidence therefore suggests the noise level is not of clinical concern, although it is advisable to check noise levels prior to using a new imaging sequence.

Fetal distress during the scan

Two studies have examined if MRI distresses the fetus. Both studies used cardiotocography, the standard way of assessing fetal distress, before and after MRI, and neither found any evidence of fetal distress[150,151].

1.9 Project Hypothesis and Objectives

The hypotheses central to this thesis were:

- That the fetoplacental vasculature is heterogenous, but with consistent geometric variation, specifically having reduced vascularisation in peripheral tissue
- That fetal placental perfusion is closely regulated to match maternal placenta perfusion, optimising transfer of oxygen from mother to fetus, and that this is disrupted in fetal growth restriction leading to lower fetal blood saturation.

The specific objectives were:

1. To develop and validate a method for human placental perfusion and micro-CT imaging (addressed in chapter 3)
2. To apply this technique in multiscale placental imaging, to investigate the heterogeneity and spatial pattern of vascular density within normal, term placenta (addressed in chapters 4 and 5)
3. To develop a placental MR model that gives parameters relevant to fetal and maternal placental perfusion, and fetal blood oxygenation (addressed in chapter 7)
4. To investigate the relationship between the maternal and fetal perfusion parameters in normal and FGR human placentas (addressed in chapters 8 and 9).

2 Micro Computed Tomography Placental Imaging and Analysis: Methodology

2.1 Summary

In this chapter I present my methods for placental perfusion, micro-CT imaging, and image analysis. The following chapter describes the approach I took to optimise the technique.

Placental collection, perfusion and imaging was my own work. The image analysis pipeline was conceived and developed in collaboration with Dr Andrew Melbourne, who provided computational expertise throughout.

Manual correction of skeletons was performed by Claire Schaaf, a visiting Summer Student from the Clinical Investigation Centre of Nancy, France.

2.2 Tissue collection

Experimental procedures were approved by Bloomsbury National Research Ethics Service Committee (REC Reference number 133888). Women undergoing elective caesarean section for uncomplicated pregnancy gave written consent.

2.3 Placental Perfusion

Placentas were taken directly from the labour ward to the laboratory, where the membranes were trimmed. The amnion was left in place. The placenta was inspected to check it was complete with minimal damage from delivery. The cord was inspected for number of arteries and veins. The placenta was weighed.

An umbilical artery was selected within the umbilical cord and cannulated using a 22-gauge cannula. The cannula was flushed with 0.9% sodium chloride with 5IU heparin/ml to ensure it was correctly located. It was then sutured in place. An umbilical cord clamp was placed distally along the cord to the point of cannulation to prevent backflow and leaking of fluid. An exit vent was created in the umbilical vein.

The placenta was then perfused with 0.9% sodium chloride with 5IU heparin/ml, using gentle manual pressure, until the fluid coming from the exit went was pink rather than red, and free from blood clots. The whole placenta was perfused in this way as cannulation of the umbilical artery was proximal to Hyrtl's anastomosis (which connects the two umbilical arteries in most placentas) is all cases. Perfusion required 100-150ml 0.9% sodium chloride with 5IU heparin/ml, depending on the size of the placenta and the amount of blood left in situ at delivery.

20ml Microfil (Flow Tech, Carver, MA) was made up in accordance with manufacturer's instructions. This was perfused through the umbilical artery cannula using gentle manual pressure. Perfusion of one placenta took 10-20 minutes, and 10-20ml Microfil depending on the size of the placenta. If one area of the placenta perfused preferentially to another, the chorionic artery supplying the well perfused area was occluded, so that Microfil was redirected to the less well perfused areas. Microfil was gently milked down peripheral chorionic arteries to ensure smaller chorionic arteries were filled. Perfusion was continued until all chorionic arteries were filled, and Microfil could be seen in some of the chorionic veins. The umbilical cord was then clamped proximal to the point of cannulation to prevent leakage of contrast, and the placenta left at room temperature for 90 minutes to allow Microfil to set, as per manufacturer instructions.

Once the Microfil had set a high-resolution photograph was taken of the placenta next to a paper tape measure for scale, using a digital single-lens reflex camera. The placenta was then placed flat in 500-750ml 4% formalin for 48 hours to fix.

This was to stiffen the placenta to prevent movement during imaging, and to preserve tissue for histological analysis.

2.4 Micro-CT Image Acquisition

The whole placenta was mounted upright, with the chorionic plate parallel to the detector, to minimise the quantity of tissue the X-ray beam needed to pass through and therefore reduce the energy needed for adequate penetration.

In order to do this the placenta was removed from formalin and dried thoroughly. It was placed in a vacuum sealer roll (Andrew James Vacuum Sealer Rolls) and vacuum sealed. The vacuum supported the tissue, helping to prevent movement during imaging, and also sealed the sample, preventing leaking into the micro-CT machine. The plastic was minimally attenuating to X-rays, so did not disrupt imaging.

The placenta was then mounted in a custom-made foam block, which had a disc of foam removed into which the placenta was placed. It was secured in place with pins through the plastic in which it was vacuum sealed (taking care not to pierce the area of the vacuum). A foam lid was then placed on top and the two pieces of foam secured together using parafilm (see Figure 6). Both foam and parafilm are minimally attenuating to X-rays, so did not disrupt imaging.

The placenta was then placed upright on the stage in the micro-CT scanner (XTH225 ST Micro-CT, Nikon Metrology, Tring, UK). The same magnification and imaging parameters were used for every case. The whole placenta was imaged with a Molybdenum target at 80kV energy, 88µA current, 1000ms exposure time, one frame per projection, 3141 projections over 360-degree rotation, with an isotropic voxel size of 116.5 µm (see chapter 4 for a discussion on image parameter optimisation). The imaging time was 53 minutes 6 seconds.

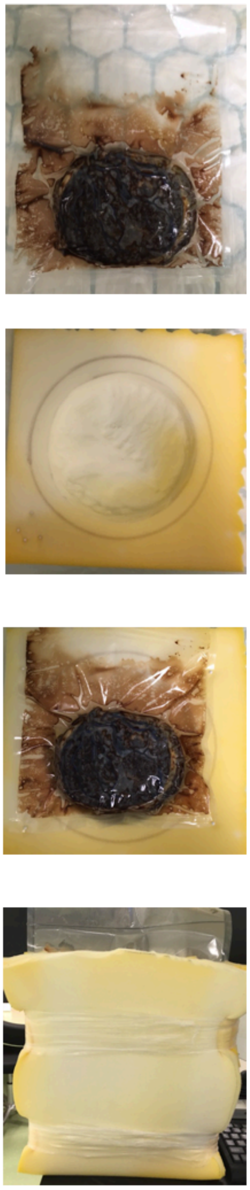

Placenta Vacuum packed to maintain shape during imaging, and prevent fluid leak

↓

Foam mounting device, with a disc of foam removed to encase the placenta

↓

Placenta pinned in place within the foam case. This kept the placenta upright and still during imaging.

↓

The foam lid was placed on top and the whole device wrapped in parafilm to ensure no movement during image.

Figure 6; Process of whole placental mounting for micro-CT.

Once the placenta had been imaged whole, the image volume was reconstructed using a modified Feldkamp filtered back projection algorithm with proprietary software (CTPro3D; Nikon Meterology). A volume rendering, grey-scale thresholded to visualize the vascular tree, was examined in VG Studio MAX 2.2 (Volume Graphics, Germany) to check imaging was of adequate quality, and that there had been no movement during imaging.

The placenta was then removed from the mount and vacuum pack, and cut into 2cm strips as is standard histological technique. Areas of placenta that appeared well perfused on both the whole placental imaging, and on visualising the placental tissue, were identified and full thickness block of 1.5 to 2cm by 1.5 to 2cm where taken. Care was taken to ensure they came from different regions of the placenta, with regard to proximity to the umbilical cord insertion site, and the feeding chorionic vessels. The location from which blocks were taken was recorded using an annotated diagram of the chorionic plate. Eight blocks were taken from each placenta. The remaining tissue was disposed of in accordance to legislation on disposing of human tissue.

The eight blocks were then imaged individually at higher magnification. Each was wrapped in parafilm, and mounted in a custom made acrylic tube, resting on a plastic stand. All blocks were imaged using the same protocol; a Molybdenum target, 50kV energy, 199μA current, 1 frame per projection, 1000ms exposure time, 3141 projections over 360-degree rotation, with an isotropic voxel size of 13.5 μm. Each block took 53 minutes and 6 seconds to image. The blocks were then placed in 30ml 4% formalin in preparation for histology.

The image volume was reconstructed using a modified Feldkamp filtered back projection algorithm with proprietary software (CTPro3D; Nikon Meterology).

2.5 Histological Slide Preparation

Two 10μm full thickness section were cut from each block and stained with hematoxylin and eosin (H&E). Preliminary work showed that Microfil often fell out of vessels with 3μm and 5μm section thickness. 10μm was therefore a balance between keeping as much Microfil within the vessels as possible for analysis of vascular fill, while maintaining a slide thickness that could be histologically assessed. Preliminary work also showed that twelve micrographs over two sections was sufficient to estimate the block vascular density (see chapter 3). For each slide, 6 micrographs at x100 magnification were taken, three in the upper half of the tissue, close to the chorionic plate, and three in the lower half of the tissue, close to the basal plate, using the template shown in Figure 7 as a guide.

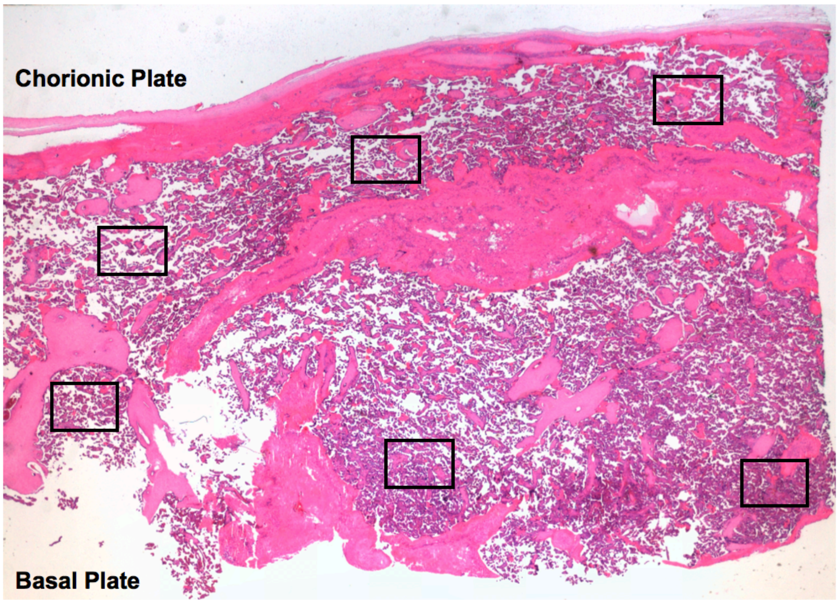

Figure 7; Micrograph sampling method for histological slides. Micrographs were taken of each full thickness placental section using the schematic above. No fixed template was used as the sections varied substantially in shape, depending on placental thickness and block size.

2.6 Describing Placental Shape and Eccentricity of Cord Insertion

The high resolution photograph of each placenta was loaded into FIJI ((ImageJ Version 2.0.0-rc-54/1.51f [152]). The scale was set using the measuring tape in the photo. A straight line was drawn between two points of known distance on the flat, zoomed in measuring tape, and the length of the line calculated automatically by FIJI. The distance in pixels was converted into the known distance in millimeters by using the set scale feature in the software.

Each placenta was measured as shown in Figure 8. The widest measurement across the placenta was taken and called A. The widest measurement perpendicular to this measurement was then taken, and called B. The distance from the cord insertion to the closest placental edge in any direction was also measured.

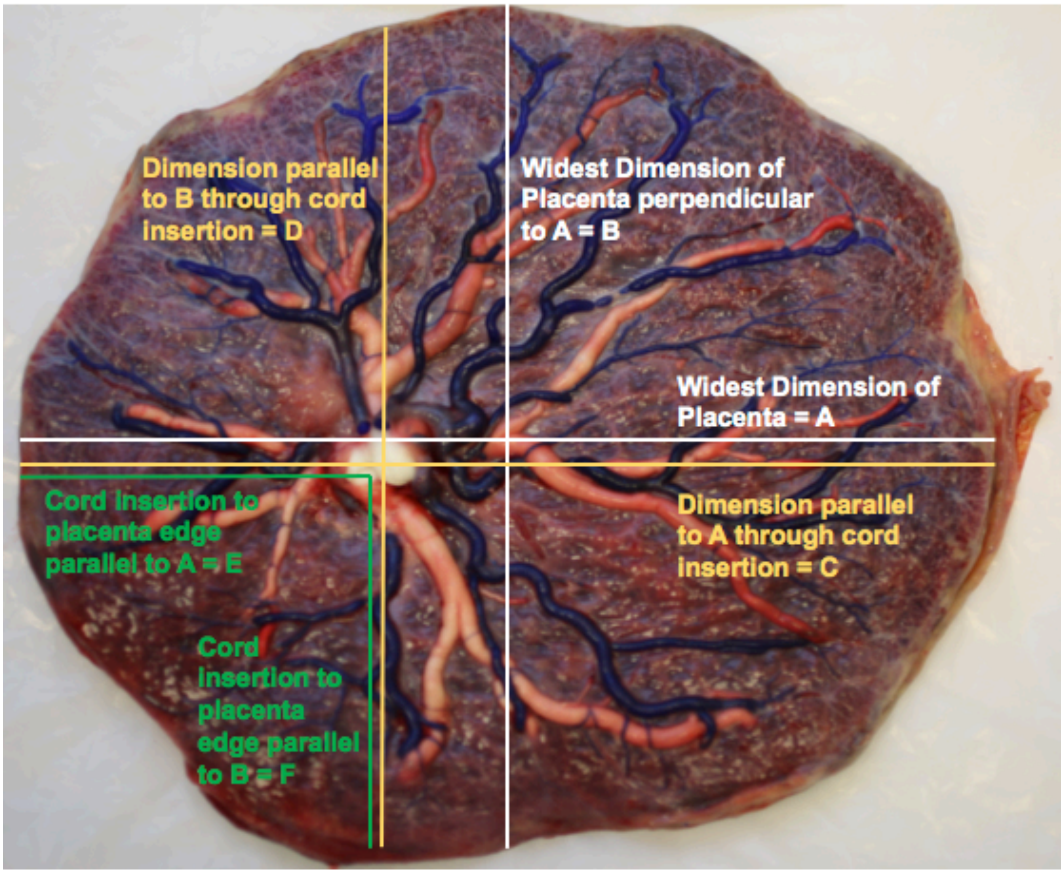

Figure 8; Schematic diagram showing measurements of placental dimensions. Widest diameter of the placenta was measured (A), and the widest dimension perpendicular to A was measured (B). The placental diameter measured through the cord insertion parallel to A (C) and B (D), and measurement from cord insertion to placental edge parallel to A (E) and B (F) were then taken.

The system of placental geometric description describe by Pathak et al[153] which uses the mathematical description for eccentricity of an ellipse, was used to describe placental eccentricity:

$$e = \sqrt{1 - {B^2}/{A^2}}$$

Placental Eccentricity

A and B are defined in Figure 8. Zero would represent a perfect circle. The closer the value to one, the more eccentric the placenta.

Cord insertion was described as proposed by Pathak et al[153]. The distance from the cord insertion to the placenta center (DCC) was calculated as:

$$\mathrm{DCC} = \sqrt{(\frac{1}{2}\mathrm{C} - \mathrm{E})^2 + (\frac{1}{2}\mathrm{D} - \mathrm{F})^2}$$

Distance of Cord from Placenta Centre

C, D, E and F are defined in Figure 8. The cord centrality index (CCI) was then calculated to describe the location of the umbilical cord insertion in relation to the placenta.

$$\mathrm{CCI} = \frac{\mathrm{DCC}}{\frac{1}{2}\mathrm{A}}$$

Cord Centrality Index

This gives a value on a scale of 0 to 1, with zero demonstrating central cord insertion, and one representing marginal cord insertion.

Block Location

Using the annotated diagram made during placental dissection, the site from which each placenta block was taken was marked onto the photograph on FIJI. The distance from the cord insertion to the center of the site from which the block was taken, and the distance from cord insertion to placental edge through the site from which the block was taken were measured.

The location of the block in relation to the point of cord insertion and the placental edge was then calculated:

$$\text{Location of block (\%)} = \left(\frac{\text{Distance from cord insertion to block}}{\text{Distance from cord insertion to placental edge through block}}\right) \text{ x } 100$$

Geometric Location of block

This expressed the location from which the placental block was taken as a percentage, with 0 representing proximity to cord insertion, and 100% proximity to placental edge.

2.7 Analysis of Whole Placental Micro-CT Imaging

All whole placenta imaging analysis was performed in MATLAB (R2016b, MathWorks, 2016) using custom designed algorithms.

In order to analyse the data within MATLAB the whole placenta volume data was saved as a stack of TIFF files, which were 266 to 492 files of 1682 to 2155 by 1475 to 2001 pixels in size. The placenta was always orientated within the stack so that each tiff sliced through the placenta parallel to the chorionic plate, and the distance from chorionic to basal plate increased through the stack of TIFFS (Figure 9).

Reading the whole placenta dataset at once was computationally prohibitive (e.g. 2000x2000x426 TIFFS = 1.16GB for one placenta). In order to make analysis feasible on any computer, the volumes were divided into 100 (10 by 10) three dimensional cubes, allowing smaller chunks of data to be processed. The cubes were labelled with their position in the volume, and could then be re-combined.

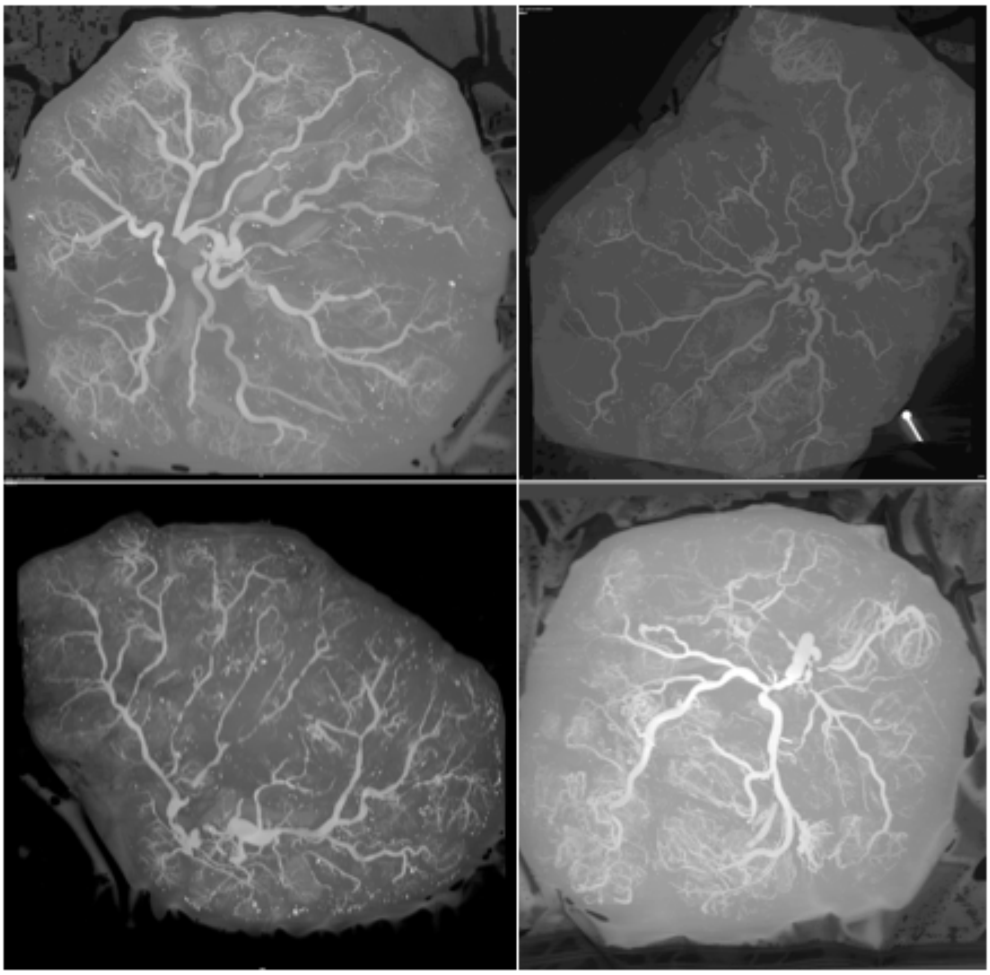

Figure 9; Maximum intensity projections of the stack of TIFF files for four whole placenta micro-CT volumes, created in MATLAB. The chorionic vascular tree and deeper branching stem vessels are apparent, as is the shape of the placenta and the point of cord insertion.

Defining Placental Geometry

Cord Insertion

In order to perform analysis that was relevant to placental structure, the axis of the placenta was defined. A graphic user interface (GUI) was created, which allowed the user the open a two-dimensional maximum intensity projection of the whole placenta stack and manually set the point of cord insertion. The location of cord insertion was defined and saved for each placenta.

Placenta Edge

To define the placental edge, placenta masks were drawn. To allow further analysis the placenta was divided according to the territory of placenta perfused by each umbilical artery. A maximum intensity projection (MIP), a 2D image of a 3D volume where the voxel with maximum intensity in every view throughout the volume is shown[154], of the whole placenta stack was used to segment the two vascular territories, by following the branching pattern of the chorionic vessels from the point of umbilical cord insertion, and then tracing around the placental edge (Figure 10).

Four to five lobules were also segmented for each placenta, choosing highly vascular areas with the appearance of lobules within the MIP, as these represented areas of good placental (Figure 10).

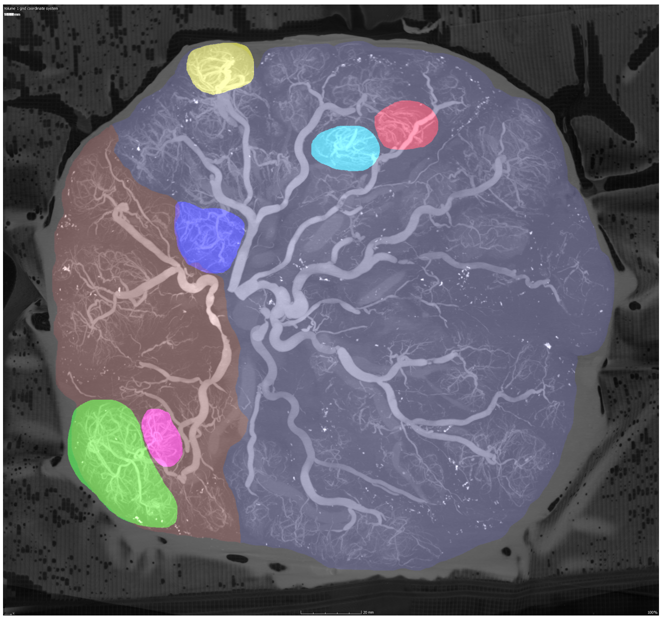

Figure 10; Segmented maximum intensity projection of a placenta. Segmenting the two vascular territories of the umbilical arteries (red and blue), and six lobules (green, magenta, blue, yellow, cyan and red).

Segmenting the Placenta Tissue and Vessels

The greyscale threshold for placental tissue and Microfil filled vessel were defined for every placenta data set. This was done in FIJI by determining the mid-point between the greyscale peaks for air and placenta as the threshold for placenta, and the point midway between the greyscale peaks for tissue and Microfil as the threshold for Microfil (Table 1). This threshold was then used in MATLAB to segment the placental tissue, and the vascular tree of each placenta (Figure 11). The resulting thresholded data was saved for each placenta.

Placenta	Placenta Tissue Threshold	Microfil Filled Vessel Threshold
1	60	109
2	10	102
3	60	125
4	60	125
5	60	105
6	47	75
7	60	105
8	60	165
9	41	85
10	60	96

Table 1; Table of tissue and Microfil greyscale threshold values for each placenta.

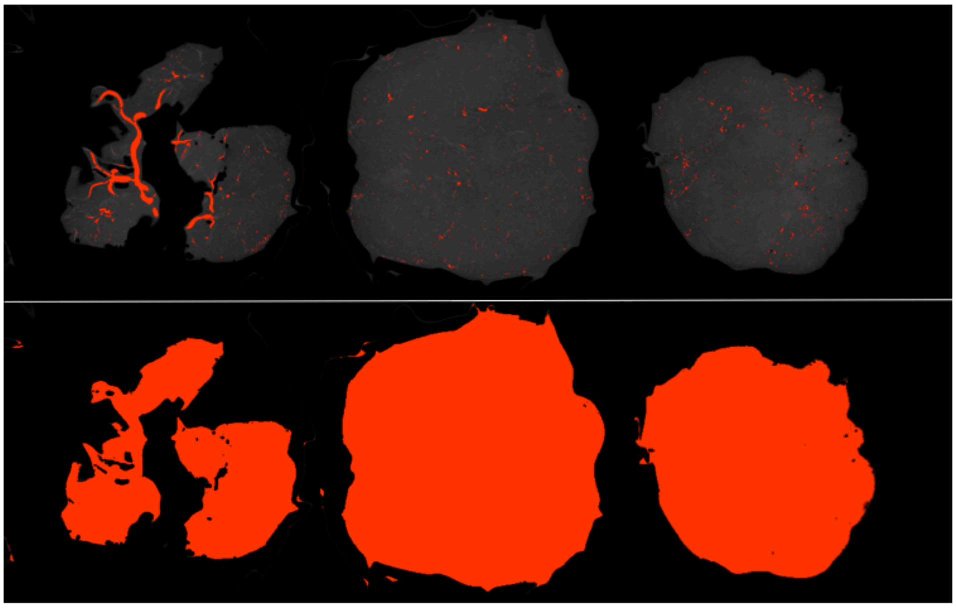

Figure 11; Figure showing thresholding of Microfil filled Vessels (upper) and placental tissue (lower) for one placenta. Slices go through the placental tissue from chorionic plate (left) towards basal plate (right). These are slices 47, 126 and 229 of a 293 stack of Tiff files.

Skeletonising the Vascular Tree

Once the vessels had been segmented a vascular skeleton could be created. Vessels were eroded from both sides in an iterative manner until only the centerline remained, this center line was defined as the vascular tree skeleton. The skeleton had breaks due to limitations in the perfusion and imaging, such as air bubbles in the Microfil causing gaps, and vessels close to the resolution of the scan appearing broken. Unperfused vessels, such as the chorionic veins, and other noise within the data caused areas that were not part of the vascular tree to be skeletonised. To improve the skeleton, it was manually corrected (itk-SNAP Version 3.2.0, 2014). Areas that were not part of the vascular tree were removed, and vessels with small gaps were connected (Figure 12).

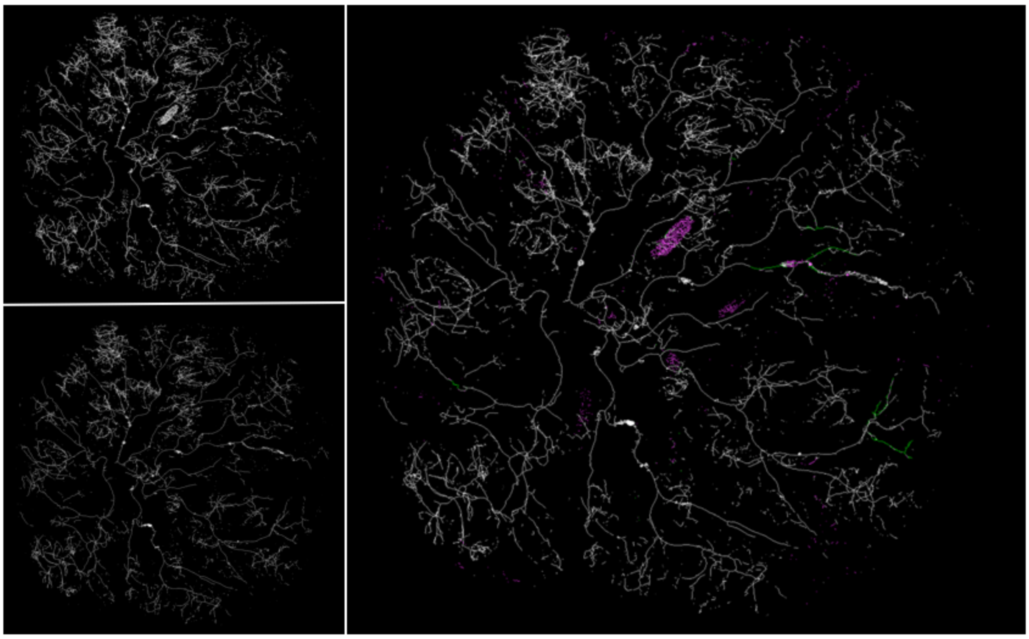

Figure 12; Example of manual corrections made to one placenta skeleton. Top left; the original skeleton, with areas not relating to the vascular tree, and broken vessels. Bottom left; the final skeleton. Right; the manual corrections made to the skeleton, with deletions shown in pink, and additions shown in green.

Measuring the Vessel Radius

After skeletonisation, the radius of every segmented vessel could be measured, as the distance from the skeletonised midline of every vessel to the boundary of the thresholded vessel. This was done by measuring the distance from the first thresholded vessel voxel to the center point, so that the edge would equal 1, and the center point would equal the radius measured in voxels. This was then multiplied by the skeleton, leaving only the radius measure (as all non-skeleton voxels equal zero on the skeleton volume). This gave the measure of the radius of the vessel for every voxel along the skeleton.

Once vessel radius was known vessels could be further divided by size. Vessels with a radius smaller than or equal to 6-voxels (equivalent to approximately 699µm due to the resolution of the whole placental imaging) were defined as villous vessels, whilst vessels with a larger than 6-voxelsl radius were defined as chorionic vessels.

Depth and Distance Maps

To allow analysis by distance from cord insertion, distance maps were created. The point of cord insertion and the edge of each placenta were already defined. The pixel distance from cord insertion to placenta edge was measured for each placenta through 360 degree, and then normalised from 0 to 1. Example distance maps for placentas with central and eccentric cord insertions are shown in Figure 13.

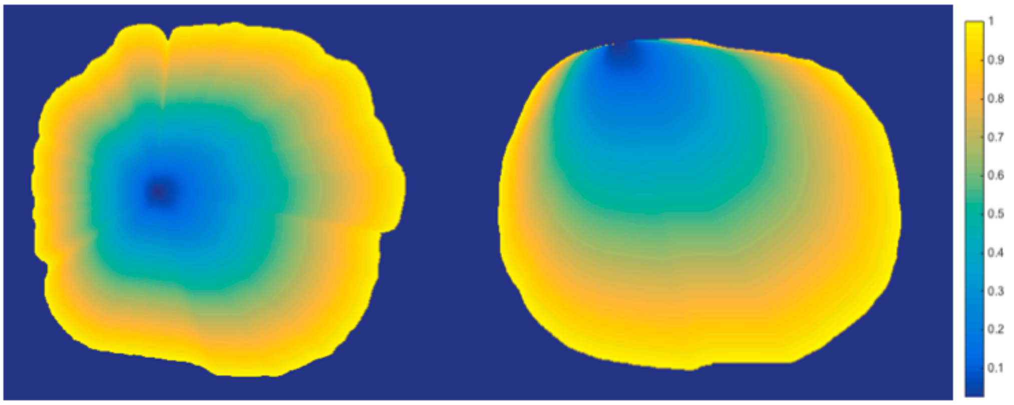

Figure 13; Example normalised distance maps. Showing distance from cord insertion to placental edge for a placenta with a quite central cord insertion, and one with an eccentric cord insertion.

Depth maps were also created to describe the depth of tissue from the chorionic to basal plate. In order to do this the volume was thresholded to include placenta tissue (see below). The chorionic plate was defined as the first voxel in the volume to be thresholded as placenta in each column of voxels through the volume. The basal plate was defined as the last voxel in each column of voxels to be thresholded as placenta. Each column voxel length from chorionic to basal plate was then measured, and normalised from 0 to 1.

Whole Placental Geometric Analysis

These data processing steps created a set of three-dimensional volumes, representing the greyscale thresholded whole vascular tree, whole tissue volume, and separated small and larger vessels (Figure 14).

Each placenta could then be analysed in relation to its structure. For example, the vascular density of villous vessels with distance from cord insertion could be calculated, using voxels thresholded as vessels with a radius less than 6-voxels, in combination with the normalised distance maps.

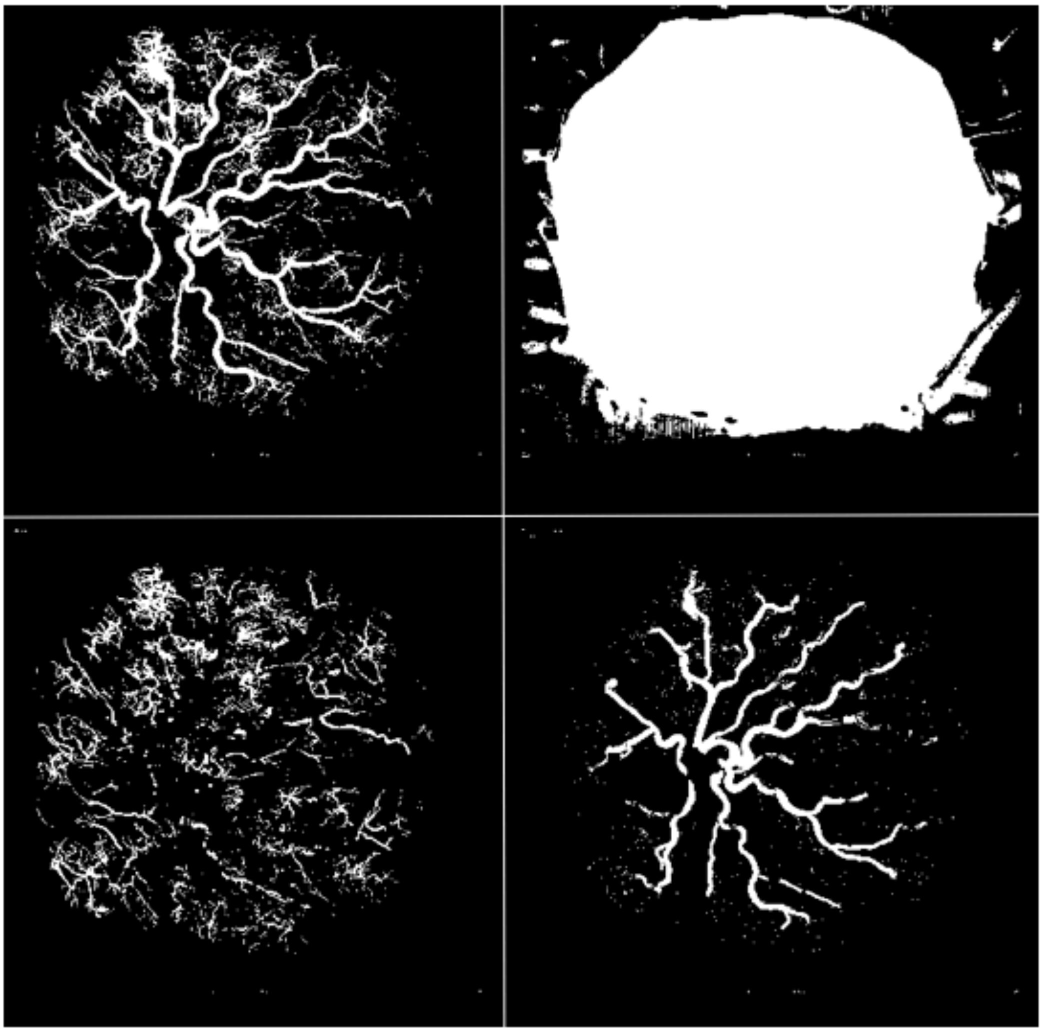

Figure 14; Maximum Intensity Projections (MIP) for thresholded placenta. Top left; the whole vascular tree, Top right; the thresholded placenta tissue and vascular tree. Bottom left; the thresholded vessels with radius equal to or less than 6-voxels, defined as villous vessels. Bottom right; the vessels with radius greater than 6-voxels, defined as chorionic vessels.

2.8 Analysis of Placental Block Micro-CT Imaging

To calculate the villous vascular density of each block of placental tissue the reconstructed block volume was loaded into VG StudioMAX 2.2 (Volume Graphics, Germany).

An area of interest was drawn over the bottom third of the tissue. This was because this area of the placenta is the location for the villous vascular tree. Volumes were thresholded using the grey-scale histogram, with the threshold set at a point midway between the intensity peaks for air and tissue to segment the placenta and vessels, and halfway between the intensity peaks for tissue and Microfil to segment the perfused vessels (Figure 15). The volume of placental tissue and vessels was then measured automatically, and the vascular density calculated as:

$$\text{Block Vascular Density} = \left(\frac{\text{Vascular volume}}{\text{Placenta tissue volume}}\right) \text{x } 100$$

Block Villous Vascular Density

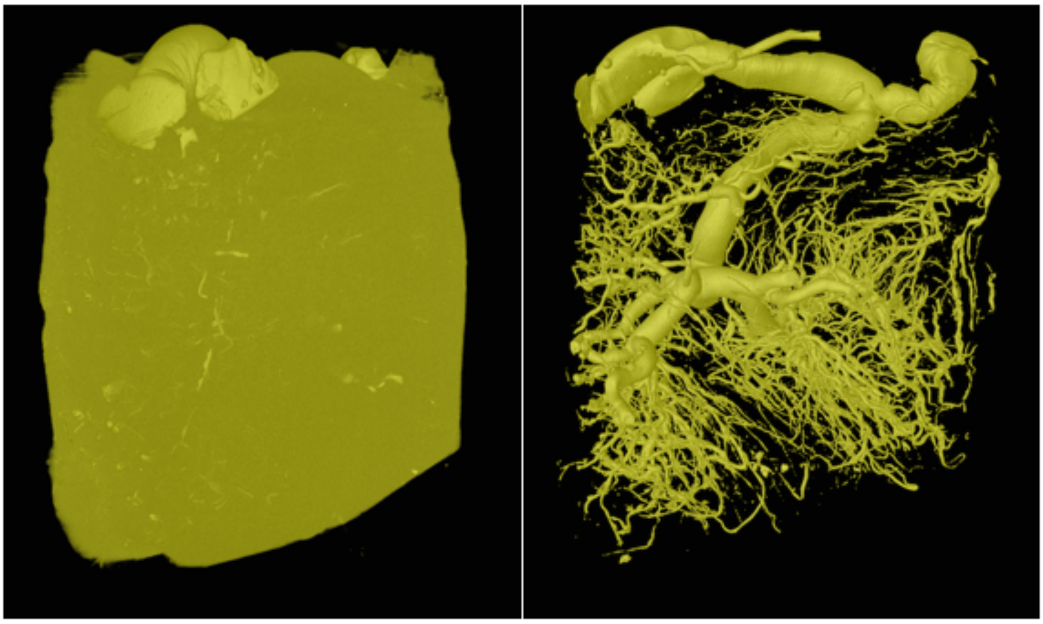

Figure 15; Images showing a placenta block segmented to measure tissue and vessel volume (left) and vessel volume (right). An area of interest was drawn over the bottom third of the volume, to calculate the villous vascular density. The majority of larger stem vessels were therefore excluded.

2.9 Histological Analysis

FIJI (ImageJ Version 2.0.0-rc-54/1.51f[152]) was used to analyse the histological sections. This is an open-source platform for biomedical image analysis[152]. The Trainable Weka Segmentation plugin (Version 3.1.2)[155] was used to segment image features on the micrographs into three classes; perfused vessels and background (Microfil and white space), un-perfused vessels (vessels containing red cells) and villous tissue, as shown in Figure 16.

A perfused vessel was defined either as a vessel that contained Microfil, or a vessel that was empty of everything including all red blood cells. This definition was chosen because preliminary work showed that Microfil fragments can spontaneously fall out of tissue during histological processing, so the absence of Microfil does not exclude perfusion. Non-perfused vessels normally contain visible red blood cells, so the absence of these cells strongly suggests perfusion with heparinised saline, and therefore likely with Microfil. It is possible vessels were perfused with heparinised saline and not the more viscous Microfil, so this definition may over estimate fill. However only counting those contained Microfil would underestimate fill. Accepting that there is no perfect definition, unperfused vessels were defined as vessels that contained red blood cells. Micrographs in which no Microfil was seen were excluded from analysis.

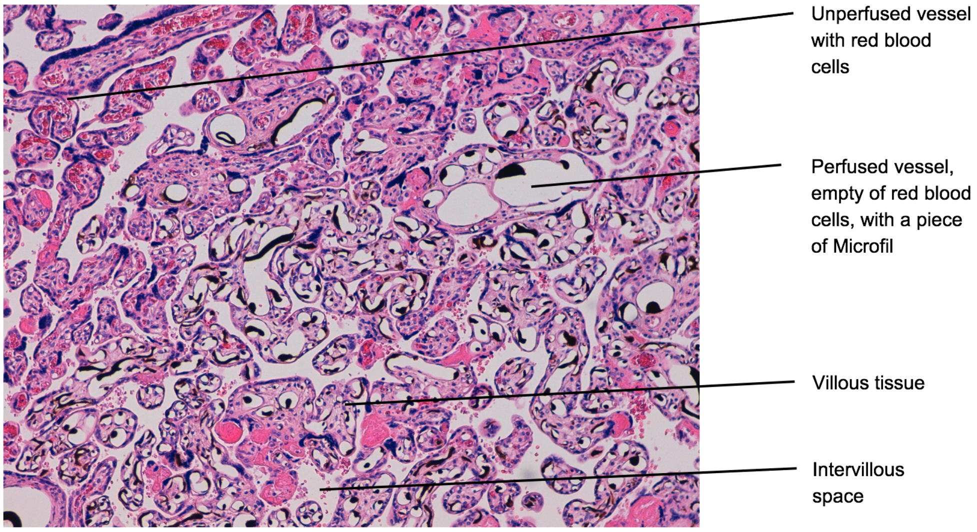

Figure 16; Example placenta histology slide. Perfused vessels appear empty, except for isolated regions of Microfil – which is known to shrink during histological preparation. Unperfused vessels remain full of red blood cells. The remaining tissue is made up of villous tissue and intervillous space.

The output images were thresholded to select the three classes defined above. The Analyse Particle tool was then used to measure the area of the perfused and unperfused vessel lumens. This applies restrictions in terms of the minimum and maximal area of the particle, and the circularity, and outputs a list of the area measurements for each particle within the limits. The tool was set to include particles with an area between 60-10,00,000μm^2 (which if the vessel is assumed to be directly transected would related to a radius of 1.7 to 1780µm, including all vessel sizes likely to be seen in the villous vascular tree), and circularity 0.20-1.00. For the villi, the whole of the segmented area was measured. Figure 17 shows the analysis pipeline.

The automated system output CSV files listing the perfused and un-perfused vessel lumen area, and the villi area, and these were input into a database, with one spreadsheet for each placenta (Microsoft Excel for Mac, Version 15.29, 2016). For a full discussion of development of automated analysis see Chapter 3.

In order to make the process truly automatic code was written that could be run in the script function of FIJI. This ran the whole image analysis pipeline in the background on folders of images, outputting a CSV file for each class on each micrograph – e.g. area of each perfused vessels, area of each un-perfused vessel, and villous area. It took approximately 3 hours to analyse the 96 micrographs generated from each placenta.

The total perfused and un-perfused vessel areas were calculated, by addition of the list of areas. The vascular fill was the calculated as:

$$\text{Vascular Fill (\%)} = \left(\frac{\text{Total Perfused Vessel Area}}{\text{Total Perfused Vessel Area} + \text{Total Unperfused Vessel Area}}\right) \times 100$$

Vascular Fill

Vascular density was defined as total vessel area divided by total villous area, and calculated as:

$$\text{Histological Vascular Density (\%)}$$
$$= \left(\frac{\text{Total Perfused Vessel Area} + \text{Total Unperfused Vessel Area}}{\text{Total Perfused Vessel Area} + \text{Total Unperfused Vessel Area} + \text{Total Villous Area}}\right) \times 100$$

Histological Vascular Density

Finally, a manual check was performed, by looking at each micrograph and checking the calculated vascular fill and density appeared reasonable. This was to guard against limitations within the automated analysis pathway causing erroneous results.

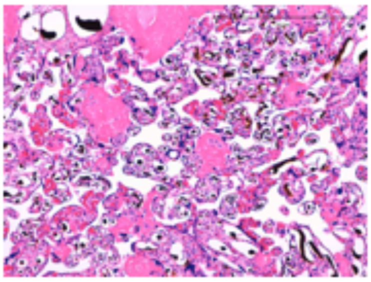

A TIFF file of the micrograph was opened in FIJI. As the files were large the image was reduced in size by half, this kept good resolution whilst allowing faster analysis. The scale was set (0.78μm=1 pixel).

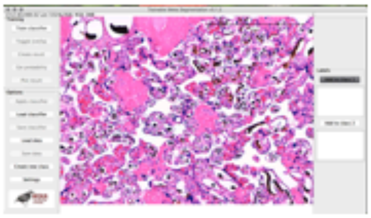

The image was loaded into the Trainable Weka Segmentation (Version 3.1.2) plugin for FIJI[13]. The trained classifier was loaded, and the tool was run to create a segmented result.

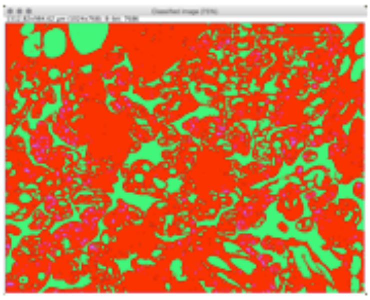

The resulting segmentation showed perfused vessels and background in green, un-perfused vessels in purple, and villi in red.

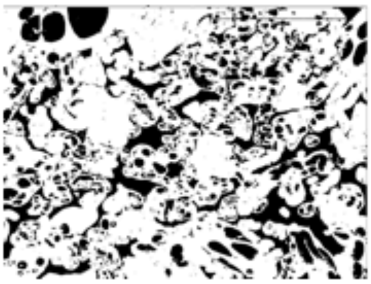

The images were thresholded to select perfused vessels and background (shown), un-perfused vessels, or villi.

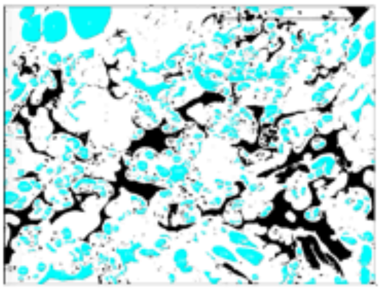

The Analyse Particle tool was used to measure area of the vessels. For vessels, the tool was set to include particles with a surface area between 60-100000μm^2, and circularity 0.20-1.00. For the villi the whole of the segmented area was measured. The tool produces a table with a list of areas.

Figure 17; FIJI Histological Analysis Pipeline.

Calculating Vascular Fill for Multiscale Image Analysis

The total perfused vessel area and un-perfused vessel area was calculated for each micrograph.

Given that detection of any vessel smaller than the voxel size cannot be relied on[73], vessels with radii less than 58μm may not be visualised when performing whole placenta imaging, so perfusion of such vessels is not relevant to the image quality. A vessel radius of 58μm correlates to a vessel area of approximately 11,000 μm^2, assuming it has been transected perpendicularly. Vascular fill for all vessels with an area greater than or equal to 10,000μm^2 was therefore calculated for every placental block, to assess whole placental vascular fill relevant to the resolution of whole placenta imaging.

Given that block imaging had a voxel size of 13.5μm, vessels with radii less than 6.75μm, corresponding to an area of approximately than 150μm^2, may not be visualised. The process was therefore repeated including only vessels that had an area greater than 200μm^2, to assess block placental vascular fill relevant to the resolution of block placenta imaging.

Calculating Villous Vascular Density

As with micro-CT block imaging, villous vascular density was calculated using micrographs from the area close to the basal plate, i.e. micrographs 1,3,5 and Figure 7. This calculated villous vascular density at a resolution that would include terminal capillaries.

2.10 Statistical Analysis

Data is presented as mean ± SD. Statistical analysis was done in SPSS Statistics (IBM version 23) (optimisation work, chapter 3) and MATLAB (analysis work, chapter 5). Comparison of means was performed using independent sample t-tests, and group comparison was done using the Kruskal-Wallis H test, with post-hoc pairwise comparison of statistically significant results using Dunn's procedure with a Bonferroni correction for multiple comparisons. Correlation was done using Pearson's correlation coefficient when the Shapiro-Wilk test for normality was fulfilled, and Spearman Rank Correlation when it was not, unless stated otherwise. Statistical significance was set at 95%.

3 Developing the Technique for Placental Perfusion and Image Acquisition for Micro Computed Tomography Imaging

3.1 Summary

There was no published, optimised technique for placental perfusion or micro-CT image acquisition. It was important to develop an optimized technique prior to investigating placental vascularisation, to ensure the maximum fill of vessels with contrast agent, and adequate image quality for subsequent processing.

In this chapter, I first develop and validate an automated histological process that was used to quantify vascular fill and density. I then investigate the optimal tissue perfusion parameters for human placenta prior to micro-CT imaging. I investigate contrast agent, perfusion pressure, cannulation location and perfusion vessel. Finally, I investigate imaging parameters important in micro-CT angiography - tube energy level and target materials.

The optimised technique ensures contrast between the maximum number of fetal vessels and surrounding soft tissue.

The work in this chapter forms the basis of the published article:

Pratt, R, Hutchinson, JC, Melbourne, A, Zuluaga, MA, Virasami, A, Vercauteren, T, Ourselin, S, Sebire, NJ, Arthurs, OJ, David, AL. Imaging the human placental microcirculation with micro-focus computed tomography: Optimisation of tissue preparation and image acquisition. *Placenta* **60,** 36-9 (2017).

3.2 Automated histological analysis

Automation of histological analysis is desirable as it yields reproducible results that are not subject to inter- or intra-observer variability, or observer fatigue. In addition, automatic analysis is hugely time saving for large data sets, and so allows larger sample sizes to be analysed than is feasible by hand. I therefore developed an automatic analysis pipeline to quantify vascular fill and density on histological micrographs taken at x 100 magnification, from hematoxylin and eosin (H&E) stained sections of human placentas perfused with Microfil. The automated analysis pipeline is described in the methods (chapter 2), but the development of the pipeline is discussed below.

In order to use the FIJI Weka segmentation plugin to segment the three classes of interest within histological micrographs; perfused vessels, un-perfused vessels, and villous tissue, the Weka segmentation tool was trained in an iterative manner until good segmentation results were achieved on 10 micrographs with different appearances. This was assessed by visual inspection of the three classes overlaid on the original histological micrograph.

The Analyse Particle tool was used to measure the area of vessels. The Weka segmentation tool segmented perfused vessels and the background of the micrograph, both white, as perfused vessel (see Figure 17, chapter 2), so vessels needed to be separated from background. The Analyse Particle tool works by applying restrictions to identify a structure of interest. The restrictions available are particle area, and particle circularity, which is scaled from 0 to 1, 1 being a perfect circle. To optimise the restriction settings, the tool was repeatedly applied using different limits for minimum and maximum particle size and circularity, on 10 segmented micrographs with a variety of features, and the included particles examined. The number of vessels that were excluded, and the number of nonvessels that were included, was noted. There was no perfect solution, as decreasing the circularity restriction would include an oblong vessel on one slide, but also include an area that was not a vessel on another, and so on. The restrictions that gave the best results over the 10 slides were selected.

Validating Automated Histological Analysis

To validate the histology analysis process 10 new micrographs were chosen representing the variety of appearances seen in placental micrographs. These were analysed using the protocol described above, producing a spreadsheet (Microsoft Excel for Mac, Version 15.29, 2016) containing columns of perfused vessel areas, un-perfused vessel areas, and the villous area.

The same 10 micrographs were manually segmented using the free drawing tool on FIJI to circumscribe each vessel or area of villi in turn, and measure the area. These results were also entered in the spreadsheet.

The total area for each class – perfused vessel, un-perfused vessel, and villi for each micrograph was calculated for each method. The degree of correlation between the two methods was calculated using Lin's Concordance Coefficient (Table 2 and Figure 18).

There was excellent correlation between the automated and manual measurement of the area of perfused vessels in each micrograph (0.99, 95%confidence interval (CI) 0.97-1.0) and good concordance between the area of un-perfused vessels and villi area in each micrograph (0.83, 95%CI 0.46-0.95 un-perfused vessel, 0.73, 95% CI 0.34-0.91 villi area).

The segmented slides were examined to determine the reason for sub-optimal correlation. The main reason was that there was a tendency for the Weka segmentation model to overestimate the total villi area, and to a lesser extent the un-perfused vessel area, when the tissue was poorly vascularised.

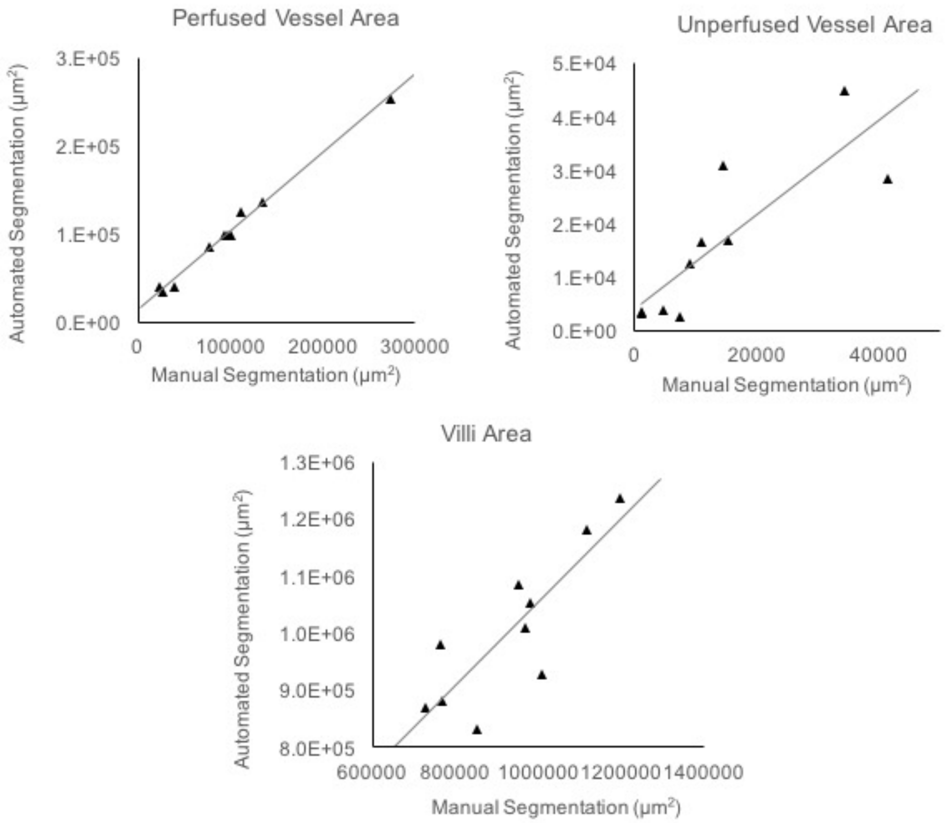

Figure 18; Graphs comparing manual and automatic segmentation of placental histological micrographs. Graphs show measurement of perfused vessel area (upper left) un-perfused vessel surface area (upper right), villi surface area (lower).

Measurement	Lin's concordance coefficient	95% Confidence Interval
Perfused vessel surface area	0.99	0.97 - 1.00
Un-perfused vessel surface area	0.83	0.46 - 0.95
Villi surface area	0.73	0.34 - 0.91

Table 2; Lin's concordance coefficient showing the degree of agreement between the manual and automated methods of measurement.

In order to assess the accuracy of analysis over a much larger sample size, but without the time-consuming process of manual segmentation of the three classes in every image, 179 micrographs were analysed using the automatic system. The vascular fill and vascular density were calculated for each micrograph using the measured perfused vessel, un-perfused vessel and villous areas.

These measurements were compared with a categorical visual estimation of vascular fill and vascular density. This was done by one observer visually assessing each image in turn, and categorising them on a scale of one to five in terms of vascular fill – the proportion of vessels perfused compared to not-perfused, and vascular density – the proportion of villi filled by vessels. 1 represented poor perfusion/vascular density, 3 moderate, and 5 high. The observer was blind to the automated result. This assessment was deemed to be sufficient as it is the standard histological approach to assessing vascular density.

The degree of correlation between the manual and automated results was calculated using Spearman's rank correlation coefficient.

There was strong correlation between the subjective visual assessment and automated calculation for both vascular fill (r_s=0.87, p<0.01) and vascular density

($r_s=0.77$, $p<0.01$) (Figure 19), showing that the automated analysis result agreed with the visual assessment most of the time.

For vascular density, the data spread was minimal with no outliers, however there were some outlying points for vascular fill.

For the outlying cases, the results of automated segmentation were examined to determine the cause. The Weka segmentation results were good in these cases; however, the Analyse Particle tool was not always accurate in including all the perfused vessels, and excluding all the background in the perfused vessel category. For example, in one case the perfused vessel area was over estimated because the micrograph had a lot of villous tissue with multiple small gaps between them. These gaps were segmented correctly as perfused vessel and background, but because they were small and quite circular they were included by the Analyse Particle tool as perfused vessel, so their area was recorded in the perfused vessel category. This meant that the vascular fill was over estimated, and the effect was greatest when overall fill was poor (Figure 20).

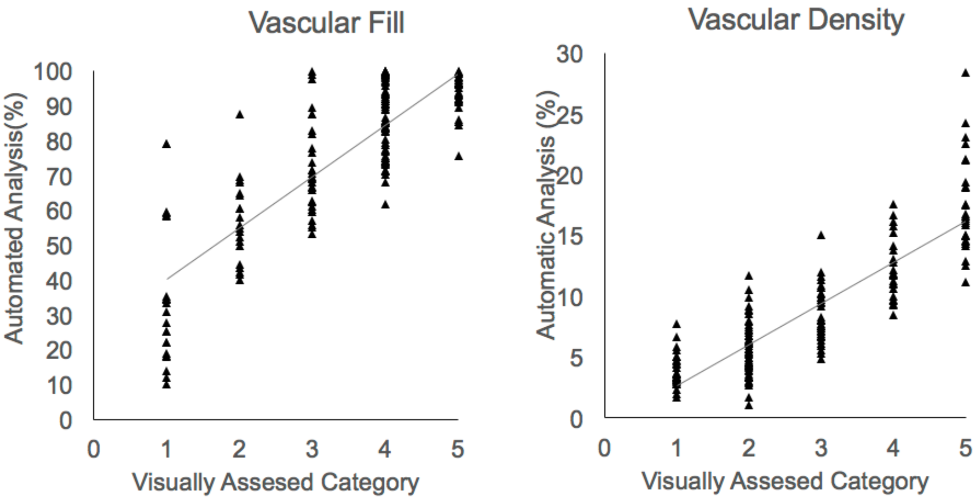

Figure 19; Correlation between manual visual assessment and automated measurement of vascular fill (left) and vascular density (right) over 179 micrographs. The assumption of normality was not satisfied by any variable (Shapiro-Wilk Test $p<0.05$). Spearman's rank correlation showed a good correlation between visual assessment and automatic analysis for both vascular fill ($r_s=0.87$, $p<0.01$ and vascular density ($r_s=0.77$, $p<0.01$).

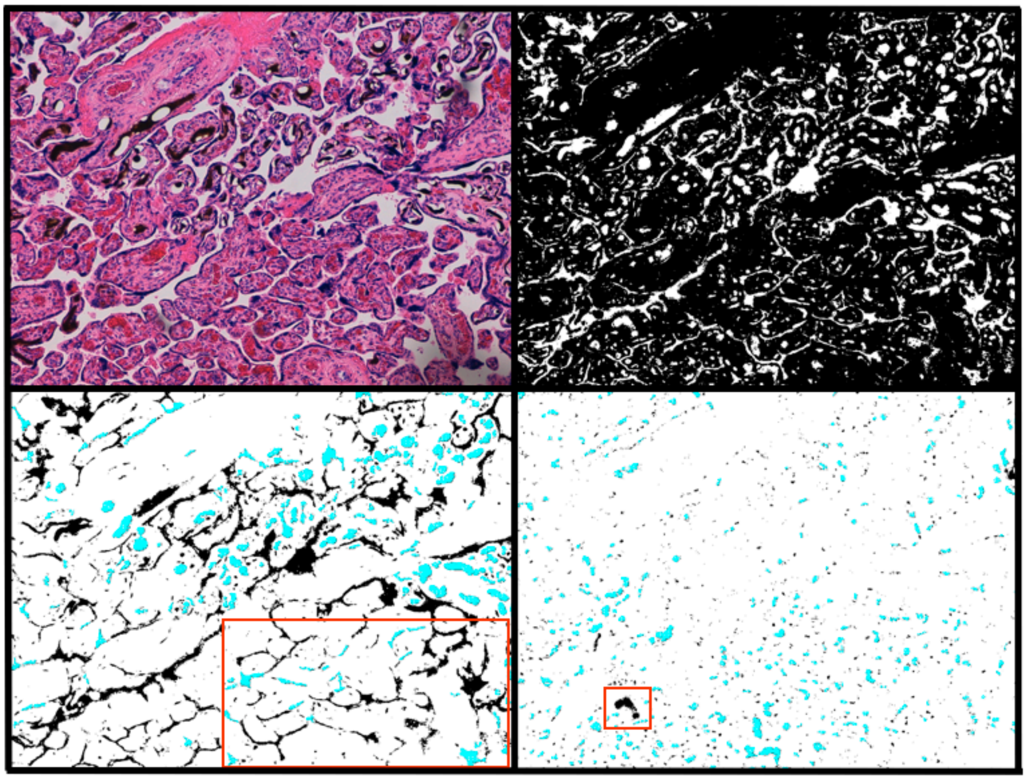

Figure 20; Example micrograph showing poorly perfused tissue. Top left; micrograph, top right; segmented villous tissue, bottom left; segmented perfused vessels, bottom right; segmented un-perfused tissue. The Weka segmentation tool worked well, however the Analyse particle tool included some background in the perfused vessel area, where villi tissue was closely packed, giving small areas of background in between (see inside red box, bottom left). Also, some un-perfused vessels were excluded by the Analyse Particle tool (see red box, bottom right). Therefore, the overall vascular fill was over estimated by the automated analysis.

The analyse particle tool restrictions were reviewed, but could not be optimised further, as improving results in one slide meant results were less good in another slide. This limitation is caused by the wide variety of appearances in placental histology with regard the spacing of the villi.

Conclusion; Automated analysis of histology

The automated analysis technique described above produces reliable quantification of perfused and un-perfused vessel area and villous tissue area, and therefore the calculated parameters of vascular fill and density.

3.3 Investigating the quantity of histology needed to estimate vascular density in a block of placenta

Although vascular density most likely varies with depth from chorionic to basal surface, it is unlikely to vary horizontally through a 1.5 to 2 cm block of placental tissue; however, it was not known how many micrographs or full thickness slices were needed to get a true estimate of the vascular density of a tissue block.

To investigate this three tissue blocks, taken from different locations within one perfused placenta, had 9 consecutive 10μm full thickness section taken, and stained with H&E. Six micrographs were taken at x 100 magnification for each section, three from the upper half close to the chorionic plate, and three from the lower half, close to the basal plate, using the method previously described in chapter 2. The micrographs were automatically analysed to measure the areas of perfused and un-perfused vessels, and villous tissue. The vascular fill and vascular density were calculated for each micrograph.

The cumulative mean, and standard error of the mean, for vascular fill and vascular density were then calculated. This was done by iteratively averaging the micrographs vascular fill or vascular density, including one additional micrograph at a time in a consecutive manner, i.e. micrographs 1, 2, 3, 4, 5 and then 6 for section one, then section two, and so on. The data was plotted as mean and standard error. A stable mean was defined as achieved once three consecutive values fell within the standard error of the mean.

The process was repeated using only micrographs from the lower half of the tissue (i.e. micrograph 1,3 and 5), representing the vessel density for the villous tree. Results are shown in Figure 21 and Table 3. The stable mean was achieved for vascular fill and density by the addition of the 12th micrographs for full thickness analysis in all but one case. In tissue block C, the stable mean of the vascular density was achieved on the addition of the 13th micrograph. The stable means of the villous vascular density and fill was achieved after 4 to 5 micrographs for tissue block A and C, but after 12 in tissue block B. Although it took much longer in B, this is because the data was much more stable throughout, making the standard error small.

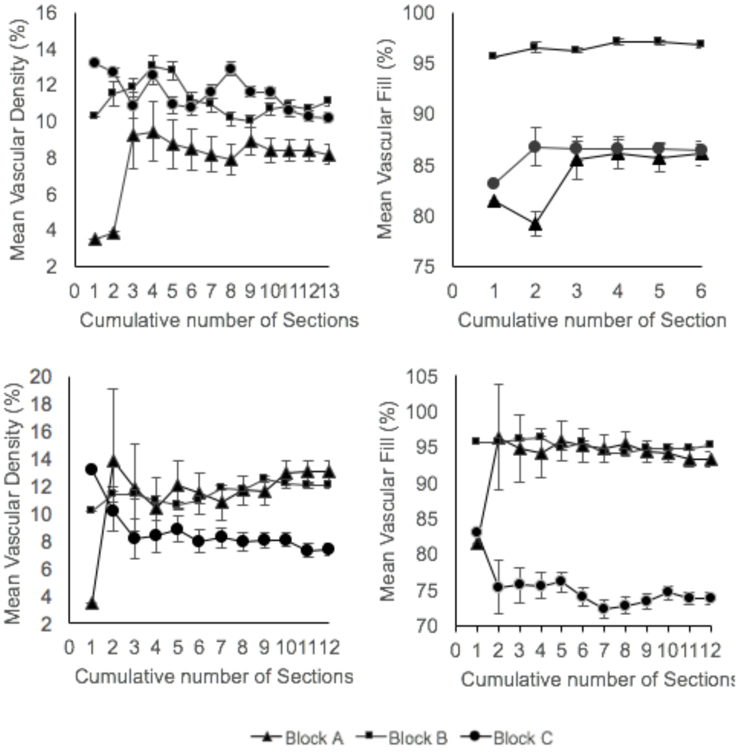

Figure 21; Graphs showing cumulative mean of vascular fill and vascular density. Mean for vascular density (left) and vascular fill (right) with cumulative micrograph additions for the whole section (upper) and lower third of the section (lower), representing villous vascular density. Micrographs were added until three consecutive means fell within the standard error of the previous mean.

	Full Thickness		Basal area	
Tissue Block	Vascular Density	Vascular Fill	Vascular Density	Vascular Fill
A	5	5	4	4
B	12	6	12	11
C	13	4	5	4

Table 3; Table showing number of micrographs added before cumulative mean fell within the standard error for three consecutive calculations. This showed that the calculation had stabilised, and suggesting a true tissue block mean had been found.

Conclusion; Investigating the quantity of histology needed to estimate vascular density in a block of placenta

Twelve micrographs, from two sections, three taken in the subchorionic region, and three in the villous region, is sufficient to establish placental block vascular fill and density. Six micrographs, taken over two sections, is sufficient to establish block villous vascular fill and density.

3.4 Optimising Placental Perfusion

Investigating contrast agent

Unlike bone, vessels have little intrinsic contrast for X-ray imaging. Contrast agents are therefore used to perfuse vessels prior to imaging. Barium sulphate ($BaSO_4$), mixed with gelatin[156] or latex[157,158] to form a gel, is frequently used as an intra-vascular contrast agent, as it has been shown to fill the entire microcirculation of some tissues under physiological perfusion pressure[156]. Microfil (Flowtech,Carver, MA, USA), a lead-containing radiopaque silicon rubber, has also been widely reported in micro-CT studies[159]. It has low viscosity allowing the complete vascular compartment to be filled with little resistance[160]. The hydrophobic qualities of silicon keep it within the vascular compartment, with extravasation only reported when inflammation caused physical leaks to be present[160].

Langheinrich et al[87] compared barium sulphate in gelatin with Microfil for human placenta perfusion, concluding that Microfil produced higher vascular fill on histological analysis than barium sulphate[87]. Micro-CT angiography of mouse placentas used Microfil, but did not investigate vascular fill[84].

To investigate the optimal contrast agent, two chorionic arteries located close to the cord insertion and perfusing different areas of a single placenta were cannulated and separately perfused with either barium sulphate mixed with gelatin (20.8g barium-sulphate (E-Z-Paque, Bracco UK Limited), 50ml 0.9% sodium chloride and 2.5g gelatine) or Microfil (Flow Tech, Carver, MA.). Three blocks were prepared from each perfused segment for histological analysis. Analysis of tissue perfused with barium sulphate was performed manually in FIJI, using the technique described above. This was because the Weka tool was developed to segment tissue perfused with Microfil, and the algorithms would therefore not correctly classify tissue perfused with barium sulphate due to its different appearance. Analysis of tissue perfused with Microfil was done using the automated process described above.

There was lower mean vascular fill with barium sulphate compared to Microfil (70% (±18%) $BaSo_4$ vs 84% (±12%) Microfil, $p=0.01$, 95% CI 3 to 24%, Table 4). In addition, barium sulphate was seen in the extravascular space in all three blocks (47% of micrographs), whereas Microfil was never seen in the extravascular space (Figure 22).

It was concluded that Microfil was superior to barium sulphate, predominantly due to the lack of extra-vascular leaking. All further work was done using Microfil.

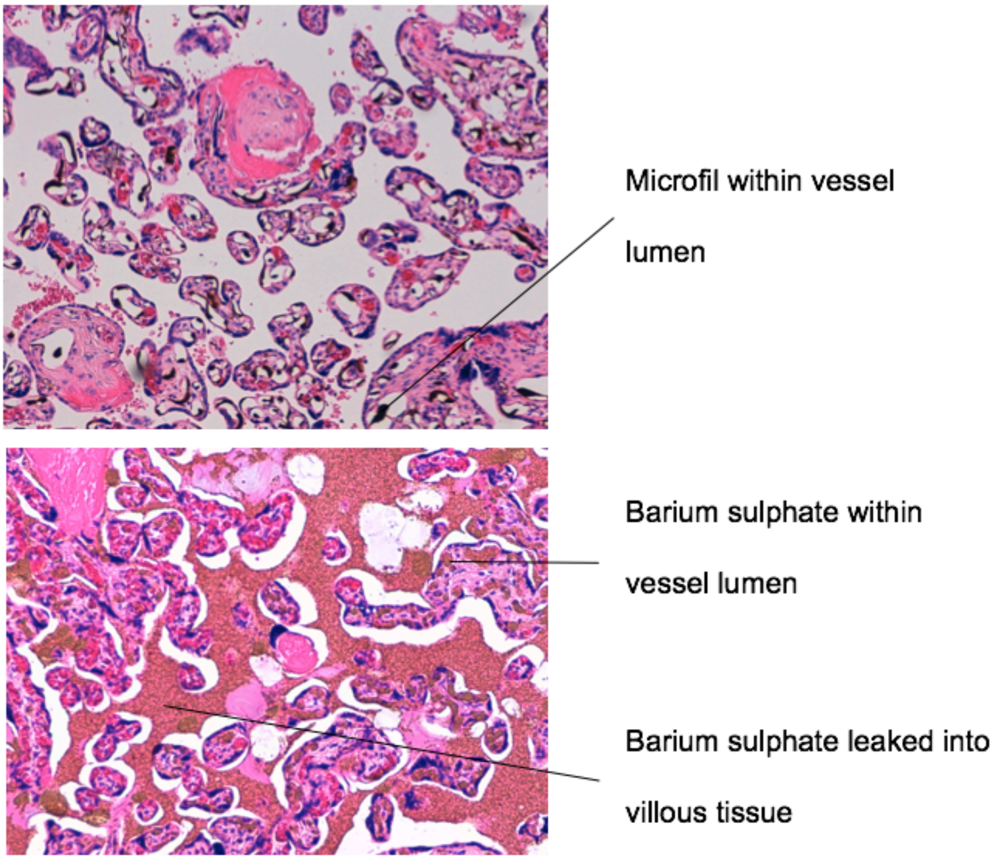

Figure 22; Micrographs of H&E stained section of term human placenta perfused with either Microfil or barium sulphate and gelatin. (A) Microfil perfusion with the majority of vessels filled and no extravascular leaking. (B) Barium sulphate perfusion showing most vessels are filled but with extensive extravascular leak of contrast agent into the placental parenchyma.

Investigating perfusion pressure

Controlled physiologically relevant perfusion pressure has been advocated for placental perfusion experiments in order to prevent damage to the tissue or dilation of the vessels[161]. 60mmHg is physiologically relevant to fetal life[162,163,164,165]. The only human placental micro-CT work published used 100cm H_2O perfusion pressure[87] (equivalent to 74mmHg). However corrosion casting work done to investigate the fetoplacental vascular tree[7], and perfusion work done to investigate anastomosis in placentas from monochorionic twin pregnancies[166] have used manual perfusion pressure, with no report of vasodilation on vessel rupture.

In theory keeping the perfusion pressure to a physiologically relevant level will keep vessels open without them being over stretched, and therefore there should be no damage to the tissue, or excessive hydrostatic pressure or oedema. However, a higher pressure may be needed to fill the vasculature completely *ex vivo*, as vasoconstriction and vasospasm may occur after delivery, and it has not been shown that higher pressures dilate or damage vessels in the short timeframes needed to fill the vasculature with contrast agent.

To assess the effect of perfusion pressure eight placentas were perfused via chorionic arteries using either: manual pressure (n=4), where a 20ml syringe containing the contrast agent was gently manually infused into the vasculature, with no quantification of perfusion pressure, but whilst observing for vascular fill and evidence of vascular dilation; or controlled pressure (n=4), where a gravity based perfusion system continuously perfused the vasculature with a pressure of 60mmHg. Blocks were taken from each perfused area and one section prepared for histological analysis from each block (manual n=13, controlled n=14).

There was no significant difference in mean vascular fill between manual or controlled 60mmHg perfusion pressure (78%(±14%) manual vs 78%(±22%) 60mmHg controlled perfusion pressure, 95% CI -7 to 6, p=0.94 (Table 4 and Figure 23)). 48% (7309/15624) of vessels were perfused using manual perfusion pressure, compared to 38% (5477/14332) of vessels with 60mmHg perfusion pressure.

To investigate fill by vessel size, vessel lumen area ranges were chosen that related to different vessel types, by measuring a selection of vessels on histological slides using FIJI. Capillaries had a luminal area less than 500μm^2, intermediate vessels mostly had a luminal area 200-5000μm^2, and stem vessels mostly had a luminal area greater than 1500μm^2. The number of perfused and un-perfused vessels for six size categories were counted - area <200μm^2 (mainly capillaries), 200 ≤ vessel < 500μm^2, 500 ≤ vessel < 1000μm^2, 1000 ≤ vessel < 1500μm2, 1500 ≤ vessel < 5000μm^2, and greater than or equal to 5000μm^2. The lowest two ranges represent capillary fill, the middle four ranges the intermediate vessels, and the last two ranges the stem vessels. The percentage of vessels filled in each category was calculated for every placental block.

The smallest vessels (capillaries) were the most poorly perfused vessels (Figure 23). The viscosity of Microfil and reduction in pressure through the vascular tree likely prevented thorough filling. Vessels with an area less than 200µm^2 were likely outside the visual resolution range of the micro-CT protocol being used, so their degree of fill was not relevant to this work. When vessels with an area less than 200µm^2 were excluded, 77% (4041/5266) of vessels were perfused with manual perfusion pressure, and 78% (2927/3765) of vessels with 60mmHg perfusion pressure. There was no statistically significant difference in the percentage of vessels perfused by either perfusion methods in any vessel size category (p=0.8, 95% CI -12 to 9) (Figure 23).

There was no difference in the distribution of vessels size between the two groups, with 91% of vessels having a lumen area smaller than 500μm in the 60mmHg perfused tissue, and 88% of vessels in the manual perfusion pressure. 3% of vessels had a surface area greater than 1500μm^2 in both groups.

Investigating location of perfusion vessel

Whole placental perfusion via the umbilical artery is desirable to fill the entire fetoplacental vascular tree, allowing imaging of the whole placenta. In addition, given the complexity of the microcirculation, perfusing centrally may fill the circulation more completely by ensuring all tributary vessels to and area are perfused. However, perfusing a single chorionic artery, and therefore only a segment of the placenta, may maintain the perfusion pressure better downstream and therefore produce a more even vascular fill. This is the technique used previously on human placentas[87].

To assess the effect of cannulation location, four placentas were perfused with controlled 60mmHg perfusion pressure via cannulation of an umbilical artery (perfusing the whole placenta due to Hyrtl's anastomosis), and blocks were taken from locations distributed throughout the placental parenchyma (n=27). One section was prepared for histological analysis for each block. The results were compared with controlled pressure chorionic artery perfusion as described in the previous section.

Perfusion via an umbilical artery achieved higher mean vascular fill than perfusion via a more peripheral chorionic vessel (84%(±18%) umbilical artery vs 78%(±22%) chorionic artery, 95% CI 0.3 to 12, $p<0.05$ (Table 4 and Figure 23)). 47% (8062/17263) of vessels were perfused by umbilical artery perfusion and 38% (5477/14332) of vessels were perfused by chorionic artery perfusion. Once vessels with a lumen area less than 200µm^2 were removed the result was 86% (4313/4999) vessels perfused via the umbilical artery compared to 78% (2927/3765) perfused via the chorionic artery. There was no statistically significant difference in the proportion of vessels perfused in any vessel size category by cannulation location (Figure 23).

Investigating arterial and venous perfusion

Both the arterial and venous circulations may be of interest to investigators in different disease settings. In FGR the arterial circulation is most likely to be of interest, as discussed in the introduction, however, it is the venous circulation that returns oxygenated blood and nutrients to the fetus, and so it is particularly important if placental territory is of interest, for example in twin pregnancies. Both have been investigated in the mouse placenta[84].

Veins are less muscular than arteries, and thus lack elasticity, so there is a greater chance of them dilating during perfusion, resulting in un-physiological measurements and causing a reduction in perfusion pressure and incomplete perfusion of the microcirculation.

To assess the effect of perfusion vessel two placentas were perfused with controlled 60mmHg perfusion pressure via cannulation of the umbilical vein, and blocks taken from locations throughout the placental parenchyma (n=8) and prepared for histological analysis. The results were compared with umbilical artery perfusion already performed.

Umbilical artery perfusion produced higher vascular fill than umbilical vein perfusion (84%(±16%) umbilical artery vs 70%(±20%) umbilical vein, 95% confidence interval 7 to 20, $p<0.01$ (Table 4 and Figure 23)). In total 47% (8062/17263) of vessels were perfused via the umbilical artery, compared to 40% (6248/15503) of vessels via the umbilical vein. When vessels with an area less than 200µm^2 were excluded 86% (4313/4999) of vessels were filled using arterial perfusion, and 70% (3680/5232) using venous perfusion. There was a statistically significant difference in the proportion of vessel filled by arterial compared with venous cannulation with an area of 200 to 500μm^2 (84%(±16%) umbilical artery vs 60%(±15%) umbilical vein, 95% CI 9 to 39, $p<0.01$ (Figure 23)) and 500 to 1000μm^2 (96% (±6%) umbilical artery vs 86% (±2%) umbilical vein, 95% confidence interval 2 -19%, $p<0.05$). During perfusion, it was noted that the chorionic veins dilated considerably, in comparison with chorionic arteries which maintained their diameter.

Perfusion Technique	Number of placentas perfused	Number of Placental Blocks	Number of Micrographs	Number of Micrographs excluded (%)	Number of vessels counted	Number of vessels filled (%)	Mean Vascular fill % (+/- SD)	P value
Contrast Agent (Chorionic artery cannulation, manual perfusion pressure)								
BaSO4	1	3	18	0 (0)	NA	NA	70 (18)	0.01*
Microfil		3	18	0 (0)	NA	NA	84 (12)	
Perfusion Pressure (Microfil as contrast agent, chorionic artery cannulation)								
Manual Pressure	4	13	78	18 (23)	15624	7309 (47)	78 (14)	0.95
Controlled 60mmHg Pressure	$4^{\wedge}$	14	84	12 (14)	14332	5477 (38)	78 (22)	
Cannulation Location (Microfil as contrast agent, controlled perfusion pressure)								
Umbilical Artery	$4^{\#}$	27	186	36 (19)	17263	8062 (47)	84 (16)	0.04*
Chorionic Artery	$4^{\wedge}$	14	84	12 (14)	14332	5477 (38)	78 (22)	
Arterial or Venous Cannulation (Microfil as contrast agent, controlled perfusion pressure)								
Umbilical artery	$4^{\#}$	27	186	36 (19)	17263	8062 (47)	84 (16)	<0.01*
Umbilical vein	2	8	48	0 (0)	15503	6247 (40)	*70 (20)*	

Table 4: Results from perfusion optimisation experiments. N = 15 placenta, superscripts symbols ($^{\wedge,\#}$) show the same group of placentas used in different comparisons. P values are independent student t-test comparison of means, significance set at 0.05, denoted with *. NA = not available

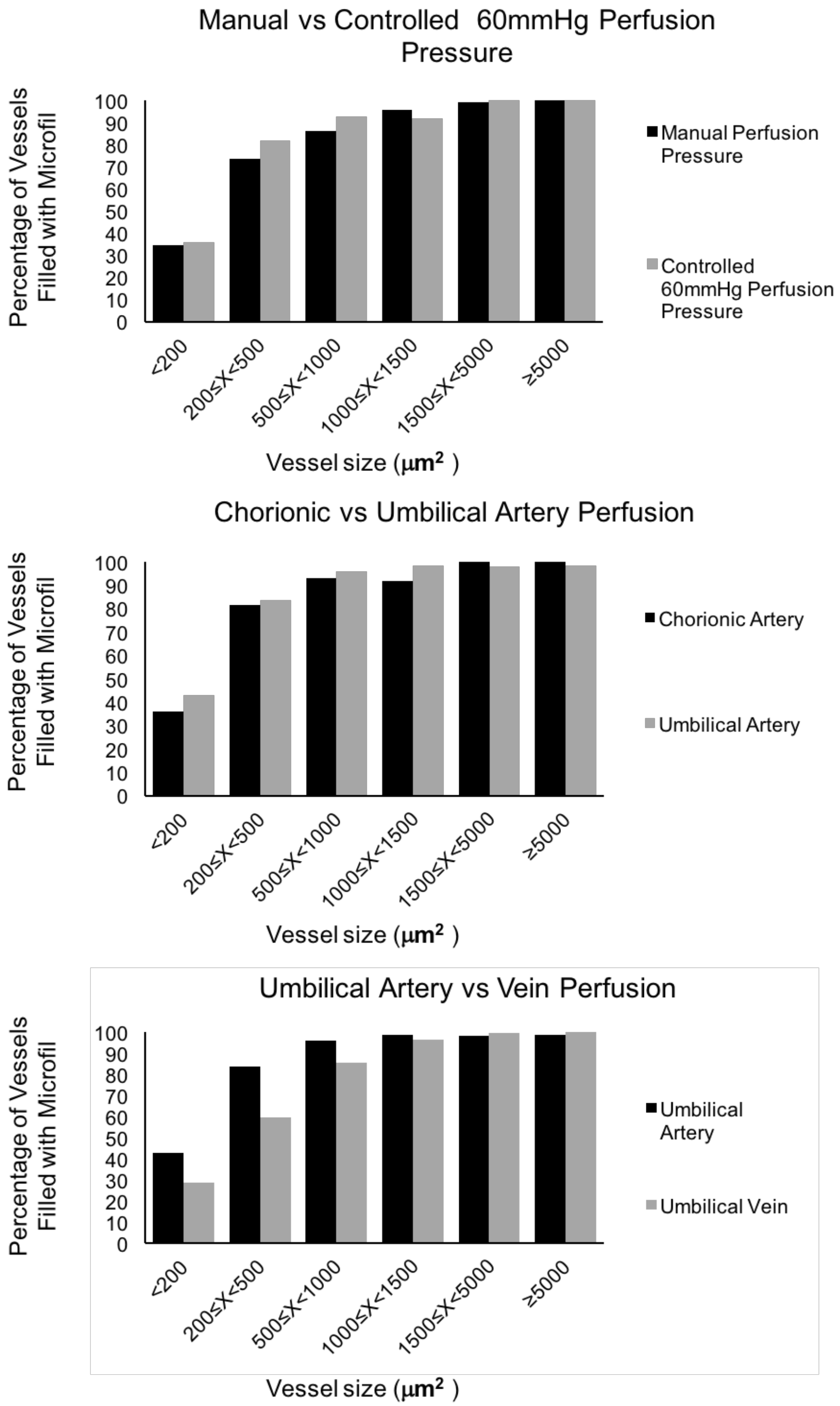

Figure 23; Graphs showing bar charts of percentage of vessels filled of each vessel size (area in μm^2) using different perfusion techniques. Top: Manual (black, n=60 micrographs) vs 60mmHg controlled (grey n=72 micrographs) perfusion pressure via a chorionic artery. Middle: Chorionic artery (black, n=82 micrographs) vs Umbilical artery (grey, n=150 micrographs) perfusion at 60mmHg pressure. Bottom: Umbilical artery (black, n=150 micrographs) vs umbilical vein (grey, n=48 micrographs) perfusion with 60mmHg perfusion pressure.

Conclusion; Placental Perfusion

In conclusion, Microfil was the superior contrast agent as it did not leak extravascularly. Using controlled continuous 60mmHg perfusion pressure or manual perfusion pressure made no difference to fill, however central cannulation location was superior to peripheral chorionic cannulation, and fill was significantly worse after umbilical venous compared to umbilical arterial perfusion. The optimised technique is shown in Table 5.

	Langheinrich[87] (Human)	Rennie et al[84] (Mouse)	Assessment Parameters	Optimised Protocol
Tissue Preparation				
Contrast Agent	Microfil and BaSO4 in gelatin	Microfil	Microfil and BaSO4 in gelatin	Microfil
Perfusion Pressure (mmHg)	74	Not reported	Manual pressure and 60	No difference
Cannulation Location	Chorionic artery – peripheral perfusion	Umbilical artery - central perfusion	Chorionic (peripheral) and umbilical (central) perfusion	Umbilical artery
Arterial or Venous Cannulation	Chorionic plate artery	Umbilical Artery/ Umbilical Vein	Umbilical artery/ Umbilical vein	Artery

Table 5; Table showing tissue preparation parameters used in previous studies, and those investigated in this study. The final column shows the optimised protocol, based on the results of this work.

3.5 Optimising Micro-CT Imaging Parameters

It was necessary to optimise micro-CT imaging parameters to maximise divergence of contrast agent filled vessel grey-scale values from tissue grey-scale values in the resulting image volumes, therefore improving separation of vessel from tissue in subsequent image processing. I therefore investigated the micro-CT parameters that produced the highest contrast to noise ratio (CNR).

An X-ray beam spectrum is dependent on the X-ray tube energy (kV), the target material, and whether filtering is used. Increasing X-ray tube energy increases both the energy of individual photons, and the number of photons in the resulting spectrum.

The amount of radiation that passes through a tissue is dependent on the amount of radiation entering the tissue; the linear attenuation coefficient of the tissue, which is dependent on tissue properties and the spectrum photon energy; and the distance the photons need to travel through the tissue (Beer-Lambert equation). Contrast is usually highest at low beam energy levels, as lower energy photos are attenuated more easily than high-energy photons. As the energy level increases more photons pass through the tissue without interacting with the tissue. This makes contrast lower, but also decreases the image noise. The beam energy needs to be high enough to sufficiently penetrate the tissue of interest, with a minimum of 10% of photons passing through the tissue being a good guide, and minimise the image noise, but low enough to have adequate contrast.

The aim of this work was to determine the energy level that optimised the CNR between placental tissue and Microfil.

X-ray Attenuation of Microfil and Placenta

To establish a theoretical optimal energy level to guide practical experimentation, the mass attenuation coefficients of Microfil and tissue were compared.

To determine the mass attenuation coefficient of Microfil an on-line database was consulted, which can determine the attenuation coefficient for any mixture when the ingredients are entered[167] (XCOM from the National Institute of Standards and Technology, available at http://physics.nist.gov/PhysRefData/Xcom/html /xcom1.html). Unfortunately, the precise ingredients in Microfil are not available. However, a previous group estimated the composition of Microfil based on information provided within the material safety data sheets, measurements of density and attenuation coefficients of the constituents shipped by the manufacturer, and comparison with similar silicone-rubber based compounds with known compositions, and these are shown in Table 6[168]. This composition was used to determine the likely attenuation cross section for Microfil.

Microfil Component	Compound	Molecular Formula	Contribution by weight (%)
MV-122 compound	Lead sulfate	$PbSO_4$	4.48
	Lead chromate	$PbCrO_4$	4.48
	Polymethylhydrogensiloxane (e.g., Dow Corning MH 1107)	$(CH_3)_6SI_2O$ $(SiOCH_4)n$	39.3
MV diluent	Dimethyl siloxane polymer (e.g., Dow Corning 200 fluid)	$(C_2H_6OSi)n$	46.8
Curing Agent	Ethyl silicate	$C_8H_{20}O_4Si$	1.95
	Dibutyltin dilaurate	$C_{32}H_{64}O_4Sn$	2.93

Table 6; The assumed composition of Microfil silicone-rubber casting compound.
Taken from Granton et al 2008[168]

To determine the mass attenuation coefficient for placenta, the Commonwealth Scientific and Industrial Research Organisation database was used. There is no data on placenta, so the attenuation for soft tissue was used (available at: https://www.ts-imaging.net/Services/Simple/ICUtilXdata.aspx).

The mass attenuation coefficients were plotted against increasing energy level for Microfil and Placenta (Figure 24).

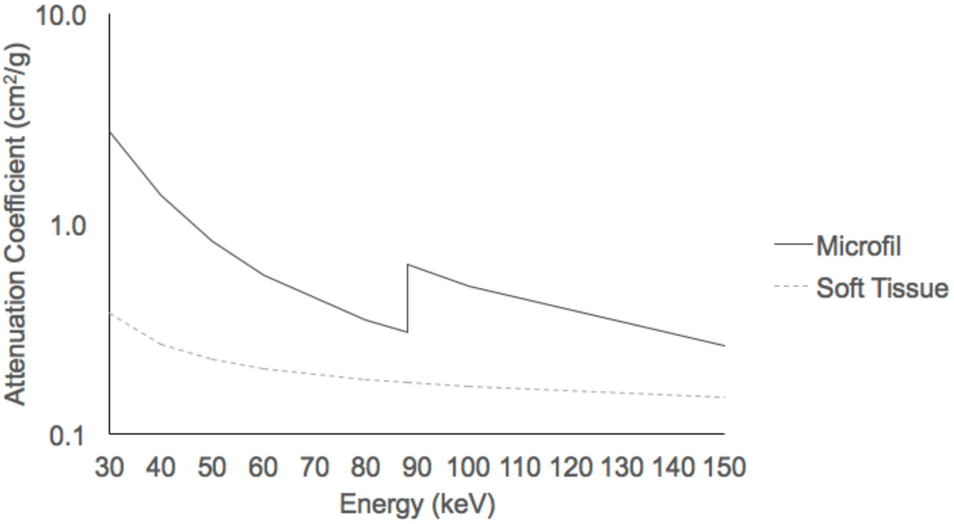

Figure 24; Plot of calculated mass attenuation coefficient for Microfil (black) and soft tissue (grey) with increasing energy level from 30 to 150kV.

Microfil has a sudden increase in mass attenuation coefficient at 88keV causing a sudden increase in contrast between Microfil and soft tissue at this energy. This sudden increase in the attenuation coefficient occurs at the photon energy just above the binding energy of the K-shell electron of the atoms interacting with the photons and is known as the K-edge. In theory contrast can be optimised by producing a high number of photons at the K-edge of the material being imaged.

However, the difference in attenuation coefficient at lower energy levels is still higher. Lowest energy levels would therefore likely provide the best contrast, however it was not known if there would be sufficient penetration, or excessive noise, at low energy levels.

Effect of Target Material on Spectrum

Unlike a synchrotron, where the energy produced is within a very fine bandwidth, micro-CT produces a spectrum of energies, with the energy set for the tube being the maximum photon energy in the resulting spectrum. This is shown in the spectrum below (Figure 25), which was measured on a micro-CT scanner set to a tube energy of 100kV, using a tungsten target.

A broad spectrum of x-rays are produced, with peaks in photon number at about 60keV and 70keV. This increase in photons occurs when the energy is equal to the binding energy of an electron shell of the target material. The energy is the least at which a vacancy can be created in the particular shell and is referred to as the emission line. These peaks are therefore unique to any given element and are important in the final spectra produced by a target made of that element.

Image contrast is therefore dependent on the target material. Given that the micro-CT scanner used was multi-source, with Tungsten, Molybdenum and Copper targets, this also warranted investigation.

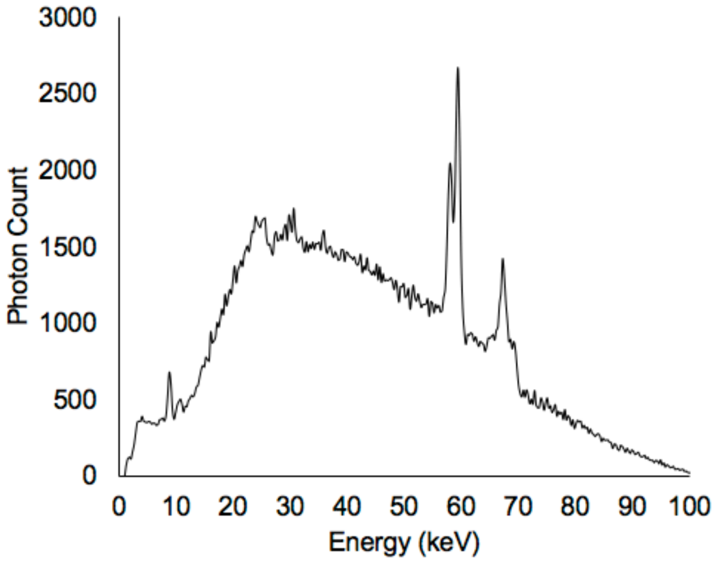

Figure 25; Tungsten Spectra at 100kV. Measured on a XTH225 M single-target micro-CT scanner (Nikon Metrology, Tring) with a spectrometer.

Investigating Contrast to Noise Ratio for Placental Angiography with Microfil

To determine the energy level that optimised contrast to noise ratio (CNR) between placenta and Microfil a 2x2cm full thickness block of human placenta was repeatedly imaged adjacent to a 3mm internal diameter tube filled with Microfil, starting with a tube energy of 30kV, and increasing to 100kV in increments of 10kV. Imaging was repeated using the Tungsten, Copper and Molybdenum targets. Imaging parameters were otherwise maintained; exposure time 500ms, 3141 projections, and current adjusted to maintain the darkest area of the radiograph above 10% of background brightness, without saturating the detector. Scans were reconstructed using a modified Feldkamp filtered back projection algorithm with proprietary software (CTPro3D; Nikon Meterology).

To calculate the CNR, an area of interest with 1mm radius was drawn in the reconstructed volume over an area of placenta, Microfil and air, and the mean grey scale value and standard deviation recorded (Figure 26). This was done at slices

660 and 1320 of the 2000 slice volume. These slices were chosen because preliminary work showed the background noise changed with slice height (Figure 27). Choosing the slices one third and two third through the volume ensured the measurements were comparable within volumes, as the change in noise was symmetrical the central slice, and most importantly comparable between samples. The mean of the two measurements was taken.

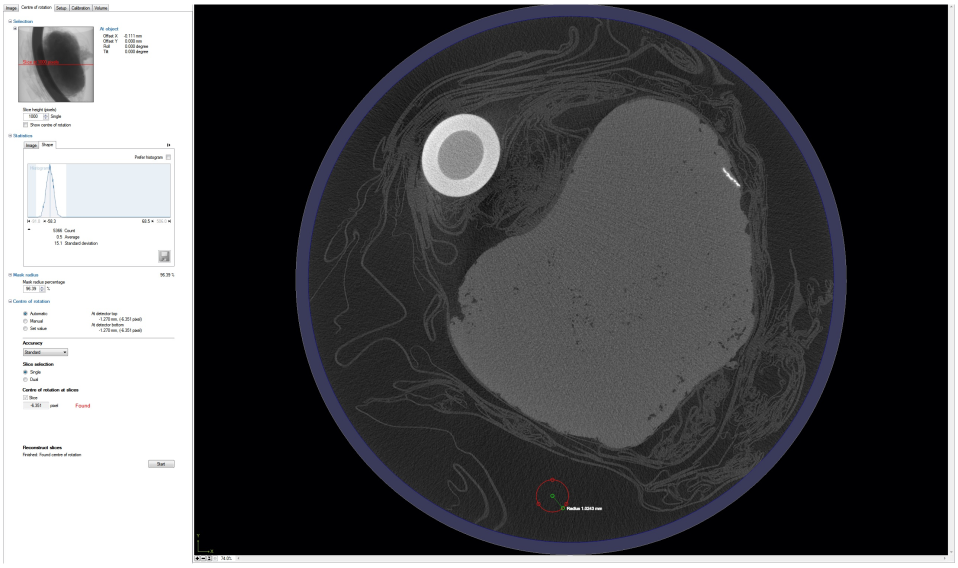

At object
Offset X -0.111 mm
Offset Y 0.000 mm
Roll 0.000 degree
Tilt 0.000 degree

Slice height (pixels) 1000 Single
☐ Show centre of rotation

Prefer histogram ☐
-91.8 -58.3 68.5 506.0
5366 Count
0.5 Average
15.1 Standard deviation

Mask radius 96.39 %
Mask radius percentage 96.39 %

● Automatic
○ Manual
○ Set value
At detector top
-1.270 mm, (-6.351 pixel)
At detector bottom
-1.270 mm, (-6.351 pixel)

Accuracy
Standard

Slice selection
● Single
○ Dual

Centre of rotation at slices
☑ Slice
-6.351 pixel Found

Reconstruct slices
Finished: Found centre of rotation

Radius 1.0243 mm

Figure 26; Screen shot showing the measurement of the standard deviation of the signal in air. The red circle shows the area of interest, and the histogram to the left of the screen shows the average signal and the standard deviation.

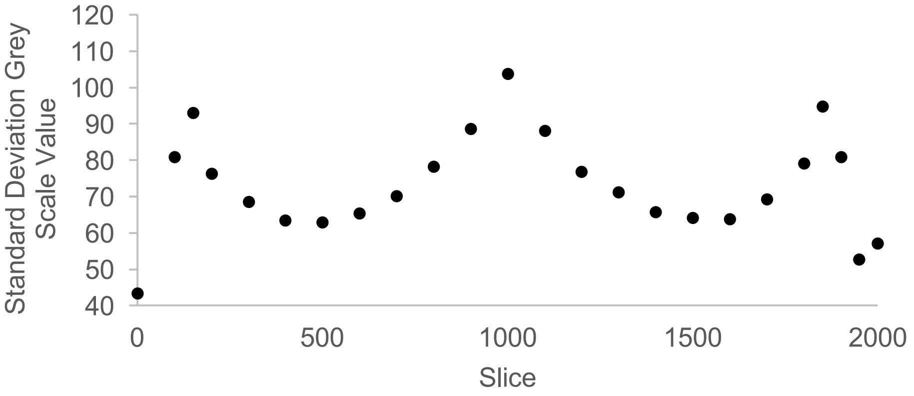

Figure 27; Graph showing standard deviation of the grey scale value in a 1mm radius area of interest drawn over air. The imaging was of an aluminium rod at 150kV with a Tungsten target. This allowed for uniformity of X-ray attenuation throughout the volume. The cause for the changes in noise throughout the volume was unknown, but the effect was repeatable on several machines produced by the same manufacturer, and was thought to be caused by the detector.

The contrast to noise ratio was calculated as:

$$\text{Contrast to Noise ratio (CNR)} = \frac{(\text{Placenta Grey Scale Value} - \text{Microfil Grey Scale Value})}{\text{Standard Deviation of Signal of Air}}$$

Micro-CT Contrast to noise ratio

The standard deviation was taken in air, as placenta is a heterogenous tissue and therefore the standard deviation of signal in placenta is large. Air was therefore used as a proxy. Results are shown in Figure 28. As expected, contrast was greatest at low energy levels, with contrast steadily decreasing as energy increased. The molybdenum target produced the highest contrast throughout the energy levels, and copper the lowest. Noise was greatest at the lower energy levels, with the spectrum produced by the molybdenum target having higher noise compared to the tungsten target. The decrease in noise level with increasing energy was greatest between 30kV and 50kV. This made CNR highest at 50kV. Molybdenum had a slightly higher CNR than tungsten, copper had the lowest.

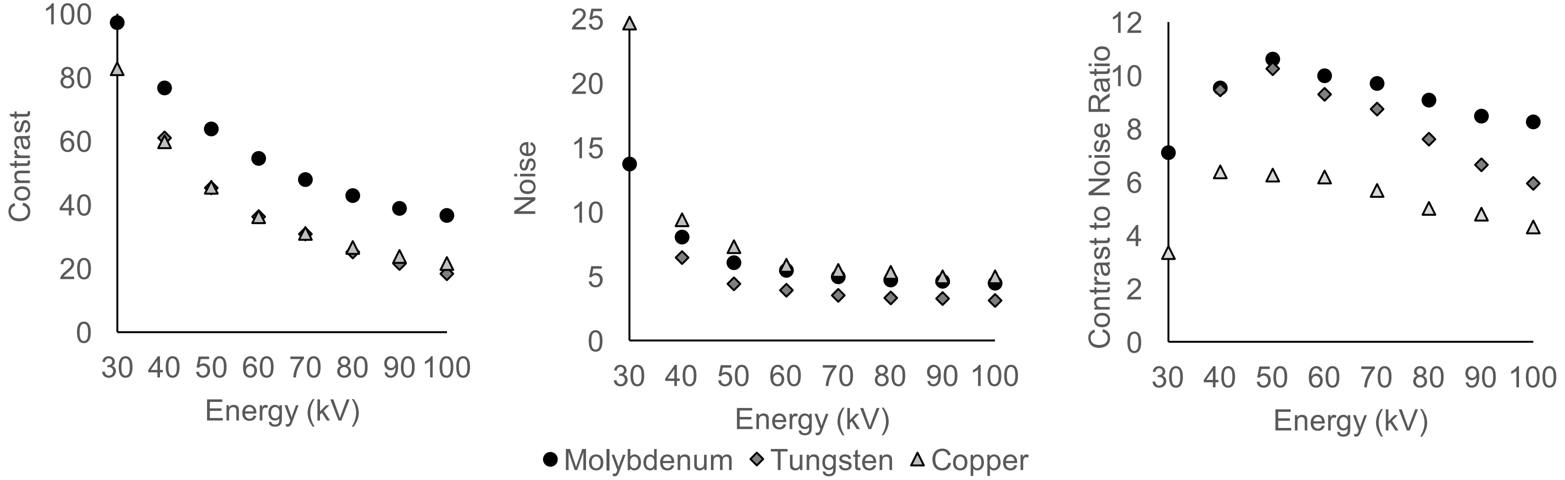

Figure 28; Figures showing difference in contrast, noise and CNR with differing beam energy and target material. A: Contrast, defined as Microfil Grey Scale value – placental tissue Grey Scale value, (arbitrary units) with increasing energy level for molybdenum, tungsten and copper target. B: Standard deviation of the signal in air, the image noise, with increasing energy level for molybdenum, tungsten and copper target. C: Contrast to noise ratio with increasing energy level for molybdenum, tungsten and copper target.

Investigating Perfused Tissue Penetration

To ensure 50kV had sufficient penetration to image the perfused placenta, a whole placenta was perfused using the optimised protocol above, and then imaged whole. It was then dissected into eight blocks, as described in the methods, and these were imaged with increased magnification.

50kV was not sufficient to penetrate the whole placenta. This was because, with the placenta mounted with chorionic plate parallel to the detector, there was a greater thickness of tissue for the beam to pass through than there had been during optimisation with a block, particularly when the placenta was aligned perpendicular to the detector making the tissue thickness equivalent to the chorionic plates widest diameter. The spectrum was largely attenuated (Figure 29). The tube energy was gradually increased, checking the greyscale value in the darkest area against the background grey scale value, on the resulting radiographs, aiming for the darkest area to be greater than or equal to 10% of the background. Sufficient penetration was achieved with 80kV (Figure 29).

For block imaging 50kV was sufficient to penetrate the perfused placenta block.

Using the optimised tissue preparation and imaging protocol, the feto-placental microcirculation was clearly visible with micro-CT imaging, allowing the 3D vascular structure to be appreciated (Figure 30).

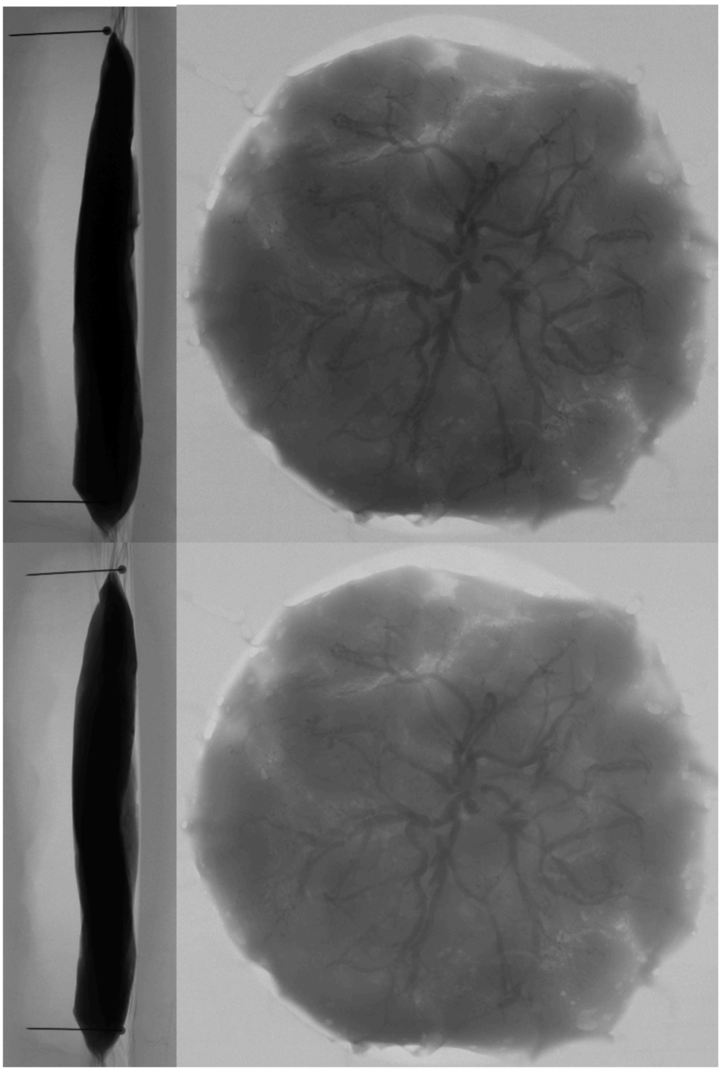

Figure 29; Radiographs of placenta lying parallel to the detector (right) and perpendicular to the detector (left) at 50kV (top) and 80kV (bottom). Increasing tube energy increased the energy and number of photons in the resulting spectrum, and therefore improved X-ray penetration. This results in a brighter radiograph, and a higher grey scale values. At 80kV the darkest area of placenta (with the placenta perpendicular to the detector) had a grey scale value 10% of the background.

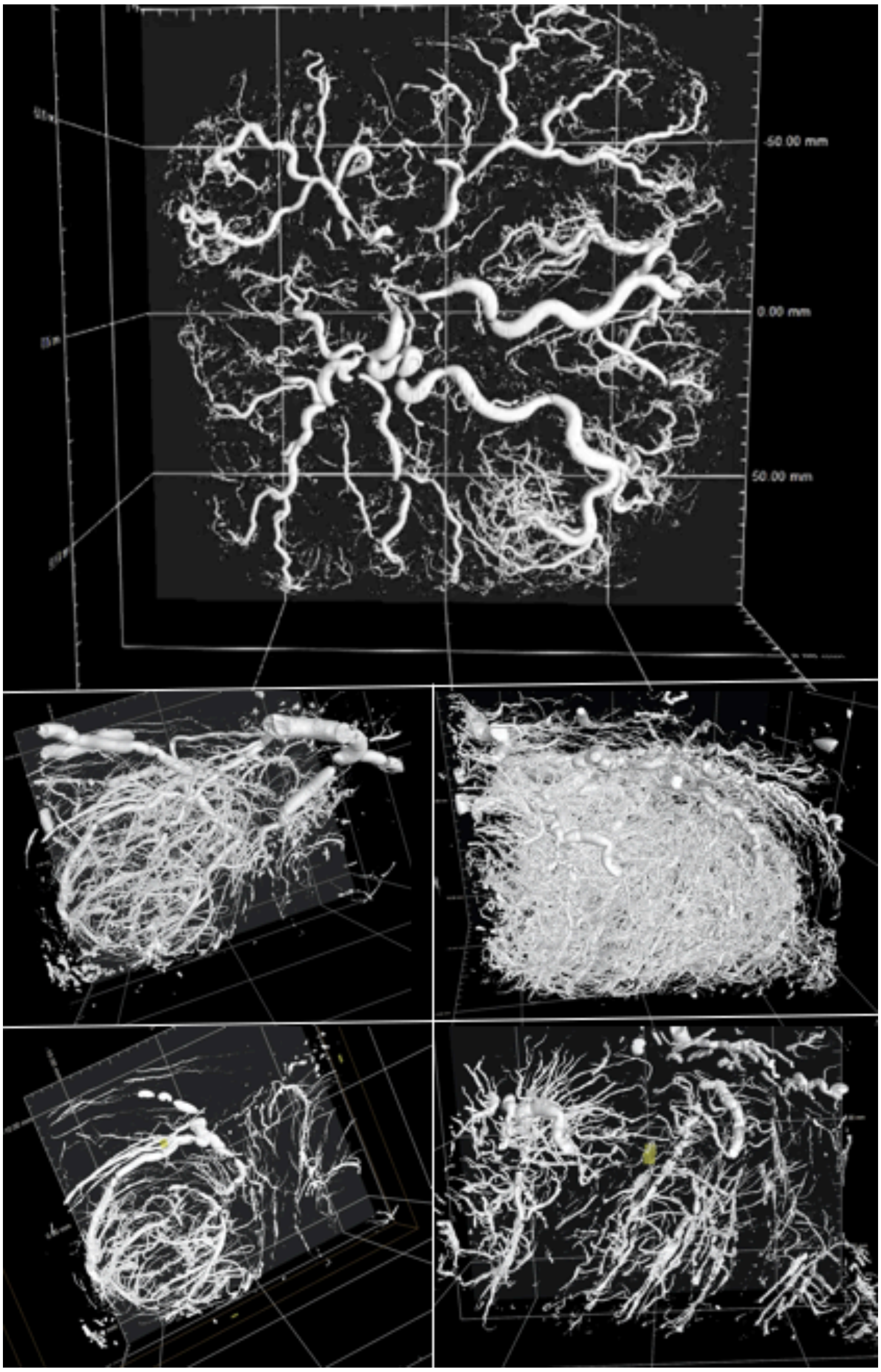

Figure 30; Micro-CT imaging of a human placenta perfused with Microfil. Surface renderings made using VG StudioMAX 2.2 (Volume Graphics, Germany) thresholded halfway between the grey scale intensities of tissue and Microfil. Top; the whole placenta imaged with 80kV energy. Bottom; two blocks taken from the placenta, imaged with 50kV energy, showing the whole volume (top) and a slice through the volume (bottom). The complex vascular tree is clearly seen, with whole imaging showing chorionic and stem vessels, and block imaging the villous vascular tree down to the terminal capillaries.

Conclusion; Optimising Micro-CT Imaging Parameters

The highest CNR was achieved using a molybdenum target and 50kV tube energy level. This gave sufficient penetration for perfused placental block imaging. For whole placental imaging a higher energy was needed. 80kV gave adequate penetration and good image quality.

3.6 Discussion

This work establishes optimal tissue perfusion technique and imaging parameters for micro-CT imaging of the human fetoplacental vascular tree. This will result in the optimal image quality. This is essential if image analysis is to be relevant to anatomy.

Automated analysis

This work was feasible due to the automated approach used for histological analysis. The segmentation of each class was not perfect, due to the large variability of appearances of histological micrographs. However, the validation showed that the system produced reliable results, sufficient for the work.

In the work investigating perfusion methods, a total of 360 micrographs were analysed using the automated process, measuring and recording the area of 62,722 vessel lumens in total. To do this manually would not be feasible. In addition, manual measurement would have inherent limitations due to human error and fatigue.

During analysis of the perfusion work, two areas were identified where the automated process did not perform well. Firstly, large vessels with a few red blood cells were classified as perfused vessel by the segmentation tool, but may not have been perfused due to the presence of red blood cells and lack of Microfil. This was a rare finding in the histology slides, and only became significant if there was low vascular density. Secondly, it was noted that on some micrographs all the vessels were empty of red blood cells and Microfil. The automated analysis of these slides calculated good vascular fill, as empty vessels are categorised as perfused vessels. However, although some Microfil can be lost in the production of histological slides, it is unlikely that it would all fall out from a well-perfused section. As it was impossible to know if these areas had been perfused it was decided to exclude sections where there was no Microfil present from analysis, but to note them as a result of interest. Otherwise the analysis worked well, with manual assessment agreeing with automated results with regard to vascular fill and density.

Tissue preparation parameters

As expected from previous work[87] (Table 5), Microfil was a superior contrast agent to barium sulphate, producing higher fill and remaining intravascular, whilst barium sulphate leaked into the extravascular space. This is important, as extravascular leak of contrast agent will be segmented in post image processing as vessel, and so will introduce noise into the image analysis.

Vascular fill was more complete with cannulation of the umbilical artery, at the center of the vascular tree, which may be because all the vessels feeding into an area were perfused, maximising the delivery of contrast agent. Perfusion pressure did not appear to affect vascular perfusion. Fill was significantly worse after umbilical venous compared to umbilical arterial perfusion. The venous vessel noticeably dilated during perfusion probably due to the deficiency of muscle in the vessel wall[169], which in turn reduced perfusion pressure and consequently under filled the microcirculation.

Previous work by Rennie et al[84] in mice found that umbilical vein diameter measurements were similar at micro-CT after perfusion as *in vivo* measured using Doppler ultrasound. However, they did not comment on vessel size more distally in the vascular tree, or investigate fill histologically. Venous vessel diameter *in vivo* was not investigated in this study; however, these results suggest that perfusion through the venous vasculature is unlikely to result in physiologically relevant vessel sizes in human placenta because of the permissive venous vessel wall[170]. This difference may be due to difference in placental morphology between species, of differences in perfusion technique.

The main limitation of whole placental perfusion is that homogeneous fill throughout the complex vascular network cannot be assumed, as contrast agent may preferentially flow to areas of lower resistance. This limitation is fundamental to all perfusion work[161].

Some sections were excluded as no Microfil was present in any vessel. When comparing manual and controlled perfusion pressures a similar number of sections were excluded from each group (3 and 2 respectively). However, in the case of whole versus segmental perfusion, and arterial versus venous, the number of excluded slides was quite different (6 whole vs 2 segmental, 6 arterial vs 0 venous). Why some sections were not perfused is uncertain. It is possible something in the tissue preparation resulted in the Microfil falling out of the vessels from these slides, such as it washing out when the tissue was cut. It is also possible these areas of tissue were perfused with heparinised saline but not Microfil, due to Microfil's higher viscosity. There was no recurring spatial pattern for where the blocks were taken from within the placentas, with regard to proximity to cord insertion or placental edge.

When the data is looked at from the perspective of the number of slides excluded per placenta, 2-3 sections were excluded for each placenta perfused for both umbilical and chorionic artery perfusion. This suggests that whatever the reason for these slides having no Microfil, the number excluded per tissue area perfused remains relatively constant, so it is unlikely to relate to perfusion technique. The exception to this is the venous perfusion, where all slides had Microfil present. Regardless the fill with venous perfusion was significantly worse so this method will not be investigated further in this thesis.

Imaging Parameters

No literature could be found on optimisation of contrast filled vascular imaging, and so no allergy could be made to imaging of other tissues. Previous work in placenta has published micro-CT protocols, but not how these protocols were reached, or why specific parameters were chosen[86,84]. This work was therefore necessary in order to develop imaging parameters that optimised the contrast to noise ratio between placenta and microfil.

The highest contrast between Microfil and placenta was at 30kV tube energy levels. In general contrast is highest between different density structures at low energy levels, fitting with these results. However lower energy spectra have reduced penetration and the imaging has higher levels of noise. 50kV gave the highest CNR. This is a lower energy level than used in previous work (60kV[86] and 80kV[84] (Table 7)).

50kV was sufficient to penetrate a perfused placental block, however it was not sufficient to penetrate the whole perfused placenta, due to the large quantity of tissue to penetrate when the placenta was perpendicular to the detector. 80kV was sufficient energy to penetrate the whole perfused placenta, and produce high quality imaging.

Other studies have not reported the target material used. The most likely target material is Tungsten, as this is what most manufacturers use for their target. This work found molybdenum gave the highest CNR. This is probably because the characteristic peaks in the molybdenum spectrum occur at 17.6keV and 19.7keV, ideal for imaging at 50kV. However, the difference between tungsten and molybdenum CNR was minimal at low energy levels, so tungsten is a valid alternative in single target machines.

	Langheinrich[87] (Human)	Rennie et al[84] (Mouse)	Optimised Protocol
Cone-beam energy (kV)	60	80	50
Target material	Not reported	Not reported	Molybdenum
Isotropic voxel size (μm)	13 and 4	13	Dependent on magnification and field of view required
Specimen rotation (degree)	180	360	360
Exposure time (ms)	2400	Not reported	1000
Number of projections	400	720	3141

Table 7; Table showing the imaging parameters used in previous work, and the optimised imaging parameters from this work.

In conclusion, this work investigated perfusion of the human term fetoplacental vascular tree, and micro-CT imaging parameters, and then presents an optimised methodology for perfusion and micro-CT imaging of the human fetoplacental vascular tree.

At the end of the process, I felt a technique had been developed for placental perfusion that would reproducibly provide the best possible fill of the fetoplacental vascular tree. This was with perfusion with Microfil, via cannulation of a central, ideally umbilical, artery. And that an imaging protocol that optimised the contrast-to-noise ratio between placental tissue and Microfil had been reached., which utilised a lower energy level than has previously been used.

This method will be used in the rest of this thesis, where I investigate the human fetoplacental vascular tree at different scales.

4 Investigating the Spatial pattern of Chorionic and Stem vessel within normal, term placenta

4.1 Summary

Variation in vascularisation through the human placenta is not well defined. Standard histological approaches of placental examination lack the spatial resolution to do this. They are also limited in only imaging the two-dimensional structure.

In this chapter I present data from whole placenta micro-CT imaging of normal, term placenta. This is the first work to investigate three-dimensional vascular density throughout the placenta, and to investigate if there is a consistent spatial pattern in vascular density between placentas.

I show that there is a large degree of variation in vascular density within and between normal term placentas, and that there is no consistent spatial pattern with regard to placental structure. This work is important because no one has quantified the normal term feto-placental vascular density at this scale, and so there is no normal definition against which pathology can be compared. The work shows that there is no area of the tissue that can be routinely sampled to ensure a good estimate of the whole placental vascularisation.

4.2 Demographic Data

Inclusion criteria for this work were:

- Women undergoing elective caesarean section after 38 completed weeks of pregnancy.
- No maternal complications of pregnancy, including but not limited to diabetes (gestational or pre-existing), hypertension, and pre-eclampsia.

- Birth weight above the 10th centile (not-customised), with no neonatal complications at delivery requiring resuscitation or admission to the Neonatal Unit.

Ten placentas delivered by elective caesarean section at term were investigated. The demographic data for the cases included are shown in Table 8.

Case Number	Maternal Age (years)	Maternal BMI	Smoking status	Gestational Age at Delivery (weeks + days)	Indication for caesarean section	Birth Weight (g) (centile (%))
1	31	22	Never	39+4	Breech presentation	3504 (76)
2	37	23	Never	39+0	Maternal choice	3950 (94)
3	46	21	Never	39+0	Previous caesarean section	3480 (62)
4	41	26	Never	38+1	Three Previous caesarean sections	3360 (78)
5	39	19	Never	39+0	Maternal choice	3220 (55)
6	37	22	Never	39+0	Previous caesarean section	3980 (95)
7	31	28	Never	39+0	Two Previous caesarean sections	3960 (94)
8	35	22	Never	39+2	Two Previous caesarean sections	3470 (61)
9	34	34	Never	38+5	Previous caesarean section	2730 (20)
10	34	19	Never	39+2	Maternal choice	4000 (96)
Median (IQR)	36 (34-39)	22 (21-26)	Never	39+0 (39+0-39+0)		3492 (3360-3960)

Table 8; Clinical characteristics of pregnancies for included placenta. All birth weights were above the 10th centile, and there were no neonatal complications.

4.3 Placental Descriptive Data

The placental weight, volume measured from whole placenta micro-CT in MATLAB, Cord Centrality Index (CCI) and Placental Eccentricity (PE) measure for each placenta are shown in Table 9. Placental weight was plotted against placental volume to check they correlated (Figure 31). There was a strong correlation between weight in grams and volume in cm^3 ($r=0.97$, $0<0.01$). The volume measure in cm^3 is smaller than weight in grams, which is expected given that one cm^3 water weighs one gram, and placental tissue with air space has a lower density than water.

The placentas were ordered by CCI throughout this chapter, to allow easy recognition of trends in the data correlating with cord insertion site. The mean CCI was 0.29(±0.25), and the mean PE was 0.61(±0.15). These results are similar to previous work with a much larger sample size of eight hundred and thirty-six (0.36(+0.21) CCI and (0.49(±0.17) PE)[153].

Case Number	Placenta weight (g)	Placenta Volume (cm^3)	Cord Centrality Index	Placental Eccentricity
1	710	511	0.06	0.68
2	745	601	0.08	0.52
3	681	495	0.08	0.49
4	712	478	0.09	0.34
5	551	408	0.17	0.71
6	MD	390	0.33	0.81
7	707	488	0.34	0.63
8	687	496	0.34	0.43
9	666	412	0.66	0.75
10	596	372	0.77	0.70
Mean (±SD)	673 (58)	465 (65)	0.29 (0.25)	0.61 (0.15)

Table 9; Table showing the placenta weight in grams, volume measured from the micro-CT data in MATLAB, and the Cord Centrality Index (CCI) and Placenta Eccentricity (PE), using measurements or high resolution photographs in FIJI. For CCI a value close to 0 represents a central cord, a value close to 1 a marginal or velamentous cord insertion. Placentas were ordered by eccentricity of cord insertion. For placenta eccentricity, a value close to 1 represents a circle, a value close to zero an ellipse. MD; missing data.

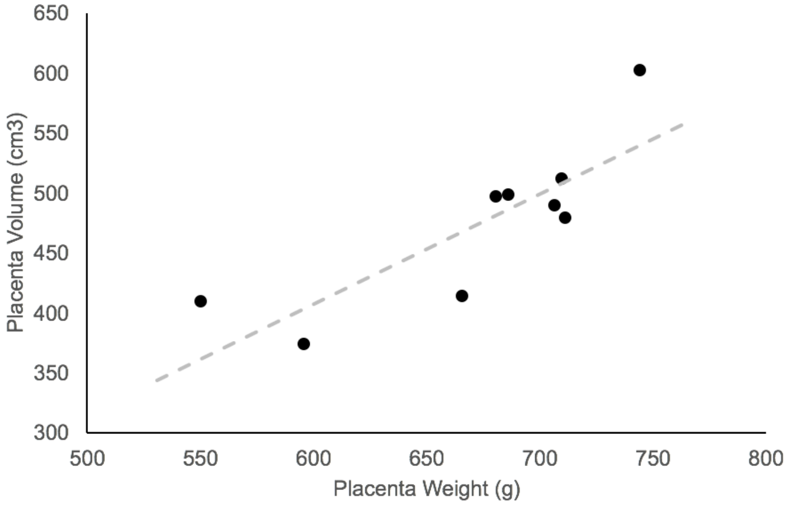

Figure 31; Correlation between weight of placenta in grams, and volume in cm^3. Volume is measured from micro-CT volume data in MATLAB. Pearson correlation coefficient r = 0.97, $p<0.01$.

4.4 Whole Placenta Vascular Fill

To investigate vascular fill for whole placenta micro-CT imaging, the proportion of vessels with an area greater than $10{,}000\mu m^2$ on histology was calculated for every block. The results are shown in Table 10.

The fill of vessels this size was generally very good, with 65 of 80 blocks having 100% fill. The lowest mean vascular fill was 77% for placenta 4. No placentas were excluded from further analysis due to poor fill.

Conclusion; Whole Placenta Vascular Fill

Vascular fill of vessels relevant to the imaging resolution was sufficient in all placentas.

Placenta	Number of blocks with total vascular fill 100%	Mean Vascular Fill over all blocks (%) (±SD)	Min Block Vascular Fill (%)
1	8	100 (0)	100
2	6	97 (8)	77
3	7	99 (3)	91
4	4	77 (40)	10
5	6 (1 block NA)	87 (31)	17
6	8	100 (0)	100
7	6	98 (5)	7
8	6	98 (3)	91
9	7	99 (2)	95
10	7	100 (1)	97
	N=65	95 (14)	17

Table 10; Table showing the vascular fill for vessels with an area greater than 10,000µm^2 for each placenta. These vessels are within the visual resolution of whole placenta micro-CT. Two sections were taken per block, and 6 micrographs per section, resulting in 96 micrographs per placenta being analysed. Number of blocks with 100% fill is shown, along with mean (±standard deviation) placental vascular fill, and vascular fill of the block with the lowest vascular fill. NA = no vessels of this size in the histological block. All placentas had vascular fill greater than 75%. Placentas 4 and 5 had the lowest fill.

4.5 Whole Placenta Micro-CT Imaging

Whole placenta micro-CT imaging allowed visualisation of vessels down to approximately 116µm diameter. This represents the chorionic vessels, and the larger villous vessels, such as the perforating stem vessels and larger intermediate vessels, making up the structural component of the placental lobules. This can be seen in Figure 32.

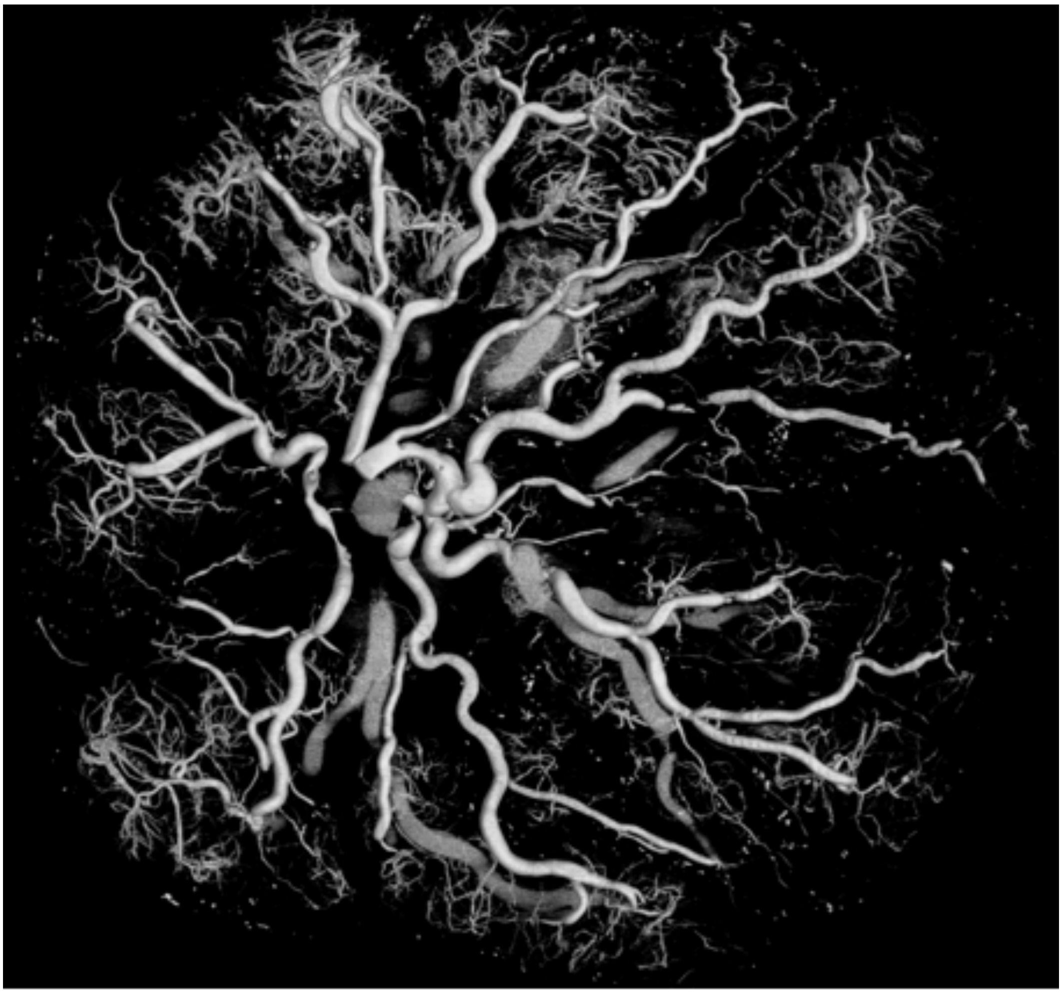

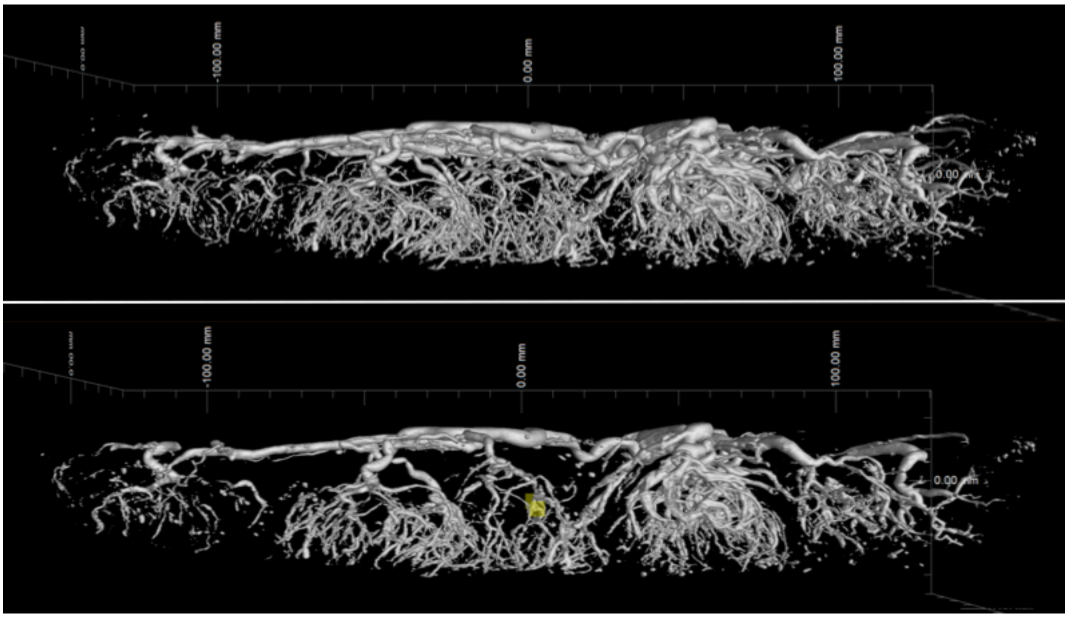

-100.00 mm
0.00 mm
100.00 mm
0.00 mm
-100.00 mm
0.00 mm
100.00 mm
0.00 mm

Figure 32; Volume rendering of whole placenta micro-CT for placenta 3, thresholded to show the Microfil filled vessels (VG StudioMAX 2.2 (Volume Graphics, Germany)). Top; view through the whole placental volume, looking down on the chorionic plate. Middel; view through the whole placental volume from the side. Bottom; a 10mm slice through the middle volume. The chorionic plate arteries are seen running horizontally across the superior placental surface to distribute the blood throughout the placental tissue. Some veins are also visible, as Microfil returned to the venous circulation in some areas before the whole placental villous system was perfused. The villous stem vessels are seen, forming separate lobules within the placenta. At the resolution of whole placental imaging, the stem and some intermediate vessels are visible, but the smaller vessels are not seen, so the more complex vascular structure of the villous vascular tree is not apparent.

4.6 **Whole Placenta Vascular Density**

Whole placenta vascular density was calculated by dividing the total volume of voxels thresholded as vessel, by the total volume of voxels thresholded as placenta, multiplied by 100, for every case. Results are shown in Table 11.

The placenta was then subdivided, using the umbilical territory placental masks described in chapter 2, to show the vascular density of the two umbilical artery territories. The vascular density for each umbilical artery territory for every placenta is shown in Figure 33, as well as the volume of tissue perfused by each umbilical artery. The smaller umbilical artery territory had a lower vascular density in every case except case 5, where the larger territory had a lower vascular density. The mean vascular density for the small umbilical territory was significantly lower than the mean vascular density for the larger umbilical territory (1.3 (±0.5)% small territory vs 1.7 (±0.7)% large territory, $p=0.02$, $n=20$).

Finally, the vascular density was calculated for the masked lobules. These were clearly visible lobules seen on volume data, suggesting high fill and vascularisation, shown in Figure 34. There was no difference in vascular density between lobules in the large and small umbilical artery territories (mean lobule vascular density 1.5 (±1.2) % large territory vs 1.6(±2.1)% small territory, p=0.86 (n=49)).

Conclusion; Whole Placenta Vascular Density

There was conflicting evidence on whether vascular density varies between the large and small umbilical artery territories

Placenta	Total Placenta Vascular Density (%)	Smaller Umbilical Artery Territory Tissue Volume (cm^3)	Smaller Umbilical Artery Territory Vascular Density (%)	Larger Umbilical Artery Territory Tissue Volume (cm^3)	Larger Umbilical Artery Territory Vascular Density (%)	Large to small umbilical artery territory volume ratio
1	1.86	214	1.76	296	1.94	1.4
2	1.04	226	0.75	375	1.21	3.2
3	1.40	116	1.14	379	1.49	3.3
4	1.23	149	0.85	330	1.40	2.2
5	2.76	103	3.68	306	2.46	3.0
6	1.48	167	1.25	223	1.65	1.3
7	1.17	202	0.99	285	1.13	1.4
8	1.15	85	0.48	412	1.29	4.9
9	1.90	83	1.29	329	2.05	4.0
10	3.11	78	2.34	294	3.31	3.8
Mean (±SD)	1.55 (0.63)	142 (57)	1.25 (0.54)	323 (55)	1.66 (0.67)	

Table 11; Table showing vascular density for the whole placenta micro-CT imaging, calculated in MATLAB. Vessel were defined as voxels thresholded as vessel within the masked area of interest (placenta or umbilical artery territory). Tissue was defined as voxels thresholded as tissue and within the relevant mask. Data is shown for the whole placental volume, and for the larger and smaller umbilical artery territories.

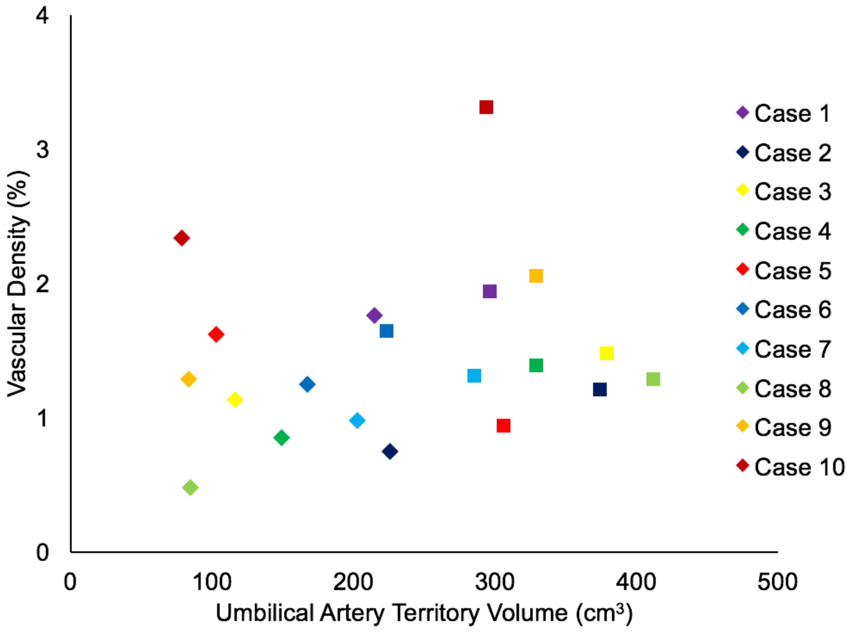

Figure 33; Graph showing umbilical artery territory volume plotted against vascular density for each placenta. Each placenta is marked with a different colour, with a diamond marker depicting the smaller umbilical artery territory, and a square marker representing the larger territory. The vascular density was greater in the larger territory in all cases except placenta 5 (red), where the smaller territory had a higher vascular density.

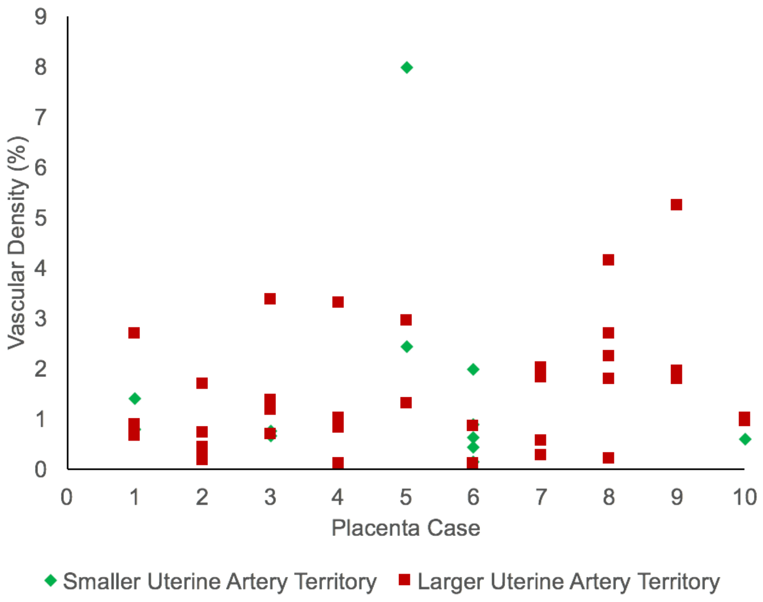

Figure 34; Scatter plot showing vascular density for each lobule segmented in each of the placenta cases. Markers of lobules located in the smaller umbilical artery territory are green diamonds, markers of lobules located in the larger umbilical artery territory are red squares. The vascular density of lobules from the smaller umbilical artery territories are not consistently lower than the vascular density of lobules taken from larger umbilical artery territories.

4.7 Chorionic vascular tree

It is important to separate the chorionic and villous vascular trees, as they provide a different function within the placenta. The chorionic vessels deliver blood throughout the tissue volume whilst the villous vessels form independent functional lobules for exchange. As such, vessels in these trees have different roles and regulation, and different changes may be seen in association with pathology.

The whole placenta vascular tree was separated by size thresholding, into vessels with a radius greater 6 voxels (699µm), representing the chorionic tree, and vessels with a radius less than or equal to 6 voxels, representing the villous tree. This arbitrary threshold was chosen as it appeared to separate the superficial traversing chorionic vessels and deeper, vertical vessels well in every case, although it is not a perfect definition (Figure 35).

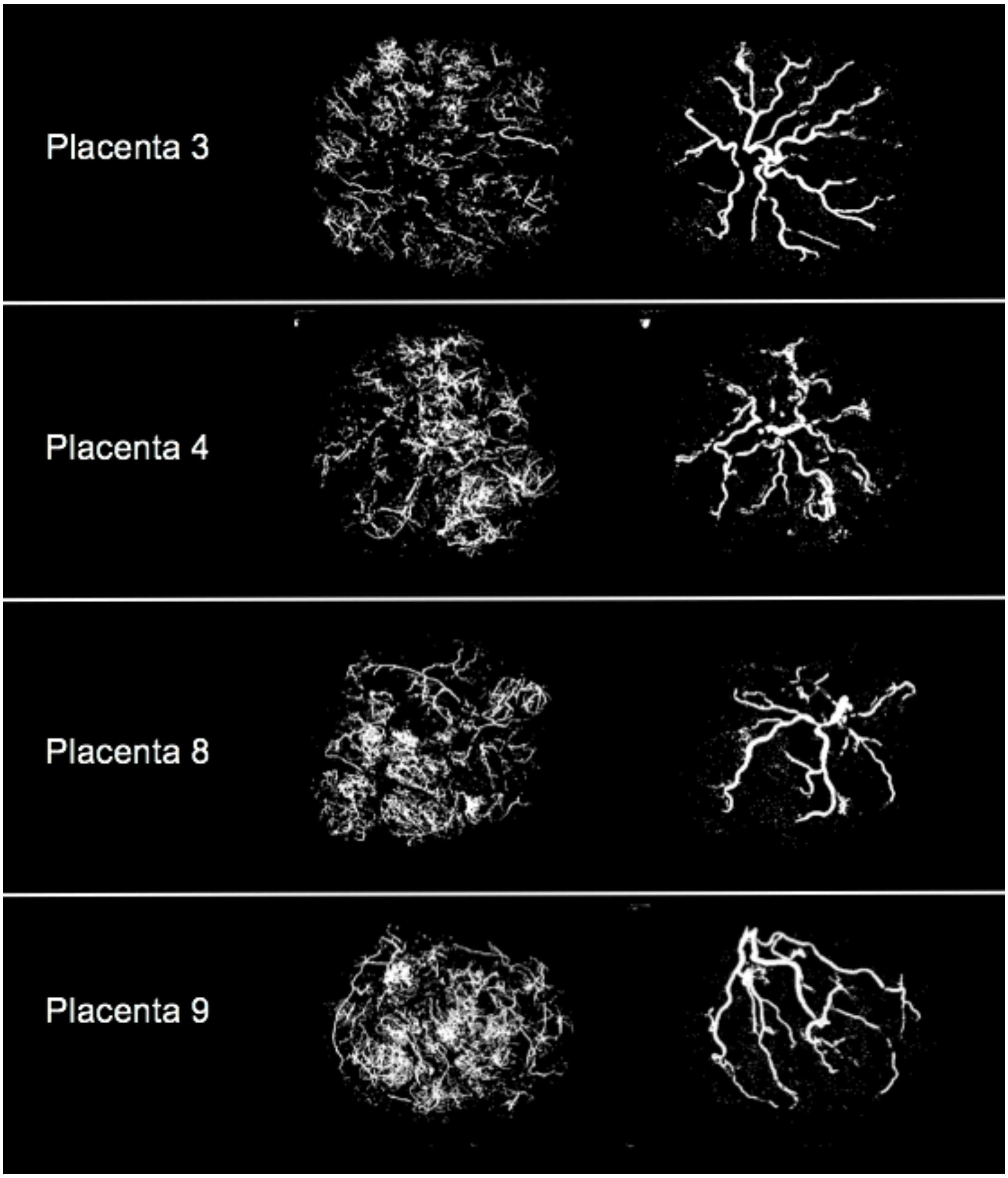

Figure 35; Maximum intensity projection (MIP) of the villous vessels (left) and chorionic vessels (right) using a size threshold of a vessel radius of 6 voxels, for placentas 3, 4, 8 and 9. The majority of chorionic vessels have been removed from the villous MIP, although some chorionic vessels can still be seen as they traverse the placental surface, particularly for case 9. Likewise, the majority of chorionic vessels are seen in the chorionic MIP, although some have been removed.

Chorionic vessel radius distribution

Figure 36 shows vessel radius distribution maps for the whole vascular tree, and vessel radius histograms for the chorionic plate, including only vessels with a radius greater than 6-voxels.

All placentas showed similar radius distributions of small to large vessels at this scale. There was no difference in radius distribution as the cord insertion became more eccentric. The number of vessels decreased as the vessel radius became larger, as is expected within any vascular tree, where vessels rapidly divide into two smaller daughter vessels.

Conclusion; Chorionic Vascular Tree

There was no difference in vessel radius distribution in the chorionic vascular tree as site of cord insertion became more eccentric in this work.

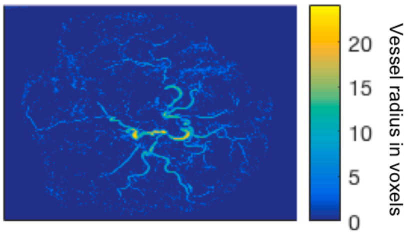
20
15
10
5
0
Vessel radius in voxels

1

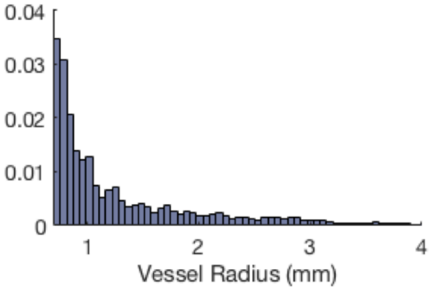
0.04
0.03
0.02
0.01
0
1
2
3
4
Vessel Radius (mm)

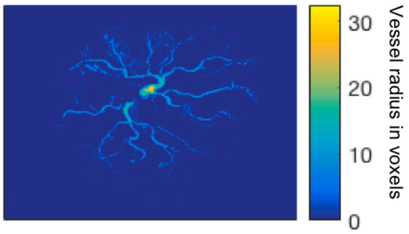
30
20
10
0
Vessel radius in voxels

2

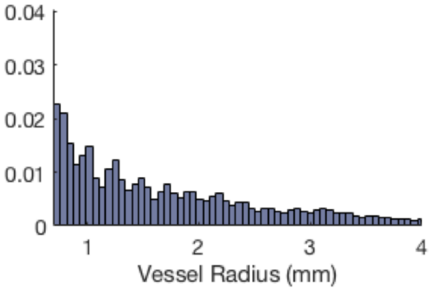
0.04
0.03
0.02
0.01
0
1
2
3
4
Vessel Radius (mm)

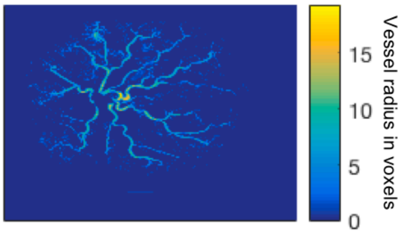
15
10
5
0
Vessel radius in voxels

3

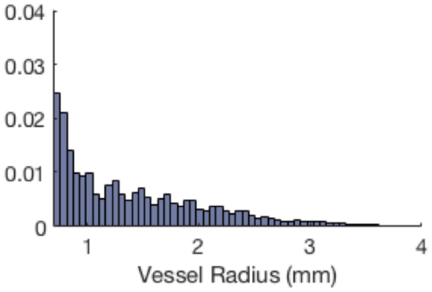
0.04
0.03
0.02
0.01
0
1
2
3
4
Vessel Radius (mm)

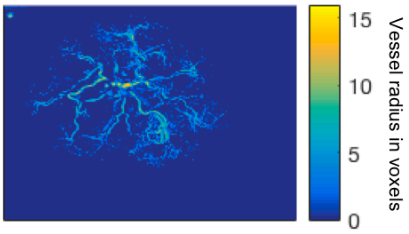
15
10
5
0
Vessel radius in voxels

4

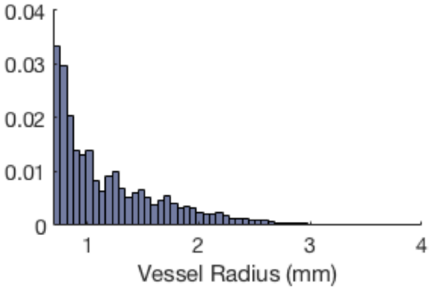
0.04
0.03
0.02
0.01
0
1
2
3
4
Vessel Radius (mm)

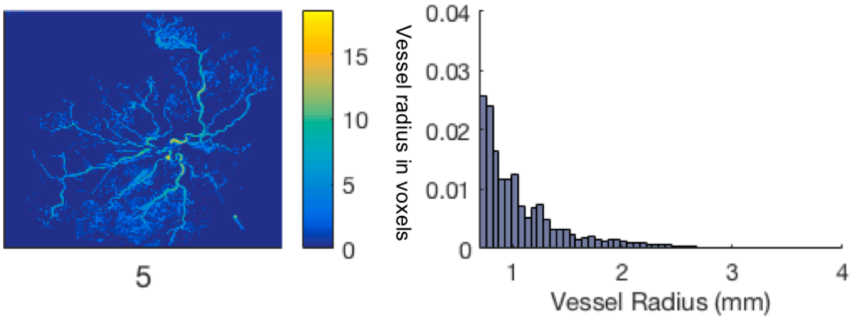
5
0
5
10
15
Vessel radius in voxels
0
0.01
0.02
0.03
0.04
1
2
3
4
Vessel Radius (mm)

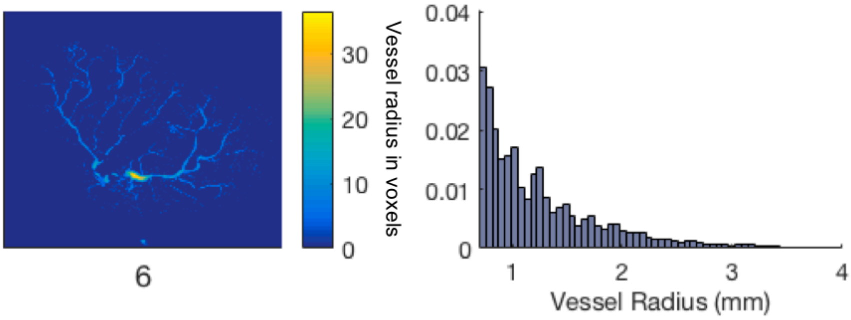
6
0
10
20
30
Vessel radius in voxels
0
0.01
0.02
0.03
0.04
1
2
3
4
Vessel Radius (mm)

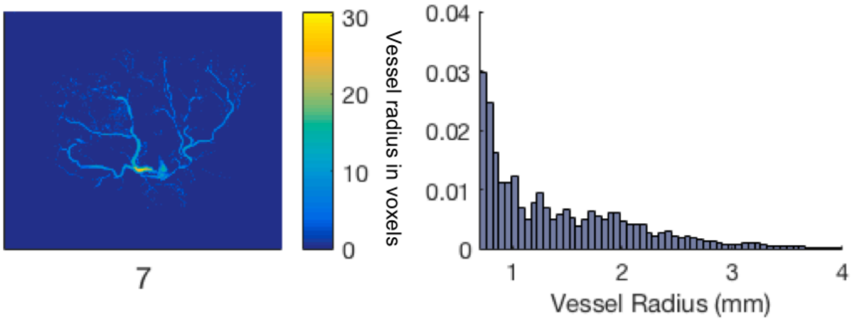
7
0
10
20
30
Vessel radius in voxels
0
0.01
0.02
0.03
0.04
1
2
3
4
Vessel Radius (mm)

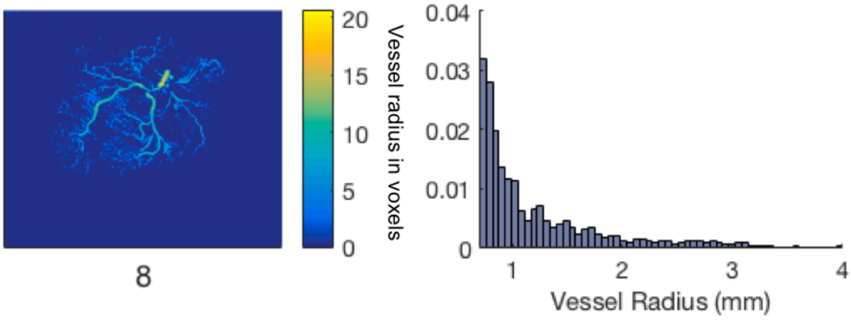
8
0
5
10
15
20
Vessel radius in voxels
0
0.01
0.02
0.03
0.04
1
2
3
4
Vessel Radius (mm)

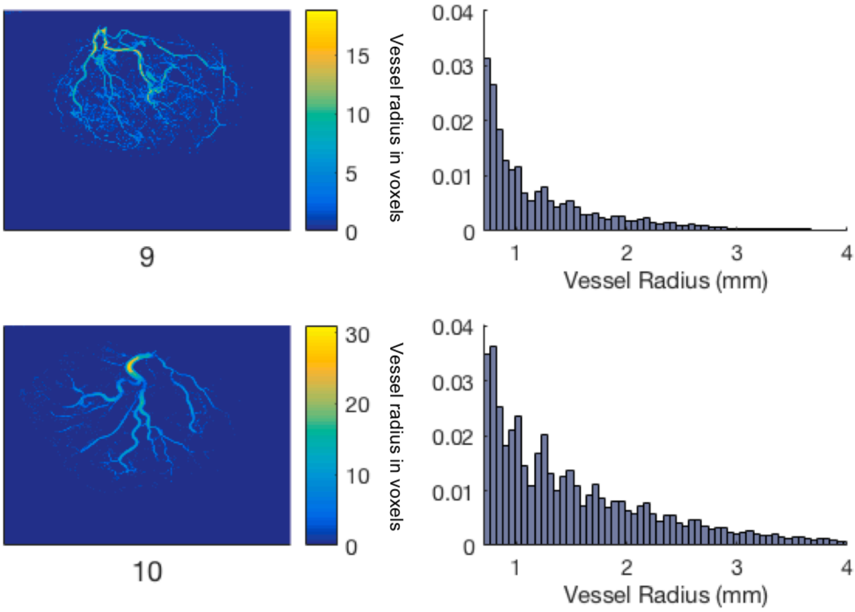

Figure 36; Figure showing vessel radius distribution maps and histograms for vessels with a radius greater than 6 voxels. Left; radius distribution maps for the whole skeletonised vascular tree of each placenta, with vessel radius in voxels. Right; corresponding histogram of vessel radius distribution, with vessel radius in mm, showing vessels with a radius greater than 0.7mm (corresponding to 6 voxels), to exclude the smaller villous vessels within the placenta.

4.8 Villous vessels

Villous Vessel Radius Distribution

The vessel radius distribution for villous vessels is shown in Figure 37. There were similar distributions of vessels for all placentas, suggesting there was no difference with centrality of cord insertion site. There were more vessels with smaller radius, as expected given the highly branching structure of the placental villous vascular tree. There was no relationship between vessel radius and eccentricity of site of cord insertion.

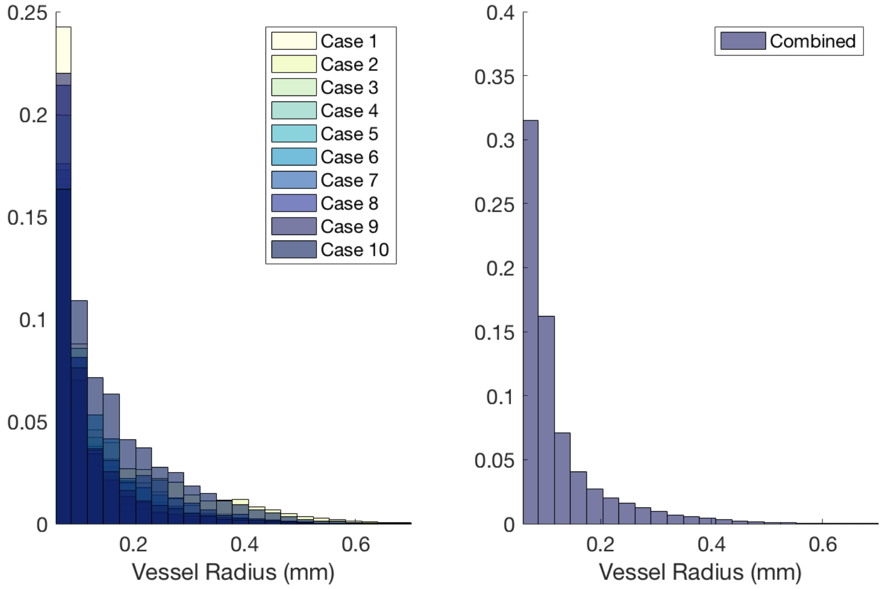

Figure 37; Histograms showing left; the vessel radius distribution for every placenta, and right; the combined vessel distribution, for vessels with a radius less than 6 voxels (0.7mm). This excluded larger chorionic vessels. As expected the number of vessels decreases as the vessel size gets larger. All placenta had similar distribution of vessels at this scale.

Villous Vessel Density

The villous vascular density was calculated for each placenta, by dividing the number of voxels thresholded as villous vessel, by the total number of voxels thresholded as tissue and vessel in each column of voxels within the placental volume (Table 12). The mean villous vascular density for all placentas was 0.5(±0.5) %.

Case	Villous vessel Density (% (±SD))
1	0.32 (0.02)
2	0.30 (0.02)
3	0.40 (0.02)
4	0.55 (0.03)
5	0.42 (0.03)
6	0.56 (0.03)
7	0.36 (0.02)
8	0.40 (0.02)
9	0.69 (0.03)
10	0.96 (0.03)
Mean	0.50 (0.05)

Table 12; Table showing the mean placental villous vascular density for each placenta.

Villous Vessel Density with Distance from Cord Insertion

To investigate villous vessel density with distance from cord insertion, vascular density maps were drawn for each placenta (Figure 38). These show how the villous vascular density varied throughout the placental volume.

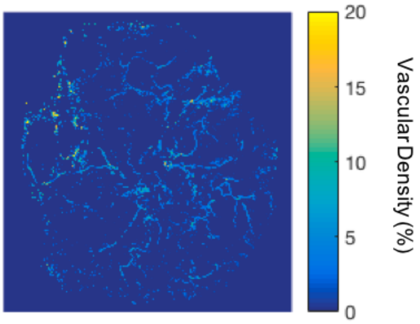
20
15
10
5
0
Vascular Density (%)

1

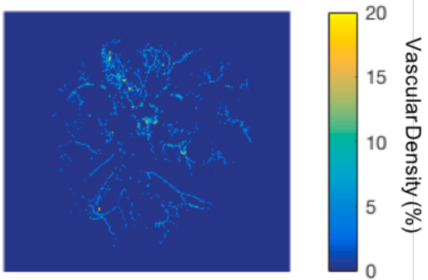
20
15
10
5
0
Vascular Density (%)

2

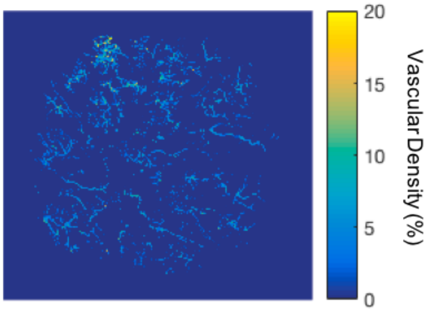
20
15
10
5
0
Vascular Density (%)

3

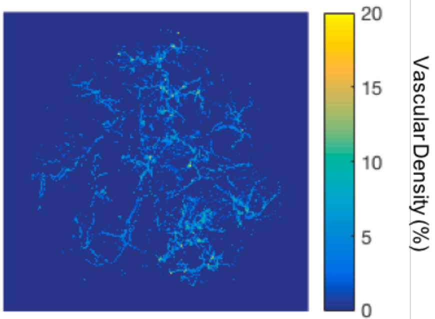
20
15
10
5
0
Vascular Density (%)

4

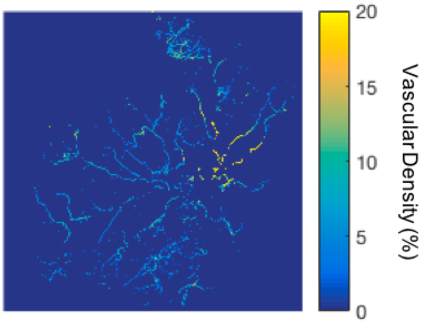
20
15
10
5
0
Vascular Density (%)

5

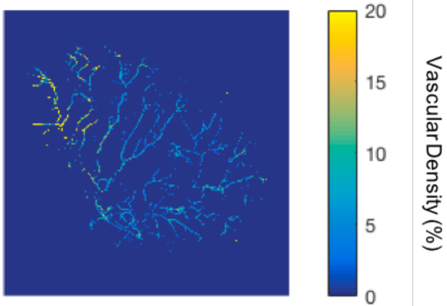
20
15
10
5
0
Vascular Density (%)

6

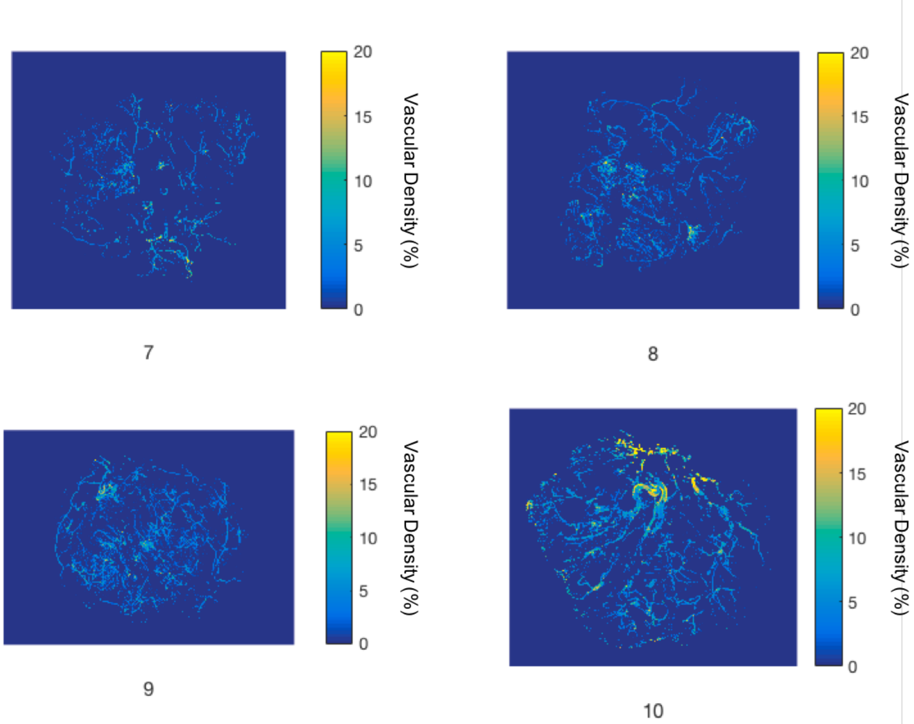

Figure 38; Vascular density maps for each placenta. These were created by dividing the number of voxels villous vessels by the total number of tissue and vessel voxels, for every column of the placental volume. The vascular density varies throughout the placenta, but there was no consistent spatial pattern between placenta, with areas of low and high vascular density being present in different locations throughout the tissue in all cases.

To investigate this further, normalised placenta distance maps were used. The normalised distance from cord insertion to placental edge was divided into 100 regions. The mean vascular density for each of these regions was calculated, and plotted against the distance from cord insertion (Figure 39).

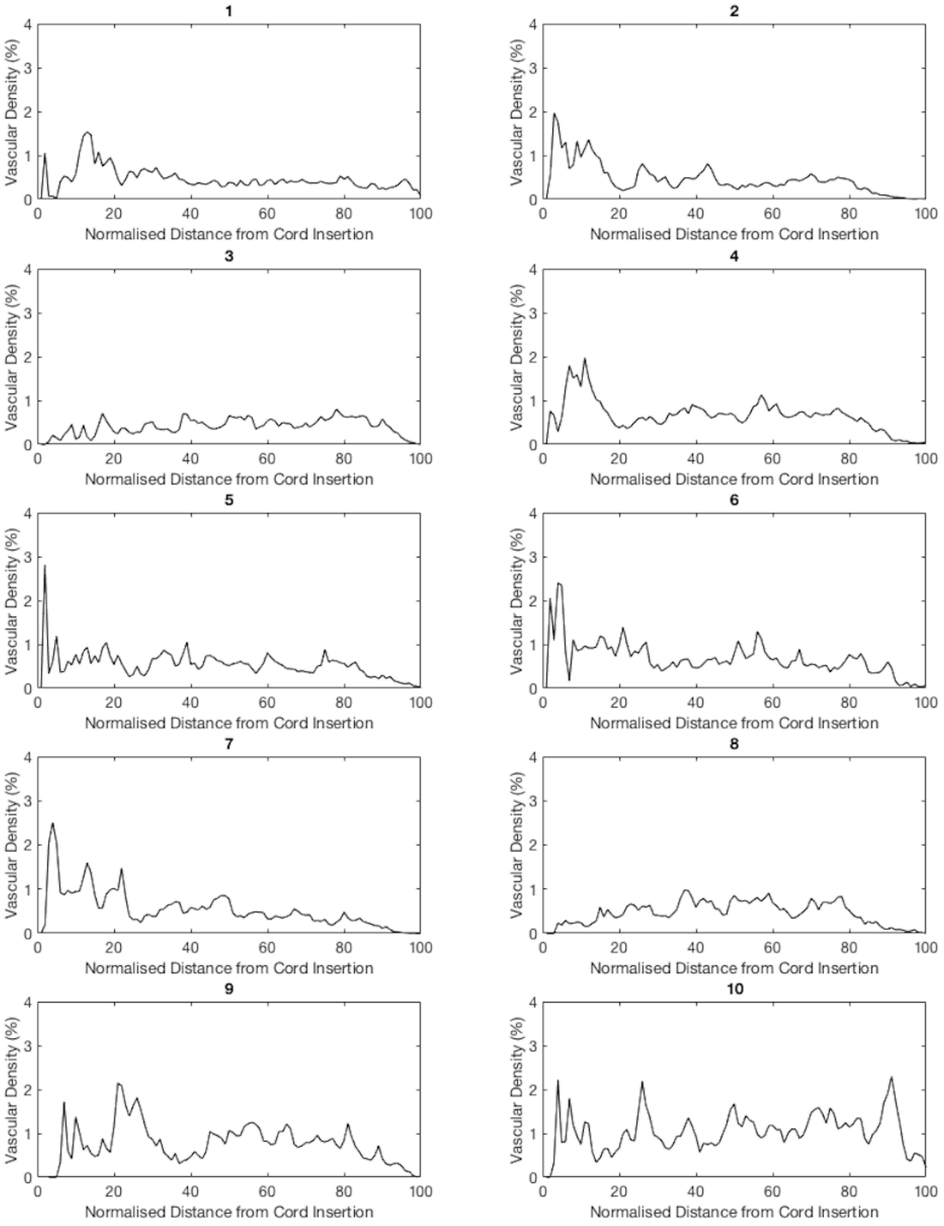
1
2
3
4
5
6
7
8
9
10
Vascular Density (%)
0
1
2
3
4
Normalised Distance from Cord Insertion
0
20
40
60
80
100

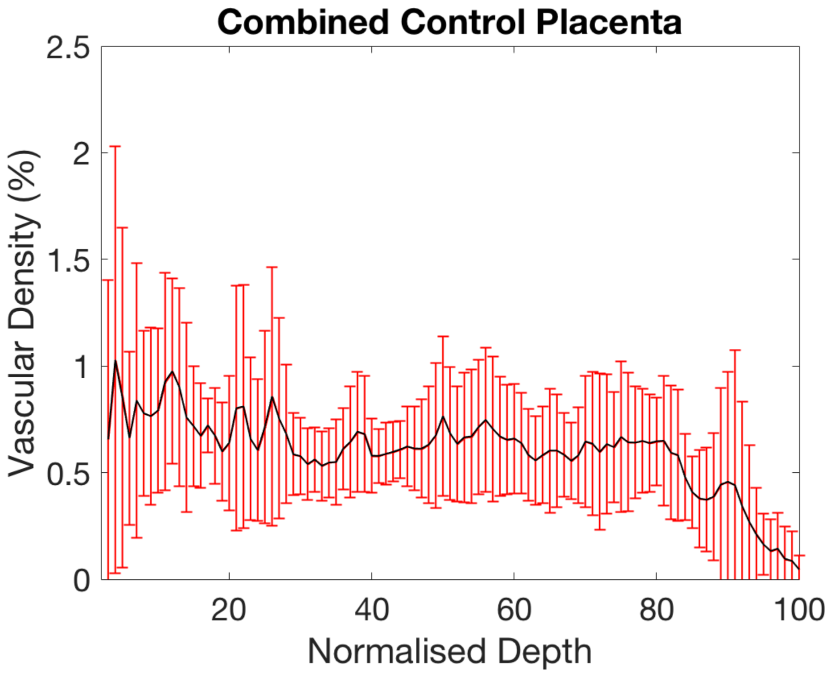

Figure 39; Upper; Vascular density plotted against normalised distance from cord insertion to placenta periphery, for every placenta, and lower; the combined mean vascular density with distance from cord insertion. There was no recurring pattern in difference in vascular density with distance from cord insertion. There appears to be a reduction in vascular density in the peripheral 20%. Combined plot error bars show standard deviation.

These plots show that there was no consistent difference in villous vessel density within the main placental tissue, however there was a trend towards reduced vascular density in the peripheral 20% of the placenta, when normalised from cord insertion to placental edge.

Vessel Density with Depth

To investigate vessel density with depth from the chorionic plate, normalised placenta depth maps were used. Each placenta was divided into 12 equal, non-overlapping strata between chorionic and basal plates. Twelve strata were chosen to allow easy division of the placenta in halves, thirds, quarters and so on. Vascular density was calculated as all vessel voxels (no size threshold) divided by all placenta or vessel voxels within each plate. Vascular density maps were drawn showing the total vascular density of the first 4 strata (the top third), the middle four strata, and the last four, deepest, strata (Figure 40). These maps show vascular density decreasing with depth from the chorionic plate. The top third of placental tissue had the highest vascular density as it included the chorionic vessels. There was a further reduction in vascular density in the lowest third of the placenta, closest to the basal plate.

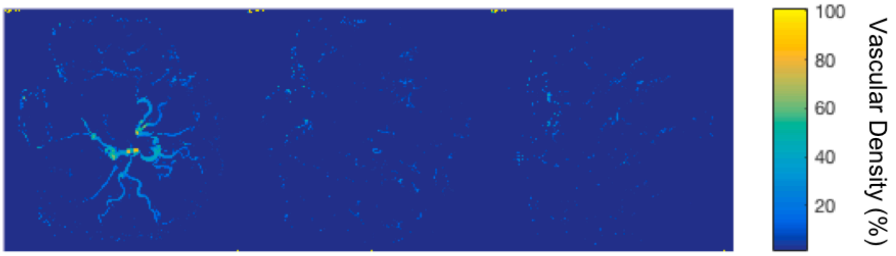
100
80
60
40
20
Vascular Density (%)

1

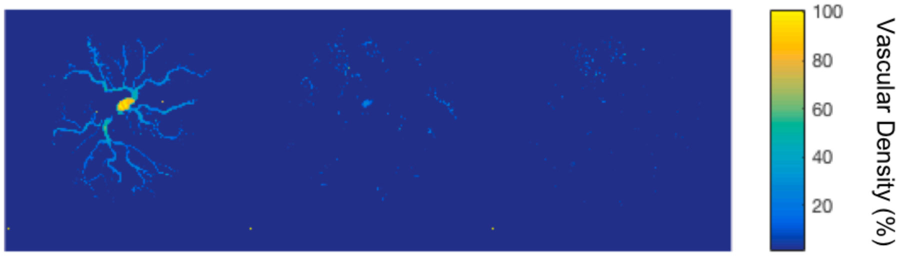
100
80
60
40
20
Vascular Density (%)

2


100
80
60
40
20
Vascular Density (%)

3

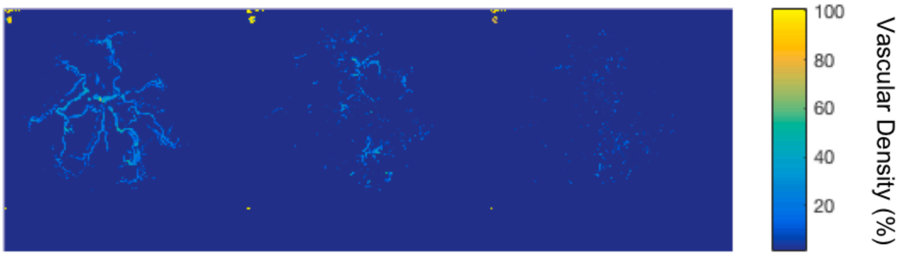
100
80
60
40
20
Vascular Density (%)

4

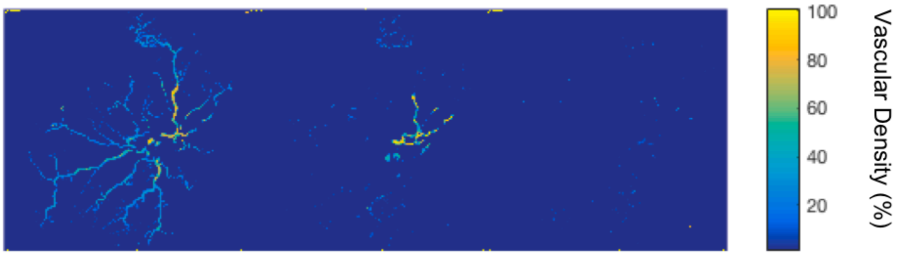
100
80
60
40
20
Vascular Density (%)

5

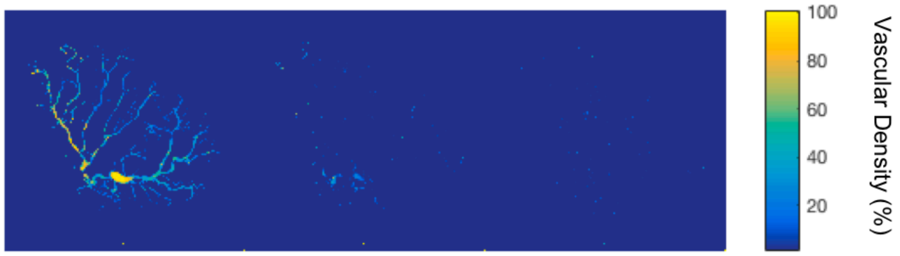
100
80
60
40
20
Vascular Density (%)

6

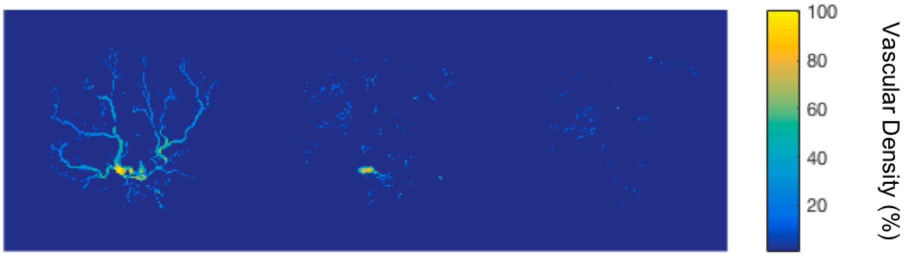
100
80
60
40
20
Vascular Density (%)

7

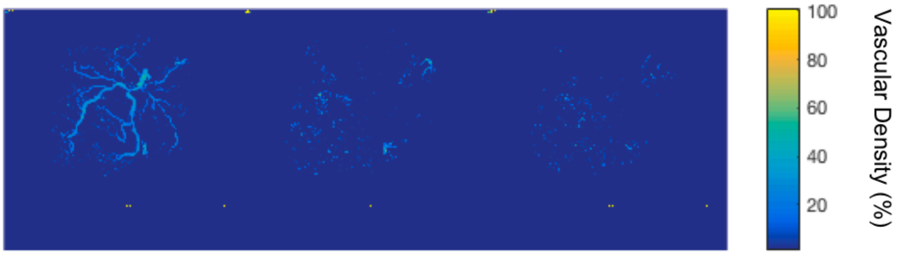
100
80
60
40
20
Vascular Density (%)

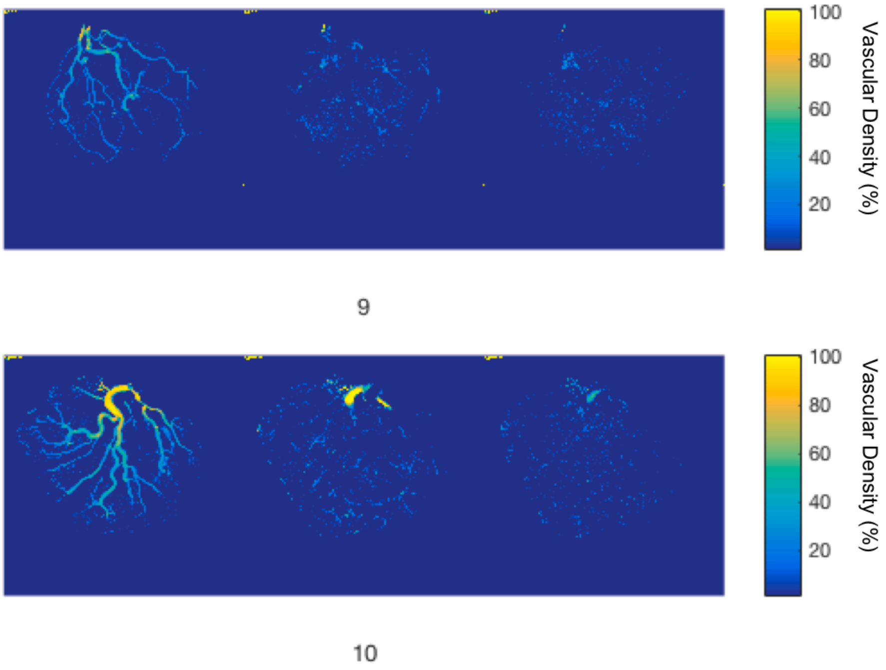

Figure 40; Vascular density (%) with depth from chorionic plate for the 10 placentas. Left; the top third of the normalised placental volume, middle; the middle third of the normalised placental volume, right; the bottom third of the normalised placental volume.

To investigate this further, mean vascular density was plotted against depth for each of the 12 strata, for every placenta (Figure 41). This showed that the greatest reduction in vascular density occurred within the top quarter of the chorionic plate, encompassing the large chorionic vessels. However, most placentas continued to show a reduction in vascular density at this resolution through the rest of the placenta, which is demonstrated clearly in the combined data.

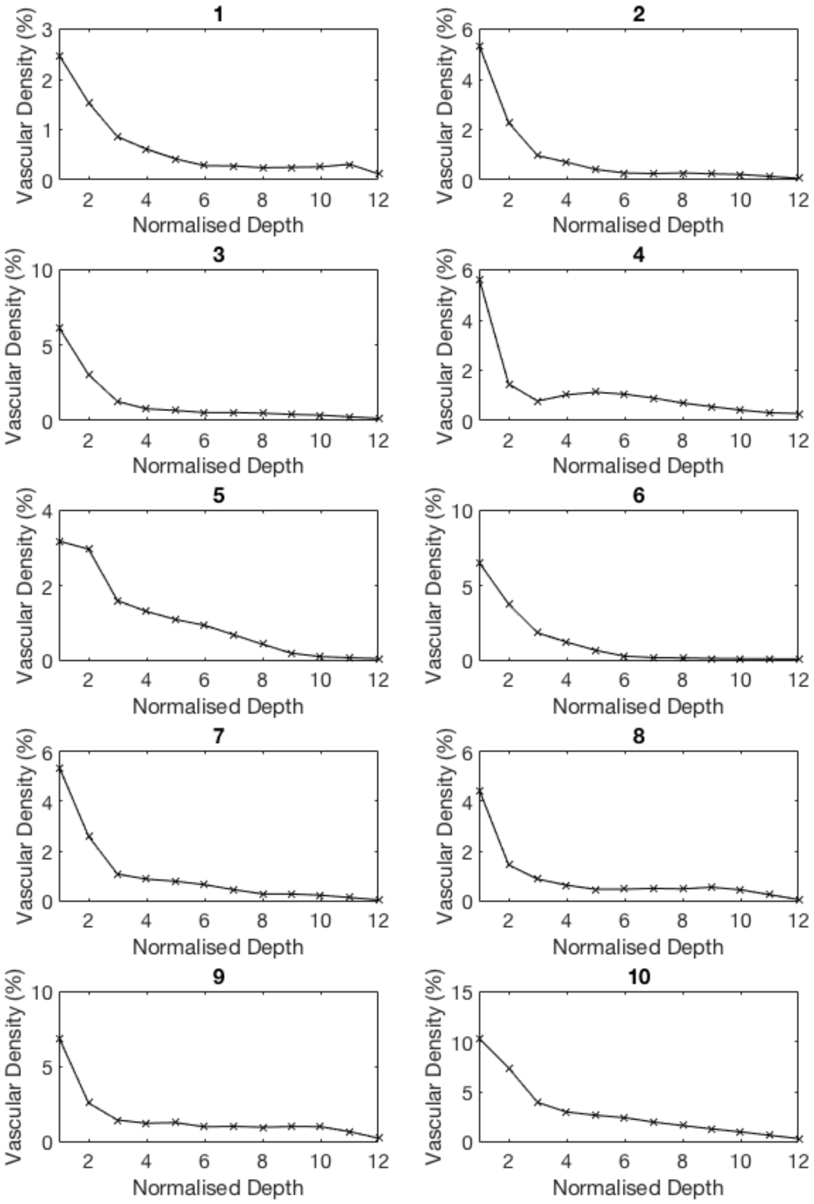
1
2
3
4
5
6
7
8
9
10
Vascular Density (%)
Normalised Depth
0
2
4
6
8
10
12
15

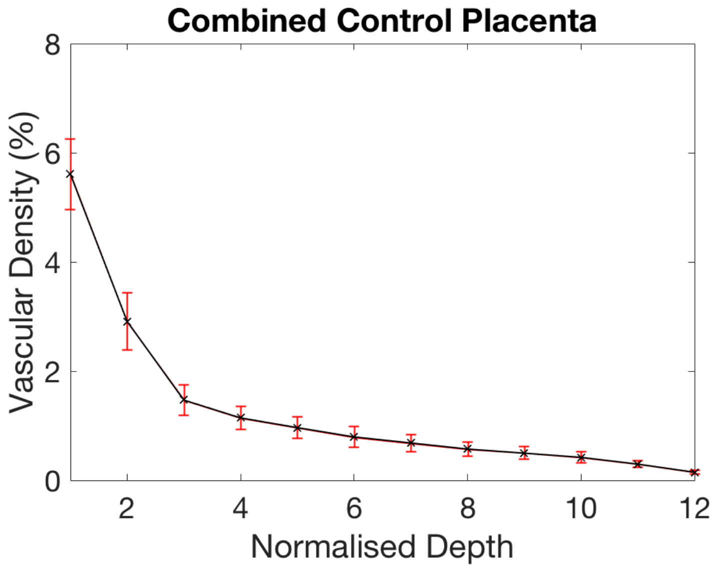
Combined Control Placenta
Vascular Density (%)
Normalised Depth
0
2
4
6
8
10
12

Figure 41; Upper; Mean vascular density with normalised depth, divided into 12 regions, for all 10 placentas, and lower; the combined mean vascular density with normalised depth (bottom). The vascular density decreases with distance from chorionic plate. Combined plot error bars show standard deviation.

Tissue Distance from Villous Vessel

To investigate the distribution of vessels in the placental parenchyma, the distance of tissue to the closest villous vessel was investigated. This was done using the 5th plate from the 12 placental depth strata. This depth was chosen because it excluded chorionic and large traversing vessels in all datasets (Figure 42).

The vascular density of each column within the 5th stratum was calculated. The Euclidean distance of each voxel to the nearest non-zero pixel was calculated in MATLAB. Tissue distance maps are shown in Figure 43. These show that at this depth villous vessels were seen throughout the placental volume. There was variation in tissue distance to the closest vessel, with some having much higher density of villous vessels, this is particularly clear in placenta 6. In other areas, the villous vessels were less densely spaced. There did not appear to be a recurring spatial pattern in the distance to closest vessel.

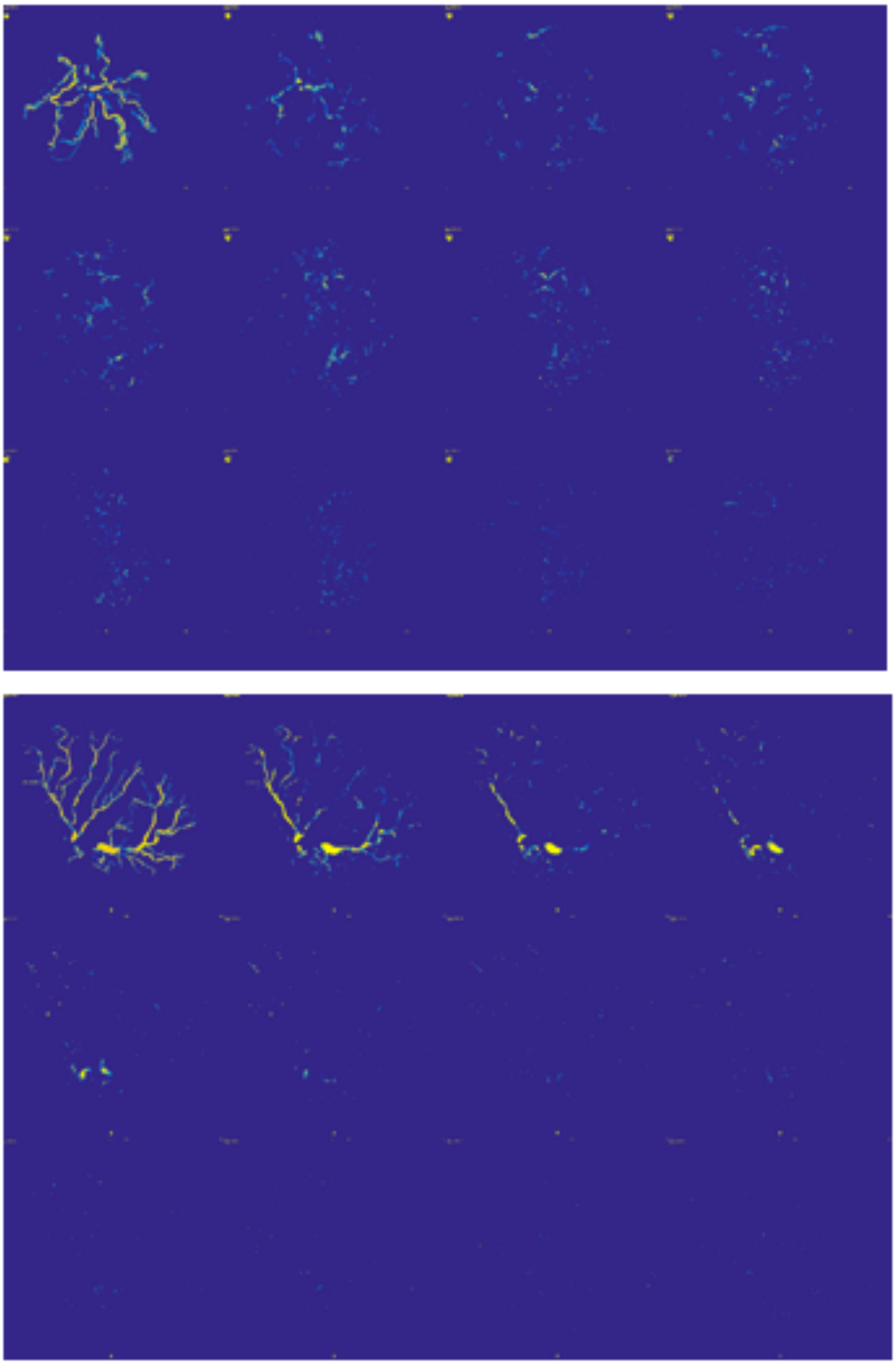

Figure 42; Example vascular density maps for the 12 strata for two placentas. Top is Case 7, bottom is Case 9. Row 1; strata 1 to 4, row 2; strata 5 to 8, row 3; strata 9 to 12. For placenta 7 the chorionic vessels were no longer apparent from the third strata, however in case 9 chorionic vessels were clearly seen until the 5th strata.

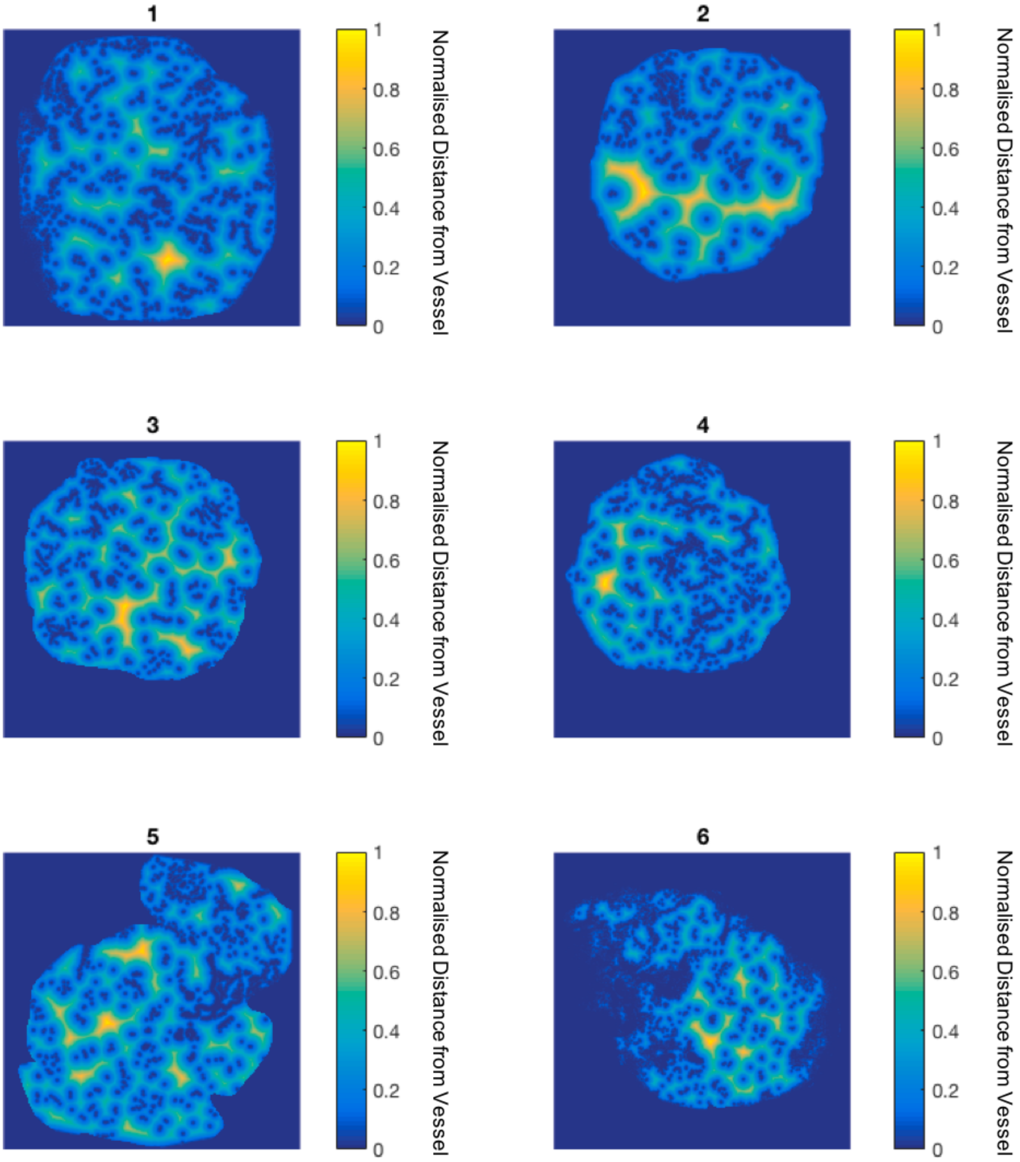
1
2
3
4
5
6
0
0.2
0.4
0.6
0.8
1
Normalised Distance from Vessel

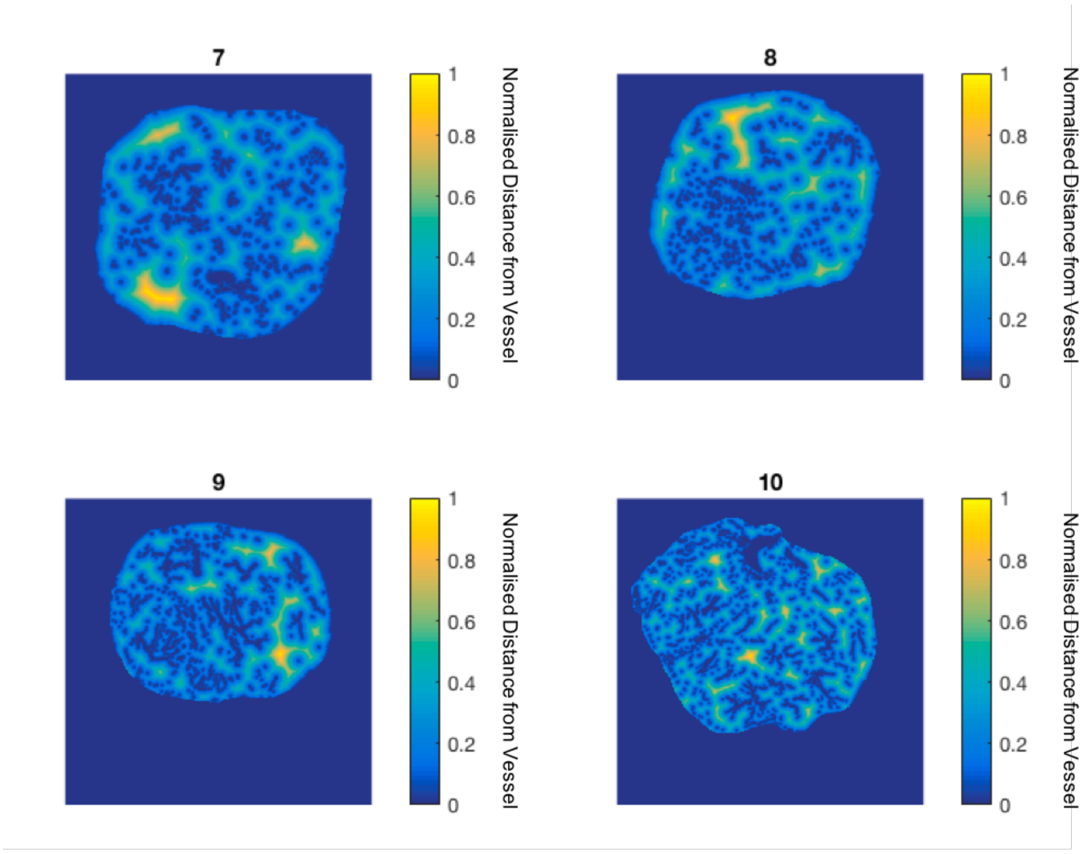

Figure 43; Normalised placenta maps showing distance from a vessel for whole placenta imaging in the 5th depth region of each placenta. There were similar patterns throughout, except in placenta 6 where there was a very densely vascularised area on the left. Distances normalised from 0 to 1, arbitrary units.

To further investigate this, histograms were drawn showing the distribution of tissue distance from closest villous vessel (Figure 44). This shows that throughout the placentas, at this depth, the majority of tissue is within 5mm of a large villous vessel. The mean distance to closest vessel for all the placental cases was 4.0 (±1) mm (Table 13).

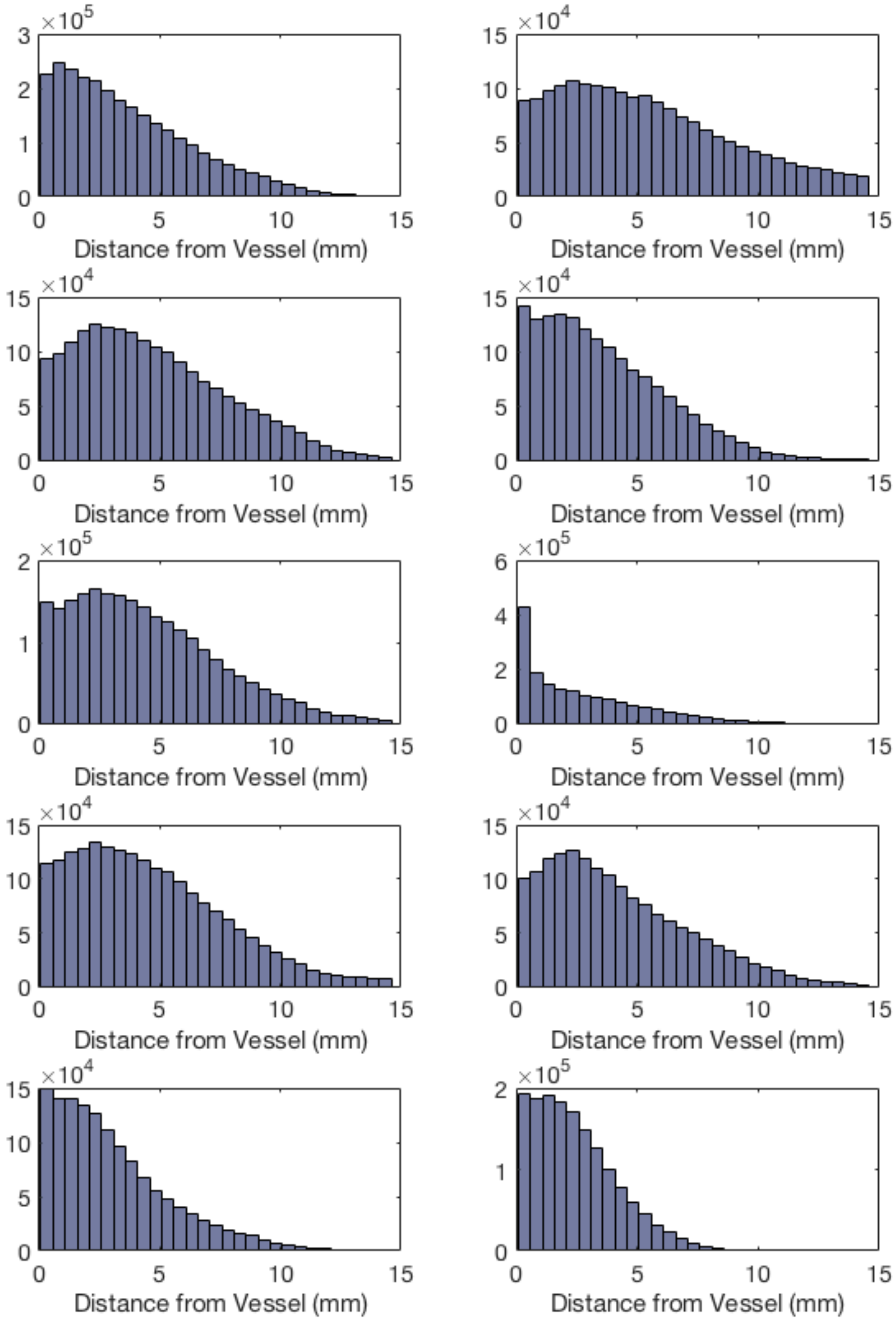

Figure 44; Histograms showing tissue distance from vessel distributions for each placenta, for the 5th normalised depth section.

Case	Mean distance from vessel (mm) (±SD)
1	3.8 (3.1)
2	6.1 (4.8)
3	4.8 (3.5)
4	3.7 (2.9)
5	4.5 (3.4)
6	2.7 (2.8)
7	4.9 (3.8)
8	4.3 (3.3)
9	3.1 (2.5)
10	2.5 (1.9)
Mean	4.0 (1.1)

Table 13; Table showing mean tissue distance (±standard deviation) from vessel in the 5th depth segment for each placental case, and the mean for all 10 cases. The means and standard deviations were calculated assuming a gamma distribution to the data.

Conclusion; Villous Vessels

This work found no difference in villous vessel radius distribution as site of cord insertion became more eccentric. There was a large degree of heterogeneity in vascular density between and within normal, term placentas. However, there was no spatial relationship between villous vascular density, or the distance of the tissue from umbilical cord insertion and placental edge. Villous vascular density decreased with depth at this imaging resolution. The mean distance of tissue from a villous vessel in the 5th strata of the placental tissue over the ten, normal placenta was 4.0mm.

4.9 Discussion

This work systematically investigated the three-dimensional vascular density of the whole normal human placenta, and whether there is a consistent spatial pattern in vascular density between placentas.

This work analysed micro-CT imaging with an isotropic voxel size of 116.5µm. The advantage of whole placental imaging is that it captures data throughout the placental volume, so that spatial analysis is possible. The disadvantage is that the large field of view is at the cost of magnification, so only the vessels of the chorionic plate and the larger villous vessels are visible.

Analysis of vascular density within the larger and smaller umbilical artery territories found the larger area to have a higher vascular density.

It is possible that the larger umbilical artery territory may have a lower resistance, due to a greater capillary network, and therefore blood may preferentially perfuse this area, via Hyrtl's anastomosis. This may cause a difference in vascular density between territories. However, when the vascular densities of lobules within each territory were compared, there was no difference in mean vascular density. It may therefore be that the observed difference in vascular density related to vascular fill. Unfortunately, not enough blocks were taken from the smaller territories to compare the vascular fill with histology, as this was not taken into consideration during tissue sampling. This therefore requires further investigation.

Radius distributions of both the chorionic and villous vascular trees showed no relationship to eccentricity of cord insertion site. This is expected in the villous vascular tree, however previous work in the chorionic tree has reported different branching patterns in central and eccentric cord insertion, with the trees of more eccentric insertions being dominated by monopodial divisions, with one small daughter vessel and one daughter vessel similar in size to the parent, whilst the trees of more central insertions are dominated by dichotomous divisions, with two similarly sized daughter vessels[5]. It might therefore be expected that there would be a difference in vessel radius distribution. It is possible that the analysis did not have the sensitivity to detect this, or that the cord insertions were not eccentric enough, and it is another area for further work.

Whole placental imaging allowed investigation of villous vessels down to approximately 117μm diameter. The mean vascular density of these vessels was 0.5(±0.51)%. This shows a large degree of heterogeneity between normal placenta. There was no consistent spatial pattern in vascular density through the placental tissue, however there was a trend towards reduced vascular density in the peripheral 20% of the tissue. It is possible that the reduction seen is due to reduced fill at the extremities, however the findings are consistent with the work of Fox et al, who found an increase in hypovascular and avascular villi near the placental edge[20]. This therefore suggests that the placental edge is less well vascularised than the more medial placental tissue, and sampling here may not be representative of the whole placental vascularisation.

There was a reduction in vascular density from chorionic to basal plate, which is expected as the vessels continue to branch into smaller vessels, beyond the resolution of this imaging. In addition, only a few villi traverse the whole placental depth (anchoring villi), with most floating freely within the parenchyma, so the density is likely to reduce towards the basal plate. The mean distance from a villous vessel to placental tissue in the 5th (out of 12) placental depth strata was 4.04 (±1.01) mm over the whole placental dataset, and again there were different spatial patterns in every normal placenta, with some areas having more closely packed vessels, and other areas more sparsely spaced. This again shows that there is no consistent spatial pattern of vascularisation at this scale.

Limitations of this work include that all imaging relies on good vascular perfusion, so changes may be secondary to biological differences, or poor vascular fill. This is a limitation of all perfusion work[161].

Attempts were made to limit the effect of poor perfusion by first optimising the perfusion technique, and secondly examining all tissue histologically after imaging and excluding data from tissue that was poorly perfused. However, there were areas of better and poorer fill, and no whole placental imaging was excluded. In future work it may be advisable to sample more areas of the placenta to check the fill.

Microfil filled vessels were separated from placental tissue using simple grey-scale thresholding. The thresholds used are shown in the method section (Table 1). The majority of cases have similar thresholds, which is unsurprising given that the range is normalised between the highest and lowest greyscale value in the volume, and the range should be similar between cases. However cases 6 and 9 have quite different threshold values for both placenta and Microfil. This is because a pin was included in the imaging field, and so the normalised scale is different. This may have affected the ability to separate placental tissue and vessels, and the range of greyscale values for each will have been reduced. Given that the results for these two placentas fall within the range seen with the other placentas the data was not excluded.

More advanced algorithms exist that may improve the segmentation, combining grey-scale thresholding and algorithms that grow the vascular tree based on proximity and similarity of grey-scale values and local vesselness properties[171,172,173,174]. This approach would optimise the number of voxels correctly identified as vessel and minimise the noise. This requires further technical work to optimise the vascular tree segmentation.

The study used a size threshold of a vessel radius of 6 voxels to separate chorionic and villous vessels. This was an arbitrary choice, chosen because visually it appeared to separate the majority of chorionic and villous vessels in most of the placenta. This has limitations, as chorionic vessels have a variety of sizes. Using the vessel location within the placenta as a threshold would have advantages in separating the trees, but it is difficult, as placentas are not completely flat during imaging. In addition, chorionic vessels can dive below the surface at times before reappearing, so location along the surface will not be entirely successful in separating the trees. Determining the best way to separate these trees is another area requiring further technical optimisation.

Improved segmentation of vessels would improve derived analysis such as skeletonisation, and with this more advanced analysis it would be possible to examine in detail the branching structure and tortuosity as has been done by Rennie et al in mice[85]. This has been attempted in corrosion cast imaging with micro-CT by Junaid et al[88]. The software they used however was limited as it was not optimised for placental data, and was not capable of locating the vascular tree spatially within the placenta. This makes the branching pattern difficult to understand or analyse in a meaningful way. Development of algorithms capable of analyzing the vascular tree in relation to placental geometry is the next important step in understanding the human placental tree.

In conclusion, this work describes the pattern of whole placental vascularisation, imaged with a voxel size of 116.5µm. We show there is a great degree of heterogeneity within and between normal placentas. No repeating pattern in vascular density with proximity to cord insertion site or placental edge was found, suggesting there is no reproducible relationship between density of the larger vessels of the vascular tree (chorionic and stem vessels) and placental geometry.

In the next chapter I examine the villous vascular density in more depth, using placental blocks imaged at a higher degree of magnification, and an isotropic voxel size of 13.5µm.

5 Investigating the Spatial pattern of Villous vessel within normal, term placenta

5.1 Summary

In this chapter I present data from block placenta micro-CT and histological imaging of the villous vascular tree in normal, term placenta. The aim of this work is to investigate if there is a consistent spatial pattern in villous vascular density between placentas.

I show that there is a large degree of variation in villous vessel and terminal capillary density within and between normal term placentas, and that there is no consistent spatial pattern with regard to placental structure. This is important because it mean there is no area of the tissue that can be routinely sampled to ensure a good estimate of the whole placental vascularisation. Placental vascularisation can only be accurately assessed by imaging the large amounts of tissue.

5.2 Placental Block Vascular Fill

The same placentas were used in this work as in the previous chapter (Chapter 4). The voxel size of imaging was 13.5μm, which relates to a vessel area of 143μm^2, assuming vessels are transected perpendicularly. Therefore, to investigate vascular fill relevant to this imaging, vascular fill of vessels with an area greater than 200μm^2 was calculated for the villous area of every placenta block imaged (n = 8 blocks per placenta). As only the lower villous area of the blocks was being analysed (as discussed in the methods, Chapter 2), the vascular fill was calculated based on the 6 micrographs taken from the lower portion of the full thickness section.

Vascular fill is shown in Table 14. Block location, with regard to umbilical cord insertion and placental edge, was plotted against vascular fill to check for any relationship between distance down the vascular tree and how completely the tissue was perfused (Figure 45). There was no correlation between block location and vascular fill (r=-0.009, p=0.9).

To ensure that vascular density calculations reflected true vascular density, and not vascular fill, all blocks with vascular fill less than 75% were excluded from further analysis. This left 38 blocks, spread between the ten placentas.

Placenta	Mean Villous Vascular Fill for 8 blocks (% (±SD))	Min Villous VF (%)	Max Villous VF (%)	Number of blocks with villous VF greater than 75%
1	85 (21)	34	99	6
2	59 (30)	18	89	3
3	68 (26)	23	95	3
4	58 (34)	8	91	3
5	55 (20)	18	75	2
6	85 (18)	43	94	6
7	62 (23)	47	93	3
8	70 (25)	16	93	4
9	72 (19)	46	97	4
10	74 (21)	37	99	4
	69 (11)	8	99	N=38

Table 14; Table showing the vascular fill for vessels with an area greater than 200µm^2 for each placenta. These are the vessels within the visual resolution of the placental block micro-CT. N = 8 blocks per placenta. Number of blocks with vascular fill greater than 75% is shown, along with mean (±standard deviation) placental vascular fill (based on 8 blocks), and vascular fill of the block with the lowest and highest vascular fill. VF = vascular fill.

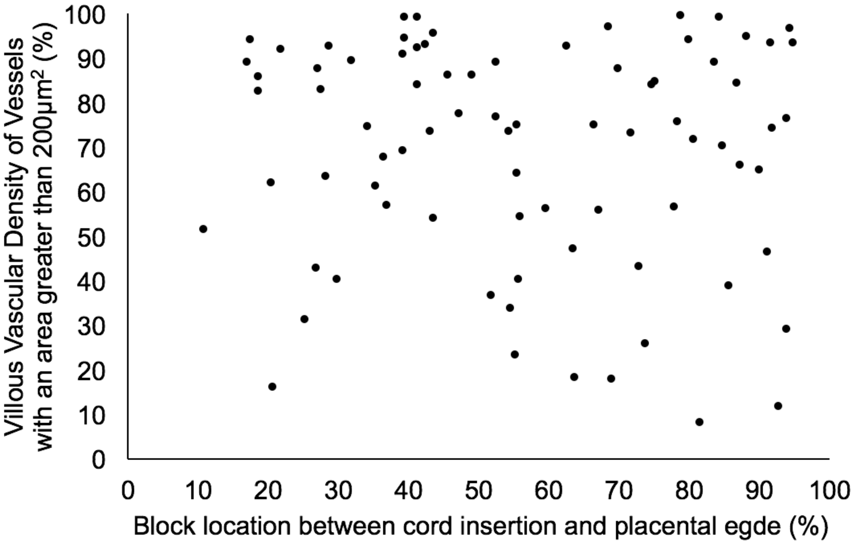

Figure 45; Graph of block vascular fill plotted against block location from cord insertion (0) to placenta edge (100). Spearman's rank-order correlation showed no statistically significant correlation between block location and vascular fill (r_s -0.009, p=0.9).

Conclusion; Placental Block Vascular Fill

Vascular fill was insufficient for reliable analysis in half of the blocks. 42 of 80 blocks were excluded from further analysis. There was no relationship between fill and tissue distance from site of umbilical cord insertion.

5.3 Placental Block Micro-CT Imaging

Placenta block micro-CT imaging allows visualisation of vessels down to 8.4µm radius. This represents a large proportion of the fetoplacental vascular tree, but likely excludes the terminal capillaries as their radius is at the limit of the resolution[175]. Volume renderings of block imaging showing the intricate vascular structure of the villous tree are shown in Figure 46. The larger vessels were within the resolution of whole placental imaging; however, the complex network of smaller vessels was beyond what could be resolved. To analyse vascular density at this scale, only the lower third of the data (showing the villous vascular tree close to the basal plate) was used. This was done to exclude the subchorionic region of the placenta, where the predominant vessel is the much more sparsely spread stem vessel branching from the chorionic plate, the spatial patterns of which had already investigated in whole placental imaging.

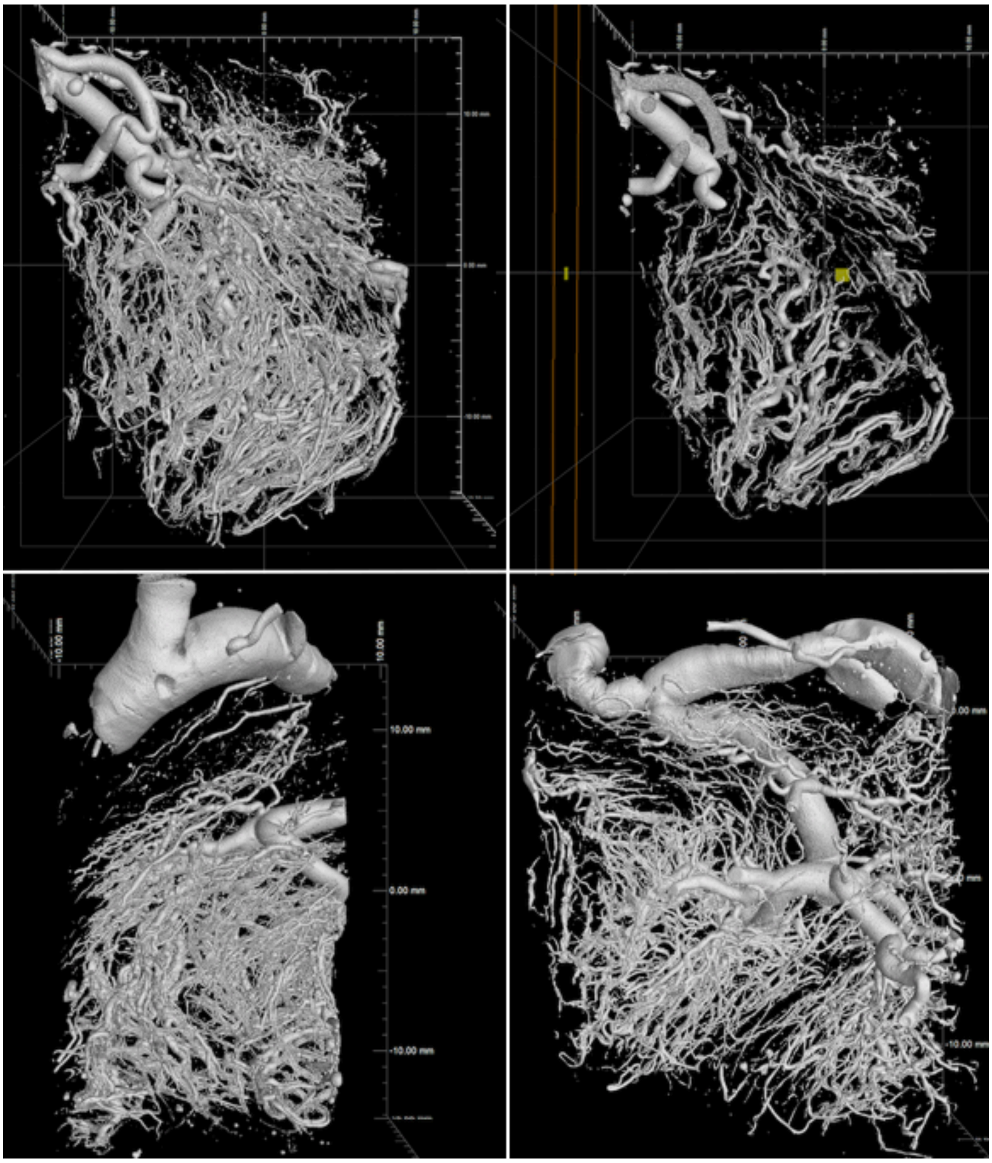

Figure 46; Volume renderings of block micro-CT imaging with a voxel size of 13.5μm, thresholded to show Microfil filled vessels (VG StudioMAX 2.2 (Volume Graphics, Germany)). Top; whole volume (left) and a slice through the volume (right) of a block from placenta 1. Bottom left; the full volume of a different block from placenta 1, and bottom right, a block from placenta 3. The complex villous vascular tree, down to, but not including, the terminal capillaries can be visualised. These full thickness blocks show large vessels descend from the chorionic plate, rapidly dividing to form complex vascular networks with small vessel radii providing a large surface area.

5.4 Placental Block Micro-CT Villous Vascular Density

Figure 47 shows a histogram of villous vascular density from all 38 included blocks, showing the distribution of vascular density throughout the data. Block villous vascular density ranged from 1 to 13%. The mean villous vascular density was 4 (±2)%.

To investigate the variation in villous vascular density between the placentas, a box plot was drawn (Figure 47). Villous vascular density within one placenta commonly varied by up to 4%, representing a 100-150% increase in vascular density between blocks. A Kruskal-Wallis H test showed that there was no statistically significant difference in the mean ranks of villous vascular density between placentas, (p=0.2).

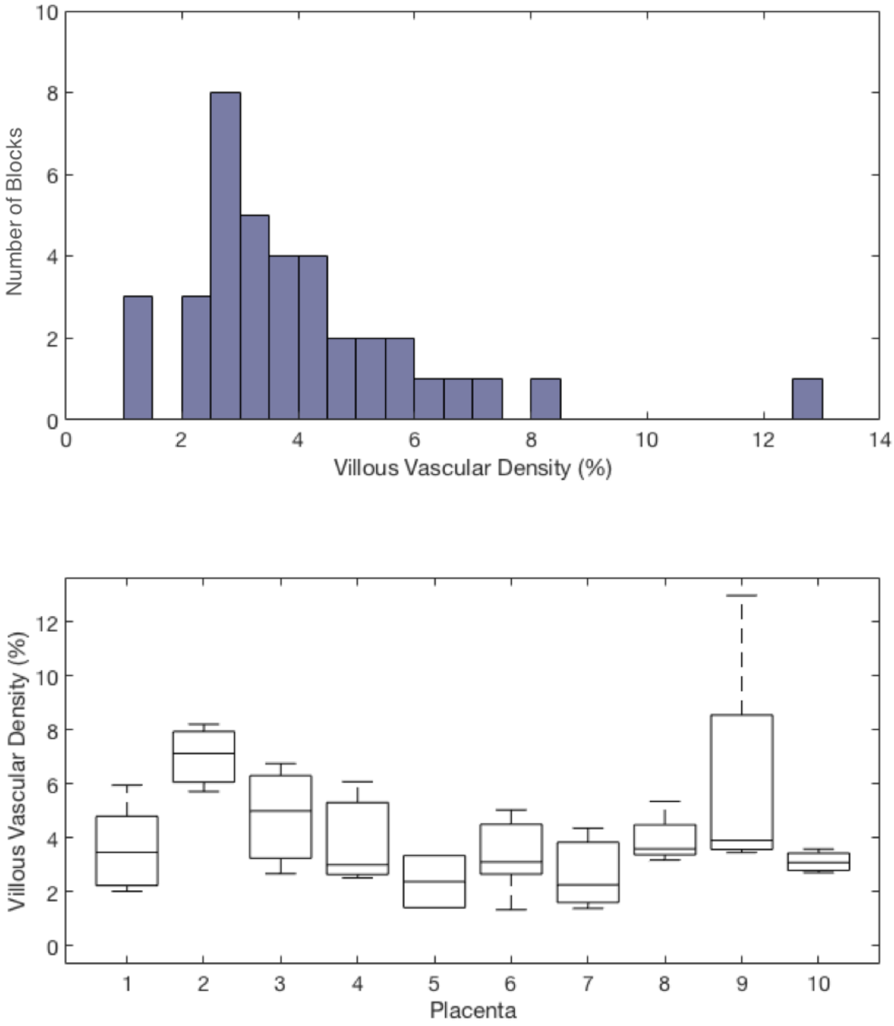

Figure 47; Figure showing histogram of block villous vascular density and box plot showing the spread of data between placentas, measured with micro-CT. Top; Histogram of villous vascular density for every included block, showing the spread of data across all placentae (n=38). Bottom; Box plot showing the spread of placental block villous vascular density measured with micro-CT.

Villous Vascular Density with Distance from Cord Insertion

To investigate if there was a difference in villous vascular density at this resolution with distance from cord insertion, villous vascular density was plotted against location from cord insertion to placental edge for each included block (Figure 48).

There was no correlation between villous vascular density and block location (r_s=0.066, p=0.7).

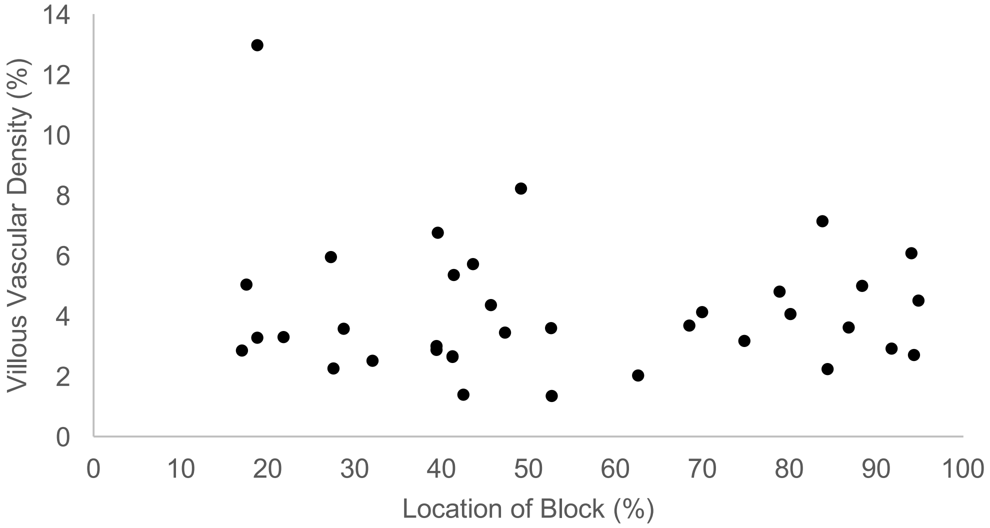

Figure 48; Graph showing correlation between micro-CT measure of villous vascular density and normalised block location in relation to cord insertion (0) and placental edge (100). Spearman's correlation showed no correlation between villous vascular density and block location (r_s 0.066, p=0.7).

Conclusion; Placental Block Micro-CT Villous Vascular Density

This work presents the spread in values for villous block vascular density within and between normal, term placentas, imaged with an isotropic voxel size of 13.5µm. No spatial relationship between villous vascular density, and the distance of the tissue from umbilical cord insertion and placental edge, was found in this work.

5.5 Histological Villous Vascular Density

To examine the villous vascular density including the terminal capillaries histological data was used. Only micrographs taken from the lower half of the full thickness placental slices, close to the basal plate, were used to represent the villous vascular tree. Figure 49 shows a histogram of mean block villous vascular density measured with histology. The vascular density ranged from 8 to 38%. The mean villous vascular density was 19 (±5)%. Example micrographs showing highly and poorly vascularised tissue are shown in Figure 50.

A boxplot was drawn to investigate the difference in vascular density between the placentas (Figure 49). The vascular density of blocks from one placenta often varied by 10%, representing an increase in vascular density of 50% between blocks from one placenta. A Kruskal-Wallis H test showed that there was a statistically significant difference in the mean ranks of villous vascular density between placentas, ($p<0.01$). Post-hoc pairwise comparisons were performed using Dunn's procedure with a Bonferroni correction for multiple comparisons. The only significant differences in vascular density were between placenta 1 and placentas 2 ($p=0.01$), 3 ($p=0.03$), 4 ($p=0.02$) and 8 ($p=0.03$).

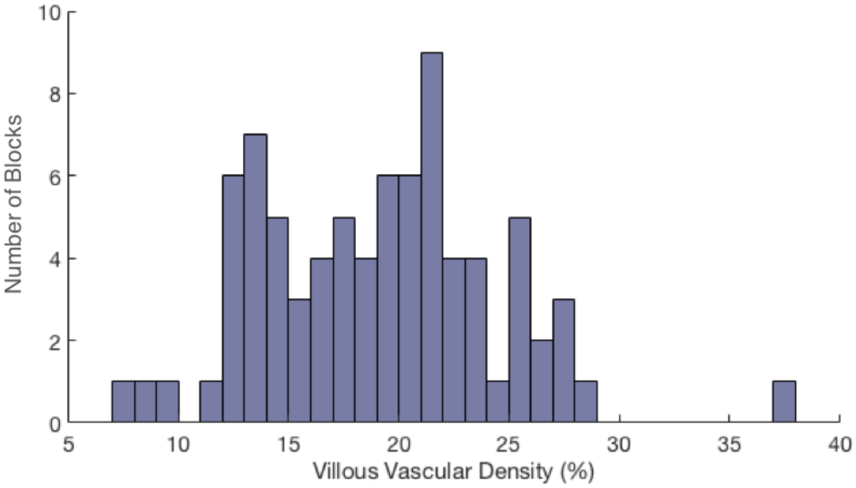

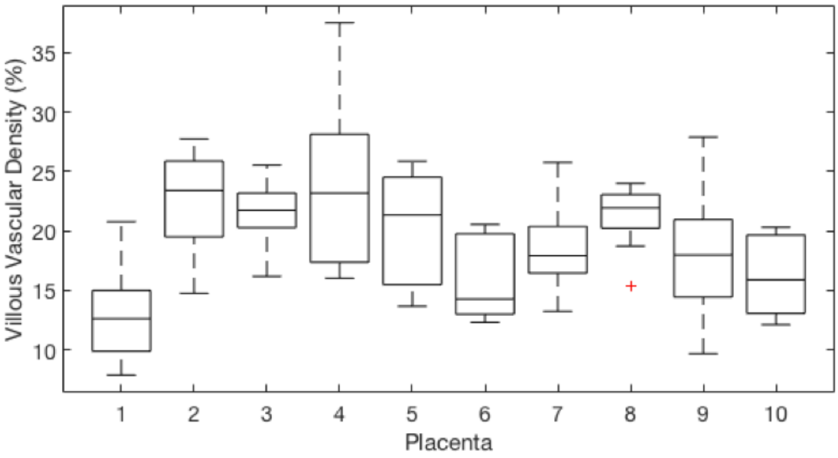

Figure 49; Figure showing histogram of block villous vascular density and box plot showing the spread of data between placentas, measured with histology. Top; Histogram showing the mean villous vascular density per placental block, based on two sections with 3 micrographs per section (total 6 micrographs) for each placenta block (n=80). Bottom; Box plots showing the spread of placental block villous vascular density measured with histology for each placenta.

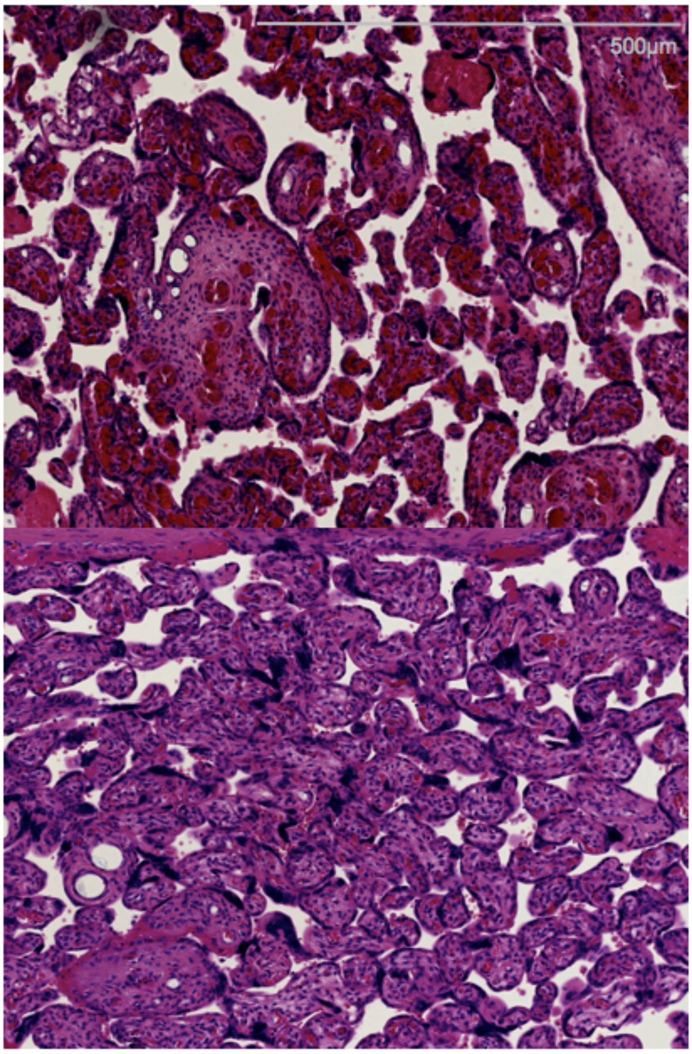

Figure 50; Figure showing examples of poorly and well vascularised histological micrographs. Upper; Example villous micrograph from the histological block with vascular density measured as 38% (placenta 4, block 8). This tissue is highly vascularised. Lower; Example villous micrograph from the histological block with a vascular density measured as 7% (placenta 1, block 5). This tissue is poorly vascularised.

Histological Villous Vascular Density with Distance from Cord Insertion

To investigate histologically measured villous vascular density (including terminal capillaries) in relation to the location of the tissue within the placenta the mean villous vascular density was plotted against location from cord insertion to placental edge for each block (Figure 51).

There was no correlation between villous vascular density and block location (r=0.06, p=0.6).

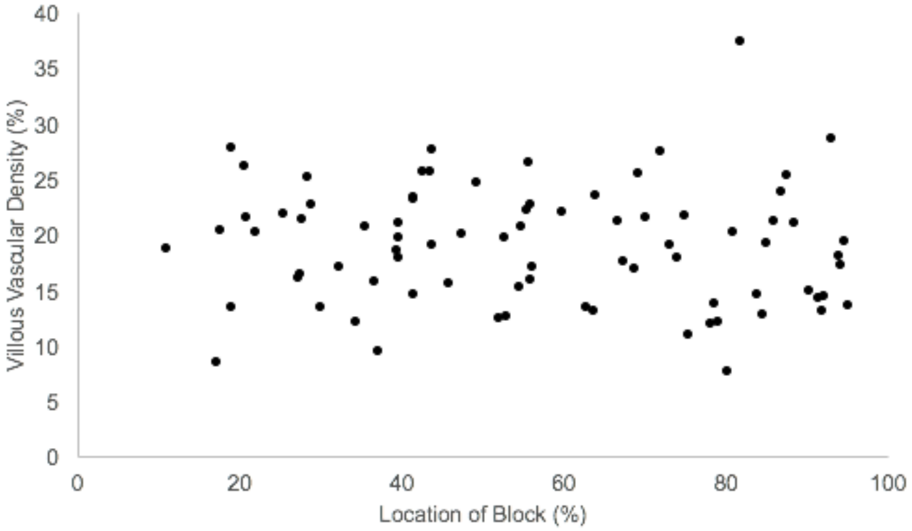

Figure 51; Graph showing correlation between histological measure of villous vascular density and normalised block location in relation to cord insertion (0) and placental edge (100). Pearson’s correlation coefficient showed no correlation between villous vascular density and block location (r=0.06, p=0.6).

Conclusion; Histological Villous Vascular Density

This work presents the spread in values for villous vascular density within and between normal, term placentas, with histological imaging. No spatial relationship between villous vascular density, and the distance of the tissue from umbilical cord insertion and placental edge, was found in this work.

5.6 Discussion

This work systematically investigated the three-dimensional villous vascular density of the normal human placenta, and investigated if there is a consistent spatial pattern in vascular density between placentas. This work is important because I have quantified the normal term feto-placental vascular density of different sized vessels within the vascular tree, to develop a normal range against which pathology can be compared.

Block placental imaging benefited from higher resolution compared to whole placental imaging, but this was at the cost of field of view. Imaging eight blocks from one placenta only imaged on average 1% of the placental volume. However, the increased magnification allowed visualisation of vessels in the villous tree, excluding only the terminal capillaries.

Histological analysis was performed to allow visualisation of all vessels within the villous vascular tree, including terminal capillaries. The disadvantage of this method was that the vessels were only seen in two-dimensional cross section, and that the histological sampling method used in this work examined on average around 1.4 x 10^{-4}% of the placental volume.

The mean villous vascular density in imaging with a voxel size of 13.5μm was 4 (±2) %. The range was 1 to 13%. This shows the large degree to which the vascular density at this scale varies through and between normal term placentas. When vascular density was examined in relation to tissue location between the umbilical cord insertion and placental edge, no relationship was found, confirming that there is a large degree of variation, but no reproducible spatial pattern, in vascularisation of the human placenta.

Histological analysis of the villous vascular tree showed a mean vascular density of 19 (±5)%, consistent with previous measures in the literature[176,177], with Mayhew et al, estimating the normal capillary vascular density as 23.8% (±1.88%)[176]. The value ranged from 8 to 38%, and again there was no spatial pattern with regard to tissue location between the point of cord insertion and the placental edge.

This work contradicts the work of Fox et al[20], who reported increased hypovascular areas near the placental edge. However it is in agreement with the finding of Mayhew et al[176], that the villous vascular density does not significantly differ with tissue location, in relation to cord insertion and placental edge. This work used just four placentas, taking 36 2x2x3mm tissue samples from each, 9 centrally and 18 peripherally, which were analysed using 2D histological slides, and manual measurements of vessel area. This approach sampled approximately 0.05% of the total placental tissue volume and imaged even less. The Micro-CT technique described here samples a much higher proportion of the placental tissue, and analyses both three-dimensional and two-dimensional data, over 10 normal term placentas. The results are therefore likely to be more representative.

It can be concluded that there is a large degree of variation in vascular density at all levels of the fetoplacental vascular tree, and at different locations within the human, term placenta, but that there is no repeatable pattern in the spatial pattern, in relation to the placental structure. To sample a placenta adequately to understand the vascularisation requires sampling of a large proportion of the tissue. This is probably one of the reasons why there is no consistent pathological finding in histological examination of placentas from pregnancies believed clinically to be complicated by fetal growth restriction.

The micro-CT measure of vascular density in this work is different from that published by Langheinrich[87], who reported a vascular density of 21 +/- 1% in healthy control placentas. This work imaged with a voxel size of 4μm, visualising the terminal capillaries, accounting for this difference. It is however surprising how low the standard deviation is, given the variation in vascular density with histological analysis found in this work. The lower micro-CT magnification used in this work allowed for a larger field of view, capturing the full thickness structure of the three-dimensional vascular tree. Langheinrich et al imaged 2mm wide biopsies, and therefore a much smaller proportion of the vascular tree. Using this technique they were unable to follow the vascular tree, and therefore not able to perform more advanced analysis, for example looking at branching patterns. In future multiscale micro-CT imaging studies, a third sampling of a small volume of placental block tissue, and imaging of the villous area at a higher degree of magnification would allow an increase in resolution down to this scale, and visualisation of the terminal capillaries. This should be considered in future work. Other imaging methods, such as confocal laser microscopy, may also be useful to further investigate the vascular tree at this scale.

Limitations of perfusion work have already been discussed in Chapter 4, as has the advantage of a non-destructive imaging technique, allowing histological assessment of vascular fill, and exclusion of poorly perfused tissue. This was particularly relevant to this work, where despite extensive work to optimise tissue preparation technique, over half of the tissue was excluded from analysis.

Limitations in analysis have also been discussed in Chapter 4, and these are also relevant to block imaging, where improved segmentation and skeletonisation may allow more advanced analysis of the complexity of the villous vascular tree. As histology suggests there is a reduction in terminal villous vascular density in early on-set FGR, advancing our ability to analyse this complex data may shed new light on the changes in the villous vascular tree that occur in this disease.

However, the data is extremely large and complex, making it computationally challenging to work with. An example dataset of one whole placenta was 2000x2000x426 TIFFS = 1.2 GB, an example dataset of one placental block was 2000x2000x2028 TIFFS = 9.8 GB, and there were eight such volumes for each placenta. This work therefore relied on simple analysis using proprietary software. The software however has not been optimised to analyse biological tissue, and it also struggled with the complexity of the data. Future work to produce bespoke image analysis tools may greatly improve our ability to analyse this data, and so understand the complex villous vascular tree.

In conclusion, this work investigated the normal human fetoplacental villous vascularisation in three-dimensions. I found a large degree in variation of vascular density between blocks taken from one placenta, but no spatial pattern in relation to placental structure.

6 Magnetic Resonance Placental Perfusion Imaging and Analysis; Methodology

6.1 Summary

In this chapter I present a novel MR model to evaluate fetal and maternal placental perfusion; Diffusion-rElaxation Combined Imaging for Detailed Placental Evaluation (DECIDE). I then present the methodology used for placental MRI and image analysis in this thesis.

The DECIDE model was originally conceived by Dr Andrew Melbourne in discussion with myself, my PhD supervisors and other members of the GIFT-Surg team, a Wellcome Trust/EPSRC funded project investigating novel fetal imaging and therapy. It was then developed in a collaborative effort between myself and Andrew throughout the course of this work.

I obtained ethics for this study, and recruited and consented all patients. I was involved in setting up GIFT-Cloud, the platform that allows transfer of anonymised imaging from University College London Hospital, to University College London, and in gaining approval from the UCLH Caldicott Guardian for this work.

Image acquisition was optimised in collaboration with Dr Magdalena Sokolska, an MR Physicist at University College London Hospital.

All data registration was performed by Dr Andrew Melbourne. I performed all tissue segmentation, model fitting and data analysis.

6.2 The DECIDE model of Placental Perfusion

Diffusion-rElaxation Combined Imaging for Detailed Placental Evaluation (DECIDE) is a multi-compartment model of placental perfusion that aims to separate signals from fetal and maternal placental perfusion, and static tissue representing the trophoblast separating the two circulatory systems[178].

The DECIDE model simultaneously fits T2 relaxometry and the diffusion weighted Intravoxel Incoherent Motion Model (IVIM) of perfusion to divide the placenta into three compartments; the fetal vascular fraction *(f)*, the maternal non-vascular blood fraction (ν) and tissue (Figure 52).

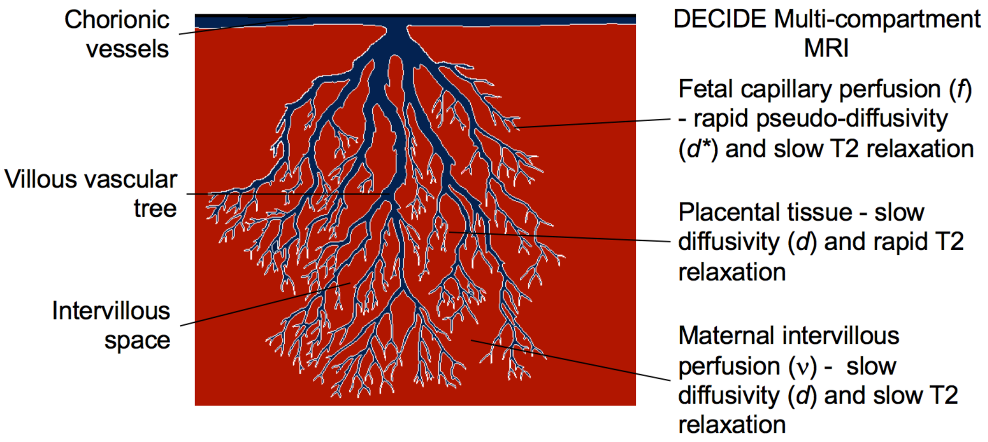

Figure 52; Diagram illustrating the three compartments of the DECIDE model.

As discussed in the introduction, IVIM is a model used to estimate tissue perfusion from diffusion weighted imaging, without the need for extrinsic contrast agent. The IVIM equation is:

$$S(b) = S_0\left[fe^{-\mathbf{bd}^*} + (1-f)e^{-\mathbf{bd}}\right]$$

Standard IVIM Equation

Where *f* is the vascular fraction, *d* the* pseudo-diffusion coefficient, and *d* the diffusion coefficient. The IVIM model does not take into account the relaxation times of the two compartments, assuming these to be the same.

However the T2 relaxation time of blood and tissue are known to be distinct, with blood having a slow T2 relaxation time, typically 240±30ms[179], whilst tissue has a much faster T2 relaxation time of 46±6ms[179]. Previous work has shown that failure to account for this in the model is likely to result in incorrect estimation of the relative blood fractions in each compartment, resulting in the vascular fraction (*f)* being over estimated[180]. The addition of T2 relaxation time to the model may therefore improve the estimation of both compartments (*f,* and 1-*f)*. Adding T2 relaxation to the IVIM model gives the equation:

$$S(b, TE) = S_0\left[f e^{-\mathbf{b}d^{*}-TE/T2b} + (1-f)e^{-\mathbf{b}d-TE/T2t}\right]$$

T2-IVIM Equation

Where TE is echo time, T2b the T2 relaxation time of blood, and T2t the T2 relaxation time of tissue.

This equation is a physiologically relevant model for the perfusion of most abdominal organs, separating the perfusing blood and tissue compartments. However, in the placenta whilst the fit of *f* relates to the fetal perfusion of the placenta, with high intercapillary pseudo-diffusion rate and long T2 relaxation time, the fit does not take account of the more slowly perfusing maternal blood of the intervillous space, which is captured within the second compartment. This is likely to make the model insufficient.

In order to correct this, the second compartment may be further divided in two, by separating signal with long T2 relaxation time relating to maternal blood, and short

T2 relaxation time relating to tissue. This gives the three compartment DECIDE model:

$$\mathrm{S(b, TE)} = \mathrm{S_0}\left[\mathrm{f}\mathrm{e}^{-\mathbf{b}\mathrm{d}^{*}-\mathrm{TE/T2fb}} + (1-\mathrm{f})\mathrm{e}^{-\mathbf{b}\mathrm{d}}\left[\mathrm{v}\mathrm{e}^{\mathrm{TE/T2mb}} + (1-\mathrm{v})\mathrm{e}^{\mathrm{TE/T2t}}\right]\right]$$

DECIDE Equation

Where *f* relates to the vascular fraction, representing fetal intercapillary perfusion, ν relates to the non-vascular blood fraction, representing intervillous maternal blood, T2fb relates to the long T2 relaxation time of fetal blood, T2mb relates to the long T2 relaxation time of maternal blood, and T2t relates to the short T2 relaxation time of tissue.

6.3 Ethical Approval

Initial imaging of healthy, non-pregnant volunteers was done with research ethical approval already in place at University College Hospital London (REC reference number 07/Q0502/15).

Imaging of pregnant women with a diagnosed fetal abnormality was already being performed at UCLH for brain abnormalities, and after laser therapy for twin-to-twin transfusion syndrome (TTTS) and other complex twin pregnancies. In order to perform research MRI on pregnant participants with a normal fetus or to extend the imaging time for those already being imaged, we applied for and were granted ethical approval from the London - Hampstead Research Ethics Committee, (REC reference number 173602), and obtained NHS approval from University College London Hospital (UCLH) R&D. As part of this process, a patient information leaflet on the safety and process of having a Fetal MRI was also developed, which is now used for all patients being offered a fetal MRI at UCLH. I led the preparation of this document, and its review by the GIFT-Surg Patient Public Involvement Group (PPIAG) and eventual publication by UCLH Patient Information Services.

6.4 Inclusion criteria

Optimisation work was first performed on the liver of non-pregnant healthy volunteers to develop the protocol. This reduced the number of pregnant participants needed and their imaging time. The liver was chosen to simulate the placenta as it is a highly perfused abdominal organ. The volunteers were recruited from within the lab, and they all gave informed, written consent to participate. There was no known pathology in the volunteers imaged.

Once the imaging protocol was known to provide data with sufficient signal to noise ratio for the model fit, women with complicated twin pregnancies having clinically indicated fetal brain MRI scans were recruited. This allowed further optimisation work to be performed on women already having MRI scans, with the addition of 20 minutes to their scan time, for which we sought written consent.

Once the protocol was optimised, women with uncomplicated pregnancies were recruited for placental MRI, in order to investigate DECIDE in a cohort of normal pregnancies, with written consent. Inclusion criteria were:

- Singleton pregnancy
- 24-34 weeks' gestational age
- Normal anomaly ultrasound scan
- Estimated fetal weight greater than the 10th centile
- Amniotic fluid deepest pool measurement in the normal range for gestation
- No known maternal complications (no evidence of pre-eclampsia, hypertension, low risk for preterm labour)

6.5 Ultrasound Imaging

All women with uncomplicated pregnancy had an ultrasound scan within one week of the MRI scan. This was done to assess fetal growth and wellbeing using standardised ultrasound parameters, to ensure that there was no evidence of fetal compromise or fetal growth problems, and to assess maternal health. All imaging was done by a trained ultrasound practitioner, on an GE Voluson E10 ultrasound machine (General Electric Company, USA), using a c1-5 2-5MHz probe.

Measurements were taken of:

- Head circumference
- Biparietal diameter
- Abdominal circumference
- Femur length

From these the Hadlock B formula[181] was used to calculate an estimated fetal weight. The deepest liquor pool was measured, and ultrasound Doppler measurements were taken of:

- Left and right uterine arteries pulsatility index
- Umbilical artery pulsatility index
- Middle cerebral artery pulsatility index

The percentile for estimated fetal weight, the uterine, umbilical, and middle cerebral artery Doppler, and the cerebroplacental ratio were calculated using the Fundació Medicina Fetal Barcelona on-line Fetal Growth calculator (http://medicinafetalbarcelona.org/calc/).

6.6 Magnetic Resonance Imaging

Imaging was performed on a 1.5T Siemens Avanto (Siemens Healthcare, Germany). Table 14 shows the image acquisition protocol. The shortest TE, and the b-value increments were constrained by the MR machine. The repetition time (TR) was set as long as possible to reduce interference from T1 relaxivity. The resolution was 1.9 x 1.9 x 6mm. All imaging was acquired with the same echo-planar read-out, with different diffusion encoding directions. The total acquisition time was 20 minutes making it tolerable for participants, even when pregnant.

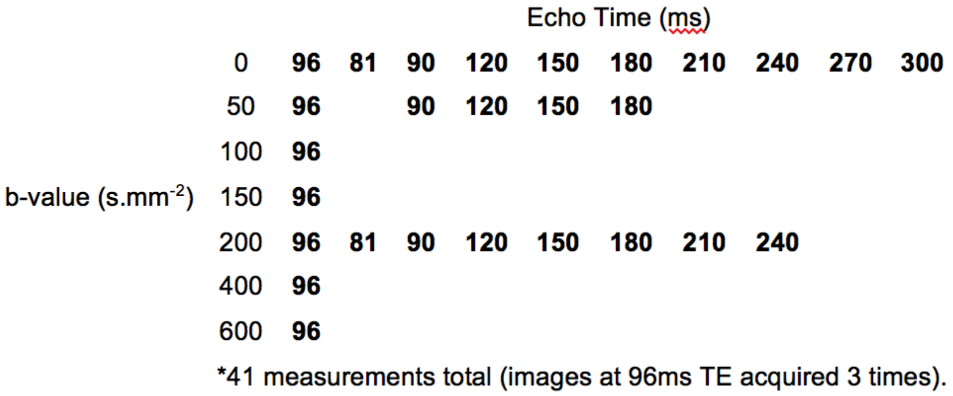

		Echo Time (ms)									
b-value (s.mm^{-2})	0	**96**	**81**	**90**	**120**	**150**	**180**	**210**	**240**	**270**	**300**
	50	**96**		**90**	**120**	**150**	**180**				
	100	**96**									
	150	**96**									
	200	**96**	**81**	**90**	**120**	**150**	**180**	**210**	**240**		
	400	**96**									
	600	**96**									

*41 measurements total (images at 96ms TE acquired 3 times).

Table 14; Image acquisition parameters used in all placental imaging.

6.7 Image Registration and Segmentation

MRI data was transferred, with approval from the UCLH Caldicott guardian, to the University College London (UCL) using GIFT-Cloud, an XNAT based platform that performs anonymisation prior to transfer[182]. The data was stored securely on the GIFT-Cloud database at UCL.

A non-rigid registration technique was first applied to align images and minimise the effect of intra-abdominal motion[183,184].

Masks were drawn manually over the area of interest in multiple slices of the 2D stack (itk-SNAP Version 3.2.0, 2014). In non-pregnant volunteers this was the liver (excluding the gallbladder), and in pregnant volunteers the placenta and a section of retro-placental myometrium were segmented. Segmentations were conservative to minimise noise from movement entering the analysis, whilst maximising the amount of tissue included. All slices where the tissue of interest was clearly visible were included, to maximise the proportion of the tissue investigated (Figure 53).

As each slice was acquired 41 times, with the possibility of motion between acquisitions, the segmentation was overlaid over every acquisition of every slice, to check for motion (FSLEYES version 0.10.1, Oxford, UK). If motion meant the segmentation went outside the tissue of interest at any time, the segmentation was modified until it remained within the tissue of interest throughout the whole dataset. If this was not possible the case was excluded.

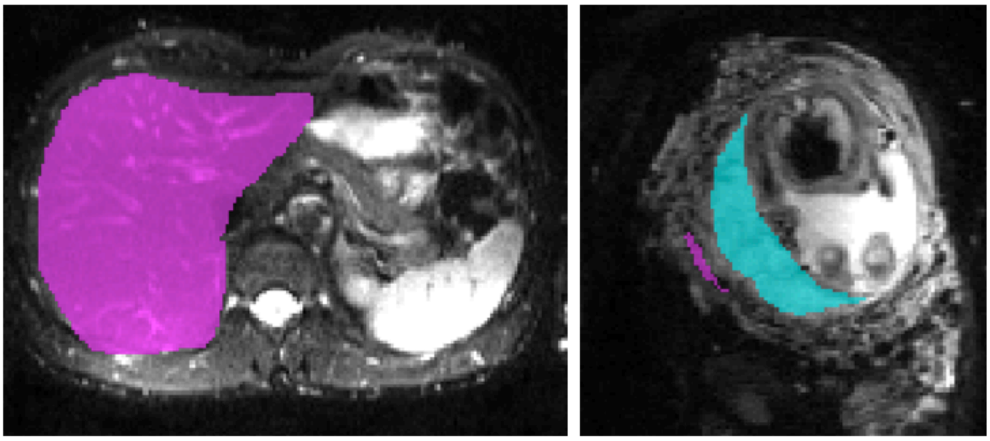

Figure 53; Figure showing liver (left image, pink), placenta (right image, blue) and myometrial (right image, pink) segmentation on 2D slices of MRI dataset. For liver and placenta note that the segmentation includes most of the tissue of interest, but avoids the tissue at the periphery, as this is the area most likely to be affected by motion, which would bias the results. Only a small area of myometrium was segmented due to the thinness of the tissue making it very motion sensitive.

6.8 Model Fitting

All model fitting was done using in-house software developed in MATLAB (The Mathworks Inc., Natick, MA USA). To improve the fit for all parameters, we first fit to average area of interest signal curves. This increased the signal to noise ratio, and so yielded robust starting estimates for each parameter. These were then used to initialise a voxel-by-voxel fit within the area of interest. The fitting proceeded as follows:

- First log-linear fitting was applied to calculate the mean diffusion coefficient (*d*) for b-values greater than 100s.mm^{-2}. This was done because diffusion weighted imaging has low signal to noise and fitting the diffusion coefficient depends only weakly on other parts of the underlying data. This was first applied to the high SNR average signal curve for the whole area of interest, and then to each voxel.
- The standard IVIM model was then fitted. Again, this was first applied to the average signal curve for the whole area of interest, which was initiated with estimation of *f* of 0.4, and *d** of 0.05. The parameter estimates from this were then used to initiate a voxel-wise fit, and the voxel wise fit of *d* was used. Parameters were constrained to biologically feasible values; between zero and one for *f* and *d**.
- The T2-IVIM model was then fitted, using the same method as the IVIM fit. The area of interest fit for T2 relaxation times was initiated using values from the literature. The parameter estimates for *f, d**, and T2 relaxation time of blood and tissue were then used to initiate a voxel-wise fit. T2 relaxation times were constrained between 0 and 1000ms.
- The DECIDE model was then fitted, using the same method as the IVIM fit. ν was constrained to be between zero and one.

Parameter maps were examined to look for trends in the data.

6.9 Statistical Analysis

Data analysis was performed in MATLAB. Results are presented as example parameter maps of 2D slices, and histograms of the voxel-by-voxel fit. Statistics are described as mean (±standard deviation).

7 Developing the DECIDE Model of Placental Perfusion

7.1 Summary

Assessment of placental function *in vivo* is essential as placental pathologies cause significant morbidity and mortality in both the mother and fetus. Current ultrasound placental assessment is sub-optimal as it is only possible to measure Doppler flow in the feeding arteries, and not in the placenta itself.

This chapter presents the development of a new MRI model of placental perfusion; the DECIDE three-compartment model.

I show this model fit is feasible, first in liver, and then in myometrium and placenta. I then go on to investigate the effect that echo time has on the model fit. I add T2 relaxation time to the model fit, investigating the T2 relaxation time of maternal blood in the myometrium, and T2 relaxation time of fetal blood in the placenta.

The final DECIDE model fits five parameters which relate to placental function – vascular fraction (*f*), pseudo-diffusion coefficient (*d**), non-vascular blood fraction (ν), diffusion coefficient (*d*), and fetal blood T2 relaxation (T2fb).

7.2 The DECIDE Model fit in the liver dataset

Liver MR imaging was performed on six non-pregnant, healthy volunteers. All volunteers gave written consent for involvement in research. The image acquisition parameters for liver imaging are shown in Table 15.

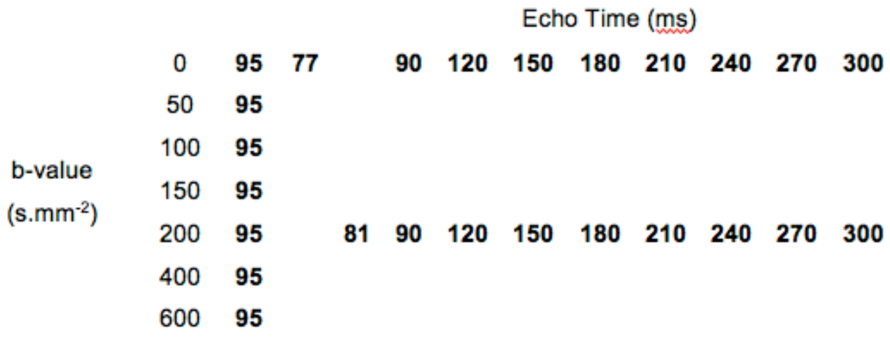

b-value ($s.mm^{-2}$)	Echo Time (ms)										
0	**95**	**77**		**90**	**120**	**150**	**180**	**210**	**240**	**270**	**300**
50	**95**										
100	**95**										
150	**95**										
200	**95**		**81**	**90**	**120**	**150**	**180**	**210**	**240**	**270**	**300**
400	**95**										
600	**95**										

Table 15; Image acquisition parameters for liver. This acquisition routine permitted T2 relaxation to be fitted with a b value of $0s.mm^{-1}$, and an IVIM like fit of data at TE 95ms.

Figure 54 shows parametric maps for one representative 2D slice of one of the liver data sets, showing vascular fraction (*f*), pseudodiffusion coefficient (*d**) and non-vascular blood fraction (ν) for the standard IVIM, T2-IVIM, and DECIDE model fits. When T2 relaxation times were used in the fit, T2 of blood was set at 240ms, and T2 tissue at 46ms. The vascular features of the liver became more apparent as T2 relaxation time was added to the model, and the vascular fraction decreased. The non-vascular blood fraction parameter (ν) was relatively low in the liver, as expected given that it does not contain a third fluid compartment. The areas of high ν at the top and to the right of the liver were likely secondary to motion artefact, being adjacent to the diaphragm.

Conclusion; The DECIDE Model fit in the liver dataset

The DECIDE model fit was feasible in the human liver. The non-vascular blood fraction parameter (ν) was low in the liver.

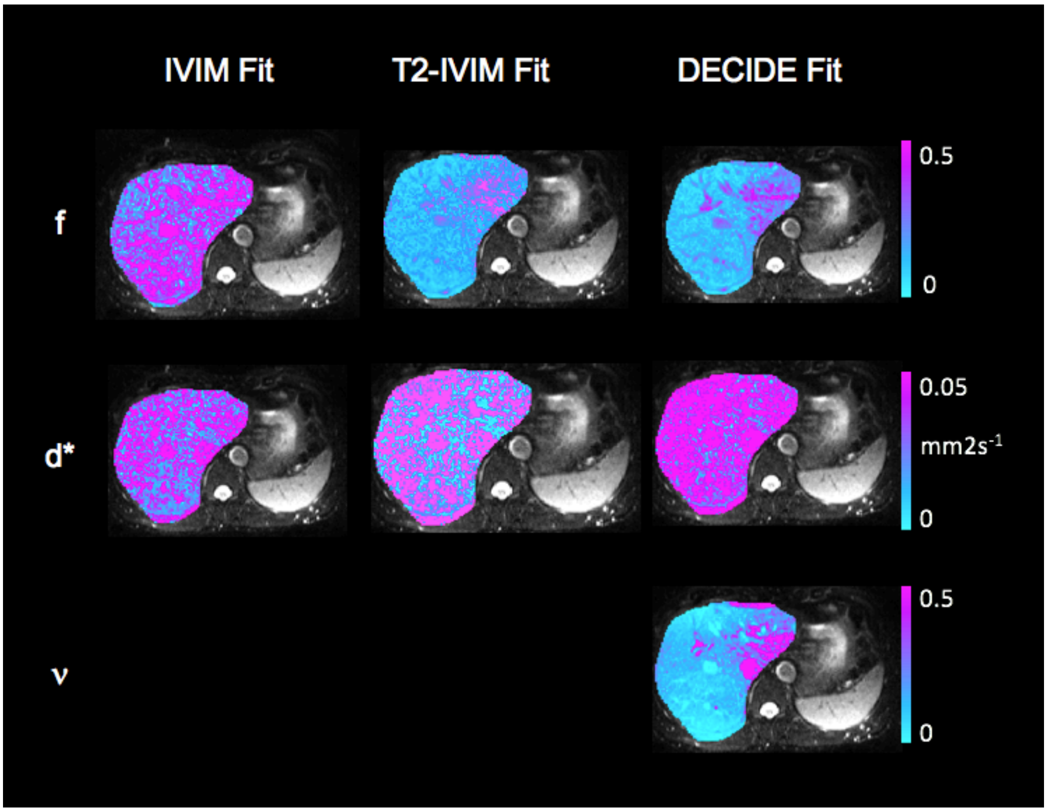

Figure 54; Parametric maps for voxel-wise fit of one example 2D slice of one liver dataset. Columns show the different fits: column 1; IVIM fit, column 2; T2-IVIM fit, column 3; DECIDE fit. Rows show parameter maps: row 1; vascular fraction (*f*), row 2; pseudoperfusion (*d**), row 3; non-vascular blood fraction (ν).

7.3 Addition of T2 Relaxometry to the fit in the liver dataset

Figure 55 shows histograms for the voxel by voxel fit for each of the liver cases, and Table 16 shows the mean and standard deviation for each parameter over the whole liver dataset. As T2 relaxation was added the spread and mean of *f* markedly decreased, with the T2-IVIM model *f* value being 40% of the IVIM *f* value. The T2-IVIM and DECIDE models had similar distributions and means of *f*. The DECIDE model parameter ν is low.

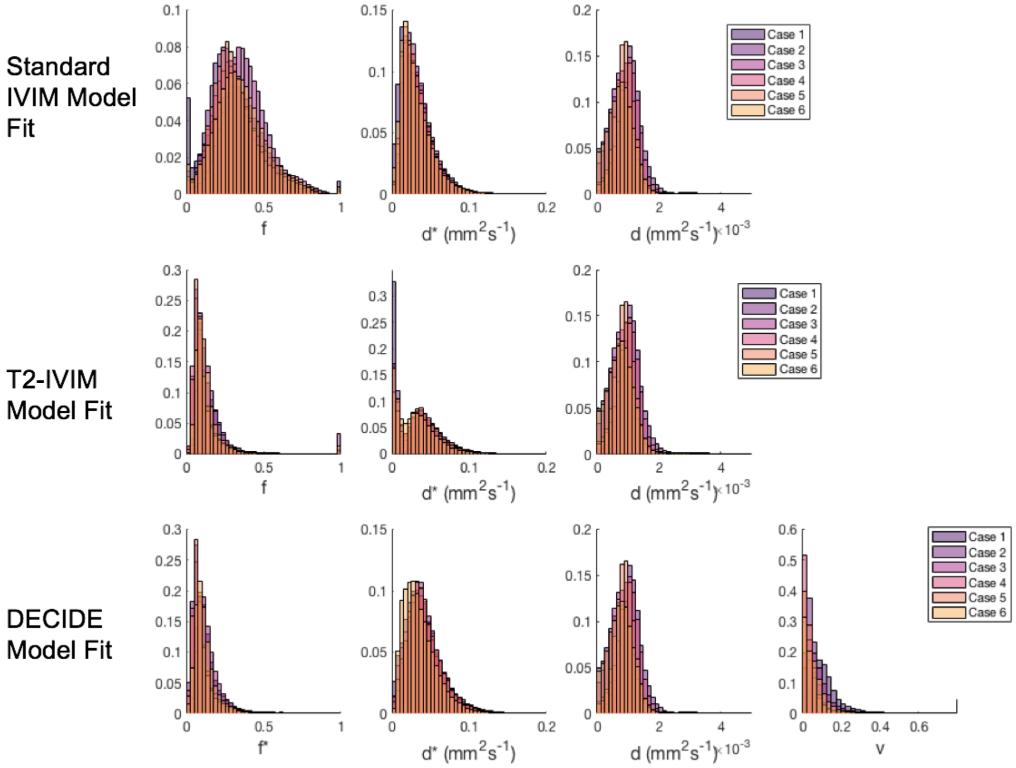

Figure 55; Voxel-wise whole liver parameter histograms for the six liver datasets, showing *f*, *d and *d* for each fit, and ν for the DECIDE Fit.** Row one; IVIM fit, row 2; T2-IVIM fit, row 3; DECIDE fit.

	IVIM Fit (mean±SD)	T2-IVIM Fit (mean±SD)	DECIDE Fit (mean±SD)
f	0.33 (0.03)	0.13 (0.03)	0.12 (0.02)
*d**(mm^{2}s^{-1})	0.070 (0.007)	0.063 (0.005)	0.072 (0.007)
ν			0.09 (0.04)

Table 16; Table showing mean and standard deviation for the parameters (*f, d and ν) for each model fit over the whole data set using a voxel-by-voxel fit (n=6).**

Conclusion; Addition of T2 Relaxometry to the fit in the liver dataset

Adding T2 relaxation time to the model fit reduced the vascular fraction (*f*) in the liver.

7.4 The effect of Image Acquisition Echo Time on the vascular fraction

Five women with complicated twin pregnancies were imaged, see Table 17 for details. All women gave written informed consented for additional research scanning time. Three women had had laser surgery for twin-to-twin transfusion syndrome, one for selective intrauterine growth restriction and one woman had a termination for fetal abnormality. At the time of MRI two pregnancies had two living fetuses, and three had one living fetus.

Case	Indication for MRI	Gestational Age at MRI (weeks + days)	Number of Surviving Fetuses at time of MRI	Estimated fetal weight of Twin 1 (g (centile))	Estimated fetal weight of Twin 2 (g (centile))
1	Laser surgery for TTTS	26+2	2	759 (4)	772 (6)
2	Laser surgery for TTTS	22+2	1	423	NA
3	Selective termination of pregnancy for anomaly	24+3	1	826 (93)	NA
4	Laser surgery for TTTS	22+6	1	488	NA
5	Laser Surgery for sIUGR	27+3	2	446 (0)	1071 (50)

Table 17; Table showing indication for MRI scan, gestational age at MRI, the number of fetuses and the estimated fetal weights for the 5 placental cases. Ultrasound estimation of fetal weight was within a week of MRI in all cases. Growth centile is shown when gestational age was greater than 24 weeks'. NA = not applicable. TTTS: twin-to-twin transfusion syndrome, sIUGR: selective intrauterine growth restriction.

After the first placenta case, the imaging protocol was adjusted, adding additional echo time (TE) acquisitions at a b-value of 50s.mm^{-2}, and removing the higher TE acquisitions (270 and 300ms) at b value 200s.mm^{-2}. This was done to make sampling across b-values richer, and because signal was minimal at the higher TEs, so removing them did not affect data fit.

		Echo Time (ms)									
b-value (s.mm^{-2})	0	**96**	**81**	**90**	**120**	**150**	**180**	**210**	**240**	**270**	**300**
	50	**96**		**90**	**120**	**150**	**180**				
	100	**96**									
	150	**96**									
	200	**96**	**81**	**90**	**120**	**150**	**180**	**210**	**240**		
	400	**96**									
	600	**96**									

*41 measurements total (images at 96ms TE acquired 3 times).

Table 18; Image acquisition parameters for placenta. This acquisition routine permitted T2 relaxation to be fitted with a b-value of 0s.mm^{-1}, and an IVIM fit of data at TE 96ms. Four extra echo times were added at b-value 50s.mm^{-2}. This allowed the fit of IVIM at TE 90, 120, 150 and 180ms.

To further investigate the effect of T2 relaxation time on the vascular fraction (*f*), in the four placental cases imaged using the new acquisition protocol, an IVIM fit using three b values (0, 50, 200s.mm^{-2}) was applied at four echo times (90, 120, 150, 180ms).

First a log-linear ADC fit was applied at an echo time of 96ms. This was done because it was the only echo time with sufficient data above 100ms for the fit. The diffusion coefficient was then fixed and used in each of the subsequent IVIM fits. The results are shown in Table 19 and Figure 56. The vascular fraction increased with increasing TE in every case. The mean *f* over all four cases was 0.27(±0.06) at TE 90ms, and 0.36(±0.09) at 180ms, an increase of 33%. This confirms the sensitivity of *f* to the acquisition echo time if it is not taken into consideration in the model fit.

	f				
TE (ms)	Case 2	Case 3	Case 4	Case 5	Mean (±SD)
90	0.32	0.32	0.19	0.26	0.27 (0.06)
120	0.35	0.38	0.20	0.31	0.31 (0.08)
150	0.40	0.43	0.21	0.35	0.35 (0.09)
180	0.41	0.44	0.23	0.36	0.36 (0.09)
% increase in *f* from TE 90 to 120ms	28	41	22	39	33

Table 19; Table showing average voxel fit of vascular fraction (*f*) for the IVIM model for each placental case, at different echo times. *f* increased with echo time in every case, with a mean increase of 33% from 90 to 180ms.

Conclusion; The effect of Image Acquisition Echo Time on the vascular fraction.

As the echo time of image acquisition increase, *f* increases, proving that *f* is sensitive to the acquisition echo time.

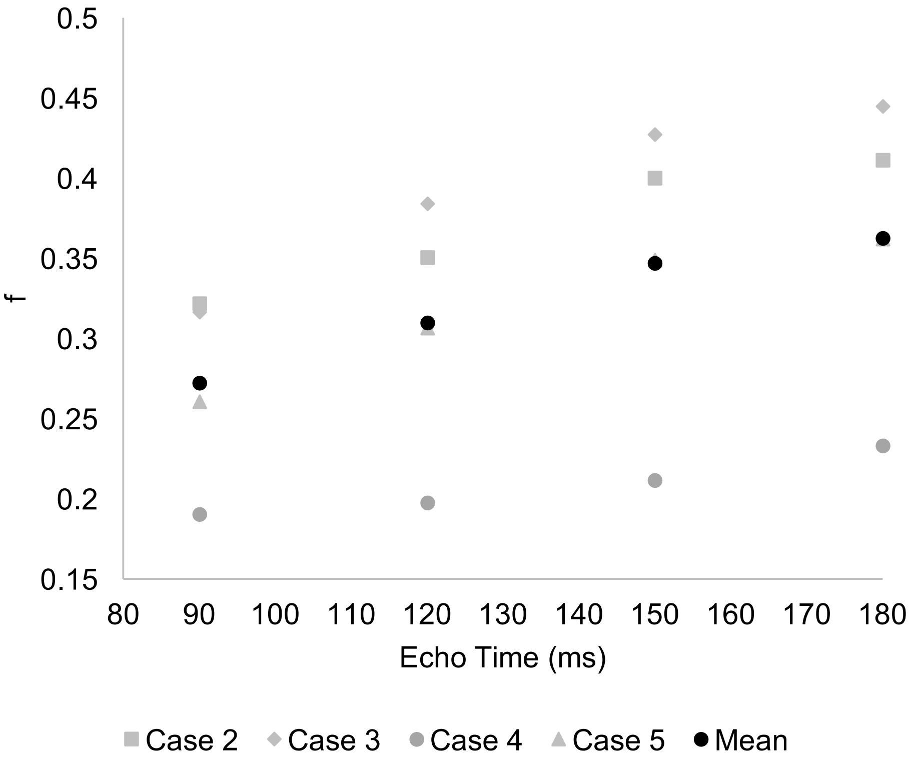

Figure 56; Graph showing increase in vascular fraction (*f*) with increasing echo time (ms) for each case, and the mean. *f* increases with echo time in every case.

7.5 The DECIDE Model fit in the placenta dataset

The three model fits were then applied to the whole placenta dataset (n=5). Figure 57 shows parametric maps for one representative 2D slice of one of the placenta data sets, showing vascular fraction (*f*), pseudodiffusion coefficient (*d**) and non-vascular blood fraction (ν) for the IVIM, T2-IVIM and DECIDE model fits. When T2 relaxation times were used in the fit, T2 of blood was set at 240ms, and T2 tissue at 46ms (in line with the values for blood and tissue in the literature).

The vascular fraction maps had a lobular appearance, suggestive of the lobular pattern of fetal placental perfusion. This became less apparent in the T2-IVIM model, with an increase in *f* over the whole placenta. In the DECIDE model the lobular appearance was once again clear. There was a higher non-vascular blood fraction (ν) than was seen in the liver dataset.

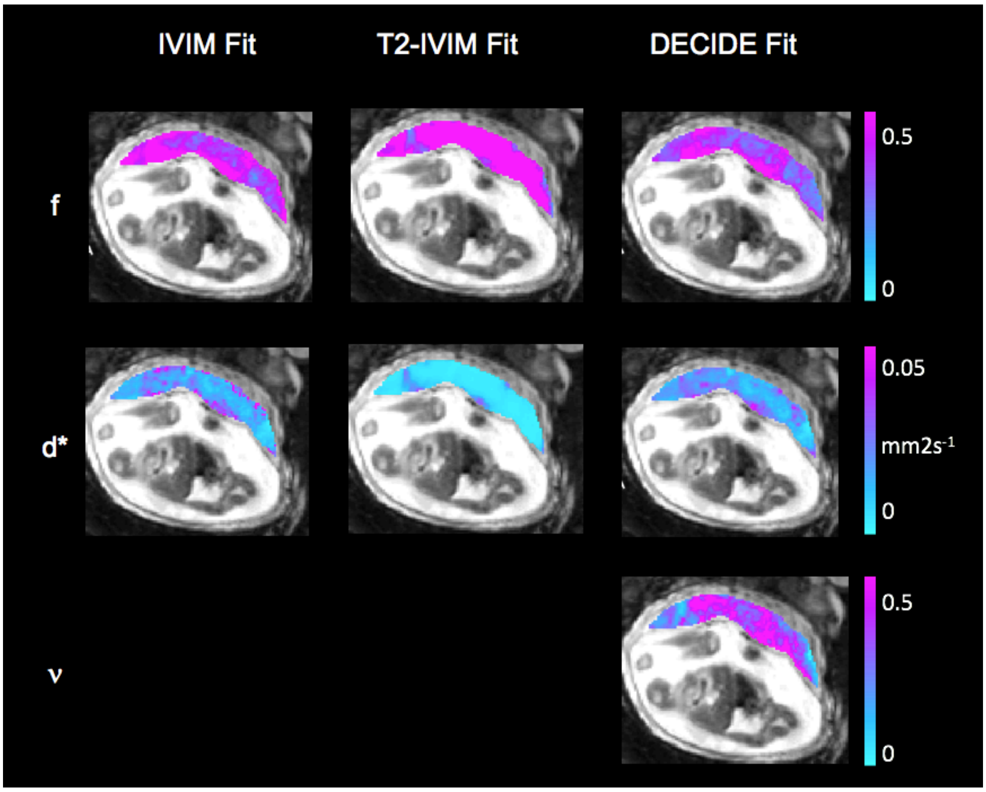

Figure 57; Parametric maps for one example 2D slice of one placenta dataset. The data shown is from case 3. Columns show the different fits: column 1; IVIM fit, column 2; T2-IVIM fit, column 3; DECIDE fit. Rows show parameter maps: row 1; vascular fraction (*f*), row 2; pseudo-perfusion (*d**), row 3; slowly perfusion non-vascular blood fraction (ν).

Conclusion; The DECIDE Model fit in the placenta dataset

The DECIDE model fit was feasible in the human placenta. The non-vascular blood fraction parameter (ν) was high in the placenta.

7.6 Addition of T2 Relaxometry to the fit in the placenta dataset

Figure 58 shows histograms of the voxel by voxel placental fit. The mean diffusion coefficient over the whole data set was $1.7\text{x}10^{-3}$ ($\pm 9.8\text{x}10^{-5}$)mm^2s^{-1}.

Table 20 shows the mean and standard deviation for the other parameter (*f*, *d** and ν) over the whole placental dataset. Adding T2 fit to the IVIM model increased the value of *f* throughout the dataset, and also increased the spread of values, whereas the DECIDE model decreased *f* to 75% of the original value.

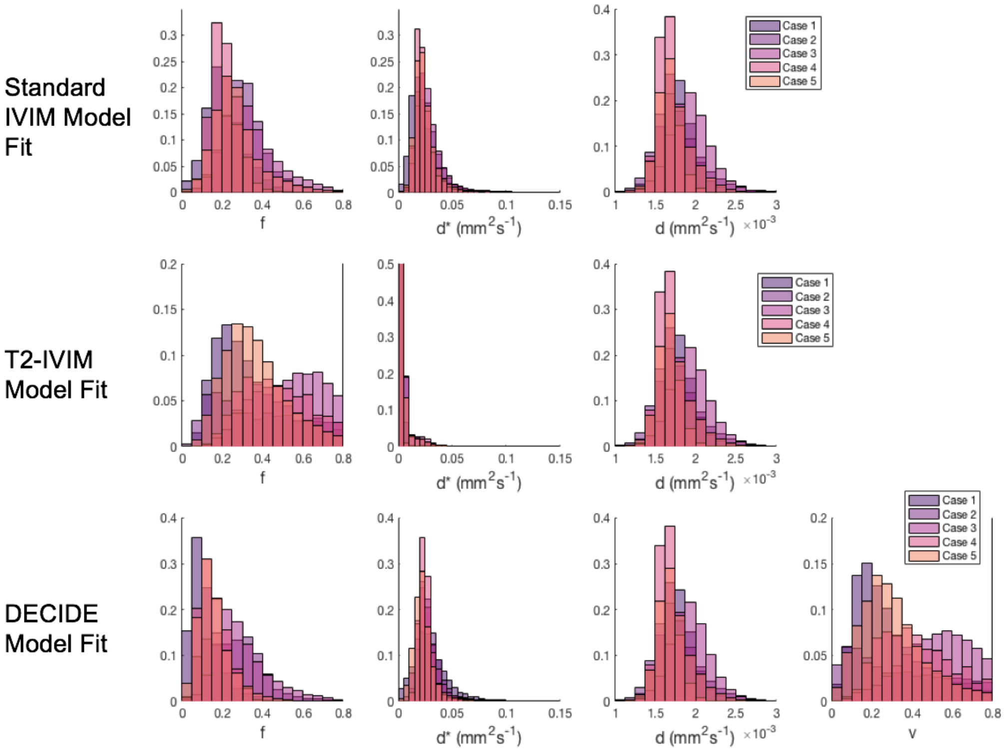

Figure 58; Voxel-wise whole placenta parameter histograms for the five datasets, showing *f*, *d and *d* for each fit, and ν for the DECIDE Fit.** Row one; IVIM fit, row 2; T2-IVIM fit, row 3; DECIDE fit.

	IVIM Fit (mean±SD)	T2-IVIM Fit (mean±SD)	DECIDE Fit (mean±SD)
f (%)	0.27 (0.06)	0.47 (0.16)	0.20 (0.08)
*d** (mm^2s^{-1})	0.032 (0.003)	0.047 (0.002)	0.028 (0.004)
ν (%)			0.45 (0.18)

Table 20; Table showing mean and standard deviation for the voxel-by-voxel fit for each parameters (*f*, *d and ν) for each model fit over the whole placenta data set (n=5).**

Conclusion; Addition of T2 Relaxometry to the fit in the placenta dataset

Adding T2 relaxation time to the model fit increased the vascular fraction (*f*) in the T2-IVIM model of placental perfusion, but reduced the vascular fraction (*f*) in the DECIDE model of placental perfusion.

7.7 Fitting T2 relaxation times in the retro-placental myometrium

We considered that pre-selecting and fixing T2 values based on figures for adult blood and abdominal tissue taken from the literature may not be accurate for placental data fitting. Fetal blood is different from adult blood, having higher concentrations of fetal haemoglobin, higher oxygen affinity, larger erythrocytes and less viscous plasma. The haematocrit is higher, and fetal oxygen saturations are lower compared to adult saturations, both of which are known to change blood T2 relaxation times[185]. Maternal blood values may also be different from average adult values, as pregnant women often have lower haematocrit due to the physiological dilution of blood associated with pregnancy. Therefore fixing non-physiological T2 values would bias the results of the model.

The T2 relaxation time of maternal blood was investigated by segmenting an area of interest within the retro-placental myometrium. Two cases were excluded due to movement; the thin depth of the myometrium meant small motion artefact moved the area of interest enough to cover areas of placenta or abdomen, and therefore made the results inaccurate. This left 3 cases to investigate (case 1,3 and 5). The IVIM and T2-IVIM models were then applied, but instead of fixing T2 values for blood and myometrium, the T2 relaxation times were fitted as additional parameters. The previously used estimations were applied to initiate the average signal curve fit (240ms for T2 blood (T2b) and 46ms for T2 myometrium (T2t)). The estimated parameters were then used to initiate the voxel wise fit. Both T2 relaxation times were constrained to values between 0 and 1000ms.

Figure 59 shows representative parametric maps for each included case. The myometrium is highly vascular in pregnancy, as shown by the high vascular fraction (*f*) in all cases. Figure 60 shows histograms for the voxel-wise fit for the myometrial area of interest. The vascular fraction decreased slightly when T2 relaxation was added to the model, but remained high. The mean value of *f* using the T2-IVIM model was 0.43 (±0.02) (Table 21). Mean maternal blood relaxation time was 230 (±34) ms, and mean myometrial T2 relaxation time was 136 (±21) ms.

Conclusion; Fitting T2 relaxation times in the retro-placental myometrium

Fitting the T2-IVIM model was feasible in the retro-placenta myometrium, although imaging was sensitive to motion artefact. The retroplacental myometrium had a high vascular fraction (*f*). Mean maternal blood relaxation time was 230 (±34) ms, and mean myometrial T2 relaxation time was 136 (±21) ms.

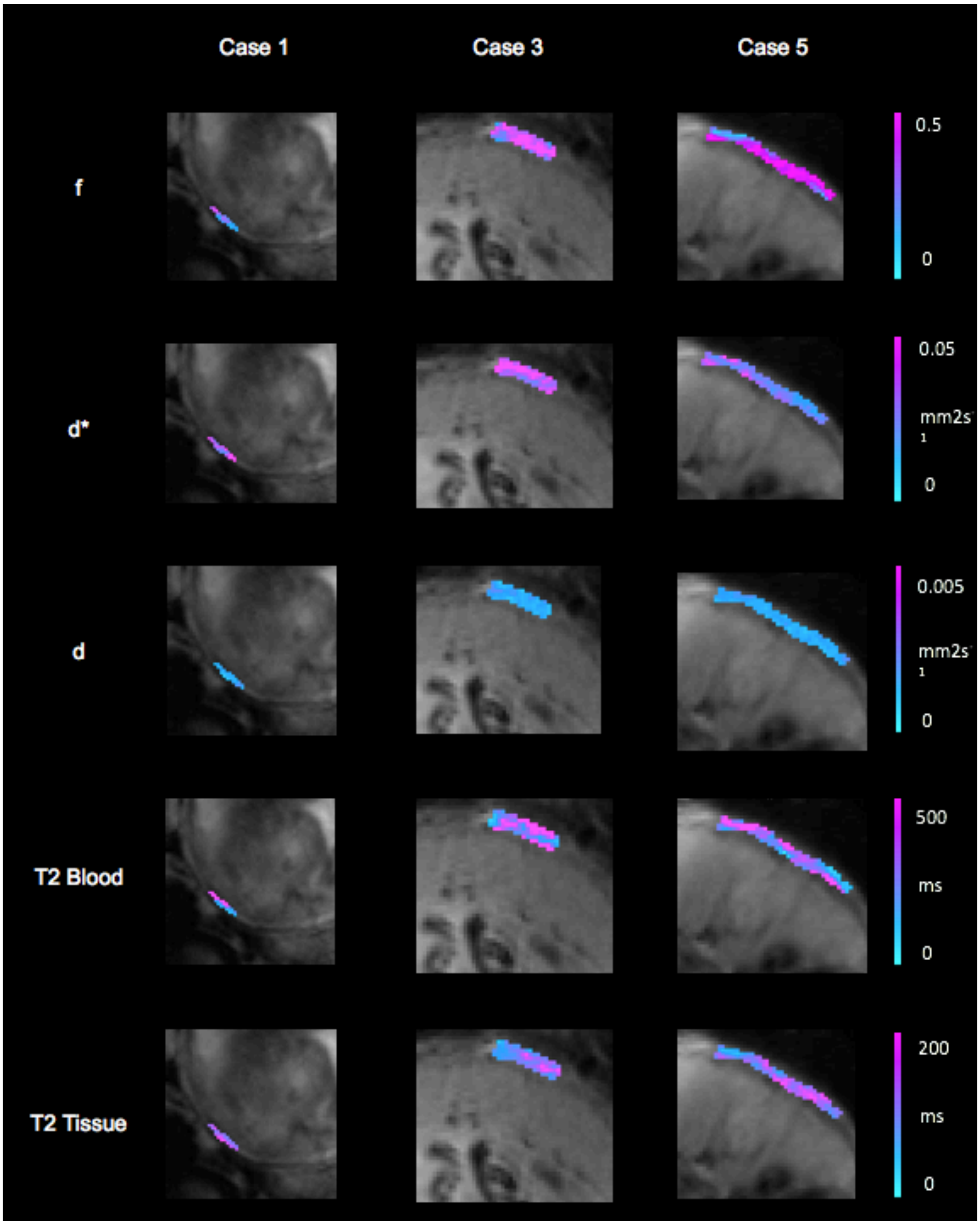

Figure 59; Parametric maps for the T2-IVIM fit on an example 2D slice for each included myometrium case. Note the thinness of the myometrium, making it more sensitive to motion. Columns show cases. Rows show the parameters fitted: *f, d*, d*, T2 relaxation time of maternal blood (T2mb) and myometrium (T2t).

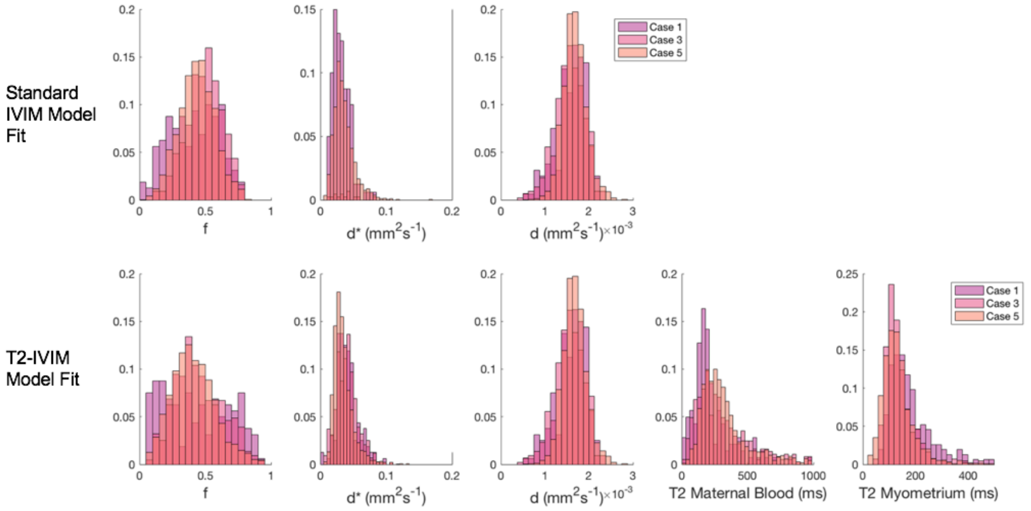

Figure 60; Voxel-wise myometrium area of interest parameter histograms for the three myometrium datasets. Row one; IVIM fit, row 2; T2-IVIM fit. *f*, *d** and *d* are shown for both models, and maternal blood and tissue T2 relaxation times for the T2-IVIM model.

	Case 1 mean (±SD)	Case 3 mean (±SD)	Case 5 mean (±SD)	Mean (±SD)
f	0.44 (0.03)	0.45 (0.2)	0.41 (0.2)	0.43 (0.02)
d*	0.044 (0.04)	0.041 (0.02)	0.035 (0.02)	0.040 (0.005)
T2 Maternal Blood	194 (111)	235 (127)	262 (104)	230 (34)
T2 Myometrium	183 (77)	138 (52)	138 (62)	153 (26)

Table 21; Table showing the mean (± standard deviation) for the voxel-by-voxel fit of *f*, *d, T2 maternal blood and T2 myometrium for each case using the T2-IVIM fit, and the mean (± standard deviation between means) of the three cases.** A normal distribution was fitted for *f*, and a gamma distribution for T2 relaxation data. The fit was constrained to positive values only, and T2 less than 500ms, to minimise the effect of noise.

7.8 Fitting T2 relaxation times in the placenta

The mean value for maternal blood T2 relaxation time, 230(±34) ms, is in accordance with the published value of 240ms. T2 relaxation time of maternal blood was therefore held fixed at 240ms. The tissue T2 relaxation time was kept fixed at 46ms. The DECIDE fit was then applied to the placenta dataset, allowing fetal blood T2 relaxation time to be fitted along with the other DECIDE parameters. The fit was initiated with a T2 relaxation time of 240ms. The average signal curve was fitted first, and the estimated values used to initiate the voxel wise fit. The T2 relaxation time of fetal blood was constrained between 0 and 1000ms.

Figure 61 compares the voxel-wise fit of the placenta using the DECIDE model with fixed fetal blood T2 relaxation times with fetal blood T2 relaxation time fitted. The spread of data for f and d^* were similar between the fits. The fit for ν appeared to have changed in case 3 when T2 was added, bringing it more in line with the other cases. This case had a T2 relaxation time for fetal blood of 305ms, which was higher than the others, and higher than would be expected when compared to normal T2 relaxation times for blood. The mean (±standard deviation) parameters are shown in Table 22 (excluding case 3). The mean T2 relaxation time of fetal blood was 205 (±38) ms.

Conclusion; Fitting T2 relaxation times in the placenta

It was feasible to fit T2 relaxation time of fetal blood in the human placenta. The mean T2 relaxation time of fetal blood was 205 (±38) ms.

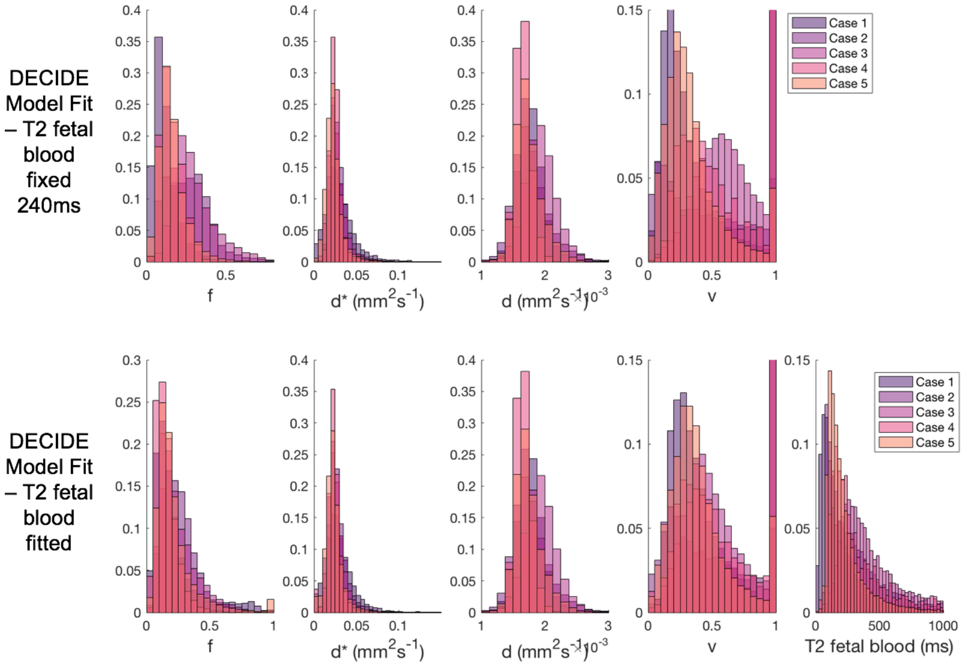

Figure 61; Voxel-wise whole placenta parameter histograms for the five placenta datasets. Row one shows *f*, *d** and ν for the DECIDE fit using fixed T2 values, of 240ms for fetal and maternal blood, and 46ms for tissue. Row 2 shows *f*, *d**, ν and T2 relaxation time of fetal blood for the DECIDE fit using fixed T2 values for maternal blood of 240ms, tissue 46m.

	DECIDE FIT	Case 1 mean (±SD)	Case 2 mean (±SD)	Case 3 mean (±SD)	Case 4 mean (±SD)	Case 5 mean (±SD)	Mean (±SD)
f	Fixed T2	0.12 (0.08)	0.26 (0.14)	0.30 (0.12)	0.16 (0.07)	0.16 (0.09)	0.20 (0.16)
	Fitted T2	0.22 (0.19)	0.25 (0.13)	0.24 (0.14)	0.15 (0.09)	0.22 (0.16)	0.21 (0.04)
d* (mm^{2}s^{-1})	Fixed T2	0.034 (0.04)	0.030 (0.02)	0.028 (0.02)	0.026 (0.01)	0.024 (0.02)	0.028 (0.004)
	Fitted T2	0.052 (0.08)	0.039 (0.06)	0.029 (0.03)	0.025 (0.02)	0.028 (0.04)	0.036 (0.01)
ν	Fixed T2	0.33 (0.24)	0.63 (0.37)	0.66 (0.25)	0.59 (0.30)	0.34 (0.22)	0.51 (0.16)
	Fitted T2	0.39 (0.22)	0.62 (0.35)	0.56 (0.26)	0.57 (0.29)	0.40 (0.23)	0.50 (0.12)
T2 Fetal Blood (ms)	Fitted Fetal T2	157 (113)	227 (121)	305 (107)	242 (107)	195 (90)	205 (38)

Table 22; Table showing the mean (±standard deviation) of the voxel-by-voxel fit for *f*, *d, ν and T2 relaxation time of the fast perfusing fluid fraction, representative of fetal blood T2, for each placental case, and the mean (±standard deviation).** Fixed T2 shows the DECIDE fit with T2 relaxation times fixed at 240ms for fetal and maternal blood, and 46ms for Tissue. Fitted Fetal T2 shows the DECIDE fit when maternal blood was set to 240ms, tissue to 46ms, and fetal blood was fitted as an additional parameter. Case 3 was excluded from the mean calculation, as the T2 relaxation time was an outlier.

7.9 Discussion

This work investigated a novel model for studying perfusion of the human placenta. The model combines the IVIM fit of diffusion weighted imaging with T2 relaxation, to divide the signal into three compartments. The model is unique because the placenta in unique – being perfused simultaneously by two (or more) individuals. There are therefore three compartments to consider, rather than two; the fetal vascular fraction (*f*), the maternal non-vascular blood fraction (ν), and the tissue.

The model was first investigated in non-pregnant healthy control liver, to reduce the need to image pregnant women. The IVIM fit gave a mean vascular fraction (*f*) of 0.33 (±0.03), compared to the T2-IVIM model which gave a mean vascular fraction (*f*) of 0.13 (±0.03). This decrease in vascular fraction to one third of the original value is comparable to that reported by Jerome et al[186] who found a mean liver vascular fraction of 0.28 (±0.06) with a standard IVIM fit, which fell to 0.18 (±0.07) when T2 was added to the fitting. Additional work (in the placenta) fitting the standard IVIM model to data acquired at different echo times further confirmed the effect of echo time on vascular fraction, showing an increase in vascular fraction of 33% when the acquisition echo time increased from 90 to 180ms. The reason for the change in vascular fraction with echo time is thought to be due to the difference in T2 relaxation time between blood and tissue, resulting in an over-estimation of the pseudo-diffusion fraction (*d**) when this is not taken into account by the model. When T2 relaxation time is added this over-estimation is corrected, and the vascular fraction decreases[186].

The DECIDE model fit in the liver gave a similar vascular fraction to the T2-IVIM fit (mean f = 0.12 (±0.02)), and a low non-vascular blood fraction (mean ν = 0.09 (±0.04)). The low value for ν is expected as this fluid pool is not relevant to the human liver (with gallbladder excluded). This data showed the model fit to be feasible, and results to be consistent with previous results in the literature, and those expected biologically.

The model was then applied to a heterogeneous placental imaging dataset, comprising of cases of complicated twin pregnancy, who were having clinically indicated fetal MR imaging of the brain. This dataset was not ideal, but was chosen as the women were already being exposed to MRI for clinical purposes, and the research added minimal time to their scan. The data was thought to be sufficient to investigate and develop the model.

The mean placental diffusion coefficient (d) in the placenta was $1.7\text{x}10^{-3}$ ($\pm 9.8\ \text{x}10^{-5}$) mm^2s^{-1}, mean pseudo-diffusion coefficient (d^*) was 0.032 (±0.003) mm^2s^{-1}, and the mean vascular fraction (f) using the IVIM model was 0.27 (±0.06). These values are comparable with those reported in the literature (Table 23) [119,120,128,187]. However, there is a larger degree of variability within reported values. This likely reflect different MR hardware, the different field strengths used, and the use of different echo times and maximum b-values in the acquisition, making it difficult to draw conclusions from this data.

Study	Field strength (Tesla)	Acquisition Echo Time (ms)	Mean reported *f* (±SD if reported) (%)	Mean reported d* (mm^2s^{-1})	Mean reported d (mm^2s^{-1} x 10^{-3})
Gowland et al 2000[119]	0.5	115	26(±6)	57±041 x 10^{-3}	1.7±0.5
Moore et al 2000[120]	0.5	NR	25(±8) fetal side 35(±11) maternal side	NR	1.7±0.9 fetal side 1.4±0.8 maternal side
Derwig et al 2013[128]	1.5	140	36.2	NR	NR
Siauve et al 2017[187]	1.5	87	42.55(±9.3)	NR	2.4±0.3

Table 23; Table of human placenta IVIM studies in the literature. This shows the MR field strength and echo times used, and the *f, d** and *d* reported. NR = not reported. Moore et al[120] used ROI dividing the placenta in half – the half closest to the fetus including chorionic plate (fetal side), and the half closest to the mother (maternal side), including basal plate.

The T2-IVIM model fit gave a mean vascular fraction (*f*) of 0.47 (±0.16). This is interesting as adding T2 relaxation time to the model fit in the liver dataset decreased the vascular fraction, for reasons described above. The reason this was not the case in placenta may be that the T2-IVIM model is not biologically relevant to the placenta. The T2 relaxation time of the second compartment in this two-compartment model was fixed at 46ms. As this compartment comprises not only of tissue but also maternal blood, with high T2 value, the model may have compensated for the forced low T2 value in the second compartment by increasing the vascular fraction in the first. This suggests this model is not satisfactory to describe placental perfusion.

When the DECIDE model was fitted, separating the second compartment in two, providing a high T2 relaxation non-vascular blood compartment and a tissue compartment, the mean vascular fraction fell to 0.20 (±0.08). This is 70% of the original IVIM vascular fraction, and in keeping with the fall in vascular fraction seen in the liver[188]. The mean non-vascular blood fraction (ν) was 0.45 (±0.18), much higher than the value seen in the liver, and larger than the fetal vascular fraction, suggesting this is estimating a separate, extra-vascular blood compartment.

Previous work in the literature has gone beyond adding fixed T2 relaxation time values to the IVIM fit, to fitting the T2 relaxation values simultaneously[186]. This has the advantage of allowing for biological variation between subjects, as well as removing any bias caused by inaccuracy in previous T2 relaxation time estimations. When applying this free fit to liver data, Jerome et al[186] found a mean liver T2 relaxation time of 42(±7)ms, comparable to values in the literature[179], and a mean blood T2 relaxation time of 78 (±30)ms. This is notably shorter than the 240-290ms described in the literature[179,180]. They suggest this divergence from literature values may be due to difficulties in estimating blood T2 values *in vivo*, or may reflect phenomena, such as water exchange, which are not accounted for by the IVIM model.

The ideal DECIDE model would fit the three relevant T2 relaxation times – fetal blood, maternal blood and tissue. However, fitting six parameters would require excellent signal to noise ratio, and is not currently feasible with this data set. Maternal blood T2 relaxation time was therefore investigated first, using the retroplacental myometrium. This was chosen as it simplified the model, only needing to fit two compartments. In addition, this is likely to be a relevant tissue in investigating fetal pathology, as differences in spiral artery perfusion are known to be an important factor in the pathology of fetal growth restriction. The T2-IVIM model was used, with free fitting of both maternal blood and tissue T2 relaxation time, in addition to *f* and *d**. This gave a mean blood T2 relaxation time of 230 (±34)ms, and a mean tissue T2 relaxation time of 153 (±26)ms. Unlike Jerome et al[186], the relaxation time for blood is consistent with previous estimations in the literature. The T2 relaxation time for the myometrium is also consistent with the value reported in the literature (117 (±14)ms[189]).

The DECIDE model was then re-fitted in the placenta. As the mean maternal blood T2 relaxation time was consistent with literature value of 240ms, this was kept fixed at 240ms. Tissue T2 was also kept fixed, at 46ms. The fetal blood T2 was fitted as an additional parameter. This gave a mean fetal blood T2 relaxation time of 205 (±38)ms.

The T2 relaxation time for fetal and maternal blood are close, and given the standard deviation it is not possible to draw definite conclusions. However, there is a biologically plausible explanation for why the T2 relaxation time of fetal blood may be lower than the T2 relaxation time of maternal blood. T2 relaxation time is known to be affected by oxygen saturation, and fetal blood is known to be less saturated than adult blood[190,191]. As oxygen saturation increases, T2 relaxation time lengthens[185]. So it is plausible that the T2 relaxation time of fetal blood will be shorter than that of adult blood. The range of fetal blood T2 relaxation time was 157-241ms, which using the correlation of T2 relaxation time to blood oxygenation in umbilical artery blood, published by Portnoy et al[185] (Figure 62), would correlate to fetal oxygen saturations of 75-100%, with a mean of 92%. These values are higher than literature values for fetal oxygen saturation, estimated to be 65% in the umbilical artery, and 85% in the umbilical vein, at 30 weeks gestational age[190]. It is difficult to draw firm conclusions, given the heterogeneity of the data set used, with some placentas supporting two twins, and some placentas supporting one twin, following demise of one twin. This is an area that needs further investigation.

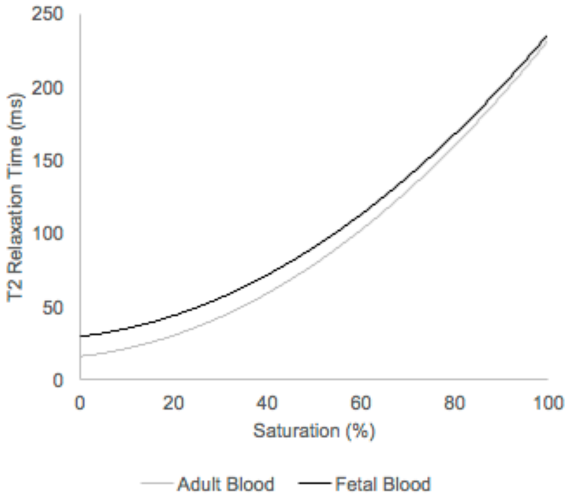

Figure 62; Plot of T2 as a function of blood oxygen saturation for umbilical cord and adult blood, generated at a haematocrit of 0.47. Data derived from Portnoy et al[185].

There was one outlier when fitting fetal T2 relaxation time, as case 3 had a mean T2 relaxation time of 305ms. When the histogram of the fit was examined, this was found to be because a larger proportion of voxels were attributed a T2 relaxation time of 1000ms when compared to the other data sets. There was no excess motion in the imaging, and the pregnancy continued normally so there is no biological explanation for this. Values of 1000ms for T2 relaxation time are unlikely to represent biological signal, so are most likely due to a problem with the imaging or fitting. It is possible the SNR was not sufficient to model the four parameters simultaneously.

The addition of fetal blood T2 relaxation time to the DECIDE model fit did not alter the mean vascular fraction (*f*), however it had different effects on *f* in different cases. When the fitted fetal blood T2 relaxation time was greater than 240ms, the previous fixed blood T2 relaxation time, the vascular fraction decreased, and when the fitted T2 relaxation time was less than 240ms the vascular fraction increased. This is in keeping with the previously discussed theory, which suggests that when T2 relaxation time is over-estimated the vascular fraction is over-estimated, and when T2 relaxation time is under-estimated the vascular fraction is under-estimated by the model. The mean non-vascular blood fraction (ν) remained stable.

All mathematical models of complex biological tissue have limitations, and only go some way to explaining the complexity of the system[186]. In MRI model fitting, attempting to fit too many parameters will lead to over fitting, and the possibility of covariant parameters[186]. In addition, the data may not have sufficient signal to noise ratio to allow multiple parameters to be simultaneously fitted. Conversely, fitting insufficient parameters will cause bias in the parameters that are fitted, which may be difficult to understand[186]. Ideally parameters should also be sensitive to detect change that is present, reproducible between subjects and sites, enabling change over time and between subjects to be investigated, and have biologically plausible behavior suggesting they are biomarkers of the physiology or pathology under investigation[192].

The DECIDE model is an attempt to model complex placental perfusion. It is limited by its inability to model the complex transfer of oxygen and water between compartments. It also simplifies complex maternal and fetal perfusion into two compartments, whereas in reality there is both faster and slower moving blood pools in both the fetal and maternal compartments. It is also difficult to validate the signals, and to know if the vascular fraction and non-vascular blood fraction truly represent fetal and maternal perfusion. Possible validation tools include correlation with uterine and umbilical artery Doppler studies, which are the current gold standard of clinical placental assessment[40], although this is limited in only measuring blood flow up stream, or by *ex vivo* histological or micro-CT examination of the fetal microcirculation, but this is limited as it is separated from *in vivo* imaging by time, and it is not possible to measure maternal perfusion[193].

Assuming the model is biologically relevant it would be ideal to fit seven parameters simultaneously – *f, d*, d*, ν, and the T2 relaxation times of fetal and maternal blood, and tissue. This is not feasible with the SNR of the current data. This may be improved in the future by performing more repetitions in image acquisition, but this is at the expense of time, and clinical imaging time constraints along with maternal comfort limits the possible scanning time. This would also increase the intra-slice motion, making analysis more challenging. Using digital, rather than analogue coils, or increasing the field strength to 3T may help in the future[95].

If constrained to choosing one T2 relaxation time to fit, fetal blood T2 relaxation time is the most important to fit. This is because it is likely to have the most pathologically relevant variability. Fetuses with a poorly functioning placenta are known to develop hypoxia[194]. Fitting the fetal blood relaxation time may therefore not only improve the model fit, but also provide additional, clinically useful information, on how poorly the placenta is functioning.

This chapter investigates the DECIDE model for placental perfusion, presenting a novel three compartment model that is both biologically relevant, and has the advantage of joint modelling IVIM and T2 relaxometry. Perfusion imaging of the placenta with MR may allow a deeper understanding of significant fetal pathologies such as early and late onset fetal growth restriction, and complications of twin pregnancies. It may also prove to be diagnostically beneficial, helping to guide clinicians in the best treatment or timing of delivery in pathological pregnancies.

In conclusion, this work develops a novel model for fitting multiparametric MRI of the human placenta. The DECIDE model fits the vascular fraction (*f*), pseudo-diffusion coefficient (*d**), non-vascular blood fraction (ν), and fetal blood T2 relaxation time (T2fb), whilst using fixed T2 relaxation values of maternal blood (T2fm = 240ms) and tissue (T2t = 46ms), and a diffusion coefficient derived from an initiating standard ADC fit of the data.

In the next chapter I use this model to investigate placental perfusion in a cohort of normal, singleton pregnancies.

8 Investigating Multi-Compartment Myometrial and Placental Perfusion and Fetal Blood Saturation Modelling in Normal Pregnancy

8.1 Summary

In this chapter I apply the optimised DECIDE model to a cohort of normal, singleton pregnancies, to investigate normal placental perfusion. I present data on normal values for myometrial *f*, *d**, and T2 of maternal blood and myometrium. I also present the normal values for placental *f*, *d**, ν and T2 of fetal blood. I go on to investigate placental perfusion, examining how the signals for *f* and ν change with depth through the placenta.

I also investigate two novel parameters of placental function:

- The maternal-fetal perfusion ratio, which examines matching of fetal and maternal blood throughout the placenta, on a voxel wise basis.
- Fetal blood oxygen saturation measured throughout the placenta, presenting values for the mean placental fetal blood oxygen saturation in normal pregnancy.

This work has been submitted and is under review for the MICCAI 2018 conference.

8.2 Ultrasound parameters for normal cases

Seven women with uncomplicated pregnancy were recruited and gave informed written consent for placental MRI. The gestational age at the time of MRI, and the results of the growth ultrasound scan and the birth weight are shown in Table 24. All participants had an ultrasound scan within one week of the MRI scan. All measured parameters were normal, except in case 5, where uterine artery Doppler PI was greater than the 99th centile.

The MRI data was registered and segmented. In case 7 there was excess placental motion, due to fetal movement distorting the uterus. This case had to be excluded from further analysis. In all other cases the registration compensated adequately for movement in the placenta, so six cases were included for analysis.

However, for segmentation of the myometrium, a thin area of tissue, motion was too large in two further cases therefore case 1 and 6 were also excluded from myometrial analysis, leaving 4 cases to investigate.

Case	Gestational age at MRI (weeks + days)	Estimated Fetal Weight in grams (percentile)	Umbilical artery Doppler PI (percentile)	MCA Doppler PI (percentile)	CPR (percentile)	Right uterine artery Doppler PI	Left uterine artery Doppler PI	Average Uterine artery PI (percentile)	Birth Weight in grams (percentile)
1*	29+1	1389 (83)	1.2 (64)	1.53 (8)	1.28 (4)	0.64	0.66	0.65 (17)	3240 (43)
2	31+3	2208 (100)	0.94 (41)	1.71 (21)	1.82 (25)	MD	MD	MD	3660 (62)
3	28+4	1237 (41)	0.91 (27)	2.22 (66)	2.44 (78)	MD	MD	MD	3487 (29)
4	34+0	2384 (75)	1.06 (64)	2.21 (80)	2.08 (46)	0.7	0.53	0.615 (25)	3724 (68)
5	28+5	1240 (63)	0.93 (29)	1.85 (28)	1.99 (43)	1.04	3.58	2.31 (>99)	MD
6*	31+1	1573 (27)	1.12 (64)	1.42 (5)	1.26 (4)	0.86	0.64	0.79 (49)	2855 (32)
7*^	25+1	798 (54)	1.41 (71)	1.94 (44)	1.37 (13)	0.89	0.90	0.90 (50)	4260 (92)

Table 24; Table showing the gestational age of each control case at MRI, the results of their most recent ultrasound scan, and the birth weight and centile. All parameters are normal, except case 5 who had increase pulsatility index (PI) in the uterine arteries. MD = missing data. CPR = cerebroplacental ratio. Case with ^ (7) excluded from placental analysis, and cases with * (1, 6 and 7) excluded from myometrial analysis, due to excessive motion.

8.3 Normal Myometrial MRI Parameters

Myometrial parameter maps for the four included myometrial cases are shown in Figure 63. *f* was high in the myometrium, which is expected given that this is a highly vascular tissue in pregnancy, delivering maternal blood to the placenta via the remodeled, dilated spiral arteries.

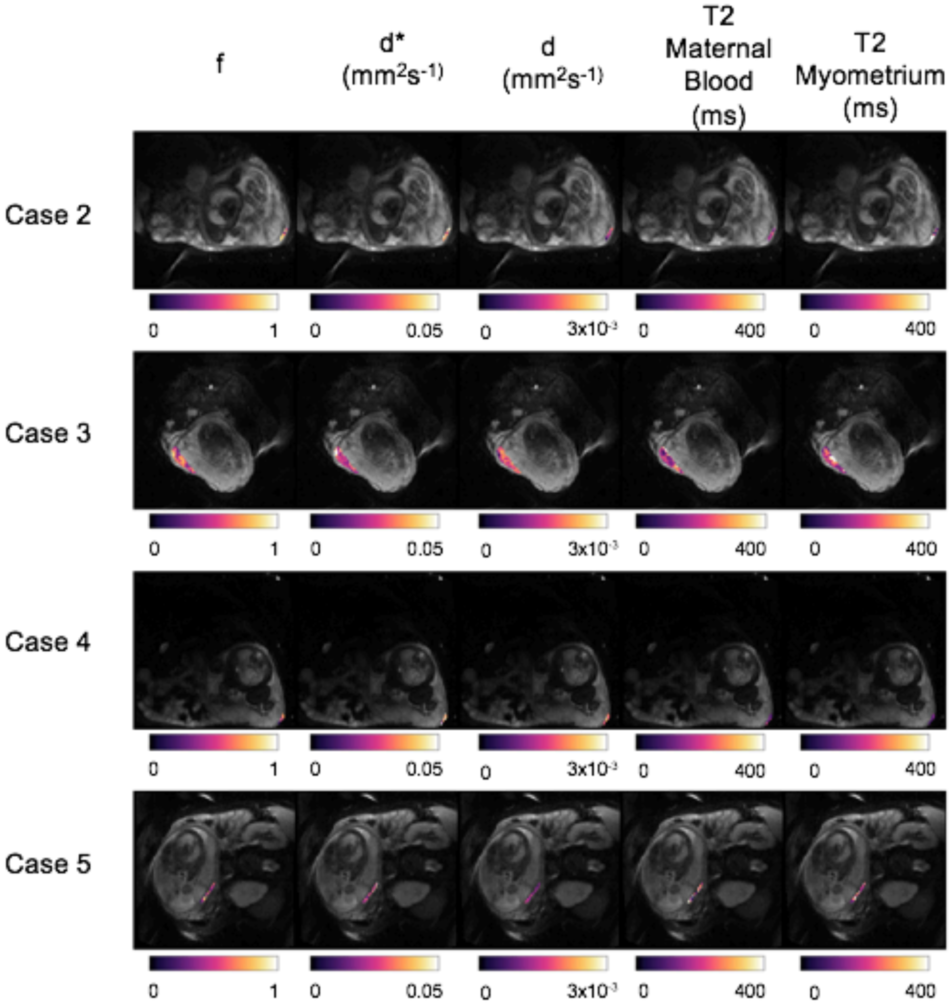

Figure 63; Parametric maps for the T2-IVIM fit for one slice from the 4 cases where myometrial analysis was feasible. Rows show cases, columns show parameter maps, from left to right, f, d*, d, T2 maternal blood and T2 myometrium.

Figure 64 shows histograms of the fit for each myometrial case for each parameter, using the Standard IVIM model, and the T2-IVIM model. Table 25 shows a comparison of the mean (±standard deviation) for each parameter for the standard IVIM fit, and the T2-IVIM fit for the myometrium. *f and d** were comparable between the two fits. The mean T2 relaxation time of maternal blood was 202 (±93) ms. This is comparable with the value in the previous chapter and in the literature. The mean myometrial T2 relaxation time was 124(±7) ms, in keeping with the literature value (117 (±14) ms[189]).

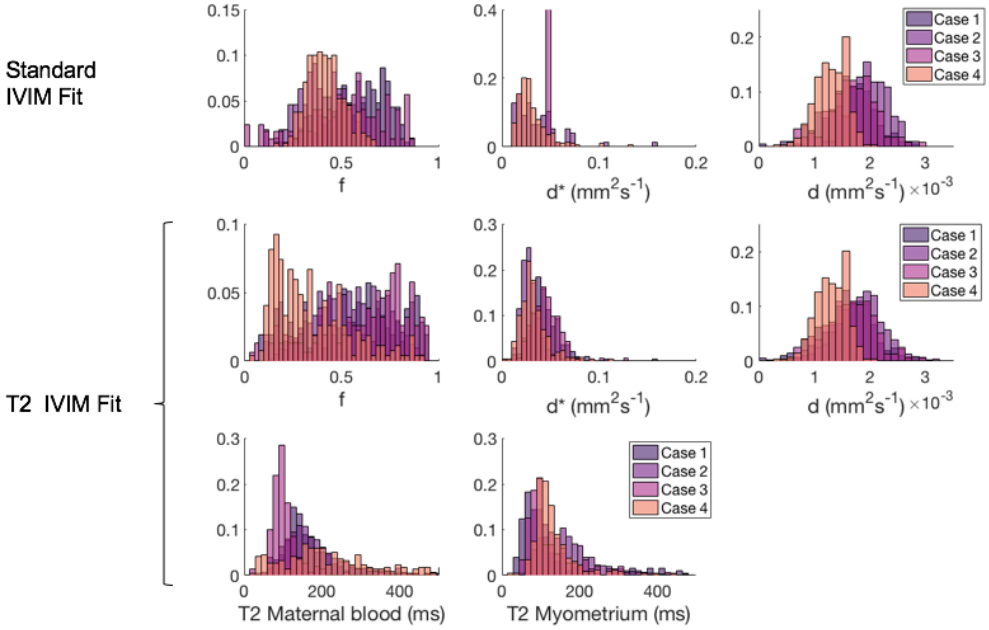

Figure 64; Histograms for the voxel-wise fit, for the four normal myometrial datasets. Row one shows f, d* and d for the Standard IVIM fit. Row 2 and 3 shows f, d*, d and T2 relaxation time of maternal blood and myometrium for the T2-IVIM fit.

	Standard IVIM fit Mean (±STD)	T2-IVIM Fit Mean (±STD)
f	0.48 (0.087)	0.44 (0.14)
d* (mm^2s^{-1})	0.051 (0.013)	0.044 (0.008)
d (mm^2s^{-1})	0.0016 (0.0003)	0.0016 (0.0003)
T2 Maternal Blood (ms)		202 (93)
T2 Myometrium (ms)		124 (7)

Table 25; Mean (±standard deviation) of voxel-wise fit for each parameter (f and d*) using the standard IVIM and the T2-IVIM model, and T2 relaxation time of maternal blood and myometrium using the T2-IVIM model. T2 relaxation times are consistent with values previously reported in the literature (T2 relaxation time of blood 240ms, and of myometrium 117ms).

Conclusion; Normal Myometrial MRI Parameters

Retro-placental myometrial T2-IVIM model fit was feasible in 4 of 7 normal cases. *f* was high in the normal myometrium.

8.4 Normal Placenta MRI Parameters

Placenta parameter maps of example slices for the six included cases are shown in Figure 66. *f* and ν show a heterogeneous, lobulated pattern, as might be expected given the structure of the placenta.

Figure 65 shows histograms of the voxel-wise fit for each placenta case for each parameter, using the Standard IVIM model, and the DECIDE model. Table 26 shows a comparison of the mean (±standard deviation) for each parameter for the standard IVIM fit, and the DECIDE fit for the placenta. *f* is slightly lower using the DECIDE fit that the standard IVIM fit, in keeping with the results in the previous chapter. There was a high ν, showing a large third compartment within the normal placenta. The mean T2 relaxation time of fetal blood was 144 (±54) ms which is lower than the mean from the population in the previous chapter (205 (±38)) ms. The previous population was a very heterogeneous population, whereas the six normal datasets presented here are more similar, and show very similar distributions.

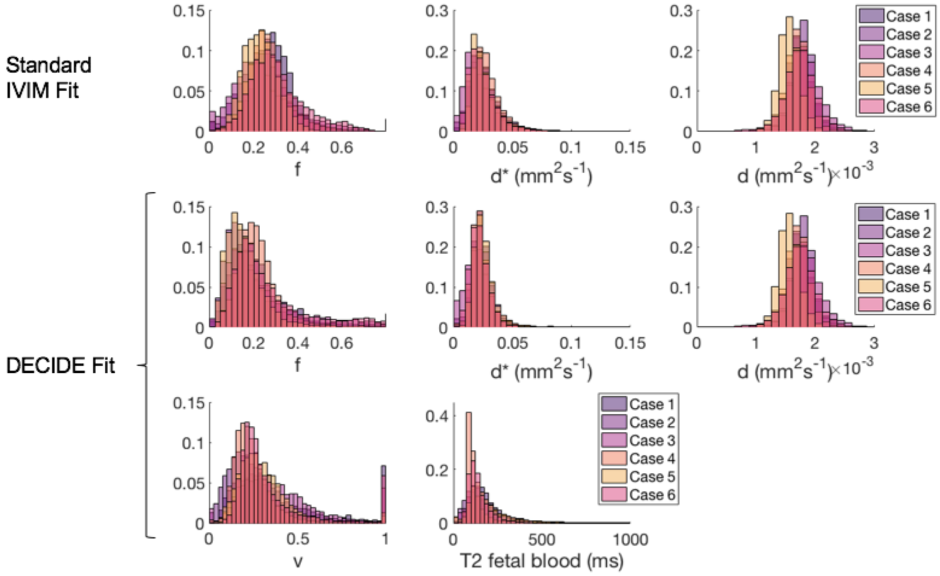

Figure 65; Voxel-wise whole placenta parameter histograms for the six normal placenta datasets. Row one shows f, d* and d for the Standard IVIM fit. Row 2 and 3 shows f, d*, d, ν and T2 relaxation time of fetal blood for the DECIDE fit. Note the close distribution of T2 relaxation time between cases.

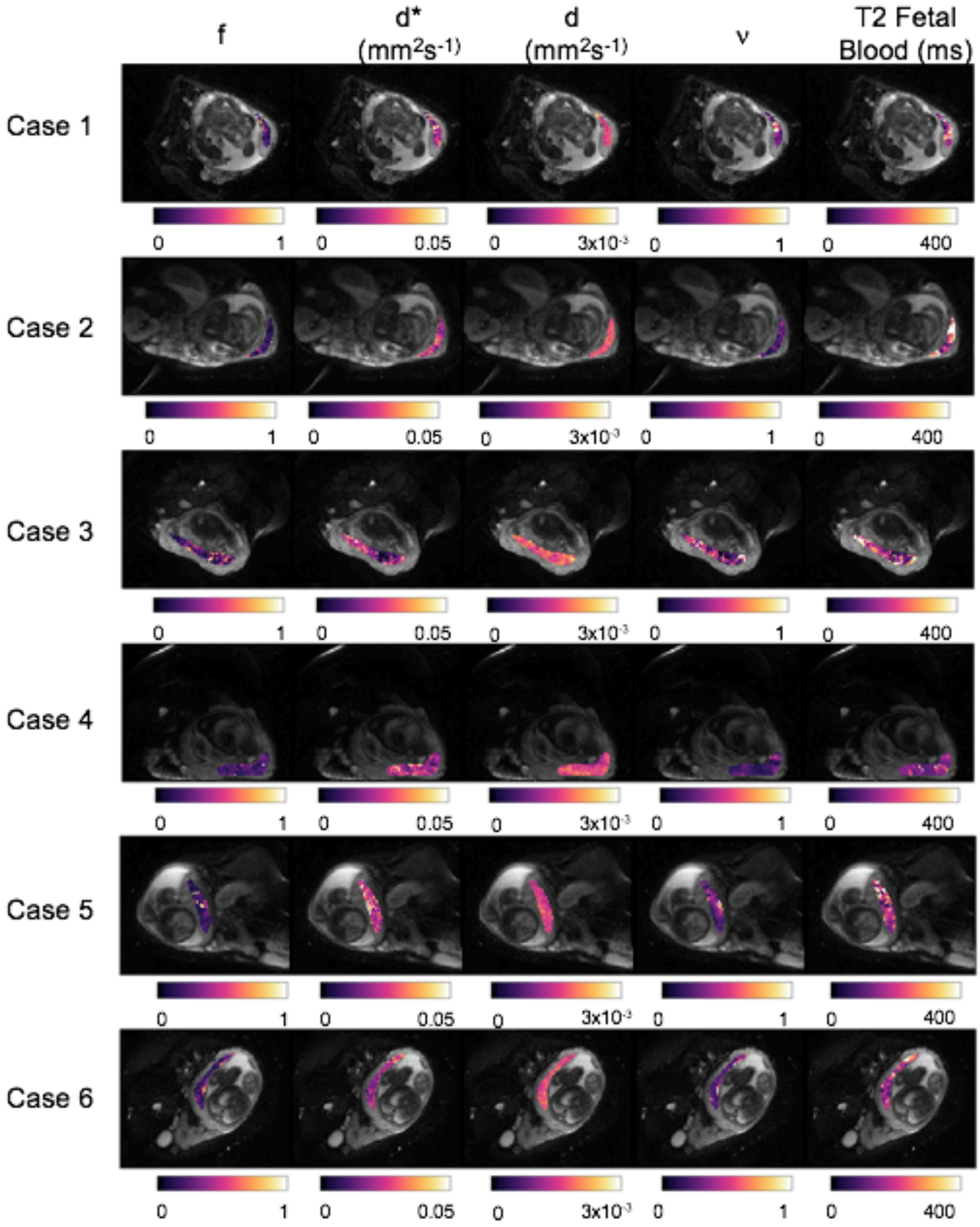

Figure 66; Parametric maps for the T2-IVIM fit for the 6 cases where placental analysis was feasible. Rows show cases, columns show parameter maps, from left to right, f, d*, d, ν, and T2 fetal blood.

	Standard IVIM fit Mean (±SD)	DECIDE Fit Mean (±SD)
f	0.27 (0.03)	0.23 (0.03)
d* (mm^2s^{-1})	0.034 (0.003)	0.028 (0.005)
d (mm^2s^{-1})	0.0017 (0.0001)	0.0017 (0.0001)
ν		0.32 (0.06)
T2 Fetal Blood (ms)		144 (54)

Table 26; Mean (±standard deviation) of voxel-wise fit for each parameter (f and d*) using the standard IVIM and the DECIDE model, and ν and T2 relaxation time of fetal blood with the DECIDE model. The placenta shows a significant third compartment (ν). Fetal blood T2 relaxation time is lower than the literature value for adult blood T2 (240ms).

Conclusion; Normal Placenta MRI Parameters

Placental DECIDE model fit was feasible in all 6 out of 7 normal cases. ν was high in the normal placenta. Mean T2 relaxation time of Fetal Blood was 144.89ms.

8.5 Maternal and Fetal perfusion variation with placental depth

To investigate how the parameters relating to fetal (*f*) and maternal (ν) perfusion varied with depth through the placenta, distance maps were created from the placenta masks. These took the basal plate to be zero, and normalised the distance to the chorionic plate on a scale of zero to ten. The mean and standard deviation of *f* and ν were then calculated in each of the ten strata for every placenta, and for every slice within each placental volume (Figure 67 shows results for *f*, Figure 68 shows results for ν).

There was no consistent pattern in variation of f nor ν with depth from the basal plate between cases. Instead the mean remained relatively stable with depth. There was however a large degree of standard deviation in the mean value. This is clearly seen in the slice-by-slice plots, where there appears to be a greater degree of variation between slices at any given depth, than there is between depth strata.

Conclusion; Maternal and Fetal perfusion variation with placental depth

This work found no difference in mean f or ν with depth from basal to chorionic plate.

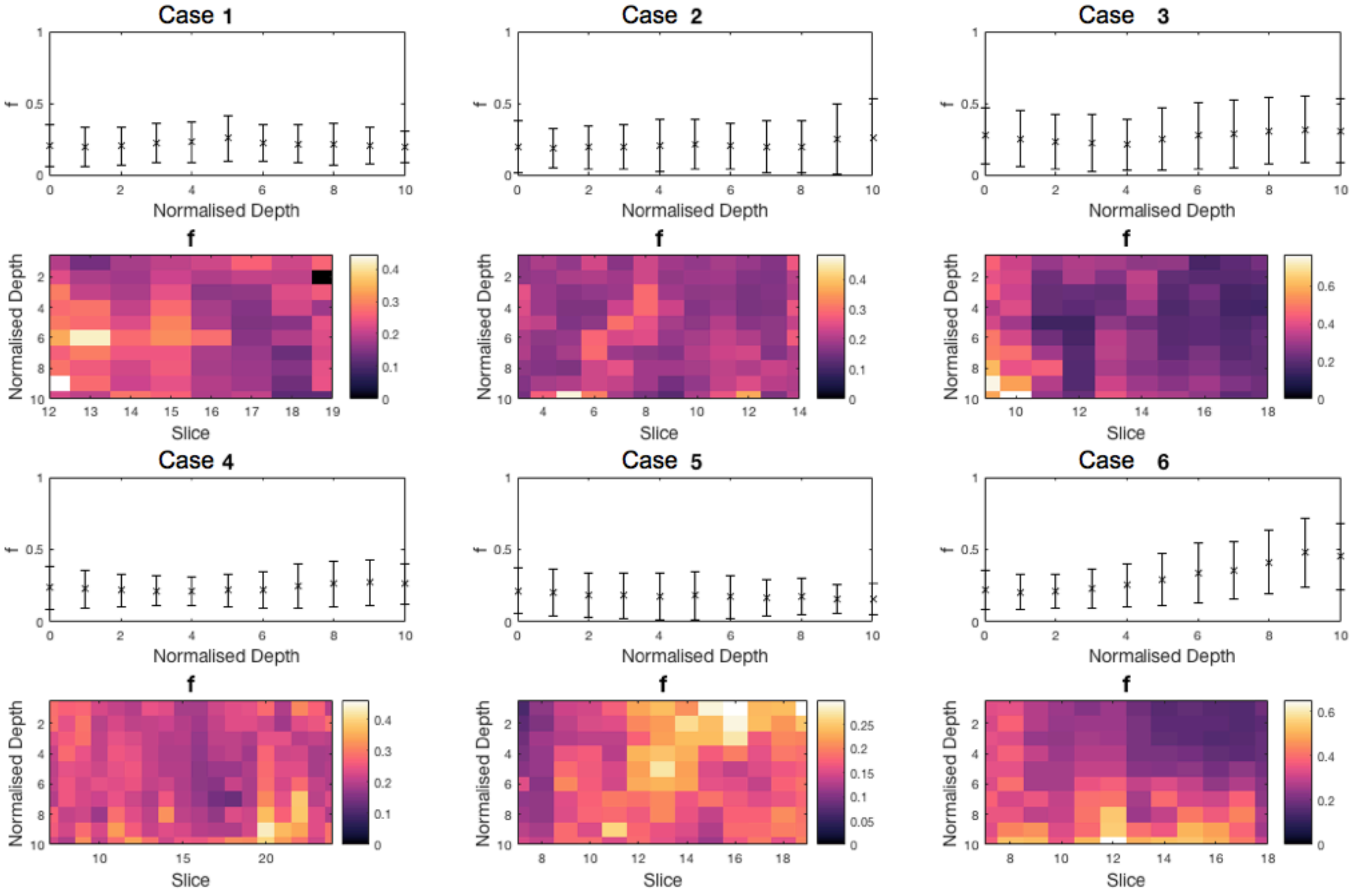

Figure 67; Graphs showing the variation in parameter f, relating to fetal placental perfusion, for every included placenta (case one to six). Rows one and three show the mean and standard deviation of f for the whole placenta with normalised depth from basal (0) to chorionic (10) surface. Rows two and four show the variation in f with depth from basal (0) to chorionic (10) surface for every slice within the placental volume.

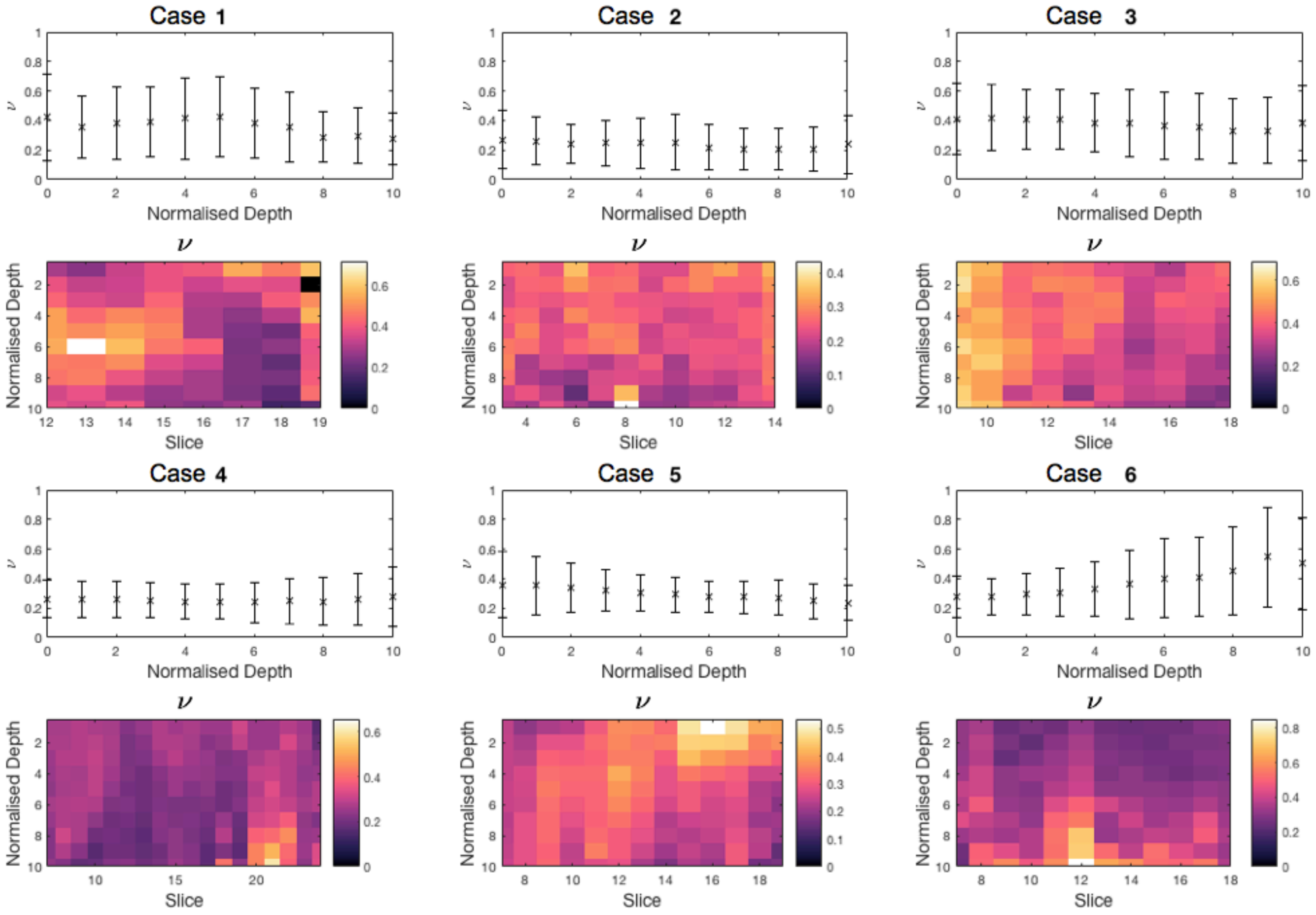

Figure 68; Graphs showing the variation in parameter ν, relating to fetal maternal perfusion, for every included placenta (case one to six). Rows one and three show the mean and standard deviation of ν for the whole placenta with normalised depth from basal (0) to chorionic (10) surface. Rows two and four show the variation in ν with depth from basal (0) to chorionic (10) surface for every slice within the placental volume.

8.6 Maternal-fetal perfusion ratio

It is possible that the fetoplacental perfusion is regulated to match maternal perfusion, via regulation of stem artery vasoconstriction. It is therefore interesting to be able to compare fetal and maternal perfusion throughout the placenta, to see if they match. To investigate the ratio of the fetal and maternal perfusion relating to perfusion over the whole placenta, the maternal-fetal perfusion ratio was calculated as:

$$\text{Maternal to fetal perfusion ratio} = \frac{\nu\,(1 - \mathrm{f})}{\mathrm{f}}$$

Maternal-fetal perfusion ratio

A histogram of the voxel wise fit of the maternal-fetal perfusion ratio in each case is shown in Figure 71. The cases show similar distributions, with the majority of voxels showing a ratio between 0.5 and 1.5 in all cases. There are however a few voxels where the ratio is higher than two, demonstrating to a much higher ν than *f*. The mean ratio for the six control cases was 1.16(±0.6).

Conclusion; Maternal-fetal perfusion ratio

Maternal-fetal perfusion ratio is a potential new biomarker of placental function. In a cohort of six normal placentas the mean Maternal-fetal perfusion ratio was 1.16.

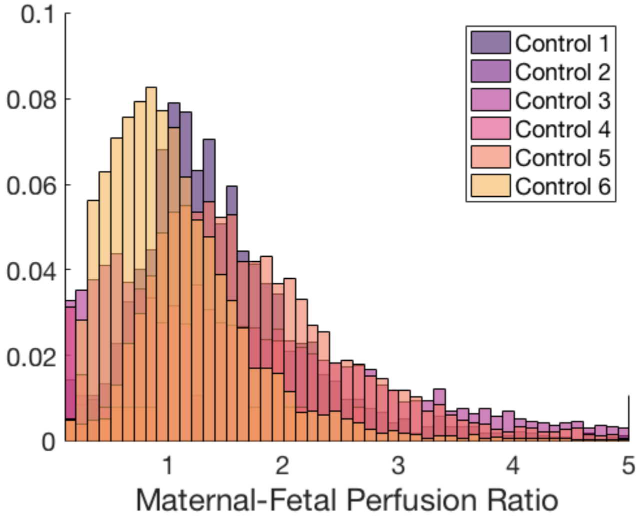

Figure 69; Histograms of voxel-wise fit of the maternal-fetal perfusion ratio for the six placenta datasets.

8.7 Fetal Blood Oxygen Saturation in Control Cases

Previous work reported in the literature has investigated fetal blood T2 relaxation time at different oxygen saturation levels[185]. An empirical curve was fitted (see Chapter 8, Figure 62), that estimates fetal blood oxygenation from blood T2 relaxation times (or vice versa) using the equation below.

$$T2 = \frac{\mathrm{a}}{(1+\mathrm{e}^{-\mathrm{b}(\mathrm{s}-\mathrm{c})})}$$

Relationship between fetal blood T2 relaxation time and blood oxygen saturation

Where *a*=386ms, *b*=0.36, *c*=0.88, and *s* is fractional saturation.

This equation was used to apply a voxel-wise fit of fetal blood saturation to the whole placenta in the six cases. Example slice parametric maps are shown for every case in Figure 70. These show a lobulated appearance, suggestive of heterogeneity throughput the placental tissue.

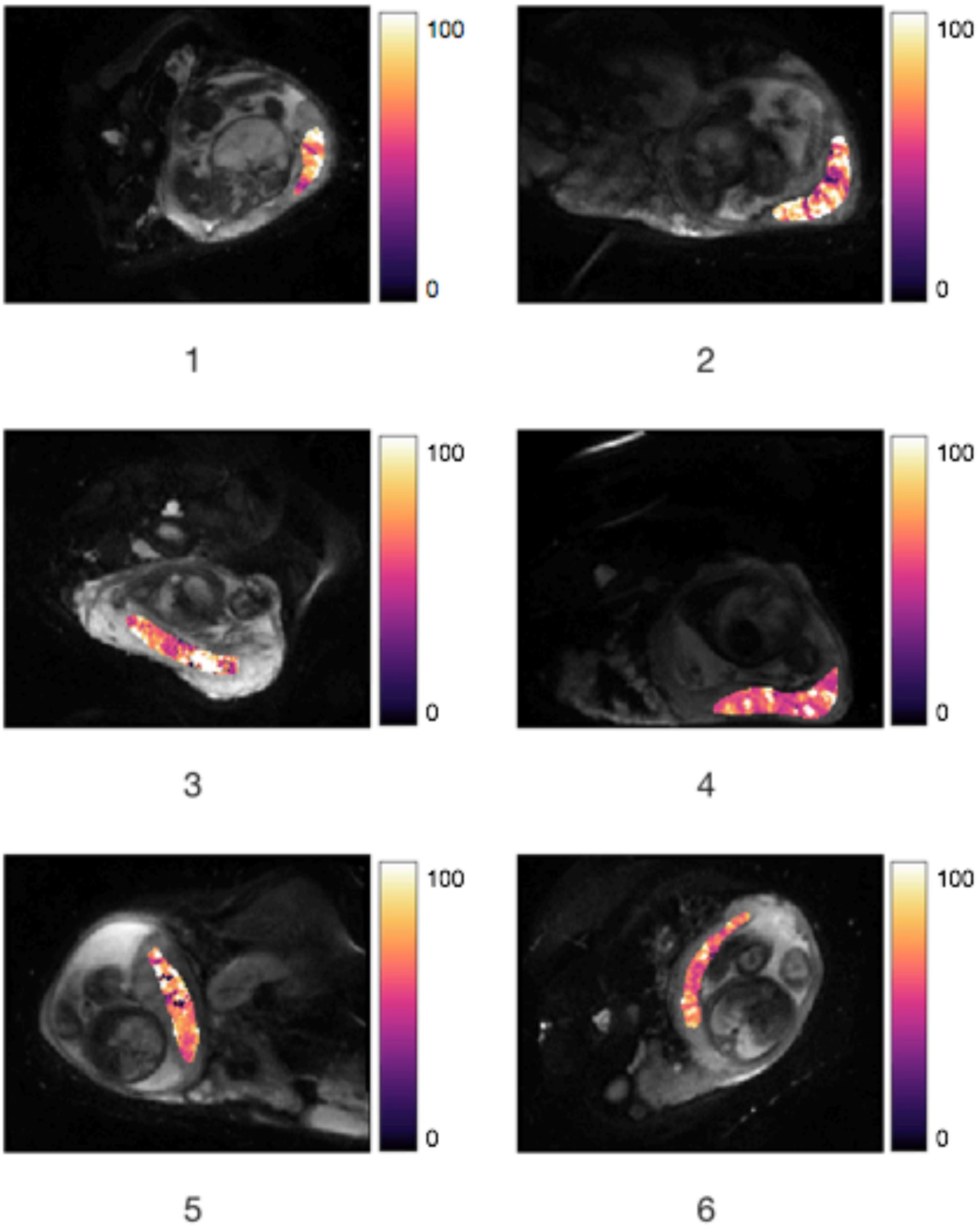

Figure 70; Parametric maps for the voxel wise fit of fetal blood oxygen saturation, derived from fetal blood T2 relaxation time. A textured appearance is visible in every map. There is heterogeneity in saturation throughout the placenta.

A histogram showing the voxel-wise fit for the whole placenta data is shown in Figure 71. The mean fetal blood saturation over the whole dataset was 71 (±5) %.

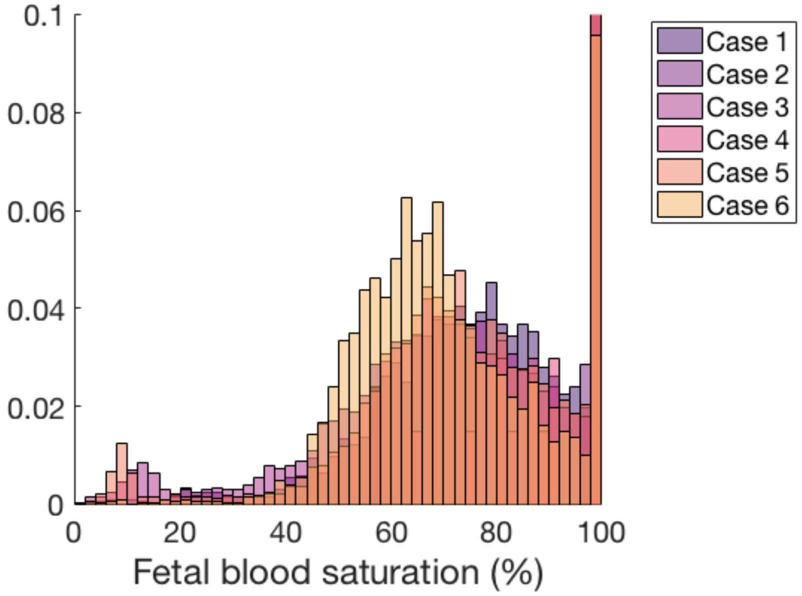

Figure 71; Histogram showing the voxel-wise fit of fetal blood oxygen saturation over the whole placenta for the six cases. There are few voxels with saturation less than 45%. The mean fetal blood saturation over the whole dataset was 71 (±5) %.

Conclusion; Fetal Blood Oxygen Saturation in Control Cases

The DECIDE imaging model may allow non-invasive estimation of fetal blood oxygen saturation for the first time. This work found a mean fetal blood oxygen saturation from 6 normal placentas of 71%.

8.8 Discussion

This chapter investigates the T2-IVIM model of myometrial perfusion, and the DECIDE model of placental perfusion, within a cohort of normally grown pregnancies. It shows that the model is feasible to fit in the majority of cases, although minimal motion is essential, especially in the case of the myometrium where there is only a thin band of tissue.

The myometrium allows investigation of maternal perfusion without the interference of fetal perfusion signal. This is useful for estimation of maternal blood T2 relaxation time, important because this value is set within the DECIDE model. However, it may also be a useful tissue to investigate. Placental insufficiency is caused by poor spiral artery remodeling in the first trimester, leading to low volume, high pressure blood flow[25,26]. It is therefore possible that *f* will be reduced in the myometrium of women with placental insufficiency, and this may be an early marker of poor invasion and high risk of placental insufficiency. Imaging the myometrium may also be beneficial in other pathologies, such as morbidly adherent placentas. Both the standard IVIM and T2-IVIM model gave high values for *f* and *d** in this normal cohort, which is expected within the highly vascular pregnant retro-placental myometrium. The T2-IVIM model gave a mean maternal blood T2 relaxation time of 202 (±93)ms, and a myometrial T2 relaxation time of 124 (±7)ms, which are in keeping with previously reported values in the literature[189].

In the placenta, the DECIDE model gave a lower *f* value than the standard IVIM model. This is expected given the results in the previous chapters. *f* and *d** values however remain high, in keeping with this representing fetal perfusion of the placenta. There was also a significant ν fraction, which is expected given that this is thought to represent maternal placental perfusion.

Fetal blood T2 relaxation time was lower than the value attributed to blood T2 in the literature[179] (145 (±54) ms in this work vs a literature value for adult blood of 240ms). However, fetal blood is different from adult blood. Haemoglobin, the oxygen carrying protein in blood, is composed of four protein subunits and four haem groups. Fetal haemoglobin is composed of two α subunits, and two γ subunits, unlike adult haemoglobin, which is composed of two α subunits and two β subunits[195]. Fetal haemoglobin functions differently from adult haemoglobin as it has a greater oxygen binding affinity than adult haemoglobin, allowing the developing fetus to take oxygen from the maternal blood more efficiently[196,197]. It is not known how the difference in protein structure affects the T2 relaxation time of blood. However, fetal blood also has a higher haematocrit than adult blood[198], and lower oxygen saturation[199]. At 30 weeks gestational age deoxygenated blood in the umbilical artery is estimated to be 65% saturated, and oxygenated blood in the umbilical vein is estimated to be 85% saturated[190]. Haematocrit and oxygen saturation are known to affect T2 relaxation times, with T2 time decreasing as haematocrit increases and oxygen saturation decreases[200]. It is therefore feasible for the T2 of fetal blood to be significantly lower than the T2 of maternal blood.

Using work by Portnoy et al[185], who reported the T2 relaxation times of *ex vivo* umbilical cord blood at different oxygen saturations, the T2 relaxation time of fetal blood was converted into a non-invasive estimation of fetal blood oxygen saturation. This allows us to estimate fetal blood oxygenation without an invasive procedure, that risks miscarriage or premature birth. The mean estimated fetal blood oxygen saturation over the whole data set was 71 (±5) %, with the majority of voxels falling between 45% and 100%. This is biologically plausible given the estimated fetal oxygen saturations above, and given that within the placental fetal circulation one would expect a mixture of deoxygenated and freshly oxygenated blood.

The maternal-fetal perfusion ratio is an attempt to investigate the correlation of maternal and fetal perfusion throughout the placenta. This is interesting because it is hypothesised that the placenta matches fetal to maternal perfusion, to optimise efficiency[201]. This data suggests that the majority of voxels showed a ratio just above 1 (mean 1.2(±0.6)). There were however a few voxels with significantly higher ratio, showing much higher fraction of ν to f.

This work also investigated the spatial pattern of *f* and ν within the placenta. No relationship was found between either parameter and distance from basal to chorionic plate. This result may be expected for *f*, which is a measure of flow, rather than vascular volume or density. However, for ν, which represents maternal perfusion, signal would be expected to decrease in the subchorionic region, where there is minimal maternal perfusion.

The main limitation of this work is the difficulty in registering data. Although the placenta is easier to image and register than the moving fetus, it is still challenging, being an intra-abdominal organ, and therefore subject to non-rigid motion from maternal breathing and bowel motion. In addition, large fetal movements can distort the uterus, or compress the placenta unpredictably, making registration more challenging than other organs affected by respiratory motion. Despite this, only one case was excluded due to motion. However, in many cases only small areas of interest were drawn on some placental slices, as motion between different acquisitions meant tissue close to the chorionic plate at one time point was within the amniotic fluid in another.

This also limits spatial interpretation of parameter values by adding variability into the model fitting. As described in the method every slice was imaged 41 times using different TE and b values. When comparing voxels in one slice by distance, a voxel close to the basal plate when imaged with one set of acquisition parameters, could be in the middle of the placenta in the next, due to motion in between acquisitions (Figure 72). This makes the distance data difficult to interpret. Further work needs to concentrate on improving the quality of the registration, reducing motion between different acquisitions.

Automatic segmentation algorithms are currently being developed for structural T2 imaging[202,203], however the reduced resolution of diffusion weighted imaging, and the different contrast with the different TE used, will make it a challenging task in the model. These however could help improve registration and therefore parameter fitting accuracy.

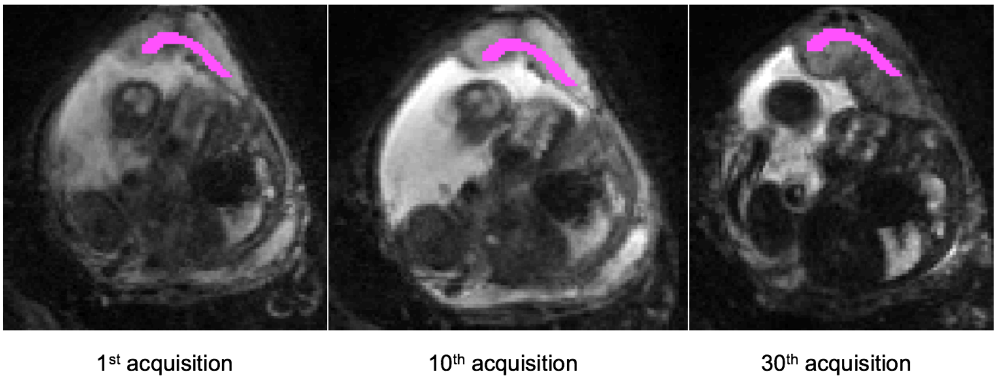

Figure 72; Figure showing limitations of current registration algorithm. Image acquisition 1, 10 and 30 for the 10th slice in case 2. Note the fetal motion between image acquisitions. There was also movement of the placenta, so the segmented area of interest is in a different region of the placenta for each acquisition, close to the chorionic plate in the 10th acquisition, and close to the basal plate in the 30th.

This work is on-going, collecting more data from a larger sample size. This will allow the mean and spread of parameters in normal placenta to be better defined. Work looking at how parameters change with gestational age will then also be possible. This is important because previous MRI work has suggested f[119] and d[112] may vary with gestational age. Work taking blood at cordocentesis suggests both umbilical vein and artery blood oxygen saturations decrease with increasing gestational age[199]. Therefore, further work is needed to characterise the parameters more fully, and this may help to further validate them.

In conclusion, this chapter presents normal values for several new imaging biomarkers in the human placenta. The findings show the mean fetal blood oxygen saturation to be 71%. This model may be useful in diagnosing placental function in utero. To explore this further, in the next chapter I will investigate how the parameters change when the model is applied to fetal growth restriction.

9 Comparing Multi-Compartment Myometrial and Placental Perfusion and Fetal Blood Saturation Modelling in Normal and Pathological Placentas

9.1 Summary

In this chapter I apply the optimised DECIDE model to a cohort of FGR pregnancies, and compare the results with those from the normal cohort discussed in chapter 9. I compare the T2-IVIM model parameters in the myometrium, and the DECIDE model parameters in the placenta. I show that maternal perfusion of the myometrium and placenta are reduced in FGR compared to normal pregnancy using the DECIDE model fit.

I also investigate the two novel parameters of placenta function described in the previous chapter in FGR:

- I show that the maternal-fetal perfusion ratio is reduced in FGR compared to normal pregnancy.
- I show reduced fetal blood oxygen saturation in FGR compared to normal pregnancy.

This work has been submitted and is under review for the MICCAI 2018 conference.

9.2 Ultrasound growth parameters for FGR Cases

Two women with pregnancies complicated by severe early onset fetal growth restriction detected before 28 weeks' gestational age were recruited and gave informed written consent for placental MRI. The gestational age at the time of MRI, and the results of the growth ultrasound scan are shown in Table 27. Both participants had an ultrasound scan on the same day as their MRI scan. Both had an estimated fetal weight on or below the 1st centile, umbilical artery Doppler pulsatility index on the 99th centile, with positive end diastolic flow, and uterine artery Doppler pulsatility index on or above the 99th centile. Both had normal MCA Doppler pulsatility index. There were no structural fetal abnormalities identified, both mothers had been tested for virus infections and had a low risk of aneuploidy. Case one was delivered 4 weeks and one day after the MRI, at a gestational age of 29 weeks and five days, due to reversed end diastolic flow in the umbilical arteries, and worsening pre-eclampsia in the mother. The baby weighed 793g (<1st centile). Case two was delivered 12 hours after the MRI, due to pathological monitoring of the fetal heart beat with cardiotocography. The baby weighed 633g (<1st centile). Both babies were admitted to the neonatal unit, and had no structural, infection or aneuploidy abnormalities detected after birth.

The MRI data was registered and segmented. There was no excess motion of the placenta or myometrium.

Throughout this chapter the results of these two FGR cases are compared with results from the normal, singleton cohort, discussed in the previous chapter (Chapter 9).

Case	Gestational age at MRI (weeks + days)	Estimated Fetal Weight in grams (percentile)	Umbilical artery Doppler PI (percentile)	MCA Doppler PI (percentile)	CPR (percentile)	Right uterine artery Doppler PI	Right uterine artery Doppler PI	Average Uterine artery PI (percentile)
1	25+4	621 (1)	1.92 (99)	1.85 (33)	0.96 (2)	2.08	3.58	2.83 (>99)
2	28+5	648 (0)	1.87 (99)	1.53 (8)	0.82 (1)	1.39	1.96	1.67 (99)

Table 27; Table showing the gestational age of each FGR case at MRI, and the results of their most recent ultrasound scan. Both cases had an estimated fetal weight below the 1st centile, and umbilical artery Doppler's above the 99th centile.

9.3 Comparing Myometrial MRI Parameters in Control and FGR

Myometrial parameter maps for the two FGR cases are shown in Figure 73. *f* appeared much lower in the myometrium of FGR cases than control cases.

Figure 74 shows histograms of the voxel-wise fit for both FGR case for every myometrial parameter, using the Standard IVIM model, and the T2-IVIM model. *f* appears quite different between the two cases using the standard IVIM model, however using the T2-IVIM model, the two fits of *f* appear very similar. The fit of maternal blood is noisy in both cases.

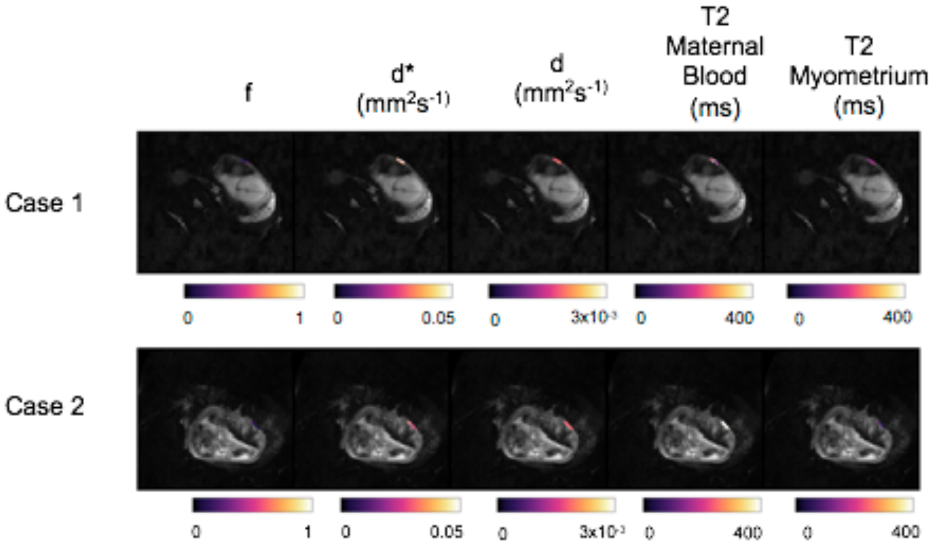

Figure 73; Parametric maps for the T2-IVIM fit of myometrium for the 2 FGR cases. Rows show cases, columns show parameter maps, from left to right, f, d*, d, T2 maternal blood and T2 myometrium.

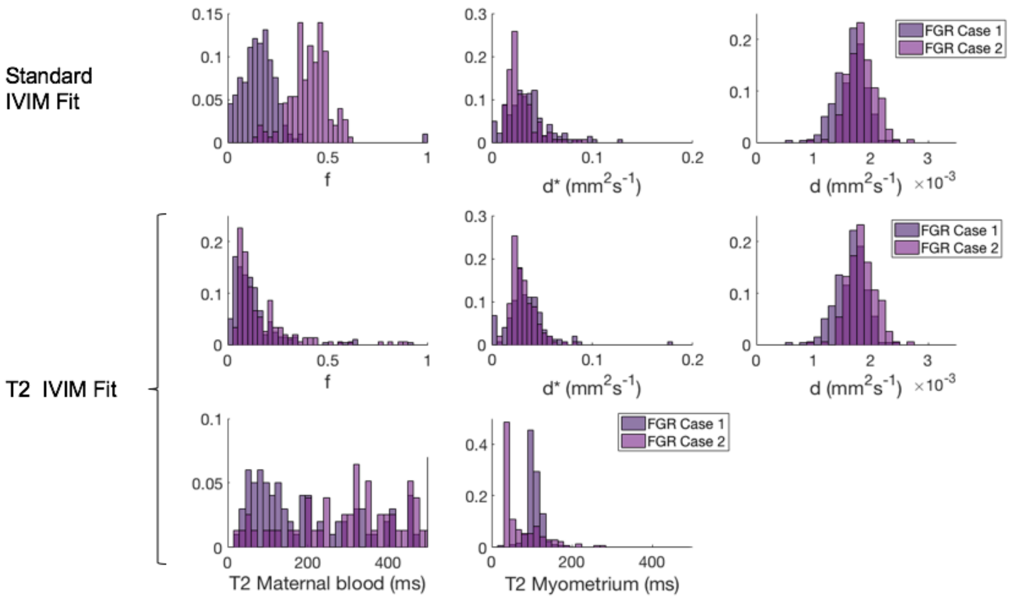

Figure 74; Voxel-wise parameter histograms for the two FGR myometrial datasets. Row one shows f, d* and d for the Standard IVIM fit. Row 2 and 3 shows f, d*, d and T2 relaxation time of maternal blood and myometrium for the T2-IVIM fit.

Table 28 shows a comparison of the mean (±standard deviation) for each parameter for a standard IVIM fit, and the T2-IVIM fit, for the control and FGR cases.

Figure 75 shows histograms comparing the combined data from the 4 included control cases, and the 2 FGR cases.

The T2-IVIM model found *f* to be lower in FGR compared to normal cases (0.44(±0.14) normal vs 0.15(±0.03) FGR). The mean T2 relaxation time of maternal blood in the FGR group was 244 (±74) ms. This is comparable with the estimate in the previous chapter and in the literature, although the histogram shows a wide distribution of data. The mean myometrial T2 relaxation time was 88(±24)ms, in keeping with the literature value (117 (±14)ms[189]).

	Control (n=4)		FGR (n=2)	
	Standard IVIM fit Mean (±STD)	T2-IVIM Fit Mean (±STD)	Standard IVIM fit Mean (±STD)	T2-IVIM Fit Mean (±STD)
f	0.48 (0.09)	0.44 (0.14)	0.29 (0.18)	0.15 (0.03)
d* (mm^2s^{-1})	0.051 (0.013)	0.044 (0.008)	0.048 (0.018)	0.037 (0.008)
d (mm^2s^1)	0.0016 (0.0003)	0.0016 (0.0003)	0.0017 (0.0001)	0.0017 (0.0001)
T2 Maternal Blood (ms)		202 (93)		244 (74)
T2 Myomtrium (ms)		124 (7)		88 (24)

Table 28; Table comparing the control and FGR cohorts mean and standard deviation of voxel-wise fit of the myometrium, for each parameter (f and d*) using the standard IVIM and the T2-IVIM model, and T2 relaxation time of maternal blood and myometrium using the T2-IVIM model. Myometrial f is lower in FGR than control placenta.

Conclusion; Comparing Myometrial MRI Parameters in Control and FGR

T2-IVIM model fit in the retro-placental myometrial found *f* was reduced in FGR pregnancies compared to normally grown controls.

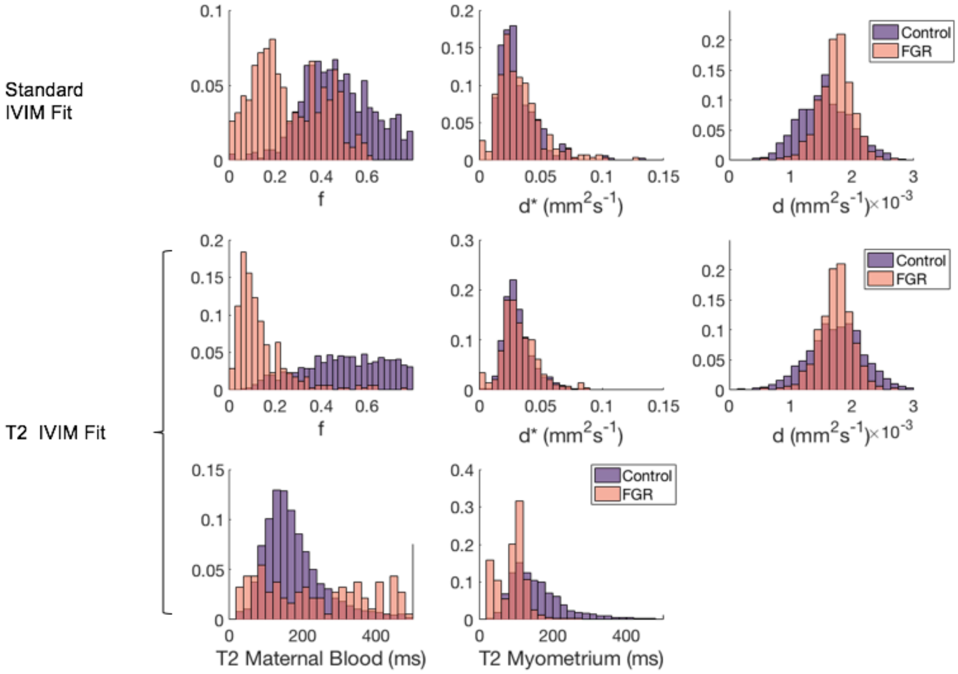

Figure 75; Histograms comparing the voxel wise fit for the myometrium, for the combined control (n=4) and combined FGR (n=2) data.

9.4 Comparing Placenta MRI Parameters in Control and FGR

Placenta parameter maps for the two FGR cases are shown in Figure 76. *f* and *d** have a more heterogeneous appearance in comparison with the control cohort, with large dark areas representing low values, interspersed with much brighter regions.

Figure 77 shows histograms of the voxel-wise fit for each FGR case for each placental parameter, using the Standard IVIM model, and the DECIDE model. The fit of both cases appears very similar for every parameter for both models.

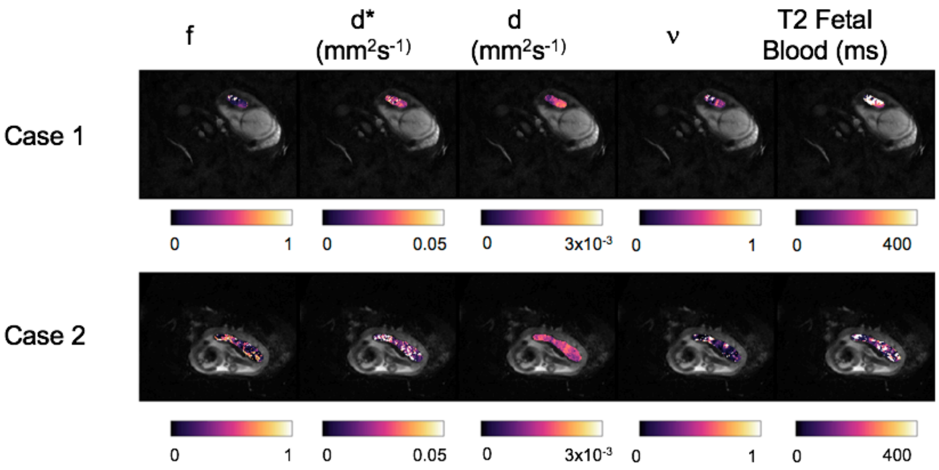

Figure 76; Parametric maps for the DECIDE fit of placenta for the 2 FGR cases. Rows show cases, columns show parameter maps, from left to right, f, d*, d, ν and the T2 fetal blood.

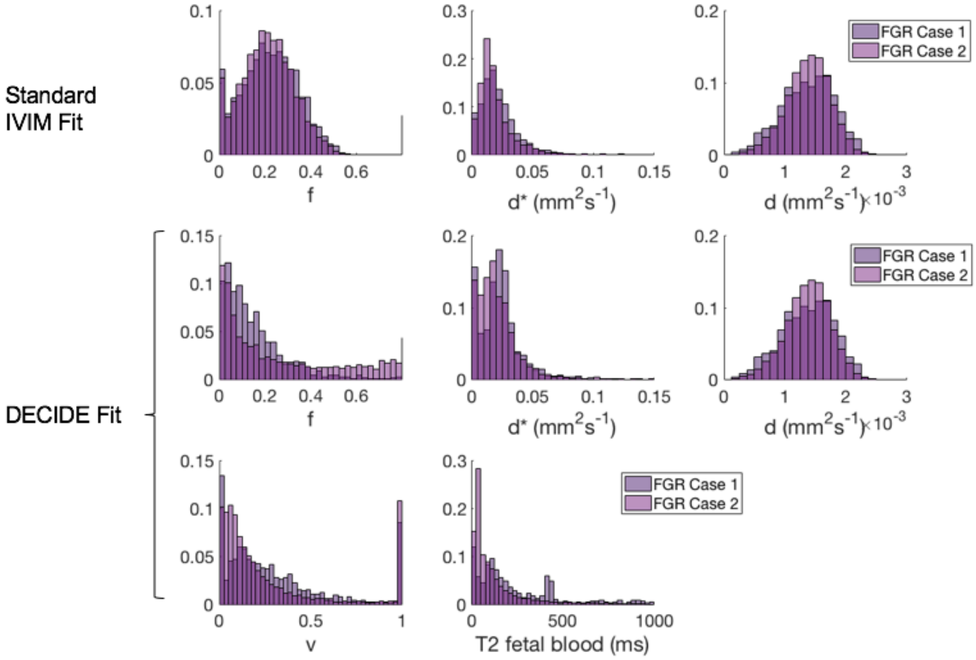

Figure 77; Voxel-wise parameter histograms for the two FGR placental datasets. Row one shows f, d* and d for the Standard IVIM fit. Row 2 and 3 shows f, d*, d, ν and T2 relaxation time of fetal blood for the DECIDE fit.

Table 29 shows a comparison of mean (±standard deviation) of the voxel wise fit for each parameter for a standard IVIM fit, and the DECIDE fit for the control and FGR placenta. Figure 78 shows combined voxel-wise histograms comparing the 6 included control cases, and the 2 FGR cases.

d was lower in FGR than control (0.0017 (±0.0001) mm^2s^{-1} control vs 0.0014 (0.0001) mm^2s^{-1} FGR). *f* was lower in FGR compared to normal cases using the standard IVIM model (0.27 (±0.03) control vs 0.24 (±0.02) FGR). However, with the DECIDE model FGR *f* was higher (0.23 (±0.03) control vs 0.29 (±0.08) FGR). The histograms show that the FGR distribution is highly skewed, with the highest frequency of voxels at a lower *f* than in the control group, but with a substantial number of voxels with higher *f*. ν was lower in the FGR group than the control group (0.32 (±0.06) control vs 0.29 (±0.03) FGR). The T2 relaxation time of fetal blood was shorter in FGR compared to control (162 (±25) ms control vs 117 (±20) ms FGR).

	Control (n=6)		FGR (n=2)	
	Standard IVIM fit Mean (±STD)	DECIDE Fit Mean (±STD)	Standard IVIM fit Mean (±STD)	DECIDE Fit Mean (±STD)
f	0.27 (0.03)	0.23 (0.03)	0.24 (0.02)	0.29 (0.08)
d* (mm^2s^{-1})	0.034 (0.003)	0.028 (0.005)	0.004 (0.008)	0.060 (0.022)
d (mm^2s^{-1})	0.0017 (0.0001)	0.0017 (0.0001)	0.0014 (0.0001)	0.0014 (0.0001)
ν		0.32 (0.06)		0.29 (0.03)
T2 Fetal Blood (ms)		162 (25)		117 (20)

Table 29; Table comparing the control and FGR cohorts mean and standard deviation of voxel-wise fit of the placenta, for f and d* using the standard IVIM and the DECIDE model, and ν and T2 relaxation time of fetal blood using the DECIDE model.

Conclusion; Comparing Placental MRI Parameters in Control and FGR

DECIDE model fit in the placenta found *d, ν* and T2 relaxation time of fetal blood *were* reduced in FGR pregnancies compared to normally grown controls. *F* was increased in FGR pregnancies compared to normally grown controls.

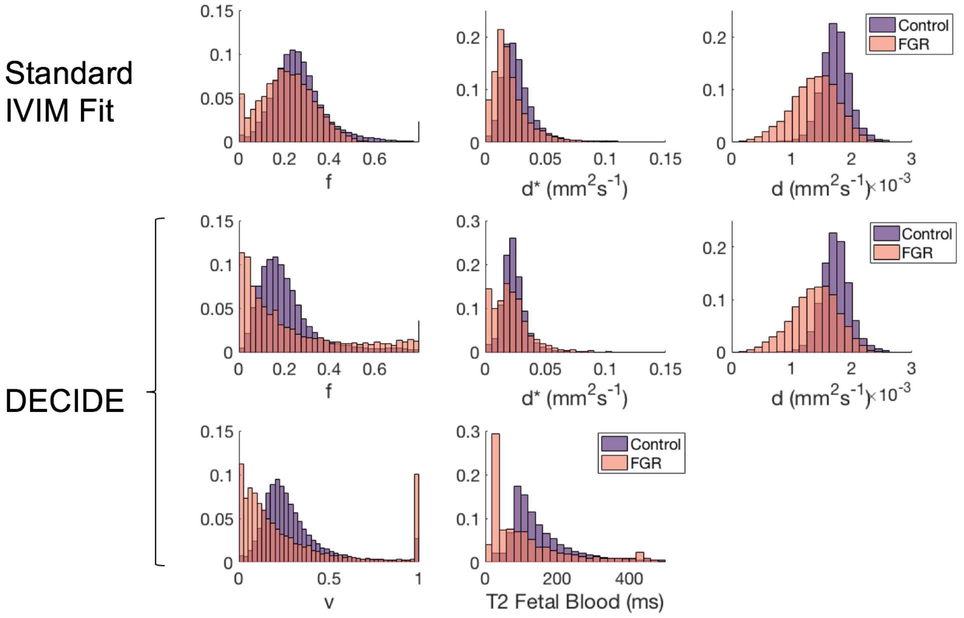

Figure 78; Histograms comparing the voxel wise fit for the placenta, for the combined control (n=6) and combined FGR (n=2) datasets.

9.5 Comparing Maternal-fetal perfusion ratio in Control and FGR

The histogram showing the voxel wise fit of the maternal-fetal perfusion ratio (described in chapter 9) for each FGR case is shown in Figure 79. The two FGR cases show similar distributions, with the majority of voxels showing a ratio below 1.5.

When comparing the combined normal and FGR datasets (Figure 79), the peak frequency of the FGR data is less than the peak frequency of the control group. The mean maternal-fetal perfusion ratio of the combined data was lower in FGR than in the control cohort (1.53 (±1.2) control vs 1.23 (±2.5) FGR).

Conclusion; Comparing Maternal-fetal perfusion ratio in Control and FGR

Mean Maternal-fetal perfusion ratio, a potential new biomarker of placental function, was lower in FGR than in the control cohort.

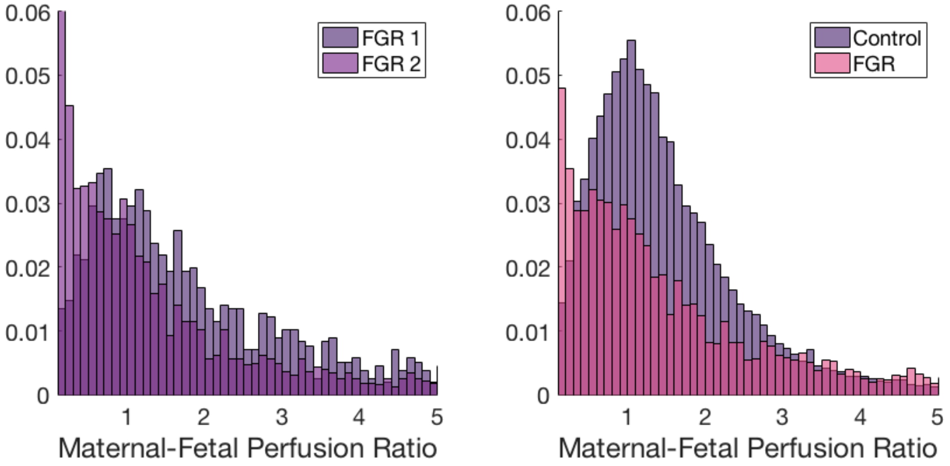

Figure 79; Histograms showing maternal-fetal perfusion ration for FGR cases, and comparing combined maternal-fetal perfusion ratio between normal and FGR placentas. Left; Histogram of voxel-wise calculation of the maternal-fetal perfusion ratio for the two FGR datasets. Right; Histogram comparing the voxel wise calculation of the maternal-fetal perfusion ratio, for the combined control (n=6) and combined FGR (n=2) data.

9.6 Comparing Fetal Blood Oxygen Saturation in Control and FGR

A voxel-wise fit of fetal blood oxygen saturation was applied to the FGR cases, as described in chapter 9. A histogram showing the fit is shown in Figure 80. The mean fetal blood saturation over the whole dataset was 52 (±11) %. The two datasets both show a significant proportion of voxels below 40% saturation, unlike the control data where there were very few voxels with saturation less than 40%. The mean fetal blood oxygen saturation for case one was 60%, and for case 2 was 45%.

When comparing the combined normal and FGR datasets (Figure 80), the peak frequency of the FGR data is much lower than the control peak. The mean oxygen saturation of the control data was 73 (±20) %, whereas the mean of the combined FGR data was 46 (±32) %.

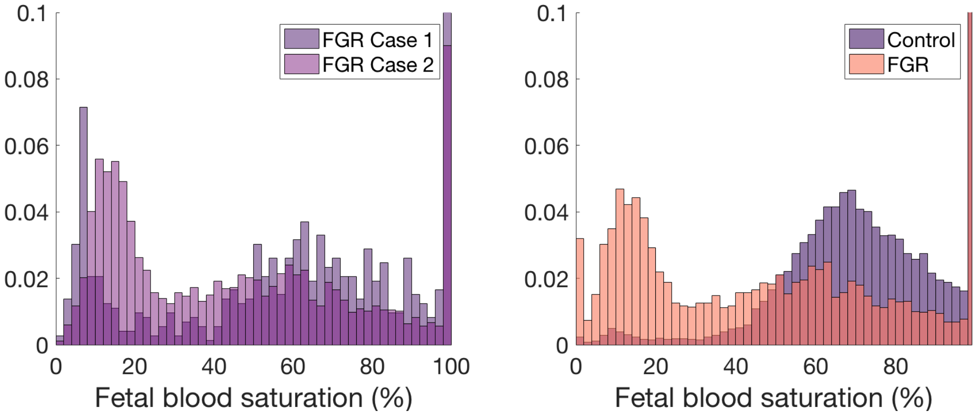

Figure 80; Histograms showing fetal blood oxygen saturation estimates for FGR cases, and comparing combined fetal blood oxygen saturation estimates between normal and FGR placentas. Left; Histogram showing the voxel-wise fit of fetal blood oxygenation saturation over the whole placenta for the two FGR cases. There are a large number of voxels with saturation less than 45%. Right; Histogram comparing the voxel wise fit of fetal blood saturation, for the combined control (n=6) and combined FGR (n=2) data.

Conclusion; Comparing Fetal Blood Oxygen Saturation in Control and FGR

Non-invasive fetal blood oxygen saturation estimation using the DECIDE model found reduced oxygen saturation in FGR compared to normally grown controls.

9.7 Discussion

This chapter compares parameters from the T2-IVIM model of myometrial perfusion, and the DECIDE model of placental perfusion, between normally grown pregnancies, and pregnancies complicated by FGR. It suggests the DECIDE model can detect differences in myometrial and placental perfusion within FGR, that likely relate to the underlying pathology. However, this work is limited by the sample size, and can only be considered proof of principle. Further work, with larger cohorts, is needed to confirm these results, and to understand how the measured parameters relate to outcome.

Within the myometrium, *f* was considerably reduced in pregnancies complicated by FGR (0.44(±0.14) control vs 0.15(±0.03) FGR). This is expected, given the pathophysiology of FGR[25,27]. Poor placentation in the first trimester causes poor re-modelling of the maternal spiral arteries, and therefore a reduction in the volumes of maternal blood perfusing the placenta[26]. The T2 relaxation time of maternal blood increased slightly in the FGR cohort (202 (±93) ms control vs 244 (±74) ms FGR). Given the large standard deviation, and small sample size, it is likely that there is no difference. The variability in the data is probably secondary to the small area of interest used. This was small because the myometrium is thin, and motion artefact prevented large areas being segmented. Both these values are in keeping with the literature values of adult blood (240ms)[179]. The T2 relaxation time of myometrium decreased in the FGR group (124 (±7) ms control vs 88 (±24) ms FGR). This could be due to the small sample size, and small area of interest used for the myometrial fit, and noise within the data. However, it could potentially also be secondary to differences in the myometrial tissue microstructure between normal and FGR pregnancies, either secondary to the poor placental invasion, or possibly even causing it. This is an area that needs further investigation with larger sample sizes, to see if this difference persists.

In the placenta, mean value of *f* was reduced in FGR compared to the control group with the standard IVIM model fit, which is in keeping with findings in the literature[121,125,128], but mean *f* increased in FGR with the DECIDE model fit. It is not certain why this is, but it may be because *f* measures flow, rather than vascular density, and flow could be increased in the vasoconstricted FGR fetoplacental vascular tree. When the fitting of *f* is examined on the combined histograms (Figure 78) it is apparent that the peak voxel frequency is at a lower *f* in FGR compared to control. However, the mean *f* is increased in FGR due to the long tail of voxels fitting to high *f* values. This may be secondary to noise within the imaging. However, the maps (Figure 76) suggest there to be a lobulated pattern to these areas of high *f*. It may be that within the damaged FGR placenta, there are areas with high flow, as large volumes of fetal blood are shunted away from where there is low flow, either due to stem vessel vasoconstriction secondary to poor maternal perfusion of these areas, or due to obliteration of stem vessel lumens. It may also be that these high areas of *f* do not relate to fetal perfusion, and reflect some other structural change within the placenta.

d was reduced in FGR compared to the control cohort (0.0017(±0.0001) mm^2s^{-1} controls vs 0.0014 (±0.0001) mm^2s^{-1} FGR)), which is a finding consistent with other work in the literature[187], and likely relates to changes in the tissue structure, such as increased fibrin deposition. ν was also lower in the FGR group compared to the control (0.32 (±0.06) control vs 0.29 (±0.03) FGR). This is expected given that the maternal perfusion of the placenta is reduced in FGR[26], and is in keeping with the results in the myometrium.

The T2 relaxation time of fetal blood was reduced in FGR compared to control cases (162 (±25) ms control vs 117 (±20) ms FGR). This related to a reduction in the calculated fetal blood oxygen saturation, from 73 (±20)% in the control cohort, to 46 (±32)% in the FGR cohort. The reduction in blood oxygen saturation in FGR is quite severe, which might question the validity of the biomarker. However, the ultrasound CPR measure suggests evidence of fetal blood redistribution, which is thought to be a sign of fetal hypoxia, in both cases, so it is possible that there may have been severe hypoxia present. In addition previous work that directly measure umbilical cord blood oxygen saturations has shown hypoxia at this level and worse in FGR cases[194], suggesting that these values are biologically feasible.

When considering the two FGR cases separately, the first had a mean saturation of 60%, and the second 45%. The second saturation is very low, but this fetus was delivered a few hours later due to evidence of fetal compromise on the cardiotocography. These findings may both be consistent with a placenta that was failing to sufficiently oxygenate the fetus. The first case, with a higher oxygen saturation, continued for a further four weeks, suggesting a placenta that was not functioning normally, but was not imminently about to fail. This conclusion is speculative given the small sample sizes, but certainly warrants further examination, as if this does relate to fetal oxygen saturation, it could be a powerful clinical tool in determining fetal wellbeing non-invasively.

The combined fetal blood oxygenation histograms show a peak in the FGR cohort at 10-20% saturation, whereas the control cohort had very little data with a saturation less than 45%. This again suggests a greater degree of heterogeneity within the FGR placenta, with areas of poorly oxygenated tissue, which may relate to areas of poor maternal perfusion, or other underlying pathology, such as infarcted villi.

The maternal-fetal perfusion ratio was reduced in the combined FGR data compared to the control data (1.53 (±1.2) control vs 1.23 (±2.5) FGR). This relates to an overall reduction in the maternal to fetal perfusion throughout the placenta. However, the combined histogram show a greater spread of data in FGR compared to the control (Figure 79). It is possible this may relate to dysregulation of maternal and fetal perfusion matching in FGR, however more data is needed before any conclusions can be reached.

The two cases of FGR used in this chapter were severe, early onset disease, and so represent the most severe placental pathology. Future work is also needed to understand how the measured parameters are affected in less severe disease, and whether they correlate to ultrasound markers of placental disease, such as uterine or umbilical artery Doppler measurements, or post-natal histological findings.

This work also has limitations in image processing, as described in the previous chapters (chapters 8 and 9). Improved registration and segmentation would allow further investigation of the spatial pattern of parameters in FGR placentas, which may be important, as understanding and defining heterogeneity is key in understanding placental function. If the spatial alignment was more consistent, it would be interesting to compare fetal blood oxygen saturation levels with maternal perfusion (ν), to investigate if there is a relationship between these two parameters.

In conclusion, this chapter presented values for the T2-IVIM model in the myometrium (f, d*, d, and T2 relaxation time of maternal blood and myometrium), and the DECIDE model in the placenta (*f, d*, d, ν and T2 relaxation time of fetal blood) in FGR, and compared results to the findings in the normal cohort. Maternal-fetal perfusion ratio, a potential new biomarker of placental function, was reduced in FGR compared to normal controls. Fetal blood saturation was estimated non-invasively in utero, using the fetal blood T2 relaxation time, and was reduced in severe cases of FGR.

10 Conclusion and Future work

10.1 Micro Computer Tomography of the Human Placenta

In this thesis, I investigated placental vascularisation with micro-CT, established that normal term feto-placental vascularisation has a large degree of heterogeneity, and that there was no consistent spatial pattern to feto-placental vascular density in relation to placental structure.

This work is important because it shows that there is no optimal area from which placental tissue can be sampled to get a true representation of the whole placental vascularisation. It also shows that a large proportion of the placenta needs to be investigated in order to determine the vascularisation.

Micro-CT is a potential tool in improving placental assessment, due to the large field of view, allowing the whole placenta to be imaged and analysed. The limitation is the resolution of imaging at this scale, as there is a trade-off between the field of view and the magnification achievable[72]. Whole placental imaging could be a useful tool to gain an overview of whole placental vascularisation, and to guide biopsy sites for further imaging at higher magnification, or with a different modality.

The reason for the large degree of heterogeneity in vascular density within the placenta is unknown, but may relate to variation in the maternal perfusion of the placenta. Within the normal placenta, areas of poor maternal perfusion due to sparsity of spiral arteries or poor spiral artery remodeling, may become less vascularly dense due to mechanical insult to the villi[26], or secondary to vasoconstriction of stem vessels, redirecting fetal blood to better perfused areas of the placenta[35].

It is known that there is a degree of redundancy within the human placenta, so a proportion of the fetal and maternal placental perfusion can be lost without causing a detrimental effect to the fetus[204]. This can be seen in women who have recurrent antepartum haemorrhage due to marginal placental bleeds, but appear to have normally grown fetus at the end of pregnancy[204]. Once this redundancy has been used up however, the fetus starts to become compromised, hypoxic and growth restricted[204]. This would explain the differences seen in FGR placental histology with age of onset of disease. Early onset represents the most severe disease, where the largest proportion of the placenta is affected, and therefore the effects are severe and seen early. In late onset FGR the placenta works well enough to support the small fetus, but demand outstrips its ability to supply later on, when the large fetus requires high levels of oxygen and nutrients.

It is therefore important to determine to what extent the placenta is redundant, i.e. how much of the placental tissue can be poorly perfused before there are fetal consequences, and whether this changes with increasing gestational age.

Micro-CT provides an opportunity to investigate this further, as although there are limitations to the technique, it provides a high level of magnification whilst maintaining the field of view to investigate the whole placenta, and therefore quantify differences in vascularisation throughout the placenta.

Further work is needed on the technical side of this work, as improving segmentation of the vascular tree would improve the derived data, and also allow more complex analysis of the branching structure of the vascular tree. This work relied on simple, grey scale thresholding, which included areas of noise, and excluded vessels with slightly lower greyscale value than the threshold that was set. It was not possible to have a perfect threshold, as there was cross over between the placental tissue and contrast filled vessel greyscale histograms. More complex tree growing algorithms exist, that use additional features, such as proximity to a voxel thresholded as vessel, to grow vascular trees[171,172,173,174]. Such approaches may improve segmentation here, but the large size and complexity of the data makes it a challenging task, requiring bespoke algorithms.

More complex analysis, such as that done be Rennie et al in the mouse placenta[205,85], would help to improve our understanding of the changes in the fetoplacental vascular tree seen in different pathologies, but again this is difficult in this complex data. At present, there is no commercially available software capable of analysing the placental vascular tree in a way that is spatially relevant to the placental structure. Development of such algorithms would allow the chorionic and villous trees to be analysed separately, and in relation to one another, and is essential if we are to be able to analyse features such as branching patterns and vessel tortuosity.

10.2 DECIDE Placental Perfusion MRI

This thesis developed a novel MRI model of placental perfusion; the DECIDE model. This attempts to divide fetal and maternal perfusion of the placenta using MRI. This is important as it estimates the two placental perfusions throughout the placental tissue, and therefore provides much more information on placental function than the ultrasound assessment currently done in clinical practice. DECIDE imaging also allowed the development of a novel parameter that matches maternal and fetal placental perfusion on a voxel wise basis.

The DECIDE model fits the fetal blood T2 relaxation time. As T2 is highly dependent on blood oxygen saturation this can be transformed into a non-invasive measure of placental fetal blood oxygen saturation. This novel parameter may be directly relevant to fetal hypoxia, and therefore predictive of poor cerebral prognosis or fetal demise.

The next step, which is currently in progress with a grant from the Radiological Research Trust and the Wellcome Trust (210182/Z/18/Z), is to investigate the parameters in larger, gestational age matched cohorts of normal and FGR pregnancies.

For this on-going work, FGR is defined as estimated fetal weight below the 3rd centile, or estimated fetal weight below the 10th centile with abnormal fetal Doppler measurements. Ultrasound measurements are being collected, which will allow correlation of uterine and umbilical artery Doppler measurements with MRI parameters. MRI parameters will also be correlated with fetal outcome, in terms of birth weight centile and condition at birth. If this study does confirm the differences in parameters between the two groups seen in this thesis, a more thorough validation study, using an animal model of placental insufficiency, would be an interesting next step.

This is important to further investigate if the fetal blood oxygen saturation estimation described in this thesis truly relates to fetal blood oxygen saturation. To do this an invasive measurement of fetal blood oxygen saturation would need to be taken directly after imaging. This would not be possible in humans but would be feasible in animal experiments. The ideal experiment would be to repeatedly reduce maternal oxygenation, and to image the placenta, and measure the maternal and fetal blood oxygen saturation at the same time. The animal model would need to have an anatomy reflecting human placental anatomy. To investigate placental imaging in an animal model the two main properties that are important are the interdigitation between maternal and fetal perfusion, and the degree of trophoblast invasion. An animal model comparable with human placental perfusion should have a complex network of fetal vessels, bathed in a pool of maternal blood (haemochorial placenta)[206], and there should be extensive trophoblast invasion. Other considerations in animal work include litter size, length of gestation, and cost.

Non-human primates would provide the best model to further investigate DECIDE placental imaging, but are expensive to care for, and ethically complex given their advanced social behavior[207]. Rodents are a more practice animal model, and benefit from a shorter gestational age, and multiple pups per pregnancy, reducing the number of animals needed[207]. Of the rodents, guinea pigs have the advantage of haemomonochorial placentas and extensive trophoblast invasions. In additional the brain development is more similar to humans than other rodents, providing a potential model for fetal brain imaging[207]. Surgical models of FGR in guinea pigs include uterine artery ligation and radial artery diathermy, providing the potential to investigate imaging with reduced maternal perfusion[207]. The disadvantage of rodents is that they have labyrinthine placentas, where maternal blood circulates through channels within the fetal syncytiotrophoblast[207]. This may alter the movement of maternal blood, compared to maternal blood movement within the human intervillous space, so work would be needed to investigate if the DECIDE model applied in rodent models, or if a modified DECIDE model would be needed.

Further work is also needed to improve the technical aspect of image analysis, in particular improving the registration of data, and creating algorithms capable of automated segmentation. This will allow more complex, spatial analysis of the placental perfusion.

The DECIDE model has two potentially important applications. Firstly, it could be important in improving our understanding of placental perfusion, due to the model's ability to measure perfusion throughout the placenta. This could be used to improve our understanding of the heterogeneity of maternal and fetal perfusion in relation to placental structure, and in how the two perfusions match one another.

Secondly, DECIDE could also be useful as a diagnostic tool in the future. In order to investigate this, future work needs to examine the predictive value of the model within a high-risk cohort of patients. This work has shown large differences in signal between placentas in normal pregnancy, and placentas in FGR where the maternal and fetal Doppler studies were abnormal. The next step is to define a high-risk cohort for FGR, image them at an early gestational age, and correlate findings with outcome data such as ultrasound imaging parameters, gestational age at delivery and birth weight centile, and maternal complications such as pre-eclampsia. If DECIDE is able to predict or exclude placental insufficiency earlier or more accurately than ultrasound imaging parameters, it could become an important clinical tool, within a high-risk population.

If the measure of fetal blood oxygen saturation is validated this will need further investigation, to correlate oxygen saturation to outcome. There is an increased rate of abnormal neurodevelopment in FGR children compared to controls, probably secondary to hypoxia *in utero* or possibly changes in cerebral perfusion. If there is a correlation between DECIDE measures of fetal blood oxygen saturation and cognitive outcome, then DECIDE could help clinicians plan when to deliver an FGR baby, potentially preventing hypoxic brain injury *in utero*, which could reduce the rate of cerebral palsy and improve the long-term outcome for these children.

Finally DECIDE may be a useful investigatory tool as treatments for FGR are developed and investigated in clinical trials. DECIDE may help to measure and monitor if there are changes in maternal and fetal placental perfusion in response to treatment.

The DECIDE model combines IVIM and T2 relaxometry imaging. As discussed in the introduction, other MR signals relevant to placental perfusion are also being investigated. T2* shows potential as a measure of placental function, with reduced signal shown in FGR cases associated with abnormal fetal Doppler measurements and placental histology[106]. BOLD studies have shown significant differences in R1 and R2* between normal and FGR placentas, and a lower difference in R1 with maternal hyperoxia in FGR compared with controls[104]. There is also interest in investigating spectroscopy within the placenta[208] to investigate metabolic changes associated with placental insufficiency. These different signals relate to different properties of the placenta, and therefore provide different information on placenta function. It is likely that combining them will be advantageous in increasing our understanding of the placenta, and possibly diagnosing placental function in the future.

In conclusion, this thesis has developed two techniques to image whole placental vascularisation, *in* and *ex vivo*. The heterogeneity of vascular density in the normal term placenta was defined at multiple scales with micro-CT. No spatial relationship between vascular density and tissue location was found at any scale. A new MRI model of placental perfusion was developed, that divided signal from fetal and maternal perfusion. The model provides new parameters to describe placental function, including a non-invasive estimation of fetal blood oxygen saturation. This has the potential to improve our understanding of placental function, and to diagnose placental insufficiency and fetal hypoxia. It could therefore impact management of FGR pregnancies in the future, and improve the outcome for the children.

References

1. Lawn, J. E. *et al.* Stillbirths: Where? When? Why? How to make the data count? *Lancet (London, England)* **377,** 1448–63 (2011).
2. Burton, G. J. & Fowden, A. L. The placenta: a multifaceted, transient organ. *Philos. Trans. R. Soc. Lond. B. Biol. Sci.* **370,** 20140066 (2015).
3. Burton, G. J., Fowden, A. L. & Thornburg, K. L. Placental Origins of Chronic Disease. *Physiol. Rev.* **96,** 1509–65 (2016).
4. Carter, A. M. Evolution of Placental Function in Mammals: The Molecular Basis of Gas and Nutrient Transfer, Hormone Secretion, and Immune Responses. *Physiol. Rev.* **92,** (2012).
5. Gordon, Z. *et al.* Anthropometry of fetal vasculature in the chorionic plate. *J. Anat.* **211,** 698–706 (2007).
6. Fox, H. & Sebire, N. J. *Pathology of the Placenta*. (Saunders Elsevier, 2007).
7. Habashi, S., Burton, G. J. & Steven, D. H. Morphological study of the fetal vasculature of the human term placenta: Scanning electron microscopy of corrosion casts. *Placenta* **4,** 41–56 (1983).
8. Lyall, F., Robson, S. C. & Bulmer, J. N. Spiral Artery Remodeling and Trophoblast Invasion in Preeclampsia and Fetal Growth RestrictionNovelty and Significance. *Hypertension* **62,** (2013).
9. Burchell, R. C. Arterial blood flow into the human intervillous space. *Am. J. Obstet. Gynecol.* **98,** 303–11 (1967).
10. Serov, A. S., Salafia, C. M., Brownbill, P., Grebenkov, D. S. & Filoche, M. Optimal villi density for maximal oxygen uptake in the human placenta. *J. Theor. Biol.* **364,** 383–396 (2015).
11. Perazzoloab, S., Lewis, R. M. & Sengersab, B. . Modelling the effect of intervillous flow on solute transfer based on 3D imaging of the human

placental microstructure. *Placenta* **60,** 21–27 (2017).

12. Huppertz, B. in *The Placenta* 36–42 (Wiley-Blackwell, 2011). doi:10.1002/9781444393927.ch5
13. Castellucci, M., Kosanke, G., Verdenelli, F., Huppertz, B. & Kaufmann, P. Villous sprouting: fundamental mechanisms of human placental development. *Hum. Reprod. Update* **6,** 485–94 (2000).
14. Jackson, M. R., Mayhew, T. M. & Boyd, P. A. Quantitative description of the elaboration and maturation of villi from 10 weeks of gestation to term. *Placenta* **13,** 357–370 (1992).
15. Kaufmann, P., Mayhew, T. M. & Charnock-Jones, D. S. Aspects of human fetoplacental vasculogenesis and angiogenesis. II. Changes during normal pregnancy. *Placenta* **25,** 114–26 (2004).
16. Pearce, P. *et al.* Image-Based Modeling of Blood Flow and Oxygen Transfer in Feto-Placental Capillaries. *PLoS One* **11,** e0165369 (2016).
17. Plitman Mayo, R., Olsthoorn, J., Charnock-Jones, D. S., Burton, G. J. & Oyen, M. L. Computational modeling of the structure-function relationship in human placental terminal villi. *J. Biomech.* **49,** 3780–3787 (2016).
18. WIGGLESWORTH, J. S. Vascular Organization of the Human Placenta. *Nature* **216,** 1120–1121 (1967).
19. Gruenwald, P. Maternal blood supply to the coneptus. *Eur. J. Obstet. Gynecol. Reprod. Biol.* **5,** 23–34 (1975).
20. Fox, H. The pattern of villous variability in the normal placenta. *BJOG An Int. J. Obstet. Gynaecol.* **71,** 749–758 (1964).
21. Romney, S. L. & Reid, D. E. Observations on the fetal aspects of placental circulation. *Am. J. Obstet. Gynecol.* **61,** 83–98 (1951).
22. Sebire, N. J. & Talbert, D. The role of intraplacental vascular smooth muscle in the dynamic placenta: a conceptual framework for understanding uteroplacental disease. *Med. Hypotheses* **58,** 347–51 (2002).

23. Hampl, V. *et al.* Hypoxic fetoplacental vasoconstriction in humans is mediated by potassium channel inhibition. *Am. J. Physiol. - Hear. Circ. Physiol.* **283,** H2440–H2449 (2002).

24. Pereira, R. D. *et al.* Angiogenesis in the Placenta: The Role of Reactive Oxygen Species Signaling. *Biomed Res. Int.* **2015,** 1–12 (2015).

25. Crocker, I. P. in *The Placenta* 237–245 (Wiley-Blackwell, 2011). doi:10.1002/9781444393927.ch31

26. Burton, G. J., Woods, A. W., Jauniaux, E. & Kingdom, J. C. P. Rheological and Physiological Consequences of Conversion of the Maternal Spiral Arteries for Uteroplacental Blood Flow during Human Pregnancy. *Placenta* **30,** 473–482 (2009).

27. Kingdom, J., Huppertz, B., Seaward, G. & Kaufmann, P. Development of the placental villous tree and its consequences for fetal growth. **92,** 35–43 (2000).

28. Bracero, L. A. *et al.* Doppler velocimetry and placental disease. *Am. J. Obstet. Gynecol.* **161,** 388–93 (1989).

29. McCowan, L. M., Mullen, B. M. & Ritchie, K. Umbilical artery flow velocity waveforms and the placental vascular bed. *Am. J. Obstet. Gynecol.* **157,** 900–902 (1987).

30. Jackson, M. R. *et al.* Reduced placental villous tree elaboration in small-for-gestational-age pregnancies: relationship with umbilical artery Doppler waveforms. *Am. J. Obstet. Gynecol.* **172,** 518–25 (1995).

31. Hitschold, T. P. Doppler flow velocity waveforms of the umbilical arteries correlate with intravillous blood volume. *Am. J. Obstet. Gynecol.* **179,** 540–3 (1998).

32. Mitra, S. C., Seshan, S. V. & Riachi, L. E. Placental vessel morphometry in growth retardation and increased resistance of the umbilical artery doppler flow. *J. Matern. Fetal. Med.* **9,** 282–286 (2000).

33. Salafia, C. M., Pezzullo, J. C., Minior, V. K. & Divon, M. Y. Placental pathology of absent and reversed end-diastolic flow in growth-restricted fetuses. *Obstet. Gynecol.* **90,** 830–836 (1997).

34. Macara, L. *et al.* Structural analysis of placental terminal villi from growth-restricted pregnancies with abnormal umbilical artery Doppler waveforms. *Placenta* **17,** 37–48 (1996).

35. Sebire, N. J. Umbilical artery Doppler revisited: pathophysiology of changes in intrauterine growth restriction revealed. *Ultrasound Obstet. Gynecol.* **21,** 419–22 (2003).

36. Souza, J. P. *et al.* Moving beyond essential interventions for reduction of maternal mortality (the WHO Multicountry Survey on Maternal and Newborn Health): A cross-sectional study. *Lancet* **381,** (2013).

37. Mol, B. W. J. *et al.* Pre-eclampsia. *Lancet* **387,** 999–1011 (2016).

38. Gordijn, S. J. *et al.* Consensus definition of fetal growth restriction: a Delphi procedure. *Ultrasound Obstet. Gynecol.* **48,** 333–339 (2016).

39. Crovetto, F. *et al.* First-trimester screening for early and late small-for-gestational-age neonates using maternal serum biochemistry, blood pressure and uterine artery Doppler. *Ultrasound Obstet. Gynecol.* **43,** 34–40 (2014).

40. Figueras, F. & Gratacós, E. Update on the Diagnosis and Classification of Fetal Growth Restriction and Proposal of a Stage-Based Management Protocol. *Fetal Diagn. Ther.* **36,** 86–98 (2014).

41. Oros, D. *et al.* Longitudinal changes in uterine, umbilical and fetal cerebral Doppler indices in late-onset small-for-gestational age fetuses. *Ultrasound Obstet. Gynecol.* **37,** 191–195 (2011).

42. Miller, S. L., Huppi, P. S. & Mallard, C. The consequences of fetal growth restriction on brain structure and neurodevelopmental outcome. *J. Physiol.* **594,** 807–823 (2016).

43. Baschat, A. A. Neurodevelopment following fetal growth restriction and its relationship with antepartum parameters of placental dysfunction. *Ultrasound Obstet. Gynecol.* **37,** 501–514 (2011).

44. Morsing, E., Asard, M., Ley, D., Stjernqvist, K. & Marsal, K. Cognitive Function After Intrauterine Growth Restriction and Very Preterm Birth. *Pediatrics* **127,** e874–e882 (2011).

45. Bernstein, I. M., Horbar, J. D., Badger, G. J., Ohlsson, A. & Golan, A. Morbidity and mortality among very-low-birth-weight neonates with intrauterine growth restriction. *Am. J. Obstet. Gynecol.* **182,** 198–206 (2000).

46. Barker, D. J. In utero programming of chronic disease. *Clin. Sci. (Lond).* **95,** 115–28 (1998).

47. Verkauskiene, R. *et al.* Birth Weight and Long-Term Metabolic Outcomes: Does the Definition of Smallness Matter? *Horm. Res.* **70,** 309–315 (2008).

48. Konje, J. C., Howarth, E. S., Kaufmann, P. & Taylor, D. J. Longitudinal quantification of uterine artery blood volume flow changes during gestation in pregnancies complicated by intrauterine growth restriction. *BJOG* **110,** 301–5 (2003).

49. McKelvey, A. *et al.* Total uterine artery blood volume flow rate in nulliparous women (TVFR) is associated with birthweight and gestation at delivery. *Ultrasound Obstet. Gynecol.* **49(1)**, 54-60 (2016).

50. Nicolaides, K. H., Rizzo, G. & Hecher, K. *Placental and fetal doppler*. (Taylor and Francis Group, 2004).

51. Barati, M., Shahbazian, N., Ahmadi, L. & Masihi, S. Diagnostic evaluation of uterine artery Doppler sonography for the prediction of adverse pregnancy outcomes. *J. Res. Med. Sci.* **19,** 515–9 (2014).

52. Yu, C. K. H., Khouri, O., Onwudiwe, N., Spiliopoulos, Y. & Nicolaides, K. H. Prediction of pre-eclampsia by uterine artery Doppler imaging: relationship

to gestational age at delivery and small-for-gestational age. **31,** 310–313 (2008).

53. Llurba, E. *et al.* Maternal history and uterine artery Doppler in the assessment of risk for development of early- and late-onset preeclampsia and intrauterine growth restriction. *Obstet. Gynecol. Int.* **2009,** 275613 (2009).

54. Gill, R. W., Trudinger, B. J., Garrett, W. J., Kossoff, G. & Warren, P. S. Fetal umbilical venous flow measured in utero by pulsed Doppler and B-mode ultrasound. *Am. J. Obstet. Gynecol.* **139,** 720–725 (1981).

55. Adamson, S. L. Arterial pressure, vascular input impedance, and resistance as determinants of pulsatile blood flow in the umbilical artery. *Eur. J. Obstet. Gynecol. Reprod. Biol.* **84,** 119–125 (1999).

56. Morrow, R. J., Adamson, S. L., Bull, S. B. & Ritchie, J. W. Effect of placental embolization on the umbilical arterial velocity waveform in fetal sheep. *Am. J. Obstet. Gynecol.* **161,** 1055–60 (1989).

57. DeVore, G. R. The importance of the cerebroplacental ratio in the evaluation of fetal well-being in SGA and AGA fetuses. *Am. J. Obstet. Gynecol.* **213,** 5–15 (2015).

58. Mifsud, W. & Sebire, N. J. Placental Pathology in Early-Onset and Late-Onset Fetal Growth Restriction. *Fetal Diagn Ther* **36,** 117–128 (2014).

59. Ferrazzi, E. *et al.* Uterine Doppler Velocimetry and Placental Hypoxic-ischemic Lesion in Pregnancies with Fetal Intrauterine Growth Restriction. *Placenta* **20,** 389–394 (1999).

60. Salafia, C. M. *et al.* Intrauterine growth restriction in infants of less than thirty-two weeks' gestation: Associated placental pathologic features. *Am. J. Obstet. Gynecol.* **173,** 1049–1057 (1995).

61. Macara, L. *et al.* Elaboration of stem villous vessels in growth restricted pregnancies with abnormal umbilical artery Doppler waveforms. *Br. J.*

Obstet. Gynaecol. **102,** 807–12 (1995).

62. Apel-Sarid, L., Levy, A., Holcberg, G. & Sheiner, E. Term and preterm (<34 and <37 weeks gestation) placental pathologies associated with fetal growth restriction. *Arch. Gynecol. Obstet.* **282,** 487–492 (2010).

63. Groom, K. M. & David, A. L. The role of aspirin, heparin, and other interventions in the prevention and treatment of fetal growth restriction. *Am. J. Obstet. Gynecol.* **218,** S829–S840 (2018).

64. Sharp, A. *et al.* Maternal sildenafil for severe fetal growth restriction (STRIDER): a multicentre, randomised, placebo-controlled, double-blind trial. *Lancet Child Adolesc. Heal.* **2,** 93–102 (2018).

65. Mehta, V. *et al.* Long-term increase in uterine blood flow is achieved by local overexpression of VEGF-A165 in the uterine arteries of pregnant sheep. *Gene Ther.* **19,** 925–935 (2012).

66. Lopez-Tello, J. *et al.* The effects of sildenafil citrate on feto–placental development and haemodynamics in a rabbit model of intrauterine growth restriction. *Reprod. Fertil. Dev.* **29,** 1239 (2017).

67. Leiser, R., Luckhardt, M., Kaufmann, P., Winterhager, E. & Bruns, U. The fetal vascularisation of term human placental villi. *Anat. Embryol. (Berl).* **173,** 71–80 (1985).

68. Leiser, R., Krebs, C., Ebert, B. & Dantzer, V. Placental vascular corrosion cast studies: A comparison between ruminants and humans. *Microsc. Res. Tech.* **38,** 76–87 (1997).

69. McCarthy, R. *et al.* Three-dimensional digital reconstruction of human placental villus architecture in normal and complicated pregnancies. *Eur. J. Obstet. Gynecol. Reprod. Biol.* **197,** 130–135 (2016).

70. Jirkovská, M., Kubínová, L., Janáček, J. & Kaláb, J. 3-D STUDY OF VESSELS IN PERIPHERAL PLACENTAL VILLI. *Image Anal Stereol Orig.*

Res. Pap. **26,** 165–168 (2007).

71. Plitman Mayo, R. *et al.* Computational modeling of the structure-function relationship in human placental terminal villi. *J. Biomech.* **49(16),** 3780–7 (2016).

72. Paulus, M. J., Gleason, S. S., Kennel, S. J., Hunsicker, P. R. & Johnson, D. K. High Resolution X-ray Computed Tomography: An Emerging Tool for Small Animal Cancer Research. *Neoplasia* **2,** 62–70 (2000).

73. Behrooz, A., Tseng, J.-C. & Meganck, J. *Image Resolution in MicroCT: Principles and Characterization of the Quantum FX and Quantum GX Systems*. at <http://www.qrm.de/content/>

74. Holdsworth, D. W. & Thornton, M. M. Micro-CT in small animal and specimen imaging. *Trends Biotechnol.* **20,** S34–S39 (2002).

75. Staude, A. & Goebbels, J. *Determining the Spatial Resolution in Computed Tomography – Comparison of MTF and Line-Pair Structures*. at <https://www.ndt.net/article/dir2011/papers/tu41.pdf>

76. Rueckel, J. *et al.* Spatial resolution characterization of a X-ray microCT system. *Appl. Radiat. Isot.* **94,** 230–234 (2014).

77. Kapadia, R. D. *et al.* Applications of micro-CT and MR microscopy to study pre-clinical models of osteoporosis and osteoarthritis. *Technol. Health Care* **6,** 361–72 (1998).

78. Genant, H. K. *et al.* Advanced imaging of bone macro and micro structure. *Bone* **25,** 149–52 (1999).

79. Lerman, A. & Ritman, E. L. Evaluation of microvascular anatomy by micro-CT. *Herz* **24,** 531–3 (1999).

80. Jorgensen, S. M., Demirkaya, O. & Ritman, E. L. Three-dimensional imaging of vasculature and parenchyma in intact rodent organs with X-ray micro-CT. *Am. J. Physiol.* **275,** H1103-14 (1998).

81. Ortiz, M. C. *et al.* Microcomputed tomography of kidneys following chronic

bile duct ligation. *Kidney Int.* **58,** 1632–1640 (2000).

82. Higgins, W. E., Ritman, E. L., Kiraly, A. P. & Shu-Yen Wan. Extraction of the hepatic vasculature in rats using 3-D micro-CT images. *IEEE Trans. Med. Imaging* **19,** 964–971 (2000).

83. Beighley, P. E., Thomas, P. J., Jorgensen, S. M. & Ritman, E. L. 3D architecture of the myocardial microcirculation in intact rat heart: A study with Micro-CT. In: Sideman S, Beyar R. (eds) Analytical and Qunatitative Cardiology. Advances in Experimental Medicince and Biology, vol 430. 165–175 (Springer, Boston, MA, 1997). doi:10.1007/978-1-4615-5959-7_14

84. Rennie, M. Y., Whiteley, K. J., Kulandavelu, S., Adamson, S. L. & Sled, J. G. 3D visualisation and quantification by microcomputed tomography of late gestational changes in the arterial and venous feto-placental vasculature of the mouse. *Placenta* **28,** 833–40 (2007).

85. Rennie, M. Y. *et al.* Vessel tortuousity and reduced vascularization in the fetoplacental arterial tree after maternal exposure to polycyclic aromatic hydrocarbons. *Am. J. Physiol. Heart Circ. Physiol.* **300,** H675-84 (2011).

86. Langheinrich, A. C. *et al.* Analysis of the fetal placental vascular tree by X-ray micro-computed tomography. *Placenta* **25,** 95–100 (2004).

87. Langheinrich, A. C. *et al.* Quantitative 3D micro-CT imaging of the human feto-placental vasculature in intrauterine growth restriction. *Placenta* **29,** 937–41 (2008).

88. Junaid, T. O., Brownbill, P., Chalmers, N., Johnstone, E. D. & Aplin, J. D. Fetoplacental vascular alterations associated with fetal growth restriction. *Placenta* **35,** 808–15 (2014).

89. Junaid, T. O., Bradley, R. S., Lewis, R. M., Aplin, J. D. & Johnstone, E. D. Whole organ vascular casting and microCT examination of the human placental vascular tree reveals novel alterations associated with pregnancy disease. *Sci. Rep.* **7,** 4144 (2017).

90. Mercé, L. T., Barco, M. J. & Bau, S. Reproducibility of the study of placental vascularization by three-dimensional power Doppler. *J. Perinat. Med.* **32,** 228–33 (2004).

91. Zalud, I. & Shaha, S. Evaluation of the utero-placental circulation by three-dimensional Doppler ultrasound in the second trimester of normal pregnancy. *J. Matern. Neonatal Med.* **20,** 299–305 (2007).

92. Merce, L. T., Barco, M. J., Bau, S., Kupesic, S. & Kurjak, A. Assessment of placental vascularization by three-dimensional power Doppler "vascular biopsy" in normal pregnancies. *Croat. Med. J.* **46,** 765–71 (2005).

93. Noguchi, J., Hata, K., Tanaka, H. & Hata, T. Placental Vascular Sonobiopsy Using Three-dimensional Power Doppler Ultrasound in Normal and Growth Restricted Fetuses. *Placenta* **30,** 391–397 (2009).

94. Guiot, C. *et al.* Is three-dimensional power Doppler ultrasound useful in the assessment of placental perfusion in normal and growth-restricted pregnancies? *Ultrasound Obstet. Gynecol.* **31,** 171–176 (2008).

95. McRobbie, D. W., Moore, E. A., Graves, M. J. & Prince, M. R. *MRI from Picture to Proton*. (Cambridge University Press, 2017). doi:10.1017/9781107706958

96. Gowland, P. Placental MRI. *Semin. Fetal Neonatal Med.* **10,** 485–490 (2005).

97. Damodaram, M. *et al.* Placental MRI in intrauterine fetal growth restriction. *Placenta* **31,** 491–498 (2010).

98. Ray, J. G., Vermeulen, M. J., Bharatha, A., Montanera, W. J. & Park, A. L. Association Between MRI Exposure During Pregnancy and Fetal and Childhood Outcomes. *JAMA* **316,** 952 (2016).

99. Cameron, I. L., Ord, V. A. & Fullerton, G. D. Characterization of proton NMR relaxation times in normal and pathological tissues by correlation with other

tissue parameters. *Magn. Reson. Imaging* **2,** 97–106 (1984).

100. Gowland, P. A. *et al.* In vivo relaxation time measurements in the human placenta using echo planar imaging at 0.5 T. *Magn. Reson. Imaging* **16,** 241–7 (1998).

101. Wright, C. *et al.* Magnetic resonance imaging relaxation time measurements of the placenta at 1.5 T. *Placenta* **32,** 1010–5 (2011).

102. Huen, I. *et al.* R1 and R2 * changes in the human placenta in response to maternal oxygen challenge. *Magn. Reson. Med.* **70,** 1427–33 (2013).

103. Ingram, E. *et al.* R1 changes in the human placenta at 3 T in response to a maternal oxygen challenge protocol. *Placenta* **39,** 151–153 (2016).

104. Ingram, E., Morris, D., Naish, J., Myers, J. & Johnstone, E. MR Imaging Measurements of Altered Placental Oxygenation in Pregnancies Complicated by Fetal Growth Restriction. *Radiology* **285,** 953–960 (2017).

105. Derwig, I. *et al.* Association of placental T2 relaxation times and uterine artery Doppler ultrasound measures of placental blood flow. *Placenta* **34,** 474–479 (2013).

106. Sinding, M. *et al.* Placental magnetic resonance imaging T2* measurements in normal pregnancies and in those complicated by fetal growth restriction. *Ultrasound Obstet. Gynecol.* **47,** 748–754 (2016).

107. Sinding, M. *et al.* Prediction of low birth weight: Comparison of placental T2* estimated by MRI and uterine artery pulsatility index. *Placenta* **49,** 48–54 (2017).

108. Sørensen, A. *et al.* Changes in human placental oxygenation during maternal hyperoxia estimated by blood oxygen level-dependent magnetic resonance imaging (BOLD MRI). *Ultrasound Obstet. Gynecol.* **42,** 310–4 (2013).

109. Ingram, E. *et al.* MRI measures of in vivo placental oxygenation differ between normal and fetal growth restricted pregnancies. *Placenta* **36,** A6

(2015).

110. Sørensen, A. *et al.* Changes in human fetal oxygenation during maternal hyperoxia as estimated by BOLD MRI. *Prenat. Diagn.* **33,** 141–5 (2013).

111. Helenius, J. *et al.* Diffusion-Weighted MR Imaging in Normal Human Brains in Various Age Groups. *AJNR Am. J. Neuroradiol.* **23,** 194–199 (2002).

112. Manganaro, L. *et al.* MRI and DWI: feasibility of DWI and ADC maps in the evaluation of placental changes during gestation. *Prenat. Diagn.* **30,** 1178–84 (2010).

113. Sivrioğlu, A. K. *et al.* Evaluation of the placenta with relative apparent diffusion coefficient and T2 signal intensity analysis. *Diagn. Interv. Radiol.* **19,** 495–500 (2013).

114. Solomon, E. *et al.* Major mouse placental compartments revealed by diffusion-weighted MRI, contrast-enhanced MRI, and fluorescence imaging. *Proc. Natl. Acad. Sci. U. S. A.* **111,** 10353–10358 (2014).

115. Bonel, H. M. *et al.* Diffusion-weighted MR imaging of the placenta in fetuses with placental insufficiency. *Radiology* **257,** 810–9 (2010).

116. Javor, D. *et al.* In vivo assessment of putative functional placental tissue volume in placental intrauterine growth restriction (IUGR) in human fetuses using diffusion tensor magnetic resonance imaging. *Placenta* **34,** 676–80 (2013).

117. Le Bihan, D. *et al.* MR imaging of intravoxel incoherent motions: application to diffusion and perfusion in neurologic disorders. *Radiology* **161,** 401–7 (1986).

118. Le Bihan, D. & Turner, R. The capillary network: a link between IVIM and classical perfusion. *Magn. Reson. Med.* **27,** 171–8 (1992).

119. Moore, R. J. *et al.* In vivo intravoxel incoherent motion measurements in the human placenta using echo-planar imaging at 0.5 T. *Magn. Reson. Med.* **43,** 295–302 (2000).

120. Moore, R. J. *et al.* In utero perfusing fraction maps in normal and growth restricted pregnancy measured using IVIM echo-planar MRI. *Placenta* **21,** 726–32 (2000).

121. Hayot, P. *et al.* OP09.01: Human placental perfusion analysis by diffusion-weighted MRI. *Ultrasound Obstet. Gynecol.* **46,** 76–77 (2015).

122. Moore, R. J. *et al.* Spiral artery blood volume in normal pregnancies and those compromised by pre-eclampsia. *NMR Biomed.* **21,** 376–80 (2008).

123. Alison, M. *et al.* Use of intravoxel incoherent motion MR imaging to assess placental perfusion in a murine model of placental insufficiency. *Invest. Radiol.* **48,** 17–23 (2013).

124. Alsop, D. C. *et al.* Recommended implementation of arterial spin-labeled perfusion MRI for clinical applications: A consensus of the ISMRM perfusion study group and the European consortium for ASL in dementia. *Magn. Reson. Med.* **73,** 102–116 (2015).

125. Gowland, P. A. *et al.* In vivo perfusion measurements in the human placenta using echo planar imaging at 0.5 T. *Magn. Reson. Med.* **40,** 467–473 (1998).

126. Duncan, K. R. *et al.* The investigation of placental relaxation and estimation of placental perfusion using echo-planar magnetic resonance imaging. *Placenta* **19,** 539–43 (1998).

127. Francis, S. T. *et al.* Non-invasive mapping of placental perfusion. *Lancet (London, England)* **351,** 1397–9 (1998).

128. Derwig, I. *et al.* Association of placental perfusion, as assessed by magnetic resonance imaging and uterine artery Doppler ultrasound, and its relationship to pregnancy outcome. *Placenta* **34,** 885–91 (2013).

129. Medicines and Healthcare Products Regulatory Agency. *Safety Guidelines for Magnetic Resonance Imaging in Cinical Use*.

130. Edwards, M. J., Saunders, R. D. & Shiota, K. Effects of heat on embryos and foetuses. *Int. J. Hyperthermia* **19,** 295–324

131. Levine, D., Zuo, C., Faro, C. B. & Chen, Q. Potential heating effect in the gravid uterus during MR HASTE imaging. *J. Magn. Reson. Imaging* **13,** 856–61 (2001).

132. Ruckhäberle, E. *et al.* In vivo intrauterine sound pressure and temperature measurements during magnetic resonance imaging (1.5 T) in pregnant ewes. *Fetal Diagn. Ther.* **24,** 203–10 (2008).

133. Hand, J. W., Li, Y., Thomas, E. L., Rutherford, M. A. & Hajnal, J. V. Prediction of specific absorption rate in mother and fetus associated with MRI examinations during pregnancy. *Magn. Reson. Med.* **55,** 883–93 (2006).

134. Hand, J. W., Li, Y. & Hajnal, J. V. Numerical study of RF exposure and the resulting temperature rise in the foetus during a magnetic resonance procedure. *Phys. Med. Biol.* **55,** 913–30 (2010).

135. Gowland, P. A. & De Wilde, J. Temperature increase in the fetus due to radio frequency exposure during magnetic resonance scanning. *Phys. Med. Biol.* **53,** L15-8 (2008).

136. Brugger, P. C. & Prayer, D. Actual imaging time in fetal MRI. *Eur. J. Radiol.* **81,** e194-6 (2012).

137. International Commission on Non-Ionising Radiation (ICNIRP), Medical Magnetic Resonance (MR) Procedures: Protection of patients. *Health Phys.* **87,** 197–216 (2004).

138. Noise: a hazard for the fetus and newborn. American Academy of Pediatrics. Committee on Environmental Health. *Pediatrics* **100,** 724–7 (1997).

139. Baker, P. N., Johnson, I. R., Harvey, P. R., Gowland, P. A. & Mansfield, P. A three-year follow-up of children imaged in utero with echo-planar magnetic resonance. *Am. J. Obstet. Gynecol.* **170,** 32–3 (1994).

140. Reeves, M. J. *et al.* Neonatal cochlear function: measurement after exposure to acoustic noise during in utero MR imaging. *Radiology* **257,** 802–

9 (2010).

141. Kok, R. D., de Vries, M. M., Heerschap, A. & van den Berg, P. P. Absence of harmful effects of magnetic resonance exposure at 1.5 T in utero during the third trimester of pregnancy: a follow-up study. *Magn. Reson. Imaging* **22,** 851–854 (2004).

142. Bouyssi-Kobar, M., du Plessis, A. J., Robertson, R. L. & Limperopoulos, C. Fetal magnetic resonance imaging: exposure times and functional outcomes at preschool age. *Pediatr. Radiol.* **45(12)**, 1823-30 (2015).

143. Strizek, B. *et al.* Safety of MR Imaging at 1.5 T in Fetuses: A Retrospective Case-Control Study of Birth Weights and the Effects of Acoustic Noise. *Radiology* **275,** 530–7 (2015).

144. Gerhardt, K. J., Abrams, R. M. & Oliver, C. C. Sound environment of the fetal sheep. *Am. J. Obstet. Gynecol.* **162,** 282–7 (1990).

145. Richards, D. S., Frentzen, B., Gerhardt, K. J., McCann, M. E. & Abrams, R. M. Sound levels in the human uterus. *Obstet. Gynecol.* **80,** 186–90 (1992).

146. Arulkumaran, S. *et al.* In-utero sound levels when vibroacoustic stimulation is applied to the maternal abdomen: an assessment of the possibility of cochlea damage in the fetus. *Br. J. Obstet. Gynaecol.* **99,** 43–5 (1992).

147. Gerhardt, K. J. *et al.* Cochlear microphonics recorded from fetal and newborn sheep. *Am. J. Otolaryngol.* **13,** 226–233 (1992).

148. Gerhardt, K. J. *et al.* Fetal sheep in utero hear through bone conduction. *Am. J. Otolaryngol.* **17,** 374–9 (1996).

149. Price, D. Safe Clinical Practice- Acoustic Noise. in *ISMRM Safety Workshop* (2012).

150. Poutamo, J., Partanen, K., Vanninen, R., Vainio, P. & Kirkinen, P. MRI does not change fetal cardiotocographic parameters. *Prenat. Diagn.* **18,** 1149–54 (1998).

151. Michel, S. C. A. *et al.* Original report. Fetal cardiographic monitoring during

1.5-T MR imaging. *AJR. Am. J. Roentgenol.* **180,** 1159–64 (2003).

152. Schindelin, J., Rueden, C. T., Hiner, M. C. & Eliceiri, K. W. The ImageJ ecosystem: An open platform for biomedical image analysis. *Mol. Reprod. Dev.* **82,** 518–529 (2015).

153. Pathak, S. *et al.* Cord coiling, umbilical cord insertion and placental shape in an unselected cohort delivering at term: Relationship with common obstetric outcomes. *Placenta* **31,** 963–968 (2010).

154. Scarfe, W. C. & Farman, A. G. What is Cone-Beam CT and How Does it Work? *Dent. Clin. North Am.* **52,** 707–730 (2008).

155. Arganda-Carreras *et al.* Trainable_Segmentation: Release v3.1.2. doi:10.5281/ZENODO.59290

156. Marxen, M. *et al.* MicroCT scanner performance and considerations for vascular specimen imaging. *Med. Phys.* **31,** 305–13 (2004).

157. Gignac, P. M. *et al.* Diffusible iodine-based contrast-enhanced computed tomography (diceCT): an emerging tool for rapid, high-resolution, 3-D imaging of metazoan soft tissues. *J. Anat.* **228(6)**, 889-909, (2016).

158. Grabherr, S., Djonov, V., Yen, K., Thali, M. J. & Dirnhofer, R. Postmortem angiography: review of former and current methods. *AJR. Am. J. Roentgenol.* **188,** 832–8 (2007).

159. Zagorchev, L. *et al.* Micro computed tomography for vascular exploration. *J. Angiogenes. Res.* **2,** 7 (2010).

160. Bentley, M. D., Ortiz, M. C., Ritman, E. L. & Romero, J. C. The use of microcomputed tomography to study microvasculature in small rodents. *Am. J. Physiol. Regul. Integr. Comp. Physiol.* **282,** R1267-79 (2002).

161. Jauniaux, E., Moscoso, J. G., Vanesse, M., Campbell, S. & Driver, M. Perfusion fixation for placental morphologic investigation. *Hum. Pathol.* **22,** 442–9 (1991).

162. Castle, B. & Mackenzie, I. Z. *Fetal Physiological Measurements*. *Fetal*

Physiological Measurements (Elsevier, 1986). doi:10.1016/B978-0-407-00450-4.50013-7

163. Weiner, C. P. *et al.* Normal values for human umbilical venous and amniotic fluid pressures and their alteration by fetal disease. *Am. J. Obstet. Gynecol.* **161,** 714–7 (1989).

164. Johnson, P., Maxwell, D. J., Tynan, M. J. & Allan, L. D. Intracardiac pressures in the human fetus. *Heart* **84,** 59–63 (2000).

165. Struijk, P. C. *et al.* Blood pressure estimation in the human fetal descending aorta. *Ultrasound Obstet. Gynecol.* **32,** 673–81 (2008).

166. Paepe, M. E. De. Examination of the twin placenta. *Semin. Perinatol.* **39,** 27–35 (2015).

167. MJ, B. *et al.* National Institutes of Standards and Technology Photon Cross Sections Database. (1998). at <http://physics.nist.gov/PhysRefData/Xcom/html/xcom1.html>

168. Granton, P. V, Pollmann, S. I., Ford, N. L., Drangova, M. & Holdsworth, D. W. Implementation of dual- and triple-energy cone-beam micro-CT for postreconstruction material decomposition. *Med. Phys.* **35,** 5030–42 (2008).

169. Learmont, J. G. & Poston, L. Nitric oxide is involved in flow-induced dilation of isolated human small fetoplacental arteries. *Am. J. Obstet. Gynecol.* **174,** 583–588 (1996).

170. Redline, R. W. Placental Pathology: A Systematic Approach with Clinical Correlations. *Placenta* **29,** 86–91 (2008).

171. Den Buijs, J. O. *et al.* Branching morphology of the rat hepatic portal vein tree: a micro-CT study. *Ann. Biomed. Eng.* **34,** 1420–8 (2006).

172. Lee, J., Beighley, P., Ritman, E. & Smith, N. Automatic segmentation of 3D micro-CT coronary vascular images. *Med. Image Anal.* **11,** 630–647 (2007).

173. Fridman, Y., Pizer, S. M., Aylward, S. & Bullitt, E. Extracting branching tubular object geometry via cores. *Med. Image Anal.* **8,** 169–176 (2004).

174. Kline, T. L., Zamir, M. & Ritman, E. L. Accuracy of Microvascular Measurements Obtained From Micro-CT Images. *Ann. Biomed. Eng.* **38,** 2851–2864 (2010).

175. Leiser, R., Luckhardt, M., Kaufmann, P., Winterhager, E. & Bruns, U. The fetal vascularisation of term human placental villi. I. Peripheral stem villi. *Anat. Embryol. (Berl).* **173,** 71–80 (1985).

176. Mayhew, T. M. *et al.* Stereological investigation of placental morphology in pregnancies complicated by pre-eclampsia with and without intrauterine growth restriction. *Placenta* **24,** 219–26

177. Burton, G. J. The fine structure of the human placental villus as revealed by scanning electron microscopy. *Scanning Microsc.* **1,** 1811–28 (1987).

178. Melbourne, A. *et al.* DECIDE: Diffusion-rElaxation Combined Imaging for Detailed Placental Evaluation. *ISMRM 25th Annu. Meet. Exhib.* (2017).

179. Stanisz, G. J. *et al.* T1, T2 relaxation and magnetization transfer in tissue at 3T. *Magn. Reson. Med.* **54,** 507–512 (2005).

180. Lemke, A., Laun, F. B., Simon, D., Stieltjes, B. & Schad, L. R. An in vivo verification of the intravoxel incoherent motion effect in diffusion-weighted imaging of the abdomen. *Magn. Reson. Med.* **64,** 1580–1585 (2010).

181. Hadlock, F. P., Harrist, R. B., Carpenter, R. J., Deter, R. L. & Park, S. K. Sonographic estimation of fetal weight. The value of femur length in addition to head and abdomen measurements. *Radiology* **150,** 535–40 (1984).

182. Doel, T. *et al.* GIFT-Cloud: A data sharing and collaboration platform for medical imaging research. *Comput. Methods Programs Biomed.* **139,** 181–190 (2017).

183. Melbourne, A. *et al.* Registration of dynamic contrast-enhanced MRI using a progressive principal component registration (PPCR). *Phys. Med. Biol.* **52,** 5147–5156 (2007).

184. Modat, M. *et al.* Fast free-form deformation using graphics processing units.

Comput. Methods Programs Biomed. **98,** 278–284 (2010).

185. Portnoy, S. *et al.* Relaxation properties of human umbilical cord blood at 1.5 Tesla. *Magn. Reson. Med.* **77,** 1678–1690 (2017).

186. Jerome, N. P. *et al.* Extended T2-IVIM model for correction of TE dependence of pseudo-diffusion volume fraction in clinical diffusion-weighted magnetic resonance imaging. *Phys. Med. Biol.* **61,** N667–N680 (2016).

187. Siauve, N. *et al.* Assessment of human placental perfusion by intravoxel incoherent motion MR imaging. *J. Matern. Neonatal Med.* 1–8 (2017).

188. Mathis, J., Raio, L. & Baud, D. Fetal laser therapy: applications in the management of fetal pathologies. *Prenat. Diagn.* **35,** 623–36 (2015).

189. de Bazelaire, C. M. J., Duhamel, G. D., Rofsky, N. M. & Alsop, D. C. MR Imaging Relaxation Times of Abdominal and Pelvic Tissues Measured in Vivo at 3.0 T: Preliminary Results. *Radiology* **230,** 652–659 (2004).

190. Siggaard-Andersen, O. & Huch, & R. The oxygen status of fetal blood. *Acta Anaesthesiol Scand Suppl.* **39,** 129–135 (1995).

191. Nikolov, A. *et al.* [Reference values range of the fetal oxygen saturation and its dispersal during labor without cardiotocographic evidence for fetal distress]. *Akush. Ginekol. (Sofiia).* **44,** 24–31 (2005).

192. Motulsky, H. & Christopoulos, A. *Fitting models to biological data using linear and nonlinear regression : a practical guide to curve fitting*. (Oxford University Press, 2004).

193. Khong, T. Y. *et al.* Sampling and Definitions of Placental Lesions: Amsterdam Placental Workshop Group Consensus Statement. *Arch. Pathol. Lab. Med.* **140,** 698–713 (2016).

194. Soothill, P. W., Nicolaides, K. H. & Campbell, S. Prenatal asphyxia, hyperlacticaemia, hypoglycaemia, and erythroblastosis in growth retarded fetuses. *Br. Med. J. (Clin. Res. Ed).* **294,** 1051–3 (1987).

195. Edoh, D., Antwi-Bosaiko, C. & Amuzu, D. Fetal hemoglobin during infancy and in sickle cell adults. *Afr. Health Sci.* **6,** 51–4 (2006).

196. 3. Fetal hemoglobin: Structure and function. *Scand. J. Clin. Lab. Invest.* **42,** 32–37 (1982).

197. Thomas, C. & Lumb, A. B. Physiology of haemoglobin. *Contin. Educ. Anaesth. Crit. Care Pain* **12,** 251–256 (2012).

198. Jopling, J., Henry, E., Wiedmeier, S. E. & Christensen, R. D. Reference Ranges for Hematocrit and Blood Hemoglobin Concentration During the Neonatal Period: Data From a Multihospital Health Care System. *Pediatrics* **123,** e333-7 (2009).

199. Soothill, P. W., Nicolaides, K. H., Rodeck, C. H. & Campbell, S. Effect of gestational age on fetal and intervillous blood gas and acid-base values in human pregnancy. *Fetal Ther.* **1,** 168–75 (1986).

200. Lin, A.-L., Qin, Q., Zhao, X. & Duong, T. Q. Blood longitudinal (T 1) and transverse (T 2) relaxation time constants at 11.7 Tesla. *MAGMA*, **25(3)**, 245-9, (2012).

201. Sebire, N. J. & Talbert, D. The dynamic placenta: II. Hypothetical model of a fetus driven transplacental water balance mechanism producing low apparent permeability in a highly permeable placenta. *Med. Hypotheses* **62,** 520–8 (2004).

202. Wang, G. *et al.* Slic-Seg : Slice-by-slice Segmentation Propagation of the Placenta in Fetal MRI using One-plane Scribbles and Online Learning. in *MICCAI***,** 29–37 (Springer, Cham, 2015).

203. Wang, G. *et al.* Slic-Seg: A minimally interactive segmentation of the placenta from sparse and motion-corrupted fetal MRI in multiple views. *Med. Image Anal.* **34,** 137–147 (2016).

204. Owens, J. A., Falconer, J. & Robinson, J. S. Effect of restriction of placental growth on umbilical and uterine blood flows. *Am. J. Physiol.* **250,** R427-34

(1986).

205. Rennie, M. Y., Whiteley, K. J., Adamson, S. L. & Sled, J. G. Quantification of Gestational Changes in the Uteroplacental Vascular Tree Reveals Vessel Specific Hemodynamic Roles During Pregnancy in Mice. *Biol. Reprod.* **95,** 43–43 (2016).

206. Grigsby, P. L. Animal Models to Study Placental Development and Function throughout Normal and Dysfunctional Human Pregnancy. *Semin. Reprod. Med.* **34,** 11–6 (2016).

207. Swanson, A. M. & David, A. L. Animal models of fetal growth restriction: Considerations for translational medicine. *Placenta* **36,** 623–630 (2015).

208. Song, F., Wu, W., Qian, Z., Zhang, G. & Cheng, Y. Assessment of the Placenta in Intrauterine Growth Restriction by Diffusion-Weighted Imaging and Proton Magnetic Resonance Spectroscopy. *Reprod. Sci.* **24,** 575–581 (2017).